Molecular mechanisms of phosphatidylinositol 4-kinase III *beta* (PI4KB) regulation and their role in human disease

by

Jacob Alec McPhail
BSc (Honours), University of Victoria, 2015

A Dissertation Submitted in Partial Fulfillment
of the Requirements for the Degree of

DOCTOR OF PHILOSOPHY

in the Department of Biochemistry and Microbiology

Supervisory Committee

Molecular mechanisms of phosphatidylinositol 4-kinase III beta (PI4KB) regulation and their role in human disease

by

Jacob Alec McPhail
BSc (Honours), University of Victoria, 2015

Supervisory Committee

Dr. John E. Burke, Department of Biochemistry and Microbiology
Supervisor

Dr. Alisdair B. Boraston, Department of Biochemistry and Microbiology
Departmental Member

Dr. Caroline E. Cameron, Department of Biochemistry and Microbiology
Departmental Member

Dr. Fraser Hoff, Department of Chemistry
Outside Member

Abstract

The lipid signalling molecule phosphatidylinositol 4-phosphate (PI4P) is an essential factor in the coordinated regulation of membrane trafficking, lipid transport and cytokinesis. At the Golgi, a key generator of PI4P is the type III phosphatidylinositol 4-kinase *beta* isoform (PI4KIIIβ), which has been identified as a host factor necessary for the replication of numerous devastating pathogenic viruses. Crucial to the regulation of PI4KIIIβ are interactions with a variety of both host and viral protein-binding partners. Additionally, parasite homologs of PI4KIIIβ have been established as essential enzymes in the proliferation of the malaria and cryptosporidiosis parasites. Therefore, study of PI4KIIIβ and its regulatory proteins is of great importance in understanding normal cellular signalling and the proliferation of viral and parasite pathogens.

To study PI4KIIIβ regulation, I utilized a multifaceted approach of biochemistry, hydrogen-deuterium exchange mass spectrometry (HDX-MS), and X-ray crystallography to elucidate molecular mechanisms of PI4KIIIβ regulation by the key protein binding partners ACBD3 and c10orf76, and viral proteins that manipulate these complexes. This synergistic approach provided a unique opportunity to study the structure and dynamics of both normal PI4KIIIβ regulation and inhibition by small molecules. This dissertation will consist of an introduction to signalling of PI4KIIIβ and its role in disease, followed by two data chapters wherein I investigate ACBD3 and c10orf76 regulatory complexes required for viral replication. A third data chapter summarizes my efforts in defining the molecular basis of inhibitor selectivity towards PI4KIIIβ and related lipid kinases. A conclusion and discussion of future directions will be presented in the final chapter.

Fundamentally understanding how PI4KIIIβ is regulated, and how viruses manipulate PI4KIIIβ signalling, will expand our knowledge of PI4KIIIβ biology and facilitate development of novel therapeutic strategies targeting this pathway. My work provides novel insight into the complex regulation of PI4KIIIβ and elucidates molecular mechanisms of selective inhibition by therapeutic small molecule inhibitors. Altogether this dissertation contributes significant advances in our understanding of the role of PI4KIIIβ in signalling and human disease.

Table of Contents

List of Figures

List of Tables

List of Abbreviations

aa	amino acid
ADP	adenosine di-phosphate
ATP	adenosine tri-phosphate
ACBD3	acyl-CoA binding domain containing protein 3
AKAP	A-kinase anchoring protein
Arf1	ADP-ribosylation factor 1, member of the Ras superfamily of small GTPases
bMe	beta mercaptoethanol
BFA	brefeldin A
c10orf76	protein encoded by chromosome 10, open reading frame 76
CFP	cyan fluorescent protein
DNA	deoxyribonucleic acid
eGFP	enhanced green fluorescent protein
EtOH	ethanol
FKBP12	FK506-binding protein 12
FRB	fragment of rapamycin binding
GEF	guanine nucleotide exchange factor
GBF1	Golgi Brefeldin A Resistant Nucleotide Exchange Factor 1, GEF for Arf1
eGFP	green fluorescent protein
GST	glutathione S-transferase
HDX-MS	hydrogen-deuterium exchange mass spectrometry
ITC	isothermal titration calorimetry
MS	mass spectrometry
MS/MS	tandem mass spectrometry
MWCO	molecular weight cutoff
Ni-NTA	nickel nitrotriacetic acid
PBS	phosphate buffered saline
PC	phosphatidylcholine
PCR	polymerase chain reaction

PDB	protein data bank
PE	phosphatidylethanolamine
PI	phosphatidylinositol
PI3K	phosphoinositide 3-kinase
PI4KIIIβ or PI4KB	phosphatidylinositol 4-kinase type III *beta*
PI4P	phosphatidylinositol 4-phosphate
PIP_3	phosphatidylinositol 3,4,5 triphosphate
PITPs	phosphatidylinositol transfer proteins
PKA	protein kinase A (cAMP-dependent protein kinase)
PKD	protein kinase D
PM	plasma membrane
PS	phosphatidylserine
Rab11	Ras-related in brain protein 11, member of the Ras superfamily of small GTPases
RFP	red fluorescent protein
RTK	receptor tyrosine kinase
SDS-PAGE	sodium dodecyl sulfate polyacrylamide gel electrophoresis
Sf9	*Spodoptera frugiperda 9*
Strep	streptavidin
TCEP	tris(2-carboxyethyl)phosphine
TEV	tobacco etch virus protease
WT	wild-type

Acknowledgments

I would first like to acknowledge that this research was supported by a doctoral scholarship from Natural Sciences and Engineering Research Council of Canada (NSERC), University of Victoria Fellowships and President's Research Scholarships, and several generous donor awards including the Howard E. Petch Research Scholarship, Robert W. Ford Graduate Scholarship, Charles S. Humphrey Graduate Award, and Julius F. Schleicher Graduate Scholarship. I am grateful for this financial support.

In particular, I want to thank Dr. John Burke for inspiring my pursuit of a PhD. You have been an excellent mentor, and your guidance over the last five years has undoubtedly helped me grow as a scientist, and as a mentor myself. Thank you for your persistence and patience, which have undoubtedly promoted my success in this program and as a researcher overall. I also appreciate your efforts made beyond the laboratory, and all the consistently sound advice. In addition, I would also like to thank my first scientific mentors Dr. Elizabeth McLachlan with the Public Health Agency of Canada and Dr. Ismail Abdullahi with the Canadian Food Inspection Agency for fueling my curiosity and providing me with the initial research opportunities that eventually led to where I am today. I would like to thank my committee members Dr. Alisdair Boraston, Dr. Caroline Cameron, and Dr. Fraser Hof for their valuable insight which has improved the work of this dissertation. I also appreciate the incredible work of collaborators Dr. Tamas Balla, Dr. Joshua Pemberton, Dr. Frank van Kuppeveld, and Heyrhyoung Lyoo, who made key contributions to the work in this dissertation. There are also many people in the UVic Biochemistry department that have helped me over the years, especially the Boulanger and Boraston laboratories for sharing equipment and help with all aspects of X-ray crystallography. I also want to thank Scott, Ryan and Steve in the Biotechnical Support Centre for their great support in keeping all of our equipment running smoothly, work which was always accompanied by great jokes.

I want to thank all of the current and past Burke Lab members, it has been a pleasure working with you all. In particular, thank you Meredith, Erik, and Reece for your significant contributions to this dissertation. I want to especially thank Meredith for putting up with me for so long, and also of course Gillian for the many laughs along the way. Finally, I want to acknowledge my family across Canada for all of their love and support on this journey, and my close friends for the countless good times that have made this all worthwhile.

Dedication

I dedicate this dissertation to my father Norman, mother Kelly, and sister Emily. We have always been a close family and have been through a lot together — I would not be where I am today without all of you.

Chapter 1: Introduction to phosphatidylinositol 4-kinase IIIβ (PI4KB), related lipid kinases, and their role in cell signalling and disease.

Partially adapted from:

1. McPhail, J.A. and Burke, J.E. (accepted). Drugging the phosphoinositide 3-kinase (PI3K) and phosphatidylinositol 4-kinase (PI4K family of enzymes for treatment of cancer, immune disorders, and viral/parasitic infections. Advances in Experimental Medicine and Biology. Invited Review.
2. Dornan, G.L., McPhail, J.A. and Burke, J.E. (2016). Type III phosphatidylinositol 4 kinases: structure, function, regulation, signalling and involvement in disease. Biochemical Society Transactions. Invited Review. 44(1):260-6.

1.1 Abstract

Many important cellular functions are regulated by the selective recruitment of proteins to intracellular membranes mediated by specific interactions phosphoinositides. The enzymes that generate lipid phosphoinositides therefore must be properly positioned and regulated at their correct cellular locations. Class I phosphoinositide 3-kinases (PI3Ks) generate the lipid species phosphatidylinositol 3,4,5 tri-phosphate (PIP_3) at the plasma membrane in response to external stimuli, and are key drivers of cell growth, immune modulation and cancers. The regulation of class I PI3Ks by numerous signalling pathways has been extensively studied. Less well characterized is the regulation of the related Phosphatidylinositol 4-kinase type III *beta* (PI4KIIIβ), which generates phosphatidylinositol 4-phosphate (PI4P) at the Golgi and plays important roles in membrane trafficking, cytokinesis and organelle identity. PI4KIIIβ has been found to be an essential host factor mediating the replication of numerous devastating pathogenic viruses. Crucial to the regulation of PI4KIIIβ are its interactions with a variety of both host and viral protein-binding partners, which are not well characterized. Additionally, the parasite variant of PI4KIIIβ has been established as an essential enzyme in the proliferation of the malaria and cryptosporidiosis parasites. The study of PI4KIIIβ and its regulatory proteins is therefore of great importance in understanding normal cellular signalling and the proliferation of viral and parasitic pathogens.

1.2 Class I phosphoinositide 3-kinases (PI3Ks) and related phosphatidylinositol 4-kinase IIIβ (PI4KIIIβ)

Phosphoinositides

Phosphoinositides are essential membrane signalling molecules that regulate a multitude of cellular processes, from membrane identity and compartmentalization to growth and cell division. While they represent a small percentage of total cellular lipid composition, their correct spatiotemporal location in a cell is an essential mechanism maintaining organelle identity and membrane trafficking (1, 2). All phosphoinositides are generated from phosphatidylinositol (PI), and the inositol headgroup can be phosphorylated at the hydroxyls present at the D3, D4 and D5 positions, generating a total of seven different phosphoinositides: phosphatidylinositol 3-phosphate (PI3P), phosphatidylinositol 4-phosphate (PI4P), phosphatidylinositol 5-phosphate (PI5P), phosphatidylinositol 3,4-bisphosphate (PI(3,4)P2), phosphatidylinositol 3,5-bipshosphate (PI(3,5)P2), phosphatidylinositol 4,5-bisphosphate (PI(4,5)P2) and phosphatidylinositol 3,4,5-triphosphate (PIP3). Numerous kinases and phosphatases function in the generation of phosphoinositides, including the class I phosphoinositide 3-kinases (PI3Ks), which function downstream of cell surface receptors at the plasma membrane and are critically involved in cancer, and related phosphatidylinositol 4-kinase type III beta (PI4KIIIβ), which functions at the Golgi, is involved in viral infection, and is a major target for treatment of parasite infections (**Fig. 1.1A**).

Class I PI3Ks

The class I PI3Ks are the most well characterized phosphoinositide kinases. Class I PI3Ks are the enzymes that mediate the phosphorylation of PI(3,4,5)P3 from the substrate PI(4,5)P2. They were originally discovered as oncoproteins derived from viral proteins associated with an unknown lipid kinase activity (3, 4). It was quite rapidly determined that the generation of PIP3 was critical in growth factor signalling (5, 6), and in immune cell regulation (7). One of the most important discoveries was on the key role of PI3Ks in regulating signalling downstream of the insulin receptor (8, 9). PI3Ks are divided into three distinct classes based upon their regulatory binding partners and lipid substrate specificity. Only the class I PI3Ks can generate PIP3 from PI(4,5)P2 at the plasma membrane *in vivo* (10). These enzymes are major components of intracellular signalling networks downstream of receptor tyrosine kinases (RTKs) and G-protein

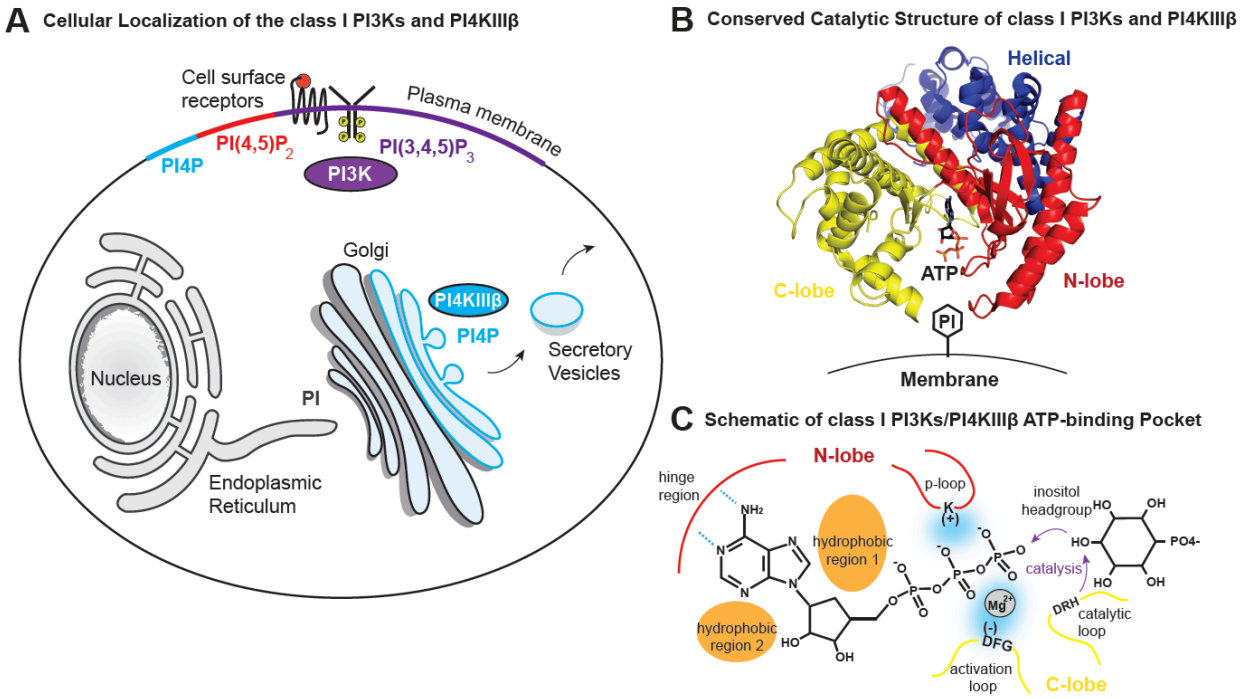

Figure 1.1. Class I PI3Ks and PI4KIIIβ utilize conserved catalytic machinery to generate specific phosphoinositides in distinct cellular locations.
(A) Cellular localizations of class I PI3Ks and related PI4KIIIβ. Class I PI3Ks are activated downstream of activated cell surface receptors, driving PIP3 production at the plasma membrane. PI4KIIIβ generates PI4P from PI at the Golgi. **(B)** Conserved catalytic structure of class I PI3Ks and PI4KIIIβ. The kinase domain consists of a well conserved N-terminal lobe and C-terminal lobe which fold to form the active site. The kinase domain packs against the helical domain, a conserved feature of all PI3K's and class III PI4K's; PDB: 1E8X. **(C)** Schematic of the class I PI3Ks/ PI4KIIIβ ATP-binding pocket. Key features of ATP binding include hydrogen bonds between the kinase hinge region and adenine moiety, accommodation of the nucleoside by hydrophobic regions, and charged interactions between ATP phosphates and lysine in the kinase P-loop.

coupled receptors (GPCRs) (11, 12). Upon activation, the generation of PIP3 by class I PI3Ks drives the recruitment of PIP3 effectors to the plasma membrane, including protein kinases (i.e. PDK1, AKT) (13), and regulators of Ras superfamily GTPases, with signal cascades downstream of these effectors playing critical roles in cell proliferation, growth, survival and tumorigenesis (11, 12, 14). Class I enzymes form heterodimers with regulatory subunits, and are further subdivided into the class IA PI3Ks (p110α, p110β, p110δ) which can bind any of five different p85 like regulatory subunits (p85a, p55a, p50a, p85b, and p55g), and the class IB PI3Ks (p110γ) which bind either a p84 or p101 regulatory subunit. The p110 subunits are commonly referred to by their gene names, PIK3CA (p110α), PIK3CB (p110β), PIK3CD (p110δ), and PIK3CG (p110γ). The interaction between catalytic and regulatory subunits plays three key roles: it stabilizes the p110 subunit, inhibits p110 activity, and allows for specific activation by pYXXM motifs present

on phosphorylated receptors and their adaptors (15, 16). These phosphorylated pYXXM motifs disrupt the SH2 domains present in the regulatory subunits that otherwise inhibit p110 kinase activity through transient inhibitory interactions (17–19). The class I PI3Ks can all be activated downstream of Ras superfamily GTPases, with PIK3CA, PIK3CD, and PIK3CG activated by Ras family GTPases (20, 21) and PIK3CB activated by Rho family GTPases (22). Class IB PI3K (PIK3CG) interacts with either a p84 (23) or p101 (24) regulatory subunits which play important roles in the activation of PIK3CG activation downstream of GPCR Gβγ subunits (25, 26). Both PIK3CA and PIK3CB are ubiquitously expressed, with PIK3CA primarily responsible for insulin signalling (27), and PIK3CB playing important roles in platelet function and blood clotting (28). The PIK3CG and PIK3CD isoforms are primarily expressed in immune cells and are important in lymphocyte activation, mast cell degranulation and leukocyte chemotaxis (29–33).

The first insight into the structural basis of regulation of these kinases was from the crystal structure of class IB PIK3CG, which revealed marked homology with protein kinases (34). The kinase domain (also referred to as a catalytic domain) exhibits a bi-lobal organization consisting of an N-terminal-lobe and C-terminal lobe that form a cleft for ATP-binding and the machinery to facilitate phosphorylation of the PI headgroup (**Fig. 1.1B**, (34, 35)).This kinase domain packs against a helical domain, a conserved feature of all PI3Ks and type III PI4Ks (36–40). The kinase hinge region, located at the cleft between the two lobes, is a key feature of the ATP binding pocket and makes critical hydrogen bonds with the adenine moiety of ATP. The nucleoside is further accommodated by hydrophobic regions and charged interactions between ATP phosphates and lysine(s) in the kinase P-loop (**Fig 1.1C**). Phosphorylation of the inositol headgroup is catalyzed by the DRH motif in the catalytic loop and is facilitated by a magnesium-dependent interaction of β and γ phosphates with the DFG motif in the activation loop (41). The very C-terminus of class I PI3Ks, class III PI3Ks, and type III PI4Ks is critical for membrane binding and kinase activity on lipid membranes and is thought to be critical in binding PI substrate (38, 42).

PI4KIIIβ

PI4KIIIβ (also frequently referred to as PI4KB) is related to class I PI3Ks. PI4KIIIβ is one of four distinct PI4Ks that generate PI4P from PI in humans: PI4KIIα (PI4K2A), PI4KIIβ (PI4K2B), PI4KIIIα (PI4KA) and PI4KIIIβ (PI4KB) (43–45). PI4KIIIβ is localized at the Golgi and trans-Golgi-network (TGN) (43–45), with PI4P pools in the Golgi apparatus generated by both

PI4KIIα and PI4KIIIβ (46). While the localization and activity of PI4KIIα is regulated through its palmitoylation, local membrane composition, and cholesterol levels (47), the activity of PI4KIIIβ is regulated by multiple protein-protein interactions and phosphorylation (38, 48, 49). PI4KIIIβ was originally identified in yeast (Pik1p) (50), with the mammalian variant identified in the late 90s through its sensitivity to the PI3K inhibitor wortmannin (51, 52). PI4KIIIβ is essential for proper Golgi formation and function, and plays important roles in mediating membrane trafficking, cytokinesis and lipid transport (53–55). The activity of PI4KIIIβ is hijacked by a number of pathogenic picornaviruses, with this playing a critical role in mediating intracellular viral replication (56–58). Finally, the parasite variants of PI4KIIIβ are essential in the replication of *Plasmodium* and *Cryptosporidium* species, which are the causative agents of malaria and cryptosporidiosis (59–62).

PI4KIIIβ makes a large fraction of the pool of Golgi PI4P, which is recognized by the oxysterol-binding-protein (OSBP), four-phosphate-adaptor protein (FAPP), ceramide transfer protein (CERT), GOLPH3, and other protein modules important for Golgi stability and lipid transport (63–66). In addition to generating PI4P, PI4KIIIβ has key non-catalytic roles, including recruiting a pool of PI4KIIIβ associated Rab11 to the TGN (53, 67). The activity of PI4KIIIβ at the Golgi is regulated by a variety of direct binding partners (**Fig. 1.2A**), including the Golgi protein Acyl CoA binding domain containing 3 (ACBD3) (57), the protein c10orf76 (56, 68), and 14-3-3 proteins mediated by PKD phosphorylation of PI4KIIIβ (69–71). In addition, there are a number of proteins that do not form direct interactions, including the GTPase Arf1 (54), and the PI transfer proteins (PITPs, Sec14 in yeast) (72, 73), which activate PI4KIIIβ activity by still unknown mechanisms.

Structural analysis of PI4KIIIβ revealed that it has a very similar overall architecture to the class I PI3Ks in respect to the helical and kinase domains (38),with the main difference being an additional extension of the N-lobe of the kinase domain including a longer disordered N-lobe kinase linker (**Fig 1.2B**). PI4KIIIβ associates with the Golgi through an interaction with the ACBD3 (57). Phosphorylation of PI4KIIIβ at Ser294 drives binding of 14-3-3 proteins, which stabilizes PI4KIIIβ and increases Golgi PI4P levels through a not fully understood mechanism (69–71). Multiple picornaviruses manipulate PI4KIIIβ-dependent PI4P levels via specifically hijacking these regulatory PI4KIIIβ interacting proteins to mediate their intracellular replication (74–77).

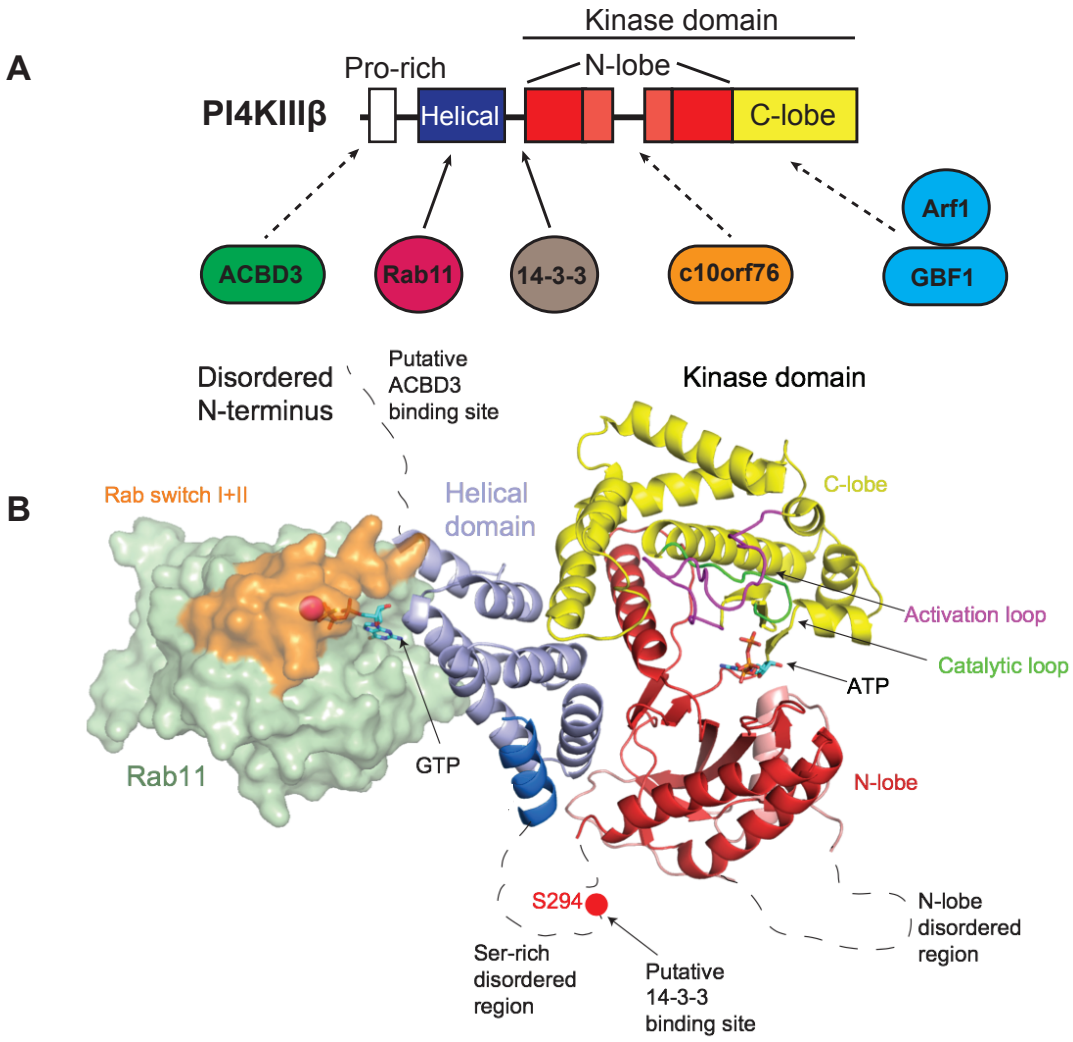

Figure 1.2. Domain organization, interactome, and structure of PI4KIIIβ.
(A) The domain organization of PI4KIIIβ is indicated. PI4KIIIβ contains a number of disordered regions, including the N-terminus, a Ser-rich region after the helical domain, and a loop within the N-lobe of the kinase domain. Interacting proteins of PI4KIIIβ are indicated, and structurally undefined interfaces are shown as a dotted line. **(B)** Structure of PI4KIIIβ bound to the GTPase Rab11. The nucleotide and switch regions of the Rab protein are labelled and colored on the figure. Important features of the kinase domain, including the active site, the activation loop, and the catalytic loop are colored and labelled on the structure. The location of disordered regions within the protein is indicated by dotted lines, and putative binding interfaces are labelled. Phosphorylation sites are indicated with a red dot.

1.3 PI4KIIIβ in viral infection

Picornaviruses are nonenveloped, positive-sense single-stranded RNA viruses with a 30 nm icosahedral capsid that infect vertebrates. Many of these viruses have been shown to specifically manipulate PI4KIIIβ, including Aichivirus, Poliovirus, Rhinovirus, Coxsackievirus, Enterovirus D68 and Enterovirus A71 (75). These viruses cause diverse human diseases such as gastroenteritis, poliomyelitis, aseptic meningitis, hand-foot-and-mouth disease, respiratory illness

and acute flaccid paralysis, and particularly affect young children (78). Direct inhibition of PI4KIIIβ itself has been shown to disrupt viral replication and overall infection progression (58). These viruses hijack host PI4KIIIβ during infection to generate replication organelles, which are essential for viral replication **(Fig 1.3)** (75). These replication organelles are abnormal, PI4P-enriched membranes upon which multiple specific lipids are enriched, along with recruitment of viral replication machinery (i.e. RNA polymerase, etc.) (74). PI4KIIIβ recruitment to replication organelles appears to be dependent on viral 3A proteins (58, 76, 79).

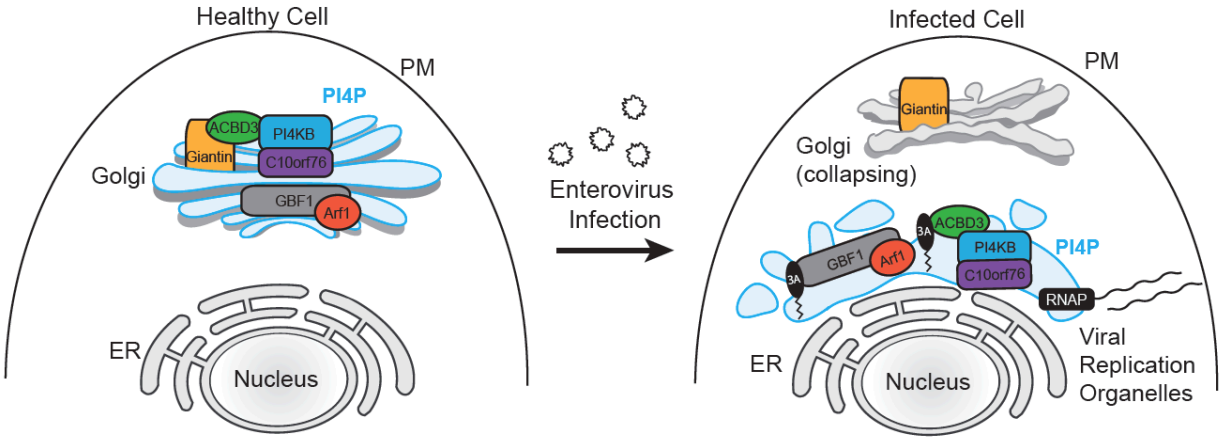

Figure 1.3. Human PI4KIIIβ (PI4KB) is hijacked by picornaviruses to facilitate viral replication.
The virus-encoded 3A protein indirectly hijacks PI4KIIIβ through its regulatory proteins and utilizes it to build PI4P-enriched replication organelles, upon which viral replication machinery assembles. PM = plasma membrane.

Viral 3A proteins do not directly bind to PI4KIIIβ, instead they recruit PI4KIIIβ -regulatory proteins such as ACBD3 and the Arf1 GEF GBF1 (**Fig 1.3**) (57, 58, 74). Specific Picornaviruses have also shown a dependence on the PI4KIIIβ-regulatory protein c10orf76 (68). As infection progresses, PI4KIIIβ hijacking via regulatory proteins and subsequent redistribution of PI4P disrupts normal trafficking and eventually leads to the collapse of the Golgi (**Fig 1.3**) (58, 80). Pharmacologically or genetically inhibiting PI4KIIIβ generally prevents the formation of replication organelles and halts viral infection progression. When considering the potential value of PI4KIIIβ inhibitors as anti-viral therapeutics it is important to note that while these inhibitors are not generally cytotoxic and effectively disrupt viral replication, some PI4KIIIβ inhibitors have been shown to have immunosuppressive effects (130,131). These currently are most useful as tool compounds for the study of the role of PI4KIIIβ in viral replication; however, in recent years non-polio enteroviruses have emerged as a threat to public health with no targeted anti-viral therapy available (81). Enteroviruses can cause devastating polio-like symptoms including acute flaccid

myelitis, which can result in debilitating paralysis and even death. The potential anti-viral benefit of human PI4KIIIβ inhibitors in these cases may outweigh the risk of immunosuppressive effects, which has reinvigorated research into the development of potent, specific PI4KIIIβ inhibitors.

There is still significant ambiguity as to how exactly viruses utilize PI4KIIIβ, as the effectiveness of PI4KIIIβ inhibition at disrupting infection varies between virus types (74). This phenomenon is likely due to the complexity of PI4KIIIβ regulation by both host and viral proteins. Positive-sense ssRNA viruses inject RNA into a host, which is immediately translated as a single open reading frame by host ribosomes into a polyprotein. The polyprotein subsequently undergoes proteolytic processing into various non-structural viral proteins, which includes viral replication machinery. PI4KIIIβ recruitment to replication organelles appears to be dependent on the viral 3A protein (58). Numerous studies have shown that the 3A proteins from Aichivirus, poliovirus, human rhinovirus, coxsackievirus, and Enterovirus 71 recruit ACBD3 to viral replication organelles (57, 79, 82). There have been a number of conflicting studies pertaining to the 3A proteins of other viruses. Several studies show ACBD3 to be essential for 3A-mediated activation of PI4KIIIβ, yet others show ACBD3 to be dispensable or even inhibitory to viral replication (76, 77, 83, 84). Another host factor, GBF1, the guanine-exchange factor (GEF) for Arf1, has also been identified as essential for PI4KIIIβ recruitment by poliovirus and coxsackie virus B3 (58, 85, 86). However, GBF1/Arf1 appear to be non-essential in the replication of human rhinovirus (87). Recently, the PI4KIIIβ-associated protein C10orf76 has been implicated in viral replication. C10orf76 knockout in human haploid HAP1 cells eliminated replication organelle formation and RNA replication during coxsackievirus A10 infection (68). The c10orf76 protein was first co-purified with PI4KIIIβ from HEK cells using affinity purification coupled to mass spectrometry (56, 88). Beyond these published details, little is known about the structure and function of the protein C10orf76, other than the presence of a C-terminal “domain of unknown function” (DUF, 441-669) commonly present in many eukaryotes (NCBI-BLAST). Further study into the regulation of PI4KIIIβ by c10orf76, ACBD3 and GBF1/Arf1, and manipulation by viral proteins are necessary to decipher the viral ambiguity in PI4KIIIβ-hijacking.

1.4 PI4KIIIβ in parasite proliferation

PI4KIIIβ activity is required for successful replication of the malaria parasite which encodes only a single PI4KIIIβ homolog (62). The vast majority of malaria cases worldwide are caused by *Plasmodium falciparum* and *Plasmodium vivax*, which are transferred to humans through the bites of infected female Anopheles mosquitoes. The parasite first infects hepatocytes in the liver, then eventually progresses to a symptomatic erythrocyte infection in the bloodstream. Artemisinin-based combination therapies have been recommended by the WHO since 2005, and have caused significant reductions in the global malaria burden and mortality; however, elimination of malaria has been threatened by the emergence of artemisinin resistance in *P. falciparum* across mainland Southeast Asia (89). Complicating matters, *P. vivax* is able to persist in the liver for years after treatment before relapsing and reinitiating a blood stage infection (90). Considering these challenges, novel medicines that cure the symptomatic asexual blood stage and clear the relapsing liver stage are necessary to eradicate malaria.

Excitingly, *Plasmodium* PI4K inhibitors target all life stages of the parasite in both mammalian hosts and the mosquito vector, kill drug-resistant parasites, and display a prophylactic effect preventing malaria infection in monkey models (60, 62). Inhibition of *Plasmodium* PI4K alters intracellular distribution of PI4P, which disrupts PI4P effector (including Rab11a) recruitment and regulation of transport vesicles destined for the ingressing plasma membrane, eventually causing failure of merozoite cytokinesis within asexual blood stage schizonts (**Fig. 1.4A**). These parasite PI4K inhibitors also display potent activity against another related parasite, *Cryptosporidium*, which is a leading cause of diarrheal death in the developing world. Inhibition of *Cryptosporidium* PI4K leads to potent reduction in intestinal infection of immunocompromised mice, and rapid resolution of diarrhea and dehydration in neonatal calves (59). While parasite PI4K inhibitors have only recently entered clinical trials, preclinical studies have been very promising, and the need for their development is clear.

P. vivax PI4K (1528 residues) and *C. parvum* PI4K (1114 residues) are larger than the human PI4KIIIβ homolog (801 residues for human isoform 2) although the parasite variants maintain the canonical class I PI3K/ class III PI4K helical and kinase domain (**Fig 1.4B**). The *P.vivax* PI4K kinase domain spanning the C-terminal region of the N-lobe and entirety of the C-lobe (residues 1245-1525) is well conserved with the human PI4KIIIβ kinase domain (residues 520-801) with 43% of residues identical and 62% similar (**Fig 1.4C**). While the C-lobe active site

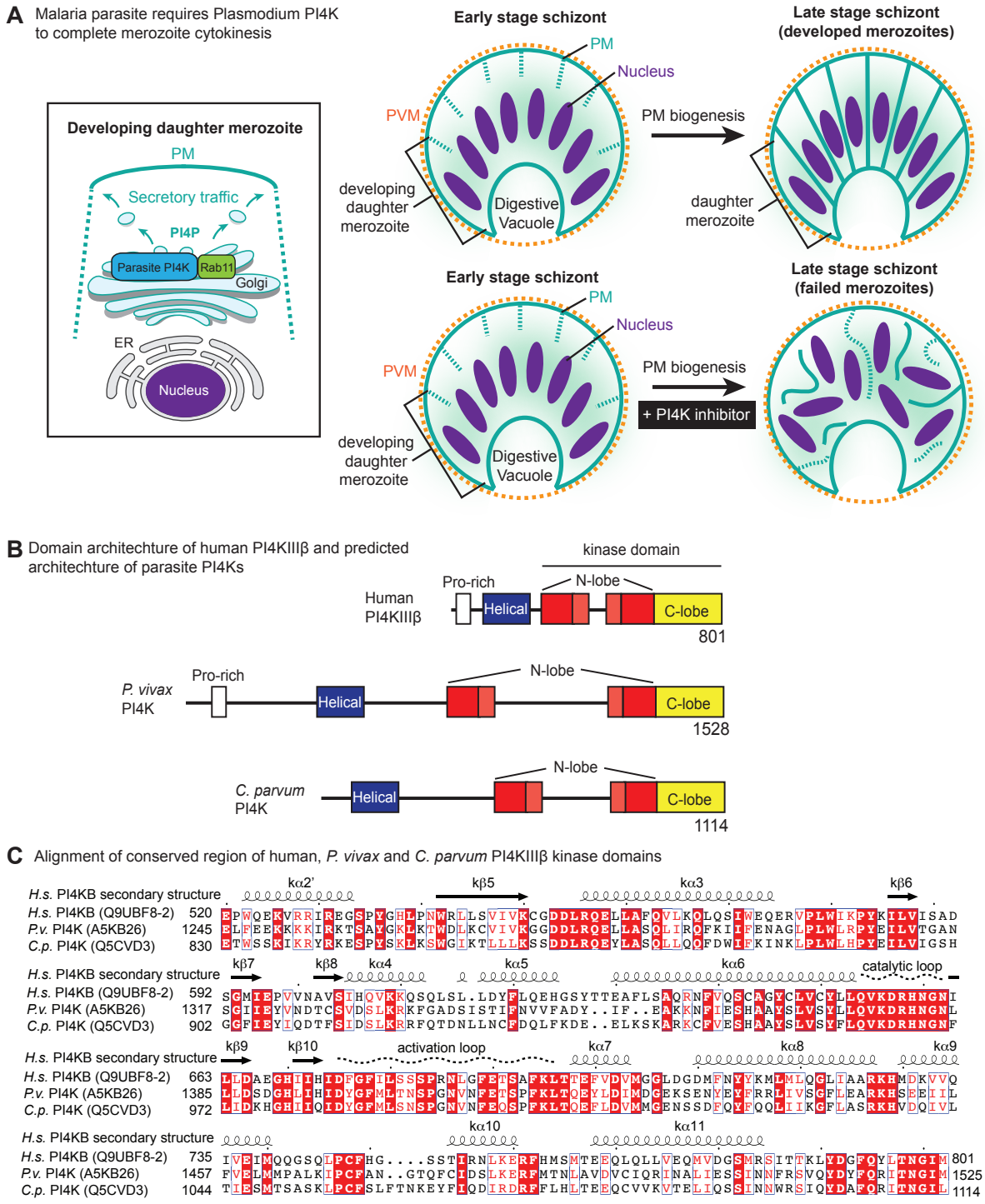

Figure 1.4. Role of Plasmodium PI4K in proliferation of the malaria parasite.
(A) The malaria parasite requires the function of Plasmodium PI4K and Rab11a for proper plasma membrane biogenesis and cytokinesis of daughter merozoites, which are disrupted upon treatment with small molecule PI4K inhibitors. PM = plasma membrane, PVM = parisitophorous vacuolar membrane. **(B)** Putative domain architecture of human, *Plasmodium* and *Cryptosporidium* PI4KIIIβ based on amino acid sequence. **(C)** Alignment of well-conserved human (residues 520-801), *Plasmodium vivax* (1245-1525) and *Cryptosporidium parvum* (830-114) PI4KIIIβ kinase domains (C-term of the N-lobe, and entire C-lobe). Alignment generated using clustal omega and Espript 3.0 (91).

residues show good conservation, the N-terminal half of the *P.vivax* N-lobe and the N-lobe linker shows poor sequence similarity to human PI4KIIIβ, including a significantly divergent P-loop. *C. parvum* PI4K is smaller than the *P. vivax* homolog, but shares greater homology in its active site with *P. vivax* PI4K (56% identical and 72% similar) than with the smaller human PI4KIIIβ (43% identical and 60% similar) in the conserved core of the kinase domain spanning the C-terminal region of the N-lobe and entirety of the C-lobe (**Fig 1.4B,C**). Intriguingly, inhibitors exist that potently target human and Plasmodium PI4Ks, but not *Cryptosporidium* PI4K (BQR695, (62)) – but inhibitors also exist that target *Plasmodium* and *Cryptosporidium* PI4Ks, but not human PI4KIIIβ (KDU-691 (59)). This suggests there are both conserved and non-conserved features within each homolog, and highlights the need for structural insights into parasite PI4K enzymes in order to define the molecular basis of PI4K inhibitor specificity to aid anti-parasite drug development.

1.5 Research Objectives

PI4KIIIβ is a master regulator of the Golgi and an essential enzyme for the proliferation of several prominent human pathogens. Mechanistic details on how many host and viral proteins interact with and activate PI4KIIIβ remain undefined, leading to an ambiguous understanding of normal PI4KIIIβ signalling and hijacking mechanisms by viruses. The proteins ACBD3, c10orf76, and viral 3A represent key PI4KIIIβ-associated proteins required for viral replication whose regulatory mechanisms remain unexplained. Defining the molecular mechanisms of PI4KIIIβ regulation will expand our understanding of this crucial Golgi-signalling enzyme, and could lead to novel therapeutic strategies for viral and parasite infections. The aims of this dissertation were to gain novel insight into the roles of ACBD3 and c10orf76 in PI4KIIIβ signalling by studying regulatory interactions with both host and viral proteins. To this end, the following questions were addressed:

1. **What is the molecular basis of the ACBD3-PI4KIIIβ interaction, and how do viruses manipulate this complex using 3A proteins?**
2. **Does c10orf76 regulate PI4KIIIβ activity? If so, what is the viral dependence on the putative c10orf76-PI4KIIIβ complex?**
3. **What is the molecular basis for selective inhibition of human PI4KIIIβ compared to related lipid kinases?**

To answer these questions, I have utilized a sophisticated approach of biochemistry, hydrogen-deuterium exchange mass spectrometry (HDX-MS), and X-ray crystallography to elucidate molecular mechanisms of PI4KIIIβ regulation by protein binding partners and small molecule inhibitors. PI4KIIIβ is a multi-domain, peripheral membrane protein that is regulated through dynamic protein-protein interfaces which sometimes only occur in the context of membranes; these conditions that are difficult to study with crystallography alone. HDX-MS probes protein-complex dynamics by measuring the changes in deuterium incorporation that typically occur in interfaces involved in complex formation. Therefore, synergistically combining HDX-MS with high resolution structural studies has provided a unique opportunity to study PI4KIIIβ regulation in a more natural context. The data presented in this dissertation have revealed the molecular basis for regulation of PI4KIIIβ by ACBD3 and c10orf76, identified mechanisms of viral dependence on PI4KIIIβ complexes, and explained the basis for selectivity of PI4KIIIβ-specific inhibitors. These findings further our overall knowledge of PI4KIIIβ signalling at the Golgi and its role in viral replication.

Chapter 2: The molecular basis of Aichi virus 3A protein activation of phosphatidylinositol 4-kinase IIIβ (PI4KB) through ACBD3

Adapted from:

McPhail, J.A., Ottosen, E.H., Jenkins, M.L., and Burke, J.E. (2017). The Molecular Basis of Aichi Virus 3A Protein Activation of Phosphatidylinositol 4 Kinase IIIβ, PI4KB, through ACBD3. Structure. 25(1):121-131.

Contributions:

At the time of this study, I was mentoring Erik Ottosen (EHO), a coop student in the Burke laboratory, and also had the assistance of Meredith Jenkins (MLJ), a laboratory technician. I designed all primers and cloned all constructs used in this study with input from John Burke (JEB), with the exception of those plasmids obtained as gifts. I performed all Sf9/baculovirus expressions for PI4KIIIβ production. *E. coli* protein expression was split between myself, MLJ and EHO. Protein purification was split between myself and EHO. I performed all pulldown assays, and the majority of kinase assays, with assistance from EHO. I performed HDX-MS experiments led by MLJ and assisted by EHO. HDX-MS analysis was completed with the help of all authors. I performed all crystallographic setup, collected synchrotron data with JEB, and JEB solved the structure of the ACBD3 GOLD domain. The manuscript was written by JEB and myself.

2.1 Abstract

Phosphatidylinositol 4-kinase III beta (PI4KIIIβ) is an essential enzyme in mediating membrane transport, and plays key roles in facilitating viral infection. Many pathogenic positive-sense ssRNA viruses activate PI4KIIIβ to generate phosphatidylinositol 4-phosphate (PI4P) enriched organelles for viral replication. The molecular basis for PI4KIIIβ activation during viral infection has remained largely unclear. We describe the biochemical reconstitution and characterization of the complex of PI4KIIIβ with the Golgi protein Acyl-coenzyme A binding domain containing protein 3 (ACBD3) and Aichi virus 3A protein on membranes. We find that 3A directly activates PI4KIIIβ, and this activation is sensitized by ACBD3. The interfaces between PI4KIIIβ-ACBD3 and ACBD3-3A were mapped with hydrogen deuterium exchange mass spectrometry (HDX-MS). Determination of the crystal structure of the ACBD3 GOLD domain

revealed a unique N-terminus that mediates the interaction with 3A. Rationally designed complex-disrupting mutations in both ACBD3 and PI4KIIIβ completely abrogated the sensitization of 3A activation by ACBD3.

2.2 Introduction

Phosphoinositides are an important class of membrane resident lipid signaling mediators. The inositol head group of phosphatidylinositol has free hydroxyl groups at positions D2 through D6, and those at positions D3, D4 and D5 can be phosphorylated by lipid kinases, resulting in seven differentially phosphorylated phosphoinositides. These phosphoinositides mediate many essential cellular processes, including growth, cytokinesis, and membrane trafficking (2). The proper generation of phosphoinositides is controlled by the regulation of a variety of lipid kinases and phosphatases. An important phosphoinositide species is the lipid phosphatidylinositol 4 phosphate (PI4P), which is generated by the action of phosphatidylinositol 4-kinases (PI4K) (43, 44). Manipulation of PI4P levels is a common strategy employed by a number of intracellular pathogens, including a number of pathogenic positive-sense single-stranded RNA (ssRNA) viruses, which hijack and activate PI4K to promote viral replication (74, 75).

In mammalian cells, four enzymes can phosphorylate phosphatidylinositol to generate PI4P, two type II PI4Ks (PI4KIIα, PI4KIIβ) and two type III PI4Ks (PI4KIIIα, PI4KIIIβ). The type II PI4Ks are lipidated, membrane-associated proteins. The type III PI4Ks are peripheral membrane proteins that transiently associate with membranes. Both PI4KIIIα and PI4KIIIβ are large, multi-domain proteins that are regulated through their interactions with a number of protein binding partners. PI4KIIIβ is composed of a disordered N-terminal region, a helical domain, and a bi-lobal kinase domain (38). PI4KIIIβ is able to interact with the small GTPases Rab11 and Arf1 (54, 67), 14-3-3 proteins (92), and also the Golgi scaffolding protein acyl-CoA binding domain-containing protein 3 (ACBD3, also referred to as GCP60) (48, 57). Both PI4KIIIα and PI4KIIIβ have been implicated as being involved in the replication of positive-sense ssRNA viruses. Regarding PI4KIIIβ, there is a key involvement of PI4KIIIβ interacting proteins in mediating viral activation with numerous proteins implicated including Arf1 (indirectly through viral recruitment of its GEF, GBF1) (58), ACBD3 (79), and the recently identified protein c10orf76 (68).

A number of viruses of the Picornaviridae family mediate the activation of PI4KIIIβ through their membrane-associated 3A protein, leading to the formation of replication organelles

(ROs) enriched in PI4P, which promote viral replication (74, 75). The molecular mechanism by which viral 3A proteins are able to recruit and activate PI4KIIIβ, and how host scaffolding proteins might mediate this process remains a major question in the field. Intriguingly, the mechanisms by which 3A proteins from different viruses accomplish this appear to be highly variable. One of the first reported mechanisms of 3A mediated recruitment of PI4KIIIβ to ROs was through the interaction of poliovirus 3A protein with the GEF for Arf1, GBF1 (85), leading to PI4KIIIβ recruitment to activated Arf1 (58). The protein c10orf76 has also recently been identified as a potential mediator of PI4KIIIβ activation downstream of 3A proteins in coxsackievirus A10 (68). Not all 3A viral proteins increase PI4P through PI4KIIIβ, as it has been shown that the 3A protein from encephalomyocarditis virus hijacks PI4KIIIα (44, 84) similar to the mechanism used by hepatitis C virus (93), where the hepatitis C viral protein NS5A directly activates PI4KIIIα. Intriguingly, there have also been mutations in 3A proteins identified that bypass the need for PI4P production in the formation of replication organelles, and viral infection (75, 94, 95).

One of the most extensively studied host proteins in mediating PI4KIIIβ activation downstream of viral 3A proteins is ACBD3, which has been shown by affinity purification studies to recruit 3A proteins from a number of pathogenic picornaviruses (79). However, there have been a number of conflicting studies for the role of ACBD3 in PI4KIIIβ recruitment to ROs in different picornaviruses. Studies in Aichi virus showed that ACBD3 was essential for activation of PI4KIIIβ downstream of 3A (57, 76). Nevertheless, studies in Coxsackievirus B3 and rhinovirus showed ACBD3 to be dispensable for viral replication (83, 87) and ACBD3 was shown to be inhibitory for viral replication in poliovirus (77). Defining the molecular basis of regulation of PI4KIIIβ downstream of both host and viral binding partners will be essential to understand the distinctions and ambiguities in how different viruses can mediate PI4KIIIβ recruitment and activation(57, 76).

To understand the molecular mechanism of how viral 3A proteins can activate PI4KIIIβ, and what role ACBD3 plays in this process, we have biochemically reconstituted the PI4KIIIβ/ACBD3/Aichi virus 3A complex on membranes and examined the lipid kinase activity of this complex, as well as defined the interactions and dynamics using hydrogen deuterium exchange mass spectrometry (HDX-MS). Intriguingly, our results reveal that the Aichi virus 3A protein is able to directly activate PI4KIIIβ on membranes, an activation that is sensitized by the presence of ACBD3. Using HDX-MS we defined the interface between PI4KIIIβ and ACBD3, and Aichi virus 3A and ACBD3. The GOLD domain of ACBD3 was identified as necessary for

3A binding, and the crystal structure of this domain was determined using an HDX-MS optimized approach, revealing an N-terminus that mediates 3A binding. Together, the GOLD domain structure and the HDX-MS results on the ACBD3-Aichi virus 3A complex revealed the putative binding site for 3A. Mutations generated based on the combined structural and dynamic information on the PI4KIIIβ/ACBD3/Aichi virus 3A disrupted both complex formation and kinase activation.

2.3 Materials and Methods

Protein expression

All *E. coli* based expression was performed using C41(DE3)RIPL cells, and affinity tags were all N-terminal. 6xHis(tev)-PI4KIIIβ wild-type, mutants (I43A, D44A and E54A) and GST(tev)-ACBD3 wild-type, mutants (FQ258AA, QI274AA, IK380AE, Y525A) were expressed in cultures grown at 37°C to an OD600 of 0.6-0.9, induced with 0.1mM of IPTG and grown overnight at 16°C. GST(tev)- Arf1 Q71L Δ1-14 and 10xHis-Arf1 Q71L Δ1-14 were expressed in cultures grown at 37°C to an OD600 of 0.6-0.9, induced with 0.5 mM of IPTG and grown 3 hours at 37°C. GST(tev)-ACBD3 GOLD domain 366-527 was expressed in a culture grown at 37°C to an OD600 of 0.6-0.9, induced with 1.0 mM of IPTG and grown 4 hours at 37°C. Cells were harvested, washed with PBS and flash frozen in liquid N2. *Spodoptera frugiperda* (Sf9) cells were also used to express 6xHis(tev)-PI4KIIIβ wild-type as previously described (38).

Purification of 10xHis-Arf1 (Q71L, Δ1-14), 10xHis-3A (1-59), 6xHis(tev)-PI4KIIIβ wt and mutants (I43A, D44A, E54A)

Cell pellets containing expressed protein were sonicated in NiNTA Buffer (20 mM Tris-HCl pH 8.0 (4°C), 100 mM NaCl, 10 mM imidazole, 5% (v/v) glycerol, 2 mM β-mercaptoethanol) containing protease inhibitors (Millipore Protease Inhibitor Cocktail Set III, Animal-Free)] for 5 minutes on ice. Triton X-100 (0.1% v/v) was added to the cell lysate and the lysed cell solution was centrifuged for 45 minutes at 20,000 x g at 1°C. Supernatant was filtered through a 5 μm filter and loaded onto a 5mL HisTrap column equilibrated in NiNTA Buffer. The column was washed with 1.0 M NaCl and 22 mM imidazole in NiNTA Buffer and protein was eluted with 200 mM imidazole in NiNTA Buffer. Eluted PI4KIIIβ mutants were immediately used for the GST-glutathione based pulldown assays without further purification. All other proteins were loaded

onto a 5mL HiTrap Q column equilibrated with Q Buffer (20 mM Tris-HCl pH 8.0, 50 mM NaCl, 5% (v/v) glycerol, 2 mM β-mercaptoethanol) and eluted with an increasing concentration of NaCl. Protein was pooled and concentrated using Amicon 10-50K concentrators and incubated overnight at 4ºC with an addition of TEV protease if cleavage was needed. Size exclusion chromatography was performed using either a GE Superdex 75 10/300 column or Superdex 200 10/300 GL increase column equilibrated in SEC Buffer (20mM HEPES pH 7.5, 150mM NaCl and 0.5-1.0 mM TCEP). Fractions containing protein of interest were pooled, concentrated, flash frozen in liquid nitrogen, and stored at -80°C.

Purification of GST(tev)-Arf1 (Q71L, Δ1-14), GST(tev)-ACBD3 GOLD domain (366-527), GST(tev)-ACBD3 wild-type and mutants (FQ258AA, QI274AA, IK380AE and Y525A

Cell pellets were lysed and spun down in Q Buffer containing protease inhibitors as described above. Filtered supernatant was incubated with 1-4mL of Glutathione sepharose 4B beads (GE) for 1-2 hours at 4°C. Beads were then washed with Q Buffer. For proteins maintaining the GST tag, protein was eluted from beads with 20 mM glutathione in Q Buffer. For proteins with a cleaved GST tag, β-mercaptoethanol was raised to 10 mM, the bead/protein mixture was incubated overnight at 4°C with TEV or lipTEV, and cleaved protein was eluted with Q Buffer. Protein was further purified using anion exchange and size-exclusion chromatography as described above. Primary GTP loading was confirmed for Arf1 constructs by incubating in 2mM EDTA at 50ºC for 10 minutes and running on a 1.0 mL HiTrap Q column.

GST Pulldown Assays

Glutathione Sepharose 4B beads (GE Healthcare) were washed three times by centrifugation and re-suspension in fresh GST buffer (20 mM Hepes pH 7.5, 100 mM NaCl, 2 mM TCEP) at 4°C. GST-tagged bait protein was then added to a concentration of 3-4 μM and incubated with the beads on ice for 30 min. Beads were washed three times with GST buffer at 4°C. Non-GST-tagged prey PI4KIIIβ proteins were then added to a final concentration of 1-2 μM at which point the input was taken for SDS PAGE analysis. The mixture was incubated on ice for an additional 30 min and then washed four times with GST buffer at 4°C, at which time an aliquot was taken for SDS PAGE analysis.

Lipid vesicle preparation

Vesicles were prepared as previously described (96). Golgi Vesicles were made to mimic the composition of the Golgi organelle [20% phosphatidylinositol (soybean PI, from Avanti), 10% phosphatidylserine (bovine brain PS from Sigma), 45% phosphatidylcholine (egg yolk PC from Sigma) and 25% phosphatidylethanolamine (egg yolk PE from Sigma)]. Nickelated vesicles were composed similar to Golgi Vesicles, with the exception of 5% DGS-NTA(Ni) substituted for 5% of the PE [5% 18:1 DGS-NTA(Ni) (Avanti), 20% PI, 10% PS, 45% PC, 20% PE]. DGS-NTA(Ni) concentration was optimized to present approximately 12.5 μM DGS-NTA(Ni) on the vesicle surface, an 8.3-fold excess of the highest concentration of His-tagged 3A used (1.5 μM). Vesicles were generated by adding lipid stocks together in choloroform and evaporating the solvent under a stream of dry nitrogen. The resultant thin lipid film was desiccated for 30 minutes and re-suspended in Lipid Buffer (20 mM HEPES pH 7.5 (RT), 100 mM KCl, 0.5 mM EDTA) by vortexing for 10 minutes. Lipid Buffer used to prepare Nickelated Vesicles was EDTA-free. Re-suspended lipids were bath sonicated for 10 minutes and subjected to 3 freeze-thaw cycles between liquid nitrogen and water at 42 ºC. Vesicles were finally extruded 11 times through a 100-nM filter using the Avanti lipid mini-extruder and stored at -80 ºC. Vesicles were thawed at room temperature prior to use.

Lipid Kinase Assays

Lipid kinase assays were carried out using the Transcreener® ADP2 FI Assay (BellBrook Labs) following the published protocol as previously described (12). Substrate stocks were made up containing 1 mg/mL Golgi-mimic vesicles and 20 μM ATP in a buffer containing 20 mM Hepes pH 7.5, 100 mM KCl and 0.5 mM EDTA, and 2 μL aliquots were added into 384 well black low volume plates (Corning 3676). No EDTA was added to substrate containing 5% NiNTA vesicles. Proteins were thawed on ice and spun down to remove precipitate. Proteins were diluted individually to 8X the desired concentration in Kinase Buffer (40 mM Hepes pH 7.5, 200 mM NaCl, 20 mM MgCl2, 0.8% Triton-X, and 0.2 mM TCEP) at 0°C. Proteins were then mixed together or with additional Kinase buffer resulting in 2X desired concentrations of each protein. To start the reaction, 2 μL of 2X protein stock was added to 2 μL of 2X substrate stock in plates. After mixing, the 4 μL reactions consisted of 30 mM HEPES pH 7.5 (RT), 100 mM NaCl, 50 mM KCl, 10mM MgCl2, 0.25 mM EDTA, 0.4% (v/v) Triton-X, 0.1 mM tris(2-carboxyethyl)phosphine

(TCEP), 10 μM ATP and 0.5 mg/mL vesicles. PI4KIIIβ was run at 150 or 250 nM, Arf1 at 750 nM, ACBD3 at 400 or 600 nM and Aichi virus 3A at concentrations ranging from 0.5 – 1.5 μM. Reactions proceeded at 23°C for 1 hour. Reactions were stopped using 4 μL of the Transcreener stop buffer (1X Stop & Detect Buffer B, 8 nM ADP Alexa594 Tracer, 50 μg/ml ADP2 Antibody-IRDye® QC-1). Fluorescence intensity was measured using a Spectramax M5 plate reader with λex = 590 nm and λem = 620 nm. Data was plotted using Graphpad Prism software, with EC_{50} values determined by nonlinear regression (curve fit). No detectable nonspecific ATPase activity was detected in reactions containing 250 nM wild-type PI4KIIIβ without vesicle substrate. No detectable nonspecific ATPase activity was detected in reactions containing up to 1.5 μM 3A, 600 nM ACBD3 or both together without PI4KIIIβ. The specific activity for apo PI4KIIIB was determined to be 0.80 (SD +/- 0.11) nmol ADP min-1 mg-1 on 5% NiNTA vesicles and 1.71 (SD +/- 0.05) nmol ADP min-1 mg-1 on Golgi-mimic vesicles.

Hydrogen deuterium exchange mass spectrometry (HDX-MS)

HDX reactions were conducted in 50 μL reactions with a final concentration of 0.2-2.5 μM of protein per sample (PI4K-ACBD3, 0.5 μM each; ACBD3-3A-0.5 μM ACBD3 and 2.5 μM 3A; 3A-ACBD3-0.2 μM 3A and 1 μM ACBD3). Reactions were initiated by the addition of 45 μL of D2O Buffer Solution (10 mM HEPES pH 7.5, 50 mM NaCl, 97% D2O) to 5 μL of protein solution, to give a final concentration of 87% D2O. Exchange was carried out for four timepoints, (3 seconds at 0°C and 3s, 30s, and 300s at 23 °C). Exchange was terminated by the addition of acidic quench buffer giving a final concentration 0.6 M guanidine-HCl, 0.8% formic acid. All experiments were carried out in triplicate. Samples were immediately frozen in liquid nitrogen and stored at −80°C until mass analysis. Protein samples were rapidly thawed and injected onto a UPLC system kept in a cold box at 2°C. The protein was run over two immobilized pepsin columns (Applied Biosystems; porosyme, 2-3131-00) stored at 10°C and 2°C at 200 μL/min for 3 min and the peptides were collected onto a VanGuard precolumn trap (Waters). The trap was subsequently eluted in line with an Acquity 1.7 μm particle, 100 × 1 mm2 C18 UPLC column (Waters), using a gradient of 5-36% B (buffer A 0.1% formic acid, buffer B 100% acetonitrile) over 16 minutes. Mass spectrometry experiments were performed on an Impact II QTOF (Bruker) acquiring over a mass range from 350 to 1500 m/z using an electrospray ionization source operated at a temperature of 200°C, and a spray voltage of 4.5 kV. Peptide identification was done by running tandem

MS/MS experiments run in data dependent acquisition mode with a 0.5 s precursor scan from 200-2000 m/z, followed by 12 fragment scans from 150 to 2000 m/z of 0.25 s. The resulting MS/MS datasets were analyzed using PEAKS7 (PEAKS), and a false discovery rate was set at 1% using a database of purified proteins and known contaminants.

HD-Examiner Software (Sierra Analytics) was used to automatically calculate the level of deuterium incorporation into each peptide. All peptides were manually inspected for correct charge state and presence of overlapping peptides. Deuteration levels were calculated using the centroid of the experimental isotope clusters. Attempts at generating fully deuterated protein samples to allow for the control of peptide back exchange levels during digestion and separation was attempted for all proteins. No successful fully deuterated samples were generated for ACBD3 or 3A. Results for these proteins are therefore presented as relative levels of deuterium incorporation and the only control for back exchange was the level of deuterium present in the buffer (87.4%). For ACBD3 and 3a, the real level of deuteration will be ∼25–35% higher than shown, based on tests performed with fully deuterated standard peptides. For PI4K, the fully deuterated sample was prepared as described previously (97). The average error of all time points and conditions for each HDX project was less than 0.2 Da. Therefore, changes in any peptide at any time point greater than both 7% and 0.7 Da between conditions with a paired t-test value of $p<0.05$ was considered significant. The full details of H/D exchange for all peptides are shown in **Appendix C** and **D**.

Crystallography

Crystallization trials of the GOLD domain of ACBD3 were set using a Crystal Gryphon (Art Robbins Instruments) in 96-well Intelliplates using sitting drops at 18°C. Protein at 4.74 mg/mL was mixed 2:1 with reservoir solution for a final drop volume of 0.3 µL. Initial hits were obtained in the JBScreen Classic 1-4 kit. Refinement plates for JBScreen Classic 3 condition B3 [16% (w/v) PEG-4000, 200 mM Ammonium Sulphate, 100 mM Hepes Salt pH 7.5 and 10% (v/v) 2-propanol] were set using the hanging drop method by gridding PEG-4000 and glycerol with various drop ratios and protein concentrations. Optimal crystals grew using the hanging drop method with protein at 5.0 mg/mL mixed 10:1 with reservoir solution [13% (w/v) PEG-4000, 200 mM Ammonium Sulphate, 100 mM Hepes Salt pH 7.5, 10% 2-propanol and 10% glycerol] for a final drop volume of 2.2 µL and reservoir volume of 300 µL. These crystals were frozen in liquid nitrogen using cryo buffer [13% (w/v) PEG-4000, 200 mM Ammonium Sulphate, 100 mM Hepes

Salt pH 7.5, 20% 2-propanol and 10% glycerol] containing glycerol and extra 2-propanol as cryoprotectant for data collection.

Structure solution/refinement

Diffraction data were collected at 100 K at beamline 08ID-1 of the Canadian Macromolecular Crystallography Facility (Canadian Light Source, CLS). Data were integrated using iMosflm 7.1.1 (98) and scaled with AIMLESS (99). The crystallography data was severely anisotropic and molecular replacement, model building and refinement was hindered. The data was corrected for anisotropy by anisotropic truncation and scaling (UCLA server, http://services.mbi.ucla.edu/anisoscale/) (100) and required truncation of data that fell outside an ellipse centered at the reciprocal lattice origin and having vertices at 1/3.1, 1/3.2 and 1/2.5 Å along a*, b* and c* respectively, which led to great improvement in maps (**Appendix E)**. Phases were initially obtained by molecular replacement using Phaser (101) with the the GOLD domain from Sec14 like protein 4 (Sec14L4) (PDB ID: 4LTG) used as the search model for the anisotropiclly truncated data, with this model used obtain phases for the full dataset. Automated model building was performed with Phenix.autobuild (102). The final model of the ACBD3 Gold domain was built using iterative model building in COOT (103) and refinement using phenix.refine (104) to Rwork = 23.83 and Rfree = 26.17. Full crystallographic statistics are shown in Table 2.1+2.2.

2.4 Results

Biochemical reconstitution and lipid kinase assays of PI4KIIIβ/ACBD3/Aichi 3A complex

To examine the molecular basis for PI4KIIIβ activation by 3A we expressed and purified constructs of PI4KIIIβ, ACBD3, and Aichi virus 3A protein. The Aichi virus 3A protein was selected due to multiple studies identifying a complex between ACBD3- PI4KIIIβ and Aichi virus 3A (57, 76). We expressed the full-length constructs of PI4KIIIβ and ACBD3 as well as a His tagged construct of the Aichi virus 3A protein that would mimic the membrane bound form (**Fig. 2.1A**). The native Aichi virus 3A protein is myristoylated (79) and contains a putative C-terminal transmembrane helix. Attempts to purify full-length 3A protein led to insoluble protein, even in the presence of detergent. Previous studies used an N-terminal MBP tag (76); however, this would be likely to disrupt myristoylation and membrane localization, so to generate the most realistic *in vitro* mimic of a membrane localized Aichi virus 3A we used a 10x His-tag at the myristoylation

site and removed the putative transmembrane helix (10xHis-3A[1-59]). To anchor the 3A protein on a membrane, we used Golgi-mimic vesicles containing 5% DGS-NTA(Ni), a synthetic lipid with a nickel-chelating headgroup, an approach that has previously been used to study membrane-associated signaling complexes (105). To verify that the Ni-NTA derived lipids would be a valid approach to study membrane localized activators of PI4KIIIβ, we reconstituted the small GTPase Arf1 using a 10x His-tag to mimic the natural N-terminal myristolation on 5% NiNTA vesicles and we saw a ~1.5-fold increase in PI4KIIIβ activity that was dependent on His-tagged Arf1 (**Appendix A**). To understand the role of ACBD3 in mediating activation of PI4KIIIβ downstream of Aichi virus 3A we carried out lipid kinase assays on PI4KIIIβ in the presence and absence of ACBD3 and His-tagged Aichi virus 3A on Golgi-mimic vesicles (**Fig. 2.1**). Experiments carried

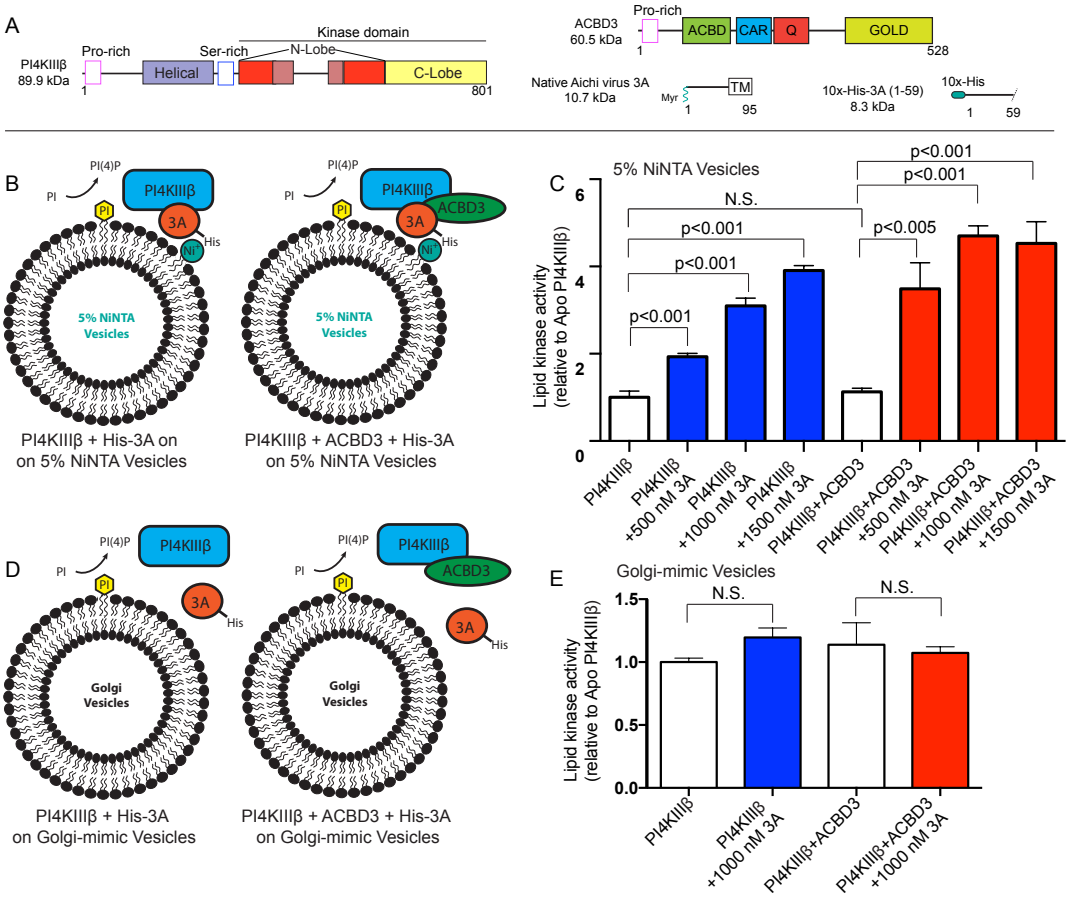

Figure 2.1. ***In vitro*** **lipid kinase assays show PI4KIIIβ is activated by membrane-bound 3A protein in a concentration-dependent manner and the presence of ACBD3 sensitizes this activation (refers to Appendix A).**

(A) Protein domain architecture - wild-type PI4KIIIβ contains a helical domain (128-243) and kinase domain (306-801) consisting of an N-lobe and a C-lobe. Wild-type ACBD3 contains an acyl-CoA binding domain (ACBD, 83-174), charged amino acids region (CAR, 182-238), glutamine rich region (Q, 241-308) and a Golgi dynamics domain (GOLD, 367-528). Native Aichi virus contains two lipid anchors in vivo, an N-terminal

myristoylation and a C-terminal transmembrane helix. An optimized 10xHis-3A (1-59) construct replaced the native myristoylation with a 10x-his tag for binding to nickelated vesicles and removed the transmembrane helix to facilitate purification. **(B)** Schematic – His-tagged 3A binds to Golgi-mimic vesicles containing DGS-NTA(Ni) (5% DGS-NTA(Ni), 10% PS, 20%PE, 20% PI, 45% PC) and recruits PI4KIIIβ. ACBD3 binds to the membrane associated PI4KIIIβ-3A complex. **(C)** For both panels B+D lipid kinase activity of PI4KIIIβ (150 nM) was monitored through the production of ADP in the presence of 0.5 mg/mL of vesicles. All specific activity measurements were normalized to PI4KIIIβ in the absence of binding partners. Membrane-bound His-tagged 3A activates PI4KIIIβ in a dose-dependent manner on 5% NiNTA vesicles. ACBD3 alone (present at 600 nM) does not activate PI4KIIIβ, but sensitizes the activation by 3A, reaching maximum activation with lower 3A concentrations. **(D)** Schematic – His-tagged 3A does not bind to Golgi-mimic vesicles (10% PS, 20% PI, 25%PE, 45% PC) lacking DGS-NTA(Ni) and does not recruit PI4KIIIβ. **(E)** His-tagged 3A does not activate PI4KIIIβ on Golgi-mimic even in the presence of ACBD3. For all experiments reactions were carried out in triplicate, and data is shown +/- SD, and results from t tests are shown, with N.S. being p values >0.05.

out on vesicles lacking DGS-NTA(Ni) showed no significant lipid kinase activation of PI4KIIIβ by either ACBD3 or Aichi virus 3A protein (**Fig. 2.1D-E**). Vesicles containing DGS-NTA(Ni) still showed no direct activation by ACBD3. Surprisingly, we found that there was a dose dependent activation of PI4KIIIβ directly by membrane localized Aichi virus 3A protein, and that the presence of ACBD3 led to a sensitization of PI4KIIIβ activation by membrane localized Aichi virus 3A (**Fig. 2.1B-C**). The activation of apo PI4KIIIβ by 3A had an approximate EC_{50} (i.e. the concentration of 3A that provokes half of its maximum activation of PI4KIIIβ) of 1 μM. In the presence of ACBD3, the estimated EC_{50} of 3A for PI4KIIIβ activation is reduced to <500 nM.

Defining the location and dynamics of the PI4KIIIβ/ACBD3 interface using HDX-MS

During the course of this study, another group showed ACBD3 and PI4KB form a tight complex, with a binding affinity of 320 +/- 130 nM (48). To understand the dynamics of this interaction, we carried out HDX-MS experiments on both PI4KIIIβ and ACBD3 both alone and in complex. HDX-MS is a powerful technique that allows for the determination of the exchange rate of amide hydrogens in proteins, and as the main determinant of amide exchange is the involvement of secondary structure, it acts as a useful readout of protein conformational dynamics. It has been particularly useful in mapping protein-protein (106) protein-membrane (107), and protein-small molecule interactions (108), as well as being a useful tool in defining disordered regions in proteins (97, 109). Critical to a successful HDX-MS experiment is the generation of peptic peptides that cover the entire sequence, and allow for localization of deuterium exchange rates. Two hundred and sixty-four peptides were identified from ACBD3 covering 92.5% of the sequence, and 302 peptides from PI4KIIIβ covering 99% of the sequence. A description of the HDX-MS methodological details are explained in **Appendix B**, and the full deuterium exchange

information for all experiments is shown in **Appendix C and D**. Hydrogen deuterium experiments were carried out at four time points (3, 30, and 300s at 23°C, and 3s at 0°C) for both ACBD3 and PI4KIIIβ alone and in the presence of a 3-fold excess of binding partner. Significant changes in H/D exchange between populations were denoted by the following criteria: Greater than 0.7 Da, and 7% change in exchange at any timepoint, and a t-test p value less than 0.05 upon comparison of the two populations. In PI4KIIIβ, there was only one region of the protein that showed decreases in exchange — this was in the N-terminus, with peptides spanning 41-67 showing a significant protection in exchange in the presence of ACBD3 (**Fig. 2.2A,C,D, Appendix C**). This protection

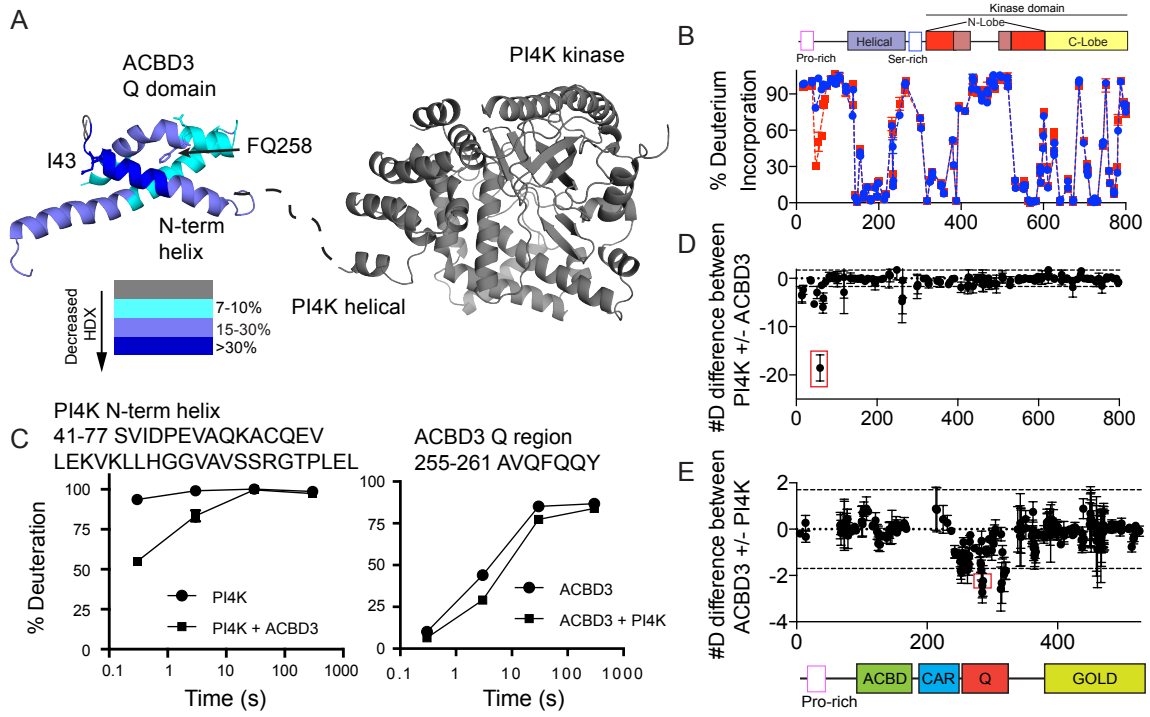

Figure 2.2. HDX-MS shows a disorder to order transition in a region between the N-terminus and helical region of PI4KIIIβ upon complex formation with ACBD3 (refers to Appendix B-C).
(A) Significant changes of deuterium incorporation (>0.7 Da and >7% at any time point) are mapped on the structural model of PI4KIIIβ (composed of the helical and catalytic domains of PI4KIIIβ (PDB:4D0L)(38) and the N-terminal helix of PI4K bound to the Q domain of ACBD3 (PDB:2N73)(48)). Changes in exchange are mapped according to the legend. Decreases in exchange in PI4KIIIβ in the presence of ACBD3 mapped to amino acids 41-67, which have been shown to form a helix that contacts the Q domain of ACBD3. I43 and FQ258 are highlighted in PI4KIIIβ and ACBD3 respectively. **(B)** Percent deuterium incorporation at 3 s D_2O exposure at 0°C of PI4KIIIβ in Apo (blue) and ACBD3-bound (red) states showed that the disordered n-terminal region of PI4KIIIβ (41-67) becomes ordered in the presence of ACBD3. **(C)** Selected peptides in PI4KIIIβ and ACBD3 that showed decreases in exchange are shown. The full list of all peptides and their deuterium incorporation is shown in Appendix C. **(D)** The sum of the difference in H/D exchange for PI4KIIIβ in the presence of ACBD3 at all timepoints is shown. **(E)** The sum of the difference in H/D exchange for ACBD3 in the presence of PI4KIIIβ at all timepoints is shown. For both panel D+E each peptide is represented as a single point corresponding to its mass centroid (x axis), peptides circled in red are shown in panel C. For panels B-E all experiments were carried out in triplicate, with error bars representing SD, in panels B+C most are smaller than the size of the point.

mapped to the same region as a recent NMR study on the interface between ACBD3 and PI4KIIIβ (48). Intriguingly, our HDX-MS results reveal that the N-terminal helix in PI4KIIIβ that forms upon interaction with ACBD3 is completely disordered in the absence of ACBD3, and undergoes a disorder-to-order transition upon ACBD3 binding (**Fig. 2.2B**). Numerous peptides spanning the Q domain of ACBD3 showed a decrease in exchange in the presence of PI4KIIIβ (**Fig. 2.2C,E**). The decreases in exchange in ACBD3 in the Q domain were of a much smaller magnitude than in PI4KIIIβ, and all putative contact sites of ACBD3 with PI4KIIIβ showed presence of secondary structure in the absence of PI4KIIIβ. Mutations in regions in both PI4KIIIβ (I43A, D44A) and ACBD3 (FQ258AA) disrupted their ability to interact with ACBD3 and PI4KIIIβ respectively as shown by GST pulldown assays (**Fig. 2.3**).

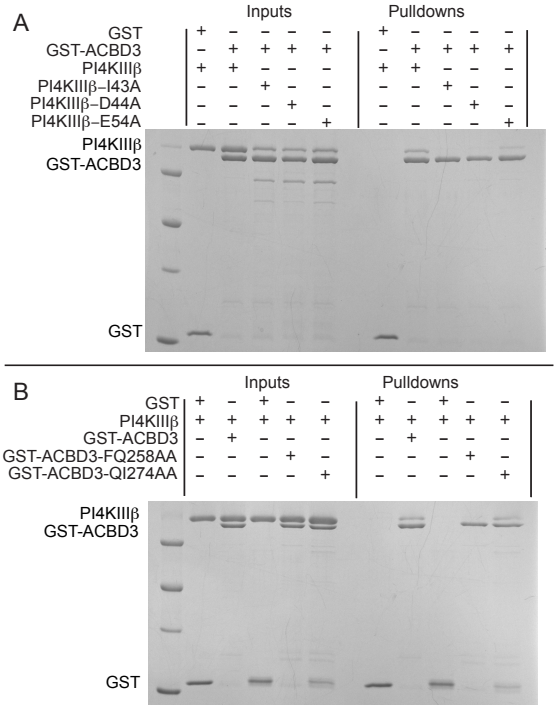

Figure 2.3. GST-glutathione pull-down assays show I43A and D44A PI4KIIIβ mutations disrupt ACBD3 binding, while the FQ248AA ACBD3 mutation disrupts PI4KIIIβ binding.
(A) GST-tagged wild-type ACBD3 pulls down wild-type PI4KIIIβ but does not pull down I43A or D44A PI4KIIIβ. **(B)** Wild-type PI4KIIIβ is pulled down by GST-tagged wild-type ACBD3 but not by GST-tagged FQ258AA ACBD3. Inputs and bound proteins were analysed on SDS gels with Coomassie Brilliant Blue stain.

Structure of the GOLD domain of ACBD3

Previous work has indicated a critical role of the GOLD domain of ACBD3 in mediating activation downstream of viral 3A proteins (79). There is no structure of the GOLD domain from ACBD3, with the only published GOLD domain being from supernatant protection factor protein

(SPF) (110). The GOLD domain is found in many proteins located at the Golgi and plays key roles in mediating protein-protein interactions (111). The ACBD3 GOLD domain is predicted to facilitate the interactions with the protein Giantin (112), which mediates the Golgi membrane localization of ACBD3. To identify the optimal construct for crystallization we used HDX-MS to define regions of disorder within ACBD3. HDX-MS identified a region of residues protected from amide exchange immediately N-terminal of the predicted start of the GOLD domain (**Fig 2.4A**). Using the HDX-MS results we generated a crystal construct composed of ACBD3 residues 367-528. The structure of the GOLD domain was solved at a resolution of 2.5 Å (full crystallization details in material and methods). The dataset was severely anisotropic, which occurs when the number of lattice contacts in a crystal is less, and subsequently diffracts weaker, in one cell direction than another. Anisotrophy was corrected through anisotropic truncation and scaling with truncation dimensions of a*, b*, c* - 3.1, 3.2, 2.5 which led to a great improvement in maps (**Table 2.1+2.2**, **Appendix E**), a method previously utilized to determine the crystal structure of PE/PPE (PDB:2G38) from an anisotropic dataset (100). The overall domain topology was very similar to the GOLD domain present in the previously solved SPF structure (110), as well as the GOLD domain present in Sec14 like protein 4 (SEC14L4, unpublished, pdb: 4TLG), with the domain adapting a jelly-roll beta barrel motif. However, the GOLD domain of ACBD3 contained an extra N-terminal extension composed of a single beta strand and alpha helix, with little to no sequence conservation of this region across other GOLD domain containing proteins (111) (**Fig. 2.4B,C**).

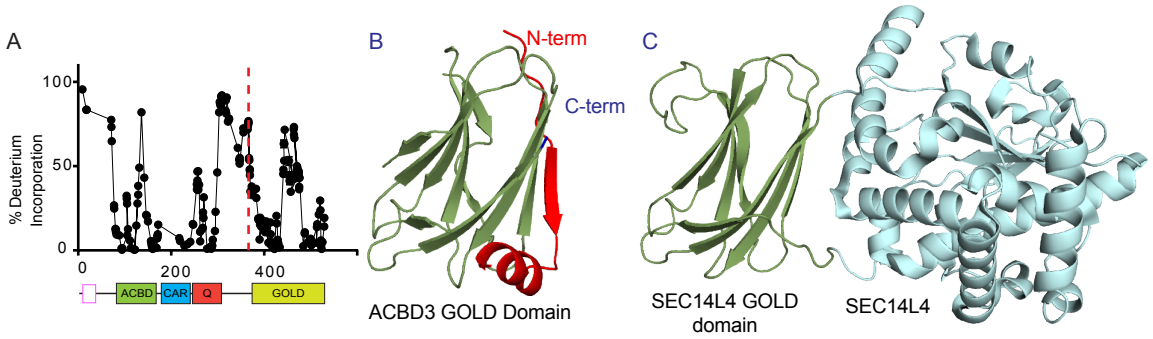

Figure 2.4. X-ray crystal structure of the Gold domain of ACBD3 to 2.5 Å reveals a unique N-terminal extension.
(A) The deuterium incorporation of ACBD3 at 3 s D_2O exposure at 0°C is mapped according to the central residue. Every point represents a single peptide. Experiments were carried out in triplicate, and error bars represent SD. Most are smaller than the size of the point. A red line represents the boundary chosen for the GOLD domain crystal construct. **(B)** The crystal structure of the GOLD domain of ACBD3, with the unique N-terminal extension colored in red. The termini of the domain are labeled. **(C)** The structure of SEC14L4 (PDB:4TLG) with its gold domain colored the same as ACBD3, reveals the lack of the N-terminal beta-strand and helix seen in ACBD3. Full refinement details summarized in Tables 2.1 and 2.2. Refers to Appendix E.

Table 2.1. Data collection and refinement statistics for ACBD3 GOLD Domain.

Data collection	**ACBD3 GOLD domain**
Wavelength (Å)	0.9797
Space group	P 31 2 1
Unit cell	(55.51, 55.51, 140.15, 90, 90, 120)
Total reflections	41169 (4665)
Unique reflections	9160 (1018)
Multiplicity	4.5 (4.6)
Completeness (%)	99.6 (100)*
Mean I/sigma(I)	8.6 (1.0)
Wilson B-factor	45.16
R-merge	0.059 (0.869)
R-meas	0.073
CC1/2	0.998 (0.840)
CC*	0.999 (0.98)
Refinement	
Resolution range (Å)	46.72 - 2.50 (2.58 - 2.50)
Reflections used for R-free	5%
R-work	24.72
R-free	26.17
Number of non-hydrogen atoms	1028
macromolecules	1028
ligands	0
water	0
Protein residues	123
RMS(bonds)	0.004
RMS(angles)	0.88
Ramachandran favored (%)	95
Ramachandran outliers (%)	0.9
Clashscore	11.99
Average B-factor	48.70
macromolecules	48.70
ligands	

Statistics for the highest-resolution shell are shown in parentheses. Values are before anisotropic scaling as requested by PDB for final model deposition. *completeness after anisotropic scaling is shown in Table 2.2, and details of anisotropic scaling are shown in Appendix E.

Table 2.2. Data completeness after anisotropic truncation and scaling for ACBD3 GOLD domain.

Bin	Resolution Range (Å)	Completeness
1	46.7248 - 5.5711	0.90
2	5.5711 - 4.4230	0.92
3	4.4230 - 3.8642	0.95
4	3.8642 - 3.5110	0.92
5	3.5110 - 3.2594	0.97
6	3.2594 - 3.0673	0.80
7	3.0673 - 2.9137	0.45
8	2.9137 - 2.7869	0.30
9	2.7869 - 2.6796	0.20
10	2.6796 - 2.5872	0.12
11	2.5872 - 2.5063	0.05

Defining the location and dynamics of the ACBD3/ 3A interface using HDX-MS

To understand the molecular basis for how ACBD3 could mediate sensitization of PI4KIIIβ activation downstream of Aichi virus 3A we carried out HDX-MS experiments on ACBD3 in the presence and absence of a five-fold excess of Aichi virus 3A protein. We also carried out the reciprocal experiment where HDX rates for Aichi virus 3A were determined in the presence and absence of a five-fold excess of ACBD3. Due to interference from overlapping peptides derived from 3A, 95 peptides covering 84% of the sequence of ACBD3 were identified and analyzed using HDX-MS and 18 peptides were identified for 3A covering 83% of the sequence.

In ACBD3, both the acyl-CoA binding (ACB) domain and the C-terminal GOLD domain showed significant decreases in deuterium exchange in the presence of 3A (**Fig 2.5A**). Previous work had implicated the GOLD domain as the main determinant of 3A recruitment (56) so the decreases in exchange in the ACB domain may be mediated through conformational changes induced by binding to the GOLD domain. Indeed HDX-MS experiments on the isolated GOLD domain in the presence of 3A still showed decreases in exchange in similar regions as the full length ACBD3 protein (data not shown). The main regions of the GOLD domain that showed a decrease in exchange upon 3A binding were an N-terminal extension (367-382), as well as the C-terminus (523-528) (**Fig. 2.5A,C,D**). For the 3A protein numerous peptides showed significant decreases in exchange across the entire primary sequence; however, the largest decrease in exchange was located at the N-terminus (**Fig 2.5B,C**).

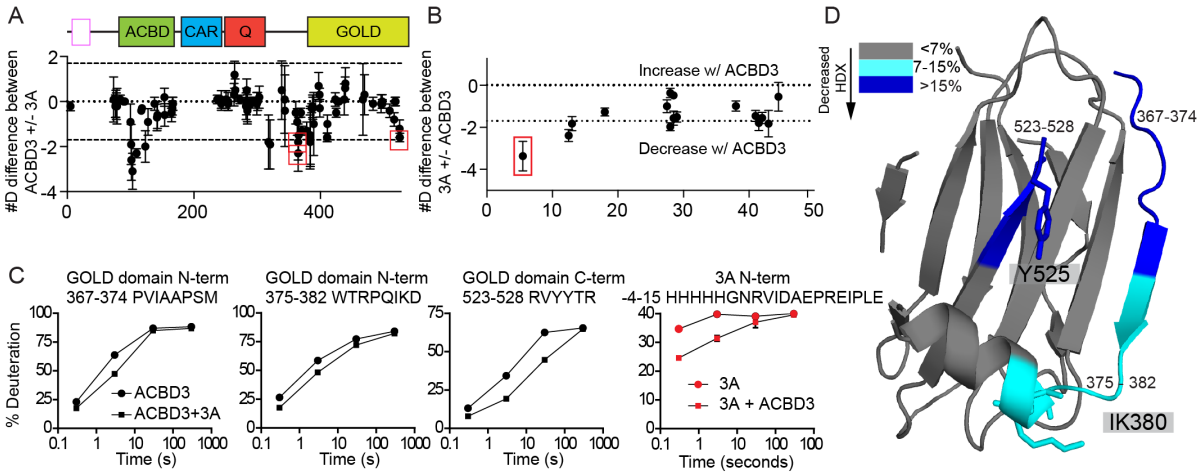

Figure 2.5. HDX-MS of the interface between Aichi virus 3A and ACBD3 shows a key role of the termini of the ACBD3 GOLD domain (refers to Appendix D).
(A) The sum of the difference in H/D exchange for ACBD3 in the presence of Aichi virus 3A at all timepoints is shown. The schematic for the domain architecture of ACBD3 is shown for reference. **(B)** The sum of the difference in H/D exchange for 3A in the presence of ACBD3 at all timepoints is shown. **(C)** The deuterium incorporation for selected peptides highlighted in red in panels A+B are shown, with the location of the peptide indicated. All peptides are shown in Appendix D. For panels A-C all experiments were performed in triplicate, and error bars represent SD, with most being smaller than the size of the point. **(D)** Significant differences in HD exchange levels at any timepoint are mapped onto the structure of the ACBD3 GOLD domain according to the legend. Key residues are shown as sticks and labeled on the structure.

Generation of mutations that disrupt the PI4KIIIβ-ACBD3-Aichi virus 3A complex

To test that we had accurately identified the contacts between both PI4KIIIβ-ACBD3 and ACBD3-Aichi virus 3A protein we generated point mutants in both PI4KIIIβ and ACBD3 for testing in our biochemical reconstitution lipid kinase assay. To test the role of the PI4KIIIβ-ACBD3 complex we examined the I43A mutation in PI4KIIIβ that disrupted ACBD3 complex formation (**Fig. 2.3**). This mutation showed similar basal kinase activity as wild-type PI4KIIIβ, but was unable to be directly activated downstream of Aichi virus 3A protein (**Fig. 2.6A,B**). To test the role of the ACBD3-Aichi virus 3A complex, mutations were designed near both the N (IK380AE) and C termini (Y525A) of the GOLD domain of ACBD3 (Fig 2.5D). HDX-MS experiments on these mutants showed no global differences in H/D exchange levels, indicating that protein remained properly folded (data not shown). These ACBD3 mutants also completely abrogated the ability of the ACBD3 to sensitize PI4KIIIβ activation downstream of Aichi virus 3A.

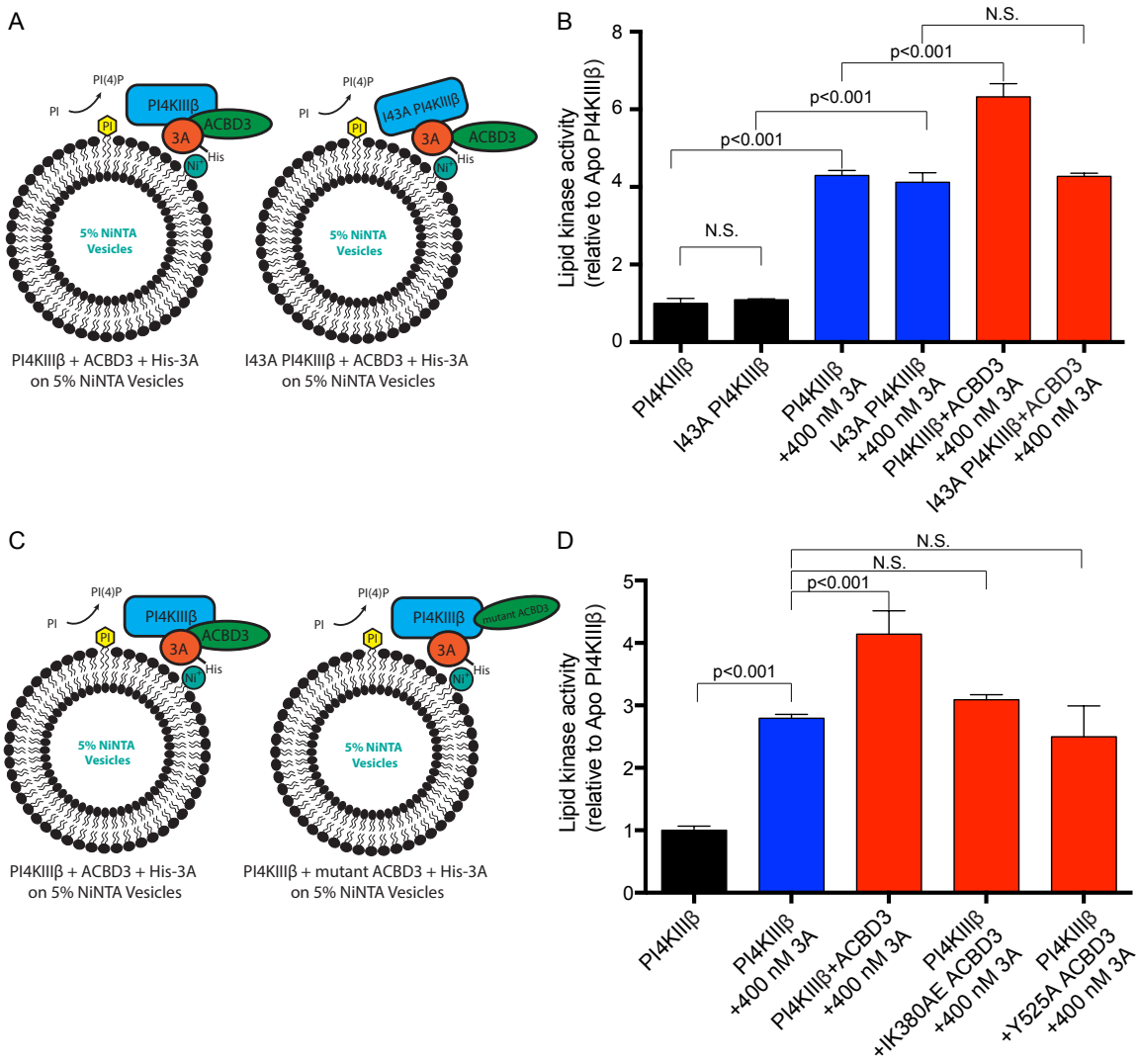

Figure 2.6. Disrupting the ACBD3 interaction with either PI4KIIIβ or 3A eliminates ACBD3's ability to sensitize PI4KIIIβ activation by membrane-bound 3A.
(A) Schematic – His-tagged 3A binds to Golgi-mimic vesicles containing DGS-NTA(Ni) (5% DGS-NTA(Ni), 10% PS, 20%PE, 20% PI, 45% PC) and recruits PI4KIIIβ. ACBD3 binds to the membrane associated PI4KIIIβ-3A complex. I43A PI4KIIIβ no longer binds to ACBD3 but maintains 3A binding. **(B)** Lipid kinase assays monitoring the production of ADP in the presence of 5% NiNTA vesicles at 0.5 mg/mL were carried out with 150 nM PI4KIIIβ for 60 minutes. ACBD3 was present at 500 nM. The I43A PI4KIIIβ mutation that disrupts PI4KIIIβ-ACBD3 complex formation does not change basal enzyme activity and maintains activation by 3A. However, the I43A PI4KIIIβ mutation eliminates ACBD3 sensitization to 3A activation. **(C)** Schematic – His-tagged 3A binds to 5% NiNTA vesicles and recruits PI4KIIIβ. ACBD3 binds to the membrane associated PI4KIIIβ-3A complex. IQ380AE and Y525 ACBD3 mutants no longer bind 3A but maintain PI4KIIIβ binding. **(D)** The IQ380AE and Y525 ACBD3 mutations that disrupt 3A-ACBD3 complex formation eliminate ACBD3 sensitization of the 3A-PI4KIIIβ activation. For panels B+D experiments were carried out in triplicate and error bars represent SD, with N.S. being shown for p values >0.05.

2.5 Discussion

Understanding the molecular mechanism of how PI4KIIIβ can be activated downstream of viral infection is an important goal in identifying potential broad-spectrum anti-viral strategies for intervention. Critical to this goal is understanding how PI4KIIIβ interacts with, and is activated by, its full complement of host binding proteins, and how host PI4KIIIβ binding proteins participate in activation downstream of viral infection. PI4KIIIβ is able to directly bind to a number of host binding partners, and different viruses appear to exploit the different binding partners of PI4KIIIβ to mediate recruitment and activation of the kinase at viral replication organelles. Using a combination of biochemical assays, HDX-MS, and structural analysis has allowed us to build the most complete model describing how PI4KIIIβ-ACBD3 and Aichi virus 3A interact, and through targeted mutations we have revealed the binding interfaces of these enzymes. Surprisingly, we find that the Aichi virus 3A protein is able to directly activate the lipid kinase activity of PI4KIIIβ when presented on a membrane surface. ACBD3 appears to play a key scaffolding role in the assembly of the complex, as the presence of ACBD3 greatly sensitizes PI4KIIIβ activation by Aichi virus 3A.

ACBD3 has been previously shown to bind PI4KIIIβ directly, and when located at membrane surfaces is able to activate PI4KIIIβ activity (48). It has been heavily implicated in mediating PI4KIIIβ activation downstream of a number of different picornaviruses, with the 3A proteins from Aichi virus, human rhinovirus 14, poliovirus, and coxsackieviruses B2, B3 and B5 all being able to pull down ACBD3 (79). Further studies examining the role of ACBD3 in mediating viral replication have been ambiguous, with ACBD3 being required for PI4KIIIβ activation in Aichi virus (57, 76), but replication in rhinovirus 14 and coxsackievirus B3 being independent of ACBD3 (83, 87), and experiments in poliovirus actually showing an inverse dependence on ACBD3 in viral replication (77). Our discovery that Aichi virus 3A protein is able to directly activate PI4KIIIβ in vitro may explain some of the discrepancies on the role of ACBD3 in viral infection. A further complication studying the role of ACBD3 during infection is that this protein plays a key role in maintaining PI4KIIIβ at the Golgi complex as well as acting as a hub connecting many signalling pathways, including cholesterol trafficking, and iron metabolism (113); therefore, ACBD3 knockdown may be deleterious in a myriad of ways to the host cell. The generation of specific point mutants for all signalling components that specifically disrupt only

single interactions will be essential to fully understand the role of each protein complex in both host and viral signalling.

The discovery of the role of the GOLD domain in mediating the interaction between 3A and ACBD3 is intriguing, as this domain also mediates the recruitment of ACBD3 to the Golgi through interactions with the protein Giantin (112). The replacement of the interaction between Giantin and ACBD3 by 3A leads to a potential mechanism of how ACBD3 can be redistributed during viral replication, and how it can act as a recruitment point for PI4KIIIβ. The discovery of a unique, non-conserved N-terminal extension of the ACBD3 GOLD domain that mediates the Aichi virus 3A interaction explains the specificity of the 3A interaction for the GOLD domain of ACBD3. Previous work using mammalian two-hybrid screening had shown that a construct comprised of 260-528 of ACBD3 (this construct partially deletes the Q domain, and contains the entire GOLD domain) is able to interact with the 3A proteins from Aichi and poliovirus (56). Surprisingly, we found that there is a very large decrease in H/D exchange in the acyl-CoA binding domain (ACB) in the presence of Aichi 3A protein, and this change may indicate that there is a large conformational change between the different domains of ACBD3 upon 3A binding. Further investigations probing potential changes in lipid transport properties of ACBD3 upon 3A binding will be useful in fully understanding the full role of ACBD3 in viral replication. The N-terminus of Aichi virus 3A was identified as the main interaction surface for ACBD3 binding, which is consistent with previous alanine screening mutagenesis, which identified a cluster of residues in this region that abolished PI4KIIIβ-ACBD3 binding (79).

ACBD3 is not the only PI4KIIIβ binding partner that has been implicated in mediating viral replication. PI4KIIIβ is able to directly bind the GTPase Rab11 (38), however, instead of Rab11 acting as the recruitment/activation signal for PI4KIIIβ, this interaction appears to be essential for the recruitment of Rab11 to the Trans Golgi network (67). It has been shown that 3A proteins from enteroviruses are able to recruit Rab11 positive recycling endosomes to replication organelles, along with PI4KIIIβ, resulting in a redistribution of intracellular cholesterol pools from the plasma membrane to viral replication organelles, which in turn leads to increased viral replication (80). The role of the direct complex between Rab11 and PI4KIIIβ in this process remains unclear. PI4KIIIβ has also been proposed to be activated directly through the action of the GTPase Arf1(54), however, no direct interaction has been determined between these proteins in solution. Enteroviruses, including poliovirus and coxsackievirus B3, use their 3A proteins to

directly interact with GBF1, the GEF for Arf1, leading to activation of PI4KIIIβ (58). However, experiments have shown that coxsackievirus B3 and rhinovirus can recruit PI4KIIIβ independent of Arf1-GBF1 (83, 87), further complicating the mechanism of how PI4KIIIβ is recruited to replication organelles. The protein c10orf76 has recently been identified as a potential binding partner of PI4KIIIβ, and its presence was required for the viral replication of coxsackievirus A10 (68). Examining the role of the different 3A proteins from other viruses using similar biochemical reconstitution experiments with PI4KIIIβ and other potential host factors will be informative into further molecular mechanisms of PI4KIIIβ activation.

The role of PI4KIIIβ in mediating viral replication has led to great interest as a potential pan-viral therapeutic target. Indeed, numerous inhibitors of PI4KIIIβ have been developed and are able to target a number of different positive-sense ssRNA viruses (114–118). Many of these compounds have shown high levels of organismal toxicity, an effect attributed to their activity against PI4KIIIβ. Fully understanding the molecular mechanisms by which PI4KIIIβ is activated will be essential to the development of novel inhibitory strategies that may be able to target viral replication either upstream or downstream of PI4KIIIβ activation. Our study provides critical insight into the mechanism by which 3A proteins can mediate the activation of PI4KIIIβ, as well as mechanisms on how PI4KIIIβ binding proteins can be involved. Rationally designed mutations from our work provide a framework for future studies on the role of different 3A proteins from multiple pathogenic viruses in mediating activation through ACBD3.

Chapter 3: Characterization of the c10orf76-PI4KB complex, and its necessity for Golgi PI4P levels and enterovirus replication

Adapted from:

McPhail, J.A., Lyoo, H.R., Pemberton, J.G, Hoffmann, R.M., van Elst, W., Strating J.R.P.M., Jenkins, M.L., Stariha J.T.B., Powell, C.J., Boulanger, M.J., Balla, T., van Kuppeveld, F.J.M., and Burke, J.E. (2019). Characterization of the c10orf76-PI4KB complex, and its necessity for Golgi PI4P levels and enterovirus replication. EMBO Reports. e48441.

Nomenclature:

This chapter will refer to PI4KIIIβ as PI4KB.

Contributions:

At the time of this study, I was mentoring Reece Hoffmann (RHM), an honors student in the Burke laboratory. I also had the assistance of Meredith Jenkins (MLJ) and Jordan Stariha (JTBS) as laboratory technicians. I designed all constructs used in this study with input from John Burke (JEB), with the exception of those plasmids obtained as gifts. I cloned the majority of constructs, including all of those with recruitable/fluorescent tags for use in microscopy studies. RHM assisted cloning of more than a dozen c10orf76 mutants to identify a PI4KB-complex disrupting mutation. I expressed all proteins produced in Sf9/Baculovirus, and *E. coli* protein expression was split between myself, RHM, MLJ and JTBS. I purified the majority of proteins, with help from RHM, MLJ and JTBS. I performed all pulldown and kinase assays, including phosphorylation of PI4KB by PKA. I performed HDX-MS experiments led by MLJ and assisted by RHM. HDX-MS analysis was completed by myself, MLJ, RMH and JEB. ITC experiments were performed by Cameron Powell (CJP) with my assistance using the instrumentation of Martin Boulanger (MJB). Viral infection assays were performed by Heyrhyoung Lyoo (HRL) and Wendy van Elst (WvE) using my fluorescently tagged constructs. HRL characterized c10orf76 knockout cells. Joshua Pemberton (JGP) and Tamas Balla (TB) performed cellular c10orf76 recruitment experiments using my fluorescently tagged constructs. I designed the research alongside Jeroen Strating (JRPM), TB, Frank van Kuppeveld (FJMK) and JEB. I wrote the manuscript along with JEB with input from all authors.

3.1 Abstract

The lipid kinase PI4KB, which generates phosphatidylinositol 4-phosphate (PI4P), is a key enzyme in regulating membrane transport and is also hijacked by multiple picornaviruses to mediate viral replication. PI4KB can interact with multiple protein binding partners, which are differentially manipulated by picornaviruses to facilitate replication. The protein c10orf76 is a PI4KB-associated protein that increases PI4P levels at the Golgi and is essential for the viral replication of specific enteroviruses. We used hydrogen deuterium exchange mass spectrometry to characterize the c10orf76-PI4KB complex and reveal that binding is mediated by the kinase linker of PI4KB, with formation of the heterodimeric complex modulated by PKA-dependent phosphorylation. Complex-disrupting mutations demonstrate that PI4KB is required for membrane recruitment of c10orf76 to the Golgi, and that an intact c10orf76-PI4KB complex is required for the replication of c10orf76-dependent enteroviruses. Intriguingly, c10orf76 also contributed to proper Arf1 activation at the Golgi, providing a putative mechanism for the c10orf76-dependent increase in PI4P levels at the Golgi.

3.2 Introduction

Phosphoinositides are essential regulatory lipids that play important roles in myriad cellular functions. The phosphoinositide species phosphatidylinositol 4-phosphate (PI4P) is widely distributed and involved in the coordinated regulation of membrane trafficking, cell division, and lipid transport (2, 119). Multiple human pathogens manipulate PI4P levels to mediate their intracellular replication, including *Legionella* (120) and multiple picornaviruses (58, 75). PI4P pools in the Golgi apparatus are generated by both PI4K2A and PI4KB (46). While the localization and activity of PI4K2A is regulated through its palmitoylation, local membrane composition, and cholesterol levels (47), the activity of PI4KB is regulated by multiple protein-protein interactions and phosphorylation (38, 48, 49). These regulatory PI4KB protein-protein interactions are in turn manipulated by many pathogenic RNA viruses that have evolved the ability to hijack PI4KB and generate PI4P-enriched replication organelles, which are essential for viral replication (74). For most picornaviruses, manipulation of PI4P levels is driven by the action of the viral 3A protein and its interactions with PI4KB-binding proteins (56, 57, 77, 79).

PI4KB plays both important catalytic and non-catalytic functions, with its regulation controlled by interactions with multiple protein binding partners, including acyl CoA Binding

Domain 3 (ACBD3), Rab11, 14-3-3, and c10orf76 (chromosome 10, open-reading frame 76, also referred to as Armadillo-like helical domain-containing protein 3 (ARMH3)). PI4KB is a multi-domain lipid kinase containing a disordered N-terminus, a helical domain, and a bi-lobal kinase domain (38, 97). Biophysical and biochemical studies have defined the domains of PI4KB that mediate complex formation with a number of binding partners. The helical domain of PI4KB forms a non-canonical interaction with the small GTPase Rab11a that mediates localization of a pool of Rab11 to the Golgi and TGN (38, 54). PI4KB is primarily localized to the Golgi through the interaction of its N-terminus with ACBD3 (48, 57). PI4KB is activated downstream of ADP-ribosylation factor 1 (Arf1) (54), however, no evidence for a direct Arf1-PI4KB interface has been found, suggesting that this may be an indirect effect. PI4KB contains phosphorylation sites in disordered linkers between domains, including Ser294 in the helical-kinase linker of PI4KB, which is phosphorylated by protein kinase D (PKD). Phosphorylation of Ser294 drives binding of 14-3-3, which stabilizes PI4KB, prevents degradation, and increases Golgi PI4P levels (69, 71, 92). Ser496 in the N-lobe linker of PI4KB is phosphorylated by protein kinase A (PKA) (121), and drives PI4KB localization from the Golgi to nuclear speckles (122). c10orf76 was identified as a putative PI4KB interacting partner in immunoprecipitation experiments (56, 88), with knockout of c10orf76 leading to decreased Golgi PI4P levels (68). The role of this protein is not known, however, it contains a domain of unknown function (DUF1741) that is well conserved in many eukaryotes.

Enterovirus proteins do not interact directly with PI4KB – they instead recruit PI4KB-regulatory proteins. A key component of manipulating PI4KB to generate PI4P-enriched replication organelles is the interaction of viral 3A proteins with host PI4KB-binding proteins. The 3A proteins from enteroviruses (i.e. Poliovirus, Rhinovirus, Coxsackievirus, Rhinovirus and Enterovirus 71) and Aichivirus recruit PI4KB to replication organelles through an interaction with ACBD3 (49, 56, 57, 76, 77, 79, 82, 123, 124). The viral 3A protein from Aichivirus forms a direct interaction with the GOLD domain of ACBD3, leading to redistribution of PI4KB to replication organelles (49, 124). Enteroviruses also manipulate other lipid signaling pathways, with viral 3A proteins able to recruit the protein Golgi-specific brefeldin A-resistance guanine nucleotide exchange factor 1 (GBF1) that activates Arf1 (58, 85, 86, 125), and subvert Rab11-positive recycling endosomes to replication organelles (80). A new component of the PI4KB hijacking process, c10orf76, was identified as a key host factor in the replication of coxsackievirus A10

(CVA10) replication, but not coxsackievirus B1 (CVB1) (68).

We hypothesized that a direct c10orf76-PI4KB interaction may be critical for the regulation of Golgi PI4P levels and play a role in enterovirus replication. To elucidate the role of c10orf76 in PI4KB-mediated signaling, we utilized a synergy of hydrogen deuterium exchange mass spectrometry (HDX-MS) and biochemical assays to characterize the novel c10orf76-PI4KB complex *in vitro*. This allowed us to engineer complex-disrupting mutations that were subsequently used to define the role of the c10orf76-PI4KB complex in Golgi PI4P-signaling and viral replication *in vivo*. We find that PI4KB and c10orf76 form a high affinity complex mediated by a disorder-to-order transition of the kinase linker of PI4KB, with complex affinity modulated by PKA phosphorylation of the c10orf76 binding site on PI4KB. Knockout of c10orf76 lead to decreased PI4P levels, and disruption of Arf1 activation in cells. Complex-disrupting mutations revealed that c10orf76 is recruited to the Golgi by PI4KB, and that viral replication of enteroviruses that require c10orf76 is mediated by the c10orf76-PI4KB complex.

3.3 Materials and Methods

Protein expression and purification: c10orf76 and PI4KB

The human *C10orf76* gene (Uniprot Q5T2E6) was synthesized by GeneArt (Thermofisher). c10orf76 and PI4KB (Uniprot Q9UBF8-2) were each expressed with an N-terminal 6xHis-tag followed by a TEV protease site. The c10orf76 and PI4KB proteins purified for HDX-MS were expressed in *Spodoptera frugiperda* (*Sf9*) cells by infecting 1-4 L of cells at a density of 1.5 x 10^6 cells/mL with baculovirus encoding the kinase. After 60-72 hours infection at 27^{o}C, *Sf9* cells were harvested and washed in phosphate-buffered saline (PBS). The c10orf76 and PI4KB proteins utilized for assays, mutational analysis and studying PKA phosphorylation were expressed in Rosetta (DE3) *E. coli* (c10orf76) or BL21 C-41(DE3) *E. coli* (PI4KB) induced overnight at 16 ^{o}C with 0.1 mM IPTG at an OD_{600} of 0.6. Cell pellets containing c10orf76 or PI4KB were sonicated in NiNTA Buffer (20 mM Tris-HCl pH 8.0, 100 mM NaCl, 20 mM imidazole, 5% (v/v) glycerol, 2 mM β-mercaptoethanol) containing protease inhibitors (Millipore Protease Inhibitor Cocktail Set III, Animal-Free) for 5 minutes on ice. Triton X-100 (0.1% v/v) was added to the cell lysate and the lysed cell solution was centrifuged for 45 minutes at 20,000 x g at 2^{o}C. Supernatant was filtered through a 5 μm filter and loaded onto a 5 mL HisTrap™ FF crude (GE) column in NiNTA buffer. The column was washed with 1.0 M NaCl and 20 mM

imidazole in NiNTA buffer and protein was eluted with 200-250 mM imidazole in NiNTA buffer. Eluted c10orf76 or PI4KB was pooled and concentrated onto a 5 mL HiTrap™ Q column (GE) equilibrated with Q buffer (20 mM Tris-HCl pH 8.0, 100 mM NaCl, 5% glycerol v/v, 2 mM β-mercaptoethanol) and eluted with an increasing concentration of NaCl. Protein was pooled and concentrated using an Amicon 30K concentrator and incubated overnight on ice with the addition of TEV protease. Size exclusion chromatography (SEC) was performed using a Superdex™ 200 10/300 GL increase (GE) column equilibrated in SEC buffer (20 mM HEPES pH 7.5, 150 mM NaCl and 0.5 mM TCEP). Fractions containing the protein of interest were pooled, concentrated, spun down to remove potential aggregate and flash frozen in liquid nitrogen for storage at -80 ºC. c10orf76-PI4KB complex SEC trace was generated by mixing c10orf76 and PI4KB in a 1:1 ratio after individual anion exchange runs and then injecting onto the Superdex™ 200 10/300 GL increase (GE) column. Elution volumes of protein standards were obtained from the GE Instruction 29027271 AH Size exclusion chromatography columns document. See *Protein Kinase A (PKA) treatment of PI4KB* for details on producing the phosphorylated variant of PI4KB.

Protein expression and purification: ACBD3, Rab11a and PKA

ACBD3 and Rab11a were expressed with N-terminal GST tags, with Protein kinase A (*M. musculus* PKA catalytic subunit alpha; Addgene 14921) expressed with an N-terminal His tag. ACBD3, Rab11a, and PKA were expressed in BL21 C-41(DE3) *E. coli* cells, with ACBD3 and Rab11 expression carried out overnight at 16 ºC with 0.1 mM IPTG, and PKA expression was carried out for 4 hours at 28 ºC with 1 mM IPTG. ACBD3, Rab11, and PKA were purified as previously published (38, 49, 126). In brief, cell pellets containing expressed ACBD3 or Rab11a were sonicated in Q Buffer (20 mM Tris-HCl pH 8.0, 100 mM NaCl, 5% (v/v) glycerol, 2 mM β-mercaptoethanol) containing protease inhibitors (Millipore Protease Inhibitor Cocktail Set III, Animal-Free) for 5 minutes on ice. Triton X-100 (0.1% v/v) was added to the cell lysate and the lysed cell solution was centrifuged for 45 minutes at 20,000 x g at 2ºC. Supernatant was filtered through a 5 μm filter and incubated with 1-4mL of Glutathione Sepharose™ 4B beads (GE) for 1-2 hours at 4ºC. Beads were then washed with Q buffer, and GST-tagged proteins were eluted with 20 mM glutathione in Q buffer. Protein was further purified using anion exchange and size-exclusion chromatography as described above and final protein was spun down to remove potential aggregate and flash frozen in liquid nitrogen for storage at -80 ºC. Nickel purification of PKA

proceeded as described for PI4KB, and nickel eluate was concentrated, spun down to remove potential aggregate and flash frozen in liquid nitrogen for storage at -80 ºC.

Nickel and GST Pulldown Assays

For His pulldowns, NiNTA agarose beads (Qiagen) (20 µL) were washed three times by centrifugation and resuspension in NiNTA buffer. His-tagged bait protein was then added to a concentration of 1-3 μM and incubated with the beads on ice for 10 minutes in a total volume of 50 μL. Beads were washed three times with 150 μL NiNTA buffer at 4 ºC. Non-His-tagged prey protein was then added to a final concentration of 1-2 μM in a total volume of 50 μL, at which point 10 μL was taken for SDS-PAGE analysis. The mixture was incubated on ice for an additional 30 minutes and then washed four times with 120 μL NiNTA buffer at 4 ºC at which time an aliquot was taken as the output for SDS-PAGE analysis.

For GST pulldowns, Glutathione Sepharose™ 4B beads (GE healthcare) were washed three times by centrifugation and resuspension in Q buffer. GST-tagged bait protein (or control GST) was then added to a concentration of 3-6 µM in 50 µL and incubated with the beads on ice for 10 minutes in a total volume of 50 µL. Beads were washed three times with 150 µL Q buffer at 4 ºC. Non-GST-tagged prey proteins were then added to a final concentration of 2-4 µM in a total volume of 50 µL, at which point the input was taken for SDS-PAGE analysis. The mixture was incubated on ice for an additional 30 minutes and then washed four times with 120 µL Q buffer at 4 ºC, at which time an aliquot was taken as the output for SDS-PAGE analysis.

Vesicle Preparation and Lipid Kinase Assays

Lipid kinase assays were carried out using the Transcreener® ADP^2 FI Assay (BellBrook Labs) following the published protocol as previously described (49). In brief, substrate stocks were made up containing 1.0 mg/mL PI vesicles or 4.0 mg/mL Golgi-mimetic vesicles (10% PS, 20% PI, 25% PE, 45% PC) and were extruded through a 100 nm Nanosizer Extruder (T&T Scientific) and then combined with in a buffer containing 20 mM Hepes pH 7.5, 100 mM KCl and 0.5 mM EDTA (200 µ*M* ATP with 1.0 mg/mL PI vesicles, 20 µ*M* ATP with 1.0 mg/mL Golgi-mimetic vesicles). Kinase reactions were started by adding 2 µL of this substrate stock in a 384-well black low volume plates (Corning 4514). Proteins were thawed on ice and spun down to remove precipitate. Proteins were diluted individually to 4X the desired concentration in Kinase Buffer

(40 mM Hepes pH 7.5, 200 mM NaCl, 20 mM $MgCl_2$, 0.8% Triton-X, and 0.2 mM TCEP) on ice. Proteins were then mixed together or with additional Kinase buffer resulting in 2X desired concentrations of each protein. To start the reaction, 2 µL of 2X protein stock was added to 2 µL of 2X substrate stock in plates. After mixing, the 4 µL reactions consisted of 30 mM HEPES pH 7.5 (RT), 100 mM NaCl, 50 mM KCl, 10mM $MgCl_2$, 0.25 mM EDTA, 0.4% (v/v) Triton-X, 0.1 mM TCEP, 10 µM ATP and 0.5 mg/mL vesicles. PI4KB was run at a final concentration of 15 nM, 20 nM or 40 nM and c10orf76 was run in 4-fold curves from 1 µM – 3.9 nM, or 1.5 µM – 23 nM, or 5-fold curves from 2 µM – 1.6 nM. Reactions proceeded at 23°C for 20-30 minutes. Reactions were stopped using 4 µL of the transcreener stop buffer (1X Stop & Detect Buffer B, 8 nM ADP Alexa594 Tracer, 97 µg/ml ADP2 Antibody-IRDye® QC-1). Fluorescence intensity was measured using a Spectramax M5 plate reader with $\lambda ex\ x = 590$ nm and $\lambda em\ m = 620$ nm (20nm bandwidth). Data was plotted using Graphpad Prism software, with IC_{50} values determined by nonlinear regression (curve fit). No detectable nonspecific ATPase activity was detected in reactions containing 250 nM wild-type PI4KB without vesicle substrate.

Mapping the c10orf76-PI4KB binding interface using HDX-MS

HDX reactions were conducted in 50 µL reactions with a final concentration of 400 nM of protein per sample (c10orf76-PI4KB, 400 nM each). Reactions were initiated by the addition of 45 µL of D_2O Buffer Solution (10 mM HEPES pH 7.5, 50 mM NaCl, 97% D_2O) to 5 µL of protein solution, to give a final concentration of 87% D_2O. Exchange was carried out for four timepoints, (3s at 1°C and 3s, 30s, and 300s at 23 °C). Exchange was terminated by the addition of acidic quench buffer giving a final concentration 0.6 M guanidine-HCl and 0.8% formic acid. All experiments were carried out in triplicate. Samples were immediately frozen in liquid nitrogen and stored at −80°C until mass analysis.

Comparison of FLH409AAA and WT c10orf76 secondary structure

HDX-MS reactions were performed with 40 µL final volume with a protein concentration of 0.25 µM in each sample. Reactions were started by the addition of 39 µL D2O buffer (100mM NaCl, 35 mM Hepes, 91.7% D_2O) to 1 µL of protein (Final: 89.4% D2O). Reactions were quenched by the addition of 30uL of acidic quench buffer (3% formic acid, 2M Guanidine) resulting in final 1.28% Formic acid and 0.85M guandine-HCl. Proteins were allowed to undergo

exchange reactions for either 3s or 300s at 23ºC prior to addition of quench buffer and flash freezing in liquid N_2. All samples were set and run in triplicate. Samples were stored at -80ºC until injection onto the UPLC for MS analysis.

HDX-MS data analysis

Protein samples were rapidly thawed and injected onto a UPLC system kept in a cold box at 2°C. The protein was run over two immobilized pepsin columns (Applied Biosystems; porosyme, 2-3131-00) stored at 10°C and 2°C at 200 µL/min for 3 min and the peptides were collected onto a VanGuard precolumn trap (Waters). The trap was subsequently eluted in line with an Acquity 1.7 µm particle, 100 × 1 mm^2 C18 UPLC column (Waters), using a gradient of 5-36% B (buffer A 0.1% formic acid, buffer B 100% acetonitrile) over 16 minutes. MS experiments were performed on an Impact QTOF (Bruker) and peptide identification was done by running tandem MS (MS/MS) experiments run in data-dependent acquisition mode. The resulting MS/MS datasets were analyzed using PEAKS7 (PEAKS) and a false discovery rate was set at 1% using a database of purified proteins and known contaminants. HD-Examiner Software (Sierra Analytics) was used to automatically calculate the level of deuterium incorporation into each peptide. All peptides were manually inspected for correct charge state and presence of overlapping peptides. Deuteration levels were calculated using the centroid of the experimental isotope clusters. Attempts at generating fully deuterated protein samples to allow for the control of peptide back exchange levels during digestion and separation were made for all proteins. Protein was incubated with 3M guanidine for 30 minutes prior to the addition of D_2O, where they were further incubated for an hour on ice. The reactions were then quenched as before. Generation of a fully deuterated sample was successful for PI4K using this method, however generation of fully deuterated c10orf76 failed. Results for c10orf76 are therefore presented as relative levels of deuterium incorporation and the only control for back exchange was the level of deuterium present in the buffer (87%). The average error of all time points and conditions for each HDX project was less than 0.2 Da. Therefore, changes in any peptide at any time point greater than both 7% and 0.5 Da between conditions with an unpaired t-test value of $p<0.05$ was considered significant. Full statistics on all HDX-MS experiments are summarized in **Appendix F**.

Protein Kinase A (PKA) Treatment of PI4KB

PKA (mouse catalytic subunit) was serially diluted and different concentrations were incubated with PI4KB in 20 µL reactions on ice for 1 hour (20 µg PI4KB, 20 mM $MgCl_2$, 200 µM ATP and either 840 ng, 168 ng, 34 ng, 7 ng or 0 ng PKA). Reactions were terminated by the addition of acidic quench buffer giving a final concentration 0.6 M guanidine-HCl and 0.8% formic acid and then flash frozen in liquid N_2 prior to MS phosphorylation analysis.

To generate *E. coli* expressed, PKA phosphorylated PI4KB for use in kinase assays and HDX-MS, phosphorylation of Ser496 was carried out using 1.0 mg PI4KB, 20 mM $MgCl_2$, 200 µM ATP and 4.2 µg PKA in NiNTA buffer, with the reaction allowed to proceed for 1 hour on ice. The reaction was quenched with 20 mM EDTA, and immediately loaded onto a GE 1 mL HisTap FF crude to remove His-tagged PKA. Phosphorylated PI4KB was concentrated followed by size exclusion chromatography as described for PI4KB above. In tandem, a non-phosphorylated PI4KB control was purified in the same manner except $MgCl_2$, ATP, and PKA were not added. Protein was flash frozen in liquid N_2 for storage at -80 ºC.

HDX-MS dose response of c10orf76 of phosphorylated PI4KB

Phosphorylated and non-phosphorylated PI4KB were generated and purified as described above. HDX reactions were conducted in 130 µl reaction volumes with a final concentration of 20nM PI4KB (phosphorylated or non-phosphorylated) per sample, with 0 nM, 5 nM, 10 nM, 20 nM, 40 nM, 80 nM, 160 nM and 320 nM c10orf76. Exchange was carried out for 5 seconds, in triplicate for each concentration of c10orf76. Hydrogen deuterium exchange was initiated by the addition of 80 µl of D2O buffer solution (10 mM HEPES (pH 7.5), 50 mM NaCl, 97% D2O) to the protein solution, to give a final concentration of 60% D2O. Exchange was terminated by the addition of 20 µl ice cold acidic quench buffer at a final concentration 0.6 M guanidine-HCl and 0.9% formic acid. Samples were immediately frozen in liquid nitrogen at − 80 °C. Data analyzed as described above in *HDX-MS data analysis.*

Phosphorylation Analysis

LC-MS/MS analysis of phosphorylated variants of PI4KB was carried out as described in the HDX-MS data analysis section. MS/MS datasets were analyzed using PEAKS7 to identify phosphorylated peptides in PI4KB and c10orf76. A false discovery rate was set at 0.1% using a

database of purified proteins and known contaminants. To measure PI4KB phosphorylation levels using Bruker Data analysis, the phosphorylated and non-phosphorylated peptides of interest were extracted, and the total area of each peptide was manually integrated to determine the amount of phosphorylated vs non-phosphorylated species under given experimental conditions. No phosphorylation was detected in *E. coli* derived PI4KB. For *Sf9* derived PI4KB Ser294 phosphorylation, the peptides KRTAS*NPKVENEDE (290-303) and KRTAS*NPKVENEDEPVRLADERE (290-312) were averaged, for Ser413 phosphorylation DTTSVPARIPENRIRSTRS*VE NLPECGITHE (395-425) was used, for Ser430 phosphorylation GITHEQRAGS*F (430-441) was used, and for Ser496 phosphorylation IAAGDIRRRLS*EQLAHTPTA (486-505) and IAAGDIRRRLS*EQ-LAHTPTAF (486-506) were averaged. No phosphorylation was detected in *E. coli* derived c10orf76. For *Sf9* derived c10orf76 Ser14 phosphorylation, LRKSS*ASKKPLKE (10-22) was used, and for the 325-351 phosphorylation (exact location of phosphorylation ambiguous) VTTPVSPAPTTPVTPLGTTPPSSD (325-348), VTTPVSPAPTTPVTPLGTTPPSSDVISS (325-352) and VTTPVSPAPTTPVTPLGTTPPSS (325-347) were averaged.

Isothermal Titration Calorimetry

Purified c10orf76, non-phosphorylated PI4KB, and Ser496-phosphorylated PI4KB were dialyzed separately into buffer containing 20 mM Hepes pH 7.5, 150 mM NaCl and 0.5 mM TCEP. All ITC experiments were carried out at 20 °C on a MicroCal iTC200 instrument (GE Healthcare). The sample cell contained non-phosphorylated PI4KB or Ser496-phosphorylated PI4KB (5 μM), and c10orf76 (50 μM) was added in 19 injections of 2 μL each. Data was processed using Origin software (MicroCal) and the dissociation constants (Kd) were determined using a one-site model. Figures are of a single experiment, but are representative of three independent experiments using protein from two different protein preparations.

Alignments

Protein sequences from the Uniprot database were aligned using Clustal Omega (127) and figures were generated using ESPript (91). Uniprot PI4KB entries used: *H. sapiens* (Q9UBF8-2), *M. musculus* (Q8BKC8), *D. rerio* (Q49GP3), *D. melanogaster* (Q9BKJ2), *C. elegans* (Q20077).

Uniprot c10orf76 entries used: *H. sapiens* (Q5T2E6), *M. musculus* (Q6PD19), *D. rerio* (Q6PGW3), *D. melanogaster* (Q7KSU3).

DNA Constructs and Antibodies

GFP-PI4KB, GFP-PI4KB RL494EA, GFP-c10orf76, and GFP-c10orf76 FLH409AAA were cloned using Gibson assembly (128) into the pEGFP-C1 vector (Clonetech). mRFP-FKBP12-PI4KB and mRFP-FKBP12-PI4KB RL494EA were generated by amplifying the mRFP-FKBP12 insert from mRFP-FKBP12-5ptpase domain (129) and replacing the N-terminal GFP in either GFP-PI4KB or GFP-PI4KB RL494EA using a single digest with NdeI. AKAP-FRB-CFP, which is used to selectively recruit FKBP12-tagged proteins to the outer mitochondrial membrane, has been described previously (130).

The following antibodies were used to examine protein localization in WT and c10orf76 knockout HAP1 cells using immunofluorescence assays (IFA) or western blot (WB): a-GBF1 (Sigma, SAB2700817, diluted 1:100 [IFA] or 1:1000 [WB]), a-CM1 (coatomer, Felix Wieland, diluted 1:500 [IFA]), a-GM130 (BD Biosc., 610822, diluted 1:200 [IFA]), a-Giantin (Enzo Life Science, ALX-804-600-C100, diluted 1:200 [IFA]), a-ERGIC53 (Enzo Life Science, ALX-804-602-C100, diluted 1:1000 [IFA]), a-βCOP (Sigma, G6160, diluted 1:100 [IFA]), a-PI4P IgM (Echelon, Z-P004, diluted 1:100 [IFA]), a-ACBD3 (Sigma, WH0064746M1-100ug, diluted 1:100 [IFA]), a-Actin (Sigma, A5316, diluted 1:30000 [WB]), a-PI4KB (Millipore, 06-578, diluted 1:100 [IFA] 1:1000 [WB]), a-COPI α/γ (Felix Wieland, diluted 1:1000 [IFA]), a-TGN46 (Novus Biologicals, NBP1-49643, diluted 1:400 [IFA]), Goat anti-Mouse IgG (H+L) Cross-Adsorbed Secondary Antibody Alexa Fluor 488 (Molecular Probes, A-11001, diluted 1:400 [IFA]), Goat anti-Mouse IgG (H+L) Cross-Adsorbed Secondary Antibody Alexa Fluor 594 (Molecular Probes, A-11005, diluted 1:400 [IFA]), Goat anti-Mouse IgG (H+L) Cross-Adsorbed Secondary Antibody Alexa Fluor 647 (Molecular Probes, A-21235, diluted 1:400 [IFA]), Goat anti-Mouse IgM (Heavy chain) Cross-Adsorbed Secondary Antibody Alexa Fluor 594 (Molecular Probes, A-21044, diluted 1:400 [IFA]), Goat anti-Rabbit IgG (H+L) Cross-Adsorbed Secondary Antibody Alexa Fluor 488 (Molecular Probes, A-11008, diluted 1:400 [IFA]), Goat anti-Rabbit IgG (H+L) Cross-Adsorbed Secondary Antibody Alexa Fluor 594 (Molecular Probes, A-11012, diluted 1:400 [IFA]), Goat anti-Rabbit IgG (H+L) Highly Cross-Adsorbed Secondary Antibody Alexa Fluor 647 (Molecular Probes, A-32733, diluted 1:400 [IFA]), IRDye 680RD Goat anti-Mouse IgG (LI-COR

Biosciences, 926-68070, 1:10000 [WB]), IRDye 800CW Goat anti-Rabbit IgG (LI-COR Biosciences, 926-32211, 1:10000 [WB].

Cell Culture, Transfection, and Live-Cell Confocal Microscopy of Rapamycin Recruitment

HEK293-AT1 cells, which stably express the AT1a rat Angiotensin II receptor (131), were cultured in Dulbecco's Modified Eagle Medium (DMEM-high glucose) containing 10% (vol/vol) FBS and supplemented with a 1% solution of penicillin/streptomycin. This cell line is regularly tested for *Mycoplasma* contamination using a commercially-available detection kit (InvivoGen) and, after thawing, the cells are treated with plasmocin prophylactic (InvivoGen) at 500 µg/ml for the initial three passages (6-9 days) as well as supplemented with 5 µg/ml of plasmocin prophylactic for all subsequent passages.

For confocal microscopy, HEK293-AT1 cells ($3x10^5$ cells/well) were plated on 29 mm circular glass-bottom culture dishes (#1.5; Cellvis) pre-coated with 0.01% poly-L-lysine solution (Sigma). The cells were allowed to attach overnight prior to transfection of plasmid DNAs (0.1-0.2 µg/well) using Lipofectamine 2000 (Invitrogen) and Opti-MEM (Invitrogen) according to the manufacturer's instructions. Please note that studies using the rapamycin-inducible protein hetero-dimerization system used a 1:2:1 ratio of plasmid DNA for transfection of the mRFP-FKBP12-tagged PI4KB enzyme, AKAP-FRB-CFP recruiter, and GFP-c10orf76 variant (total DNA: 0.4 µg/well). After 18-20 hr of transfection, cells were incubated in 1 mL of modified Krebs-Ringer solution (containing 120 mM NaCl, 4.7 mM KCl, 2 mM $CaCl_2$, 0.7 mM $MgSO_4$, 10 mM glucose, 10 mM HEPES, and adjusted to pH 7.4) and images were acquired at room temperature using a Zeiss LSM 710 laser-scanning confocal microscope (Carl Zeiss Microscopy). Rapamycin treatment of cells was carried out at a final concentration of 100 nM. Image acquisition was performed using the ZEN software system (Carl Zeiss Microscopy), while the image preparation was done using the open-source FIJI platform (132).

Cell Culture, Transfection, and Live-Cell Confocal Microscopy of HAP1 WT and c10orf76 Knockout Cells

HAP1 WT cells and HAP1 c10orf76 knockout cells were obtained from T. Brummelkamp, and are now carried by Horizon Discovery. The generation and validation of the Hap1 c10orf76 KO cell clone was described previously (68). HeLa R19 cells were obtained from G. Belov

(University of Maryland and Virginia-Maryland Regional College of Veterinary Medicine, US). HeLa PI4KB knockout cells were described previously (123). HAP1 cells were cultured in IMDM (Thermo Fisher Scientific) supplemented with 10% fetal calf serum (FCS) and penicillin–streptomycin. HeLa cells were cultured in DMEM (Lonza) supplemented with 10% FCS and penicillin–streptomycin. All cells were grown at 37°C in 5% CO_2. The following enteroviruses were used: CVA10 (strain Kowalik, obtained from the National Institute for Public Health and Environment; RIVM, The Netherlands), CVB3 (strain Nancy, obtained by transfection of the infectious clone p53CB3/T7 as described previously (133), PV1 (strain Sabin, ATCC). Virus titers were determined by end-point titration analysis and expressed as 50% tissue culture infectious dose ($TCID_{50}$).

Replication rescue assay

HeLa cells were transfected with plasmids carrying WT or mutant PI4KB (RL494EA), Golgi-targeting EGFP (pEGFP-GalT) or kinase-dead PI4KB (PI4KB-KD) as a negative control. At 24 h post-transfection, the cells were infected with CVA10, CVB3, and PV1. At 8 h p.i., the infected cells were frozen, and virus titers were determined by end-point titration analysis and expressed as 50% tissue culture infectious dose ($TCID_{50}$).

Immunofluorescence microscopy of WT and c10orf76 knockout HAP1 cells

HAP1 cells were grown on ibiTreat slides μ-slide 18-wells (Ibidi) one day prior to infection. Cells were fixed by submersion in a 4% paraformaldehyde solution for 15 minutes at room temperature. Specific antibodies and their dilutions used are described in methods above. PI4P staining was performed at room temperature as previously described (134). In brief, cells were washed 3 times with PBS (plus 50 mM NH_4Cl) after fixation. Cells were then permeabilized with 10 μM digitonin in Buffer A (20 mM Pipes pH 6.8, 137 mM NaCl, 2.7 mM KCl) for 10 minutes and blocked with 5% normal goat serum (NGS) in PBS (plus 50 mM NH_4Cl) for 45 minutes. Cells were incubated with anti-PI4P diluted in 5% NGS in PBS for 1 hour, followed by 3 washes with PBS. Cells were incubated with goat anti-mouse IgM and DAPI diluted in 2% NGS in PBS for 1 hour, followed by 3 washes with PBS. Cells were then fixed with 2% formaldehyde for 10 minutes and washed with PBS (plus 50 mM NH_4Cl). For all other immunofluorescence experiments (other than PI4P staining), the following procedure was followed at room

temperature: cells were permeabilized with 0.1% Triton-X in PBS for 10 minutes, washed 2 times with PBS, incubated with primary antibody diluted in 2% NGS in PBS for 45 minutes, washed 3 times with PBS, incubated with secondary antibody diluted in 2% NGS in PBS for 45 minutes and washed 3 times with PBS. Confocal imaging was performed with a Leica SpeII confocal microscope

3.4 Results

c10orf76 forms a direct, high affinity complex with PI4KB

c10orf76 was previously identified as a putative PI4KB-binding partner through immunoprecipitation experiments (56, 88); however, it was not clear if this was through a direct interaction. To identify a potential direct interaction between PI4KB and c10orf76 *in vitro*, we purified recombinant full-length proteins using a baculovirus and *Spodoptera frugiperda (Sf9)* expression system. Experiments on PI4KB used the slightly smaller isoform 2 variant (1-801, uniprot: Q9UBF8-2), compared to PI4KB isoform 1 (1-816 uniprot: Q9UBF8-1), similar to previous structural studies (6). His-pulldown assays using NiNTA-agarose beads and purified recombinant proteins showed a direct interaction between PI4KB and His-tagged c10orf76 (**Fig. 3.1A**). To examine the stoichiometry of the c10orf76-PI4KB complex, we subjected apo c10orf76 (79 kDa) and c10orf76 with PI4KB (89 kDa) to size exclusion chromatography. Apo c10orf76 eluted from the size exclusion column at a volume consistent with a monomer, while the c10orf76-PI4KB complex (158 kDa) eluted at a volume consistent with a 1:1 complex (**Fig. 3.1B).** Since cellular knockout of c10orf76 has been shown to reduce PI4P levels *in vivo* (68) , we investigated the effect of c10orf76 on PI4KB lipid kinase activity with biochemical membrane reconstitution assays using phosphatidylinositol (PI) vesicles. Intriguingly, c10orf76 was a potent inhibitor of PI4KB, with inhibition being dose-dependent and possessing an IC_{50} of ~90 nM (**Fig. 3.1C**). This inhibitory effect was observed on both pure phosphatidylinositol (PI) vesicles, and vesicles that mimic the composition of the Golgi (20% PI, 10% PS, 45% PE, 25% PC) (**Fig. 3.1D**). This paradoxical PI4KB-inhibitory result *in vitro* conflicts with observed Golgi PI4P decreases in c10orf76 deficient cells (68). This suggests that biochemical assays may not fully recapitulate the environment of the Golgi. Pulldown experiments carried out with the PI4KB binding partners Rab11 and ACBD3 revealed that although c10orf76 did not directly bind Rab11 or ACBD3 alone, it could form ternary PI4KB-containing complexes with both (**Fig 3.2E,F**), indicating a unique

c10orf76 binding interface on PI4KB compared to Rab11 and ACBD3. To further define the role of this complex we focused on defining the molecular basis of this interface, allowing for generation of binding-deficient mutants for downstream cellular and viral experiments.

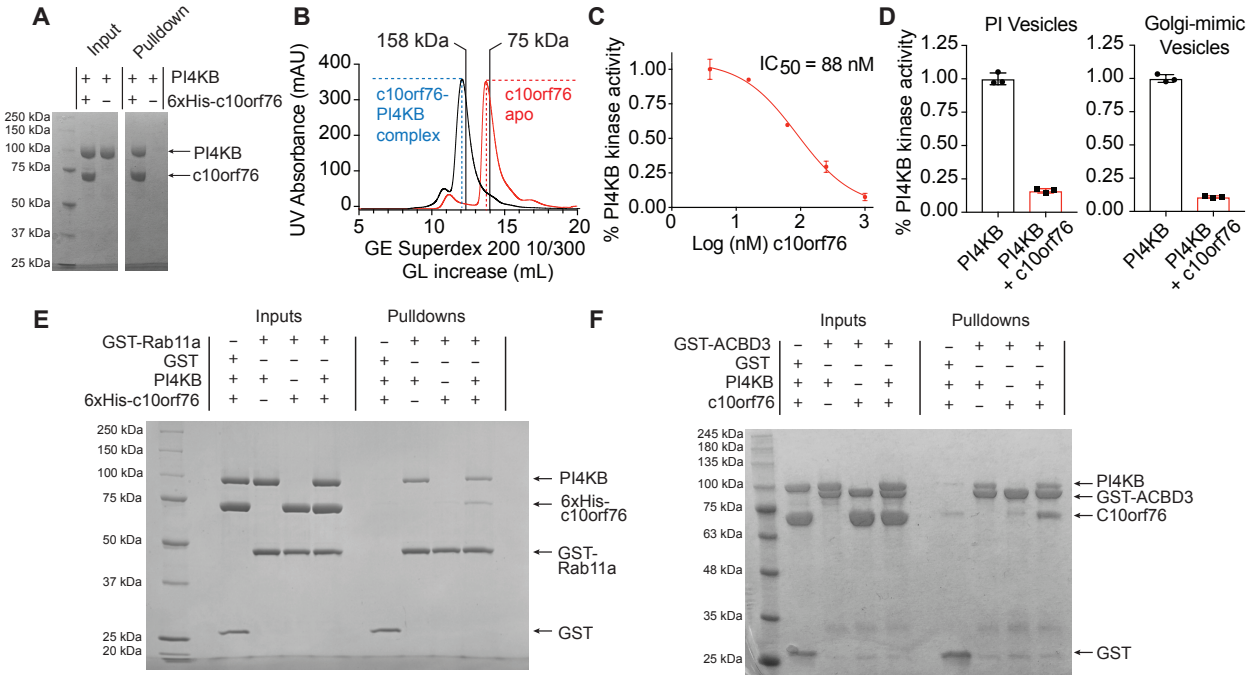

Figure 3.1. PI4KB directly binds c10orf76 and forms ternary complexes with c10orf76, Rab11a and ACBD3.

(A) Recombinant c10orf76 directly binds to PI4KB *in vitro.* His-pulldown assays of baculovirus/*Sf9* produced 6xHis-c10orf76 (3 μM) were carried out with untagged PI4KB (2.5 μM). **(B)** PI4KB and c10orf76 form a stable complex. The complex of c10orf76-PI4KB eluted from a S200 superdex 10/300 GL increase gel filtration column (GE) at a volume consistent with a heterodimer (169 kDa), while c10orf76 alone eluted at a volume consistent with a monomer (79 kDa). Lines with MW values indicate elution of MW standards (158 kDa aldolase, 75 kDa conalbumin). **(C)** PI4KB is potently inhibited by c10orf76 in a dose-dependent manner *in vitro*. Kinase assays of PI4KB (20 nM) in the presence of varying concentrations of c10orf76 (1.6 nM-1 μM) were carried out on pure PI lipid vesicles (0.5 mg/L) in the presence of 100 μM ATP. The data was normalized to the kinase activity of PI4KB alone. IC_{50} values were determined by one binding site, nonlinear regression (curve fit) using Graphpad. Error bars represent standard deviation of independent technical replicates (n=3). **(D)** PI4KB is potently inhibited by c10orf76 on pure PI vesicles and vesicles mimicking Golgi composition. Kinase assays of PI4KB and c10orf76 were carried out on lipid substrate composed of pure PI vesicles (0.5 mg/mL) with 100 μM ATP, and Golgi mimic vesicles (0.5 mg/ml, 10% PS, 20% PI, 25% PE, 45% PC) with 10 μM ATP. PI4KB was present at 20 and 300 nM in the PI and Golgi substrate assays respectively, with c10orf76 present at 500 nM in both experiments. The data is normalized to the kinase activity of PI4KB alone. Error bars represent standard deviation of independent technical replicates (n=3). **(E)** PI4KB can form ternary complexes with Rab11a and c10orf76 *in vitro.* GST-pulldown assays were carried out using GST-Rab11a(Q70L) (6 μM) or GST alone (3 μM) as the bait, using 6xHis-c10orf76 (4 μM), PI4KB (2 μM) as the prey. **(F)** PI4KB can form ternary complexes with ACBD3 and c10orf76 *in vitro.* GST-pulldown assays were carried out using GST-ACBD3 (4 μM) or GST alone (4 μM) as the bait, and 6xHis-c10orf76 (3 μM) and PI4KB (2 μM) as the prey. Samples were washed a total of 4 times in all experiments.

HDX-MS reveals that PI4KB and c10orf76 form an extended interface involving a disorder-to-order transition of the PI4KB N-lobe linker

To identify the putative interface between PI4KB and c10orf76, we employed hydrogen-deuterium exchange mass spectrometry (HDX-MS) to map regions protected in both proteins upon complex formation. HDX-MS is an analytical technique that measures the exchange rate of amide hydrogens in proteins. Because one of the main determinants for amide exchange is the presence of secondary structure, their exchange rate is an excellent readout of protein dynamics. HDX-MS is thus a potent tool to determine protein-protein, protein-ligand, and protein-membrane interactions (14). H/D exchange was carried out for three different conditions: apo PI4KB, apo c10orf76, and a 1:1 complex of PI4KB with c10orf76. Deuterium incorporation experiments were carried out at four different timepoints (3, 30 and 300 seconds at 23°C and 3 seconds at 1°C). Deuterium incorporation is determined by quenching the exchange reaction in a solution that dramatically decreases the exchange rate, followed by rapid digestion, peptide separation, and mass analysis. A total of 185 peptides covering 96.9% of the PI4KB sequence, and 108 peptides covering 73.9% of the c10orf76 sequence were generated (**Fig. 3.2A-D, Appendix F-H**). Significant differences in deuterium exchange between conditions were defined as changes in exchange at any timepoint that met the three following criteria: greater than 7% change in deuterium incorporation, a greater than 0.5 Da difference in peptide mass, and a p-value of less than 0.05 (unpaired student's t-test).

Multiple regions of PI4KB were protected from amide exchange in the presence of c10orf76, revealing an extended binding interface (**Fig. 3.2A,B,D; Appendix G,I)**. The most prominent difference in exchange was at the C-terminus of the disordered N-lobe linker (residues 486-498), where the presence of c10orf76 led to a significant ordering of this region. This region had no protection from amide exchange in the apo state, revealing it to be disordered, with a very strong stabilization (>80% decrease in exchange) in the presence of c10orf76, indicating a disorder-to-order transition upon c10orf76 binding (**Fig. 3.2D**). This N-lobe kinase linker is dispensable for lipid kinase activity, as it can be removed with a minimal effect on PI4KB catalytic activity (97). In addition to this change there were multiple smaller decreases in exchange in the helical domain (131-138, 149-157, 159-164, and 183-204) and kinase domain (676-688, 725-734, and 738-765). The helical domain of PI4KB mediates binding to Rab11. However, the PI4KB-

Rab11 complex was still able to form in the presence of c10orf76 (**Fig 3.1E)**.

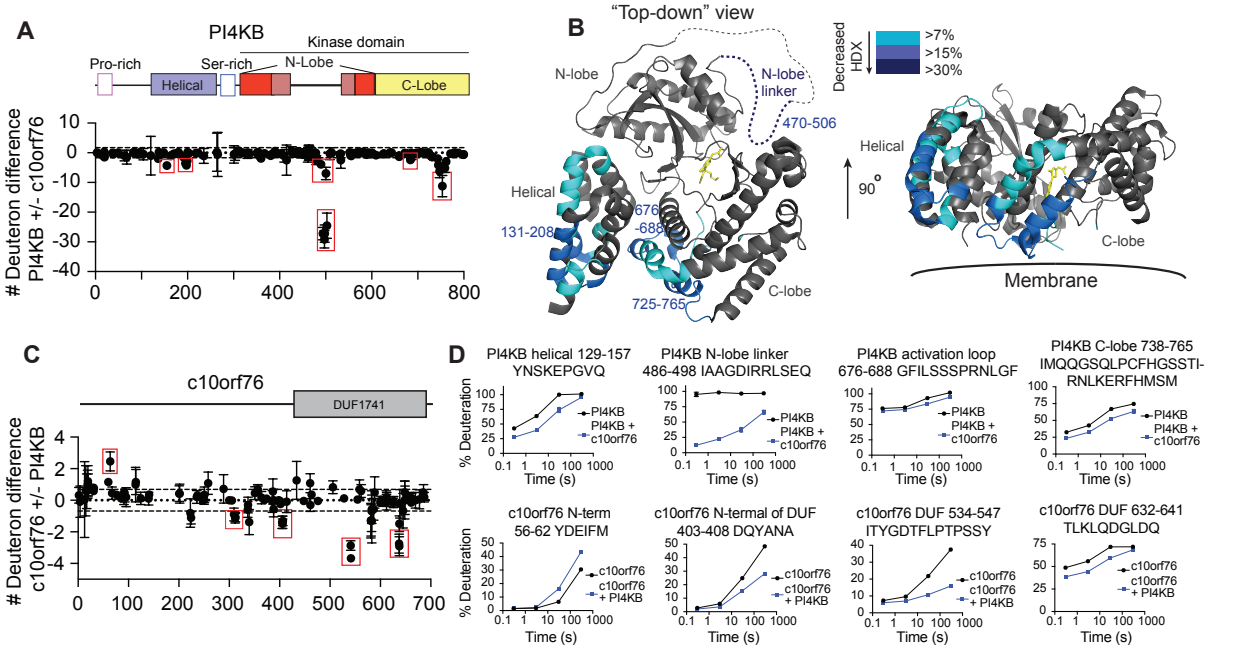

Figure 3.2. PI4KB binds c10orf76 through a disorder-to-order transition of the kinase domain N-lobe linker (refers to Appendix F-I).
(A) Changes in deuterium incorporation PI4KB in the presence of c10orf76 showed a profound ordering of the kinase domain N-lobe linker and smaller changes in the helical domain and C-lobe of the kinase domain. The sum of the difference mapped as the difference in number of deuterons incorporated for PI4KB (400 nM) in the presence and absence of c10orf76 (400 nM) over all time points (3s at 1 ºC; 3s, 30s, and 300s at 23 ºC). Each dot represents a peptide graphed on the x-axis according to the central residue. The red boxes highlight key regions that showed significant changes (>7% decrease in exchange, >0.5 Da difference, and unpaired two-tailed student t-test $p<0.05$). For all panels error bars represent standard deviation of independent technical replicates (n=3).**(B)** c10orf76 binding induces differences in HDX throughout multiple domains of PI4KB. Regions of >7% difference in deuterium exchange in the presence of c10orf76 are colored onto the structure of PI4KB according to the legend (PDB: 4D0L). The N-lobe linker of the kinase domain is disordered in the structure and is represented by a dotted line. **(C)** Changes in the deuterium incorporation of c10orf76 in the presence of PI4KB. H/D exchange reactions displayed as the sum of the difference in HDX in the number of deuterons for c10orf76 (400 nM) in the presence of PI4KB (400 nM) at all time points (3s at 1 ºC; 3s, 30s, and 300s at 23 ºC) analyzed. Red boxes highlight regions that showed significant changes (>7% decrease in exchange, >0.5 Da difference, and unpaired two-tailed student t-test $p<0.05$). Error bars represent standard deviation of independent technical replicates (n=3). **(D)** The PI4KB N-lobe linker undergoes a disorder-to-order transition upon binding c10orf76. Selected peptides (including the sequence, domain information, and numbering) of both PI4KB and c10orf76 displayed as the % deuteration incorporation over time. Errors bars represent standard deviation of independent technical replicates (n=3) and are typically smaller than the size of the point on the graph.

The decreases in exchange with c10orf76 observed in the kinase domain were located in the activation loop (676-688) and the C-lobe (738-765), which may mediate the inhibition observed *in vitro*. The protected surface on PI4KB extensively spans the membrane face of the kinase, which

may prevent PI4KB from directly interfacing with the membrane and accessing PI in the presence of c10orf76, at least in the absence of other binding partners *in vitro* (**Fig. 3.2B).**

The presence of PI4KB also caused multiple differences in H/D exchange in c10orf76, with increased exchange at the N-terminus (56-62) as well as decreased exchange N-terminal of, and within, the domain of unknown function (DUF1741; 403-408, 534-547, 632-641) (**Fig. 3.2C,D; Appendix H,I**). There are no clear structural determinants of c10orf76, with limited homology to any previously solved structure; however, it is predicted to consist of a primarily helical fold arranged into armadillo repeats. The uncharacterized DUF1741 domain of c10orf76 is present throughout many eukaryotes; however, even though the DUF1741 domain is strongly conserved in evolution, c10orf76 is the only protein that contains this domain in humans.

The largest observed change in deuterium incorporation in either protein was in the PI4KB N-lobe linker (486-496). Interestingly, this region contains a consensus PKA motif (RRxS) that corresponds to Ser496 (Ser511 in PI4KB isoform 1), which is phosphorylated *in vivo* and conserved back to the teleost fishes (**Fig. 3.3A**) (122). Systems level analysis of PKA signaling networks also show that phosphorylation of this site is decreased >90% in PKA knockout cells, indicating that it is likely a direct PKA target (121). To better understand the regulation of the c10orf76-PI4KB complex, we sought to characterize the effects of Ser496 phosphorylation.

PI4KB is directly phosphorylated at Ser496 by PKA to modulate the affinity of the c10orf76-PI4KB complex

There are three well-validated phosphorylation sites on PI4KB: Ser294, Ser413, Ser496 (135). To test the role of phosphorylation of PI4KB at Ser496, we generated stoichiometrically phosphorylated PI4KB at only Ser496 using an *in vitro* phosphorylation approach that relied on the production of the purified mouse PKA catalytic subunit in *E. coli*. To minimize complications from any background phosphorylation that occurs in *Sf9* cells, we used PI4KB expressed in *E. coli* to ensure the starting protein substrate was non-phosphorylated. Dose response assays for the phosphorylation of PI4KB Ser496 using *E. coli*-produced protein were then carried out with increasing concentrations of purified PKA, and the resulting product was analyzed by mass spectrometry for the site-specific incorporation of the phosphate moiety (**Fig. 3.3B)**. No phosphorylation was identified from *E. coli* produced proteins untreated with PKA, as expected **(Fig 3.3C)**. Analysis of the *Sf9*-produced PI4KB revealed significant phosphorylation of Ser294,

Ser413, Ser430 and Ser496, while *Sf9*-produced c10orf76 had evidence of phosphorylation of Ser14, and an additional Ser/Thr phosphorylation in the 325-351 region, although the specific residue is ambiguous from the MS data. Ser496 in PI4KB was phosphorylated efficiently by PKA, with >99% phosphorylation at Ser496 occurring with a 1:500 ratio of PKA to PI4KB and no detectable phosphorylation at the other major PI4KB phosphorylation sites (**Fig 3.3C**).

Lipid kinase assays were then carried out using different concentrations of c10orf76 for both phosphorylated and non-phosphorylated PI4KB. The phosphorylated form had a 3-fold increase in the IC_{50} value, suggesting that Ser496 phosphorylation decreases c10orf76 binding affinity, with no shift in the IC_{50} value for the S496A PI4KB mutant (**Fig. 3.3D)**. Kinase assays carried out on both Ser496 phosphorylated PI4KB and non-phosphorylated PI4KB showed that there is no direct effect of the phosphorylation events on basal lipid kinase activity (**Fig. 3.3E**). PKA-mediated phosphorylation-dependent changes in the affinity of protein-protein complexes have been previously described (136, 137). We utilized HDX-MS to test if the altered inhibition profile we saw was due to decreased affinity between c10orf76 and PI4KB, a method previously utilized to quantify the affinity of protein interactions (138). These experiments were carried out at a single time point of D_2O exposure (5 seconds at 20°C) with differing levels of c10orf76 present. Plotting the difference in deuterium incorporation versus c10orf76 concentration gives a characteristic binding isotherm for both phosphorylated and non-phosphorylated PI4KB; displaying a 2-3-fold decreased affinity for the phosphorylated form of PI4KB (85 nM vs 36 nM, **Fig 3.3F,G).** Phosphorylated PI4KB Ser496 also displayed a ~2 fold decrease in affinity for c10orf76 when determined by isothermal titration calorimetry (**Fig. 3.3H**). Phosphomimic PI4KB mutants S496D and S496E did not mimic the phosphorylation-dependent reduction of c10orf76 affinity, so they could not be utilized to study this effect *in vivo* (**Fig 3.3I**). To better characterize the role of the c10orf76-PI4KB complex *in vivo*, we sought to generate c10orf76-PI4KB complex-disrupting mutations.

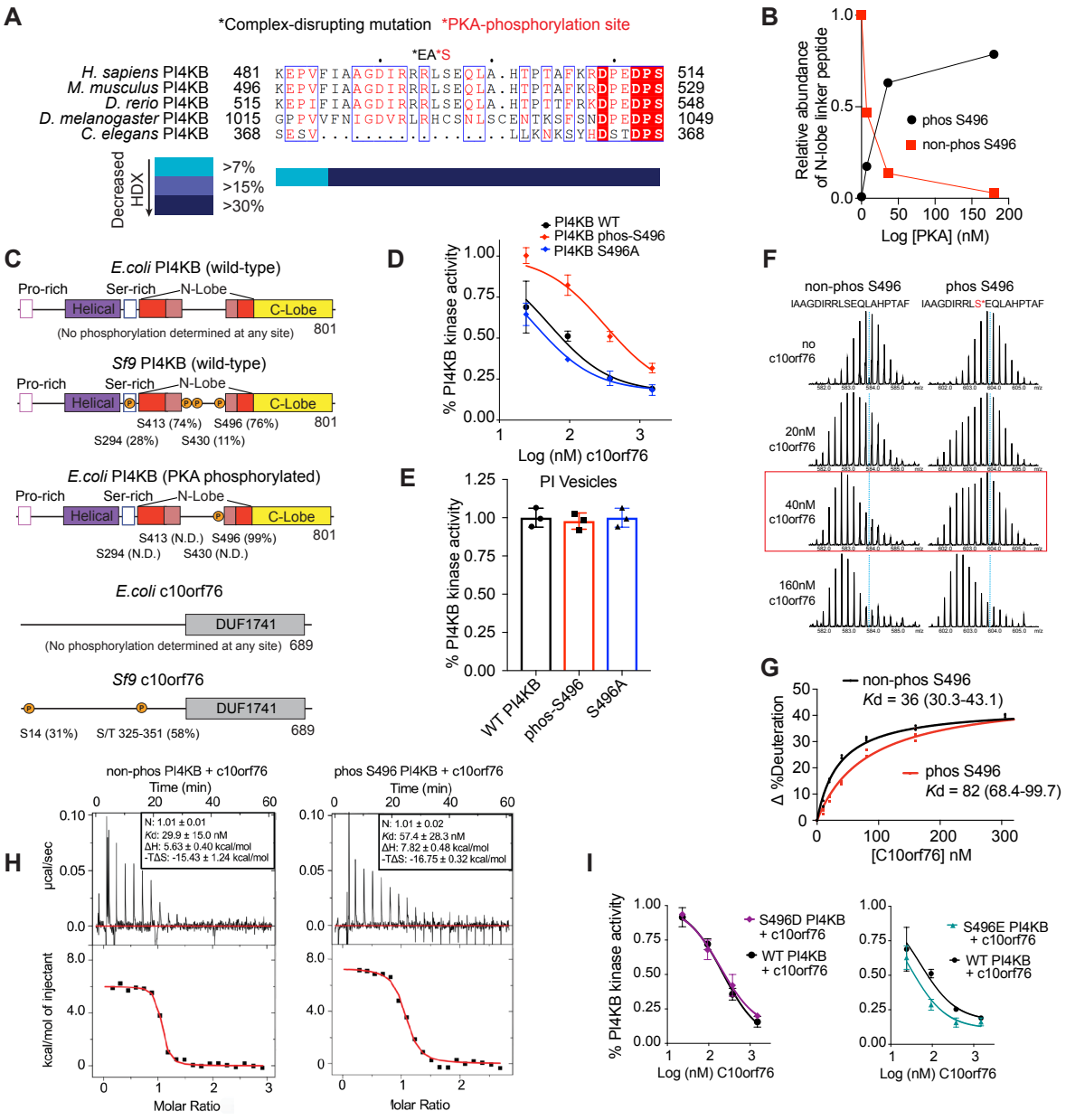

Figure 3.3. The PI4KB-c10orf76 interface is conserved and can be post-translationally modified by PKA. **(A)** The N-lobe kinase linker region of PI4KB is strongly conserved back to *D. rerio*. The N-lobe linker region of PI4KB sequences of the organisms indicated were analysed using Clustal Omega/ ESpript 3. The consensus PKA motif (RRXS) that is conserved back to *D. rerio* is indicated on the sequence, as well as the RL494EA point mutation.**(B)** The N-lobe kinase linker of PI4KB can be efficiently phosphorylated by PKA. Recombinant PKA at different concentrations (0, 7, 34, 168, or 840 ng) was incubated with recombinant (*E. coli*) wild-type PI4KB (20 μg) for 1 hour with 200 μM ATP and the amount of phosphorylation was followed using mass spectrometry. Relative abundance of Ser496 phosphorylated PI4KB was calculated using the relative intensity (total area) of the phosphorylated vs non-phosphorylated peptide (486-506). **(C)** Relative abundance of phosphorylated PI4KB at Ser294, Ser413 and Ser496 sites and c10orf76 at S14 and S/T from 325-351 expressed in *Sf9*, *E. coli*, or expressed in *E. coli* and treated with PKA (PI4KB) were calculated using the relative intensity (total area) of the phosphorylated vs non-phosphorylated peptides (290-303, 290-312, 395-425, 430-441, 486-505 and 486-506) for PI4KB and (10-22 and 325-351) for c10orf76. For 325-351 the definitive phosphorylated

Ser/Thr residue could not be determined. N.D. indicates no phosphorylation was identified. **(D)** PI4KB phosphorylation by PKA alters the affinity for c10orf76. The kinase activity of different variants of PI4KB (15 nM) was measured in the presence of varying amounts of c10orf76 (23 nM-1.5μM) with 100% PI lipid substrate (0.5 mg/L) and 100 μM ATP. The data was normalized to the kinase activity of PI4KB alone Error bars represent standard deviation of independent technical replicates (n=3). **(E)** PI4KB has the same kinase activity when Ser496 is phosphorylated or mutated to alanine. Kinase assay of PI4KB non-phosphorylated, phos-Ser496 or S496A (15 nM) on pure PI lipid vesicles (0.5 mg/L) with 100 μM ATP. The data was normalized to the kinase activity of WT PI4KB. Error bars represent standard deviation of independent technical replicates (n=3). **(F)** Raw deuterium incorporation data for PI4KB peptide 488-508 used to generate panel C. The deuterium incorporation for the phosphorylated and non-phosphorylated variants of PI4KB are shown in the presence of different concentrations of c10orf76. Dotted blue line indicates mass centroid of PI4KB peptide in absence of c10orf76, red box highlights the clear difference in deuterium incorporation at 40 nM c10orf76 between non-phosphorylated and phosphorylated Ser496 PI4KB. **(G)** Phosphorylation of Ser496 reduces PI4KB affinity for c10orf76. Deuterium incorporation of the PI4KB kinase linker region peptide 488-508 (20 nM) at a single time point (5 seconds of D_2O exposure at 23°C) was monitored in the presence of increasing concentrations of c10orf76 (0-320 nM c10orf76). K_d values were generated using a one binding site, nonlinear regression (curve fit), and are shown with 95% confidence intervals. Error bars represent standard deviation of independent technical replicates (n=3), most are smaller than the size of the point. **(H)** Representative ITC binding isotherms following the titration of c10orf76 into a solution of non-phosphorylated PI4KB (left) or Ser496 phosphorylated PI4KB (right). Parameter values are an average with standard deviation of independent technical replicates (N=3). **(I)** PI4KB S496D/E mutants do not mimic Ser496 phosphorylation modulation of c10orf76 binding. The kinase activity of S496D/E variants of PI4KB (15 nM) was measured in the presence of varying amounts of c10orf76 (23 nM-1.5μM) with 100% PI lipid substrate (0.5 mg/L) and 100 μM ATP. The data was normalized to the kinase activity of PI4KB alone. Error bars represent standard deviation of independent technical replicates (n=3).

Rationally engineered PI4KB and c10orf76 mutants that disrupt complex formation

The c10orf76 binding site within the N-lobe kinase linker of PI4KB identified by HDX-MS is highly conserved in vertebrates, with much of the region also conserved in *D. melanogaster,* but not in *C. elegans* (**Fig. 3.3A**). We used a combination of both the sequence conservation and HDX-MS results to design a complex-disrupting mutant. The RL residues at 494-495 were mutated to EA (RL494EA), effectively causing both a charge reversal and decrease in hydrophobicity. The RL494EA mutant disrupted binding to His-tagged c10orf76 bait in a His pulldown assay (**Fig. 3.4A**) and prevented inhibition by c10orf76 in kinase assays (**Fig. 3.4B**). This mutant had exactly the same basal kinase activity as the WT PI4KB on both PI vesicles and Golgi-mimetic vesicles (**Fig. 3.4C)**, strongly suggesting that the mutant kinase is properly folded. In an attempt to design rational mutations of c10orf76 that also disrupted binding to PI4KB, multiple mutations were tested in regions 403-408, 534-547 and 632-641 that were identified using HDX-MS. Combining the HDX-MS data and sequence homology, we designed a triple alanine mutant at the end of a putative helix (QYANAFL) that was well conserved in vertebrates (**Fig. 3.4D)**, close to the HDX-MS protection (FLH residues 409-411 to AAA, referred to as FLH mutant afterwards). The FLH mutant expressed well, significantly reduced binding to PI4KB in a His-

pulldown assay (**Fig. 3.4E**), and also showed a marked reduction in its ability to inhibit PI4KB activity (**Fig. 3.4F**). See **Table 3.1** for a summary of all mutants generated to identify complex-disrupting mutations. To confirm the c10orf76 FLH mutant does not affect global protein structure, we compared deuterium incorporation of the c10orf76 wild-type and FLH mutant and observed no changes in deuterium incorporation outside of the predicted helix containing the FLH residues (**Fig 3.4G, Appendix J).** The engineering of complex-disrupting mutants that do not alter catalytic activity or protein folding provided an excellent tool to test the importance of the c10orf76-PI4KB complex in cells.

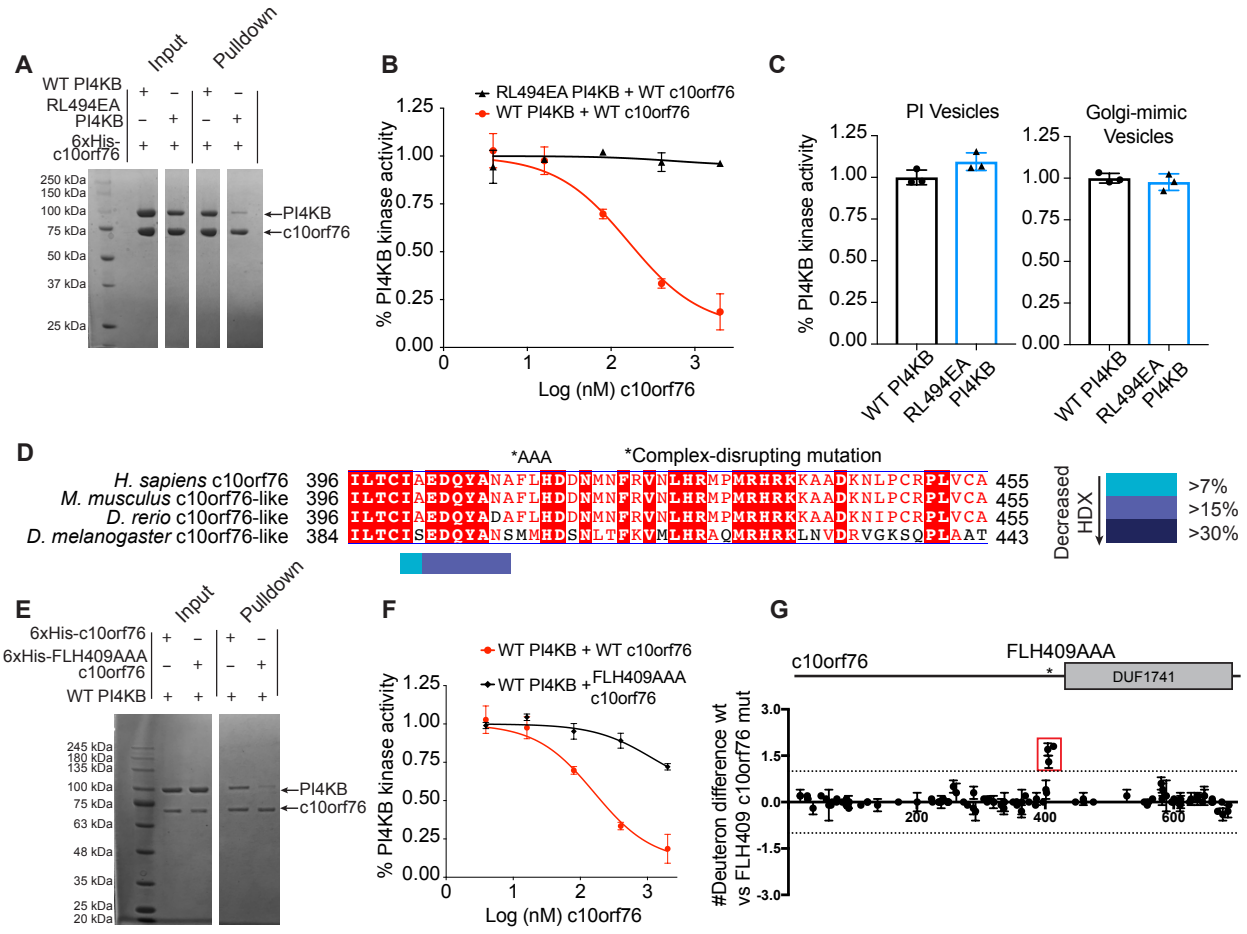

Figure 3.4. Rationally designed mutations in the conserved c10orf76-PI4KB interface disrupt complex formation and do not perturb overall protein folding (refers to Appendix J).
(A) Engineered RL494EA PI4KB mutant shows decreased binding to c10orf76. His-pulldown assays of 6xHis-c10orf76 (3 μM) with wild-type or RL494EA PI4KB (1-2 μM). **(B)** RL494EA PI4KB activity is not inhibited by c10orf76. Kinase assays of either wild type or mutant RL494EA PI4KB (40 nM) were carried out with varying concentrations of c10orf76 (3.9 nM-2μM) with 100% PI lipid vesicles (0.5 mg/L) and 100 μM ATP. The data was normalized to the kinase activity of PI4KB alone. Error bars represent standard deviation of independent technical replicates (n=3).**(C)** Wild-type PI4KB and RL494EA PI4KB mutant have the same lipid kinase

activity. Kinase assays of either wild-type and mutant PI4KB (10 nM) were carried out with 100% PI lipid vesicles (0.5 mg/L), 100 μM ATP, and PI4KB (300 nM) on Golgi-mimic vesicles (0.5 mg/mL) with 10 μM ATP. The data was normalized to the kinase activity of WT PI4KB. Error bars represent standard deviation of independent technical replicates (n=3). **(D)** The PI4KB-binding region of c10orf76 is strongly conserved back to *D. rerio*. Clustal Omega/ ESpript 3 alignment of the FLH409 region of c10orf76 that binds PI4KB. **(E)** FLH409AAA-c10orf76 mutant shows decreased affinity for PI4KB. His-pulldown assays of 6xHis-c10orf76 (1 μM) with wild-type PI4KB (1 μM). Samples washed a total of 4 times. **(F)** Kinase assay shows FLH409AAA c10orf76 inhibition of PI4KB is greatly reduced. Kinase assay of PI4KB (40 nM) and a concentration curve of c10orf76 (3.9 nM-2μM) on pure PI lipid vesicles (0.5 mg/L) with 100 μM ATP. The data was normalized to the kinase activity of PI4KB alone. Error bars represent standard deviation of independent technical replicates (n=3). **(G)** The FLH409AAA c10orf76 mutant maintains similar overall secondary structure to wild-type with a destabilization at the mutation site**;** Differences in the changes in the deuterium incorporation of wild type and FLH409AAA mutant c10orf76. H/D exchange reactions of c10orf76 (400 nM) were carried out for 3s and 300s, and the average difference in number of deuterons incorporated between wild-type and FLH409AAA c10orf76 (400 nM) was graphed. Error bars represent standard deviation of 2-3 independent technical replicates independent technical replicates.

Table 3.1 Summary of PI4KB and c10orf76 mutants generated to identify complex-disrupting mutations. Mutations in bold were utilized for further study.

Protein	Mutation	Expression	Complex Disruption (1 μM)
PI4KB	DI490KA	Soluble (*E. coli*)	yes
	RL494EA	**Soluble (*E. coli*)**	**yes**
C10orf76	K635E	Soluble (*Sf9*)	no
	Y406A	Soluble (*Sf9*)	no
	QD637KA	Soluble (*Sf9*)	no
	FI534AA	Soluble (*Sf9*)	no
	DDN413AAA	Soluble (*Sf9*)	no
	FNM531AAA	No soluble expression (*Sf9*)	n/a
	FIT534AAA	Soluble (*Sf9*)	no
	YGD537AAA	No soluble expression (*Sf9*)	n/a
	PTP543AAA	Soluble (*Sf9*)	no
	LQD636AAA	Soluble (*Sf9*)	no
	YAN406AAA	Soluble (*Sf9*)	no
	DQY404AAA	Soluble (*Sf9*)	no
	FLH409AAA	**Soluble (*Sf9*)**	**yes**
	FLH409AAA + N408A	Soluble (*Sf9*)	yes

PI4KB recruits c10orf76 to the Golgi

To define the role of the c10orf76-PI4KB interface in cellular localization we utilized fluorescently-tagged variants of the wild-type and complex-disrupting mutants of both PI4KB and c10orf76. All fluorescent constructs generated in this study are summarized in **Table 3.2**.

Table 3.2 Summary of fluorescently-tagged PI4KB and c10orf76 constructs generated to study the role of the PI4KB-c10orf76 complex *in vivo*.

Fluorescent Construct	Function
GFP-PI4KB	localization of wild-type
GFP-PI4KB(RL494EA)	localization in absence of c10orf76 binding
mRFP-FKBP12-PI4KB	inducible recruitment to mitochondria
mRFP-FKBP12-PI4KB(RL494EA)	inducible recruitment to mitochondria (without c10orf76 binding)
mRFP-FKBP12-PI4KB(S496A)	inducible recruitment to mitochondria (without S496 phosphorylation)
GFP-c10orf76	localization of wild-type
GFP-c10orf76(FLH409AAA)	localization in absence of PI4KB binding
CFP-FRB-AKAP	mitochondrial recruitment of FKBP12 upon rapamycin addition

Fluorescence microscopy of HEK293 cells expressing GFP-tagged wild-type PI4KB revealed that it primarily localizes to the Golgi (**Fig. 3.5A**). GFP-PI4KB RL494EA, which is deficient in c10orf76 binding, also localized mainly to the Golgi, which suggests that c10orf76 plays a minimal role in the Golgi recruitment of PI4KB (**Fig. 3.5A**). The wild-type GFP-c10orf76 also localizes to the Golgi. However, the PI4KB binding-deficient FLH mutant is redistributed to the cytosol; revealing an important role for PI4KB in the proper cellular localization of c10orf76 (**Fig. 3.5B**). Note that the Golgi localization of GFP-PI4KB or GFP-c10orf76 is only visible with low expression levels as the endogenous binding sites are quickly saturated and the excess cytoplasmic GFP-tagged protein eventually masks the Golgi-bound pools at higher levels of expression.

To further analyze the role of PI4KB in the recruitment of c10orf76, we utilized a chemically-inducible protein heterodimerization system that relies on the selective interaction of the FKBP12 (FK506 binding protein 12) and FRB (a 9 kDa fragment of mTOR that binds rapamycin) modules upon treatment with rapamycin (48, 139). Specifically, we fused the FRB domain to residues 34–63 of a CFP-tagged mitochondrial localization signal from mitochondrial A-kinase anchor protein 1 (AKAP1), and fused mRFP-FKBP12 onto the wild-type or mutant variants of human PI4KB **(Fig. 3.5C)**. These constructs allowed us to examine the localization of the wild-type or mutant GFP-c10orf76 following the acute sequestration of PI4KB to the outer mitochondrial membrane, where other Golgi-associating proteins are not present. To best demonstrate their co-recruitment upon rapamycin addition, mRFP-FKBP12-PI4KB and eGFP-c10orf76 were expressed at high levels, and thus present as mainly cytosolic due to saturation of endogenous binding sites **(Fig. 3.5D)**. Treatment with rapamycin (100 nM) caused the rapid recruitment of mRFP-FKBP12-PI4KB to the mitochondria, which also caused the rapid co-recruitment of c10orf76 **(Fig. 3.5D)**; suggesting that PI4KB is the only component necessary for

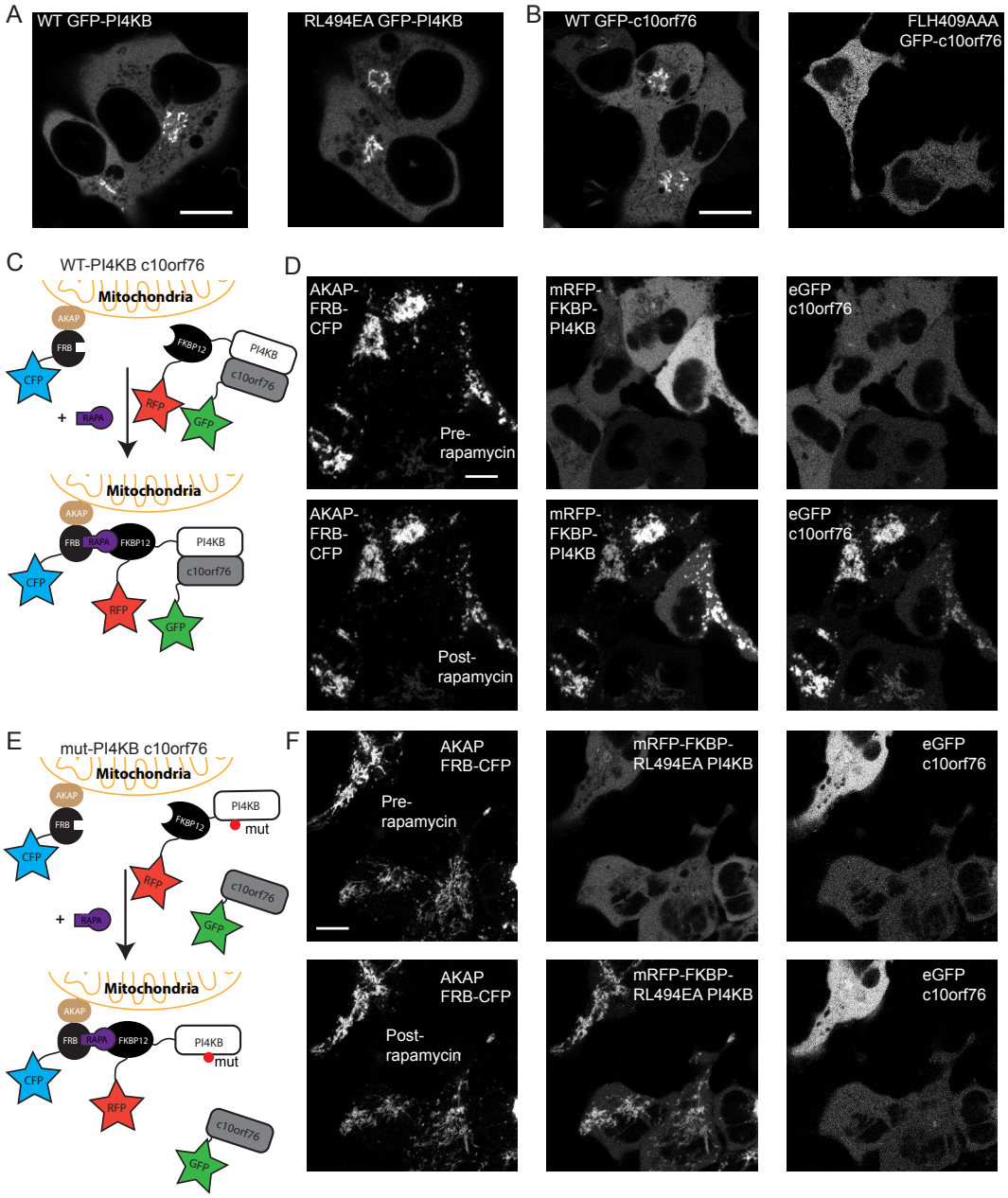

Figure 3.5. PI4KB recruits c10orf76 to the Golgi *in vivo* (refers to Appendix K).
(**A**) Transfections of HEK293 cells revealed that both wild-type GFP-PI4KB and RL494EA GFP-PI4KB localize to the Golgi. (**B**) WT c10orf76 also localized to the Golgi, however, the PI4KB binding deficient mutant of c10orf76 (FLH409AAA) predominantly localized to the cytosol. (**C**) Cartoon schematic of rapamycin-inducible mitochondria recruitment. The AKAP1-FRB-CFP construct is localized to the outer mitochondrial membrane, while the mRFP-FKBP12-PI4KB and eGFP-c10orf76 are localized in the Golgi as well as within the cytoplasm where they can form a complex. Upon addition of rapamycin, the mRFP-FKBP12-PI4KB construct is translocated to the mitochondria. (**D**) Mitochondria recruitment experiment with wild-type PI4KB and c10orf76. Left: AKAP1-FRB-CFP is localized to the mitochondria before (top) and 5 minutes after rapamycin (100 nM) treatment (bottom). Middle: mRFP-FKBP12-PI4KB at high expression level is located in the cytosol before rapamycin (top) and translocates to the mitochondria after rapamycin induction (bottom). Right: eGFP-c10orf76 at a high expression level is located in the cytosol before rapamycin (top) and translocates to the mitochondria after rapamycin induction (bottom). (**E**) Schematic of the rapamycin-inducible mitochondria recruitment

experiment with mutant PI4KB and WT c10orf76. (**F**) Mitochondria recruitment experiment with mutant PI4KB and WT c10orf76. Left: AKAP1-FRB-CFP is localized to the mitochondria before (top) and 5 minutes after (bottom) rapamycin treatment. Middle: mRFP-FKBP12-PI4KB(RL494EA) is located in the cytosol before rapamycin (top) and translocates to the mitochondria after rapamycin induction (bottom). Right: eGFP-c10orf76 is located in the cytosol before (top) and after (bottom) rapamycin induction. Data information: Scale bars represent 10 μm.

membrane recruitment of c10orf76. Experiments using mRFP-FKBP12 PI4KB RL494EA showed that although the mutant kinase is relocated to the mitochondria, GFP-c10orf76 does not co-localize **(Fig. 3.5E,F)**. To test any effect of the PI4KB S496 phosphorylation site on localization, although the S496E and S496D mutants did not properly mimic phosphorylation **(Fig 3.3I)**, recruitment experiments were performed with the non-phosphorylatable PI4KB mutant (S496A). At lower expression levels, mRFP-FKBP12 PI4KB S496A and eGFP-c10orf76 maintained normal Golgi localization, and treatment with rapamycin caused recruitment to the mitochondria **(Appendix K)**. At higher expression levels, mRFP-FKBP12 PI4KB S496A and eGFP-c10orf76 quickly saturate Golgi sites and flood the cytosol, and treatment with rapamycin caused robust recruitment to the mitochondria, suggesting phosphorylation of PI4KB S496 is not important in the normal localization of either protein **(Appendix K)**. Taken together, these live-cell studies corroborated the protein interaction studies completed in vitro and also demonstrate that the newly defined c10orf76-PI4KB interface is required for proper localization of c10orf76 to the Golgi. Compellingly, these findings reveal a novel function of PI4KB in the recruitment of c10orf76.

c10orf76 regulates active Arf1 dynamics and maintains Golgi PI4P levels

The paradoxical finding that the loss of c10orf76 leads to decreased PI4P levels in cells, yet c10orf76 decreased the catalytic activity of PI4KB in vitro, suggested that there was an unknown lipid or protein constituent in cells that is not present in our *in vitro* experiments. To determine the role of c10orf76 in cells we examined the distribution of different Golgi-localized signaling components in c10orf76-deficient (knockout) HAP1 cells. In agreement with previous studies (68), we found that there were decreased PI4P levels at the Golgi in c10orf76 knockout cells, as indicated by decreased Golgi staining by an anti-PI4P antibody **(Fig. 3.6A)**. Intriguingly, there was an apparent increase in Golgi localized PI4KB in the c10orf76 knockout cells **(Fig. 3.6A),** similar to what occurs upon treatment with a PI4KB inhibitor (95), clearly indicating that decreased PI4P production was not due to loss of PI4KB recruitment in the absence of c10orf76.

We tested the localization of different Golgi markers to verify that decreased PI4P was not due to disruption of Golgi morphology. Giantin, a marker of the cis/medial Golgi, and ACBD3, which binds to Giantin and recruits PI4KB to Golgi membranes (48, 57), both showed similar localization in both WT and c10orf76 knockout cells **(Fig. 3.6B)**. Markers for the cis Golgi (GM130), the trans-Golgi network (TGN46), and the ER-Golgi intermediate compartment (ERGIC53) were also similar, suggesting that Golgi morphology was maintained in the c10orf76 knockout HAP1 cells **(Fig. 3.6B)**.

We next tested the localization of the Arf1-GEF GBF1, as active GTP-bound Arf1 is a putative activator of PI4KB (54). We confirmed similar expression levels of PI4KB, GBF1 and β-Actin in WT and c10orf76 KO cells to verify any observed differences were not due to protein expression levels **(Fig. 3.6C)**. In c10orf76 knockout cells there was a redistribution of GBF1, with GBF1 being more diffuse, with less localized at the Golgi **(Fig. 3.6D)**. The generation of active GTP-bound Arf1 by Arf-GEFs leads to recruitment of multiple effector proteins, with one of most well characterised being the coatomer proteins, which form COPI coated vesicles that mediate Golgi to ER trafficking. In c10orf76 knockout cells there was more diffuse staining outside of the Golgi for the active Arf1-binding coatomer components COP-β or COP-α/γ **(Fig. 3.6D)**. Antibody staining with the CM1 antibody, which recognizes the native form of coatomer (140), showed similar distribution for both WT and c10orf76 knockout cells, indicating the formation and distribution of native cytosolic coatomer was not affected (Fig. 3.4D). This puzzling difference may be caused by an altered recruitment of a subset of coatomer components (COP-β or COP-α/γ), and minor effects on the native coatomer complex. Importantly, the major phenotypic observations in the HAP1 c10orf76 knockout cells (i.e. reduced PI4P and increased PI4KB levels on an intact Golgi, and a more diffuse GBF1 and COP-I staining with less localization at the Golgi), were also observed in HeLa cells in which c10orf76 was knocked out (H.R. Lyoo and F.J.M. van Kuppeveld, personal observation). Overall, these results suggest that c10orf76 plays a role in the regulation of GBF1/Arf1 dynamics at the Golgi.

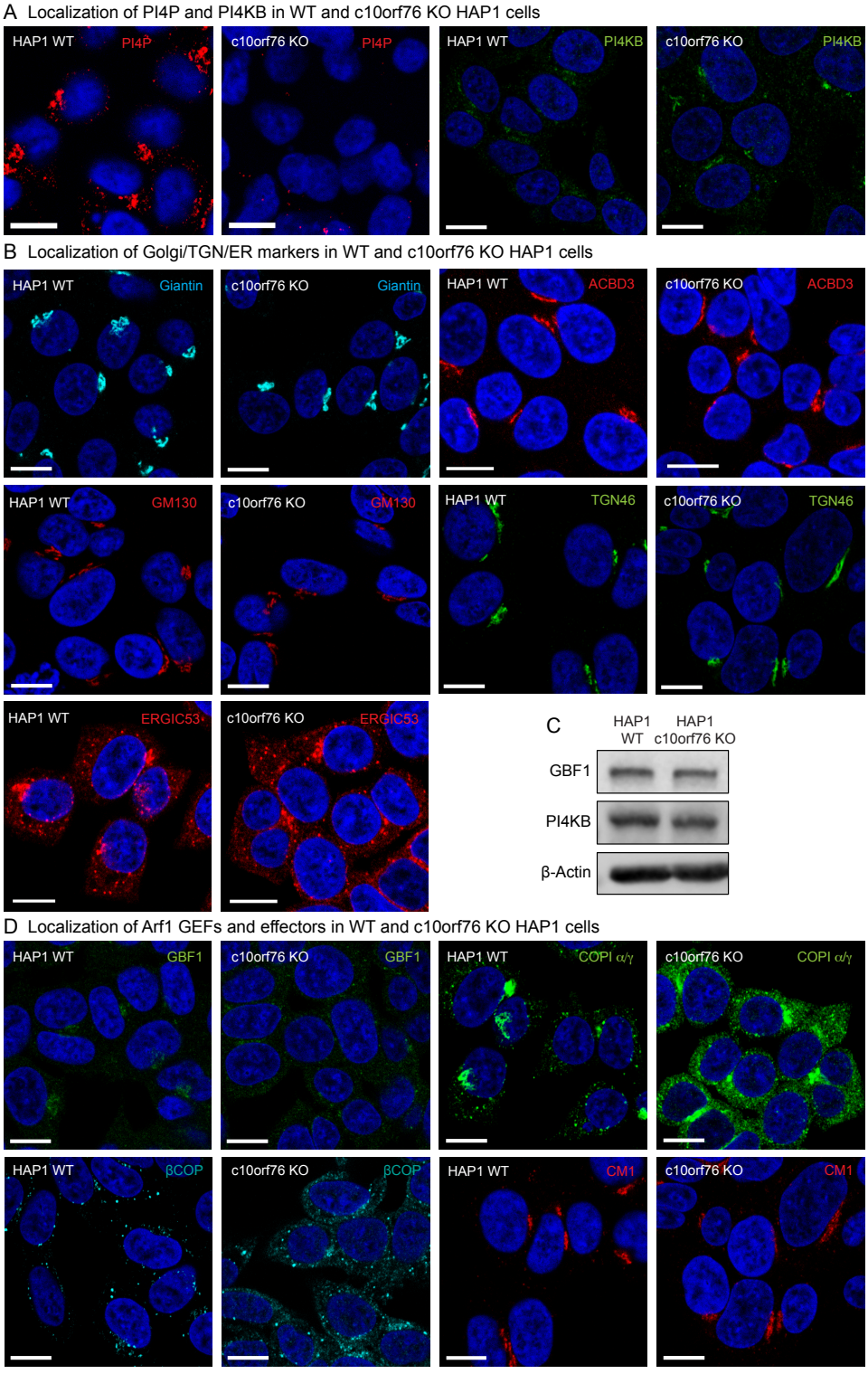

Figure 3.6. Knockout of c10orf76 in HAP1 cells leads to decreased PI4P levels and disruption of GBF1/ active Arf1 localization despite minimal effects on Golgi morphology.
(A, B) HAP1 cells were fixed and stained with antibodies examining PI4P and PI4KB (**A)** and Golgi morphology markers (**B**). (**C**) Western blot of GBF1, PI4KB and B-Actin levels in both wild-type and c10orf76 KO HAP1 cells.(**D**) Markers of Arf1 activation – the coatomer proteins COPIα/γ and βCOP act as a readout for GTP-bound

Arf1, while the native coatomer was detected with the CM1 antibody. Nuclei were stained with DAPI (blue). Data information: Scale bars represent 10 μm.

Replication of c10orf76-dependent enteroviruses requires intact c10orf76-PI4KB interaction

All enteroviruses depend on PI4KB kinase activity for replication. Despite the physical and functional connection between PI4KB and c10orf76, enteroviruses showed different dependencies on c10orf76 (68). Specifically, while Coxsackievirus A10 (CVA10) replication was impaired in c10orf76 knockout cells, the replication of Coxsackievirus B1 (CVB1) was not. Furthermore, c10orf76 was identified as a pro-viral factor for replication of poliovirus (PV1) (141). We set out to investigate the importance of the c10orf76-PI4KB interaction for replication of CVA10 and PV1. We first made a side-by-side comparison of virus replication in HAP1 wildtype and c10orf76 knockout cells in a single cycle of replication. The replication of CVA10 was significantly impaired in c10orf76 deficient cells, with partial inhibition of PV1 replication, and no impairment for replication of Coxsackievirus B3 (CVB3) **(Fig. 3.7A)**. Due to the notoriously difficult nature of transfecting HAP1 cells, we determined the importance of the c10orf76-PI4KB interaction for virus replication in HeLa PI4KB knockout cells transfected with different PI4KB expression plasmids as previously described (123). Expression of wild type PI4KB efficiently restored the replication of all viruses **(Fig. 3.7B)**. Expression of the PI4KB RL494EA mutant that is deficient in binding c10orf76 fully rescued replication in CVB3, only partially rescued PV1 replication, and failed to rescue CVA10 replication. These observations suggest that the c10orf76-PI4KB interaction is necessary for CVA10, and to a lesser extent, PV1 replication and thereby implies that functions of c10orf76 are selectively hijacked by specific viruses.

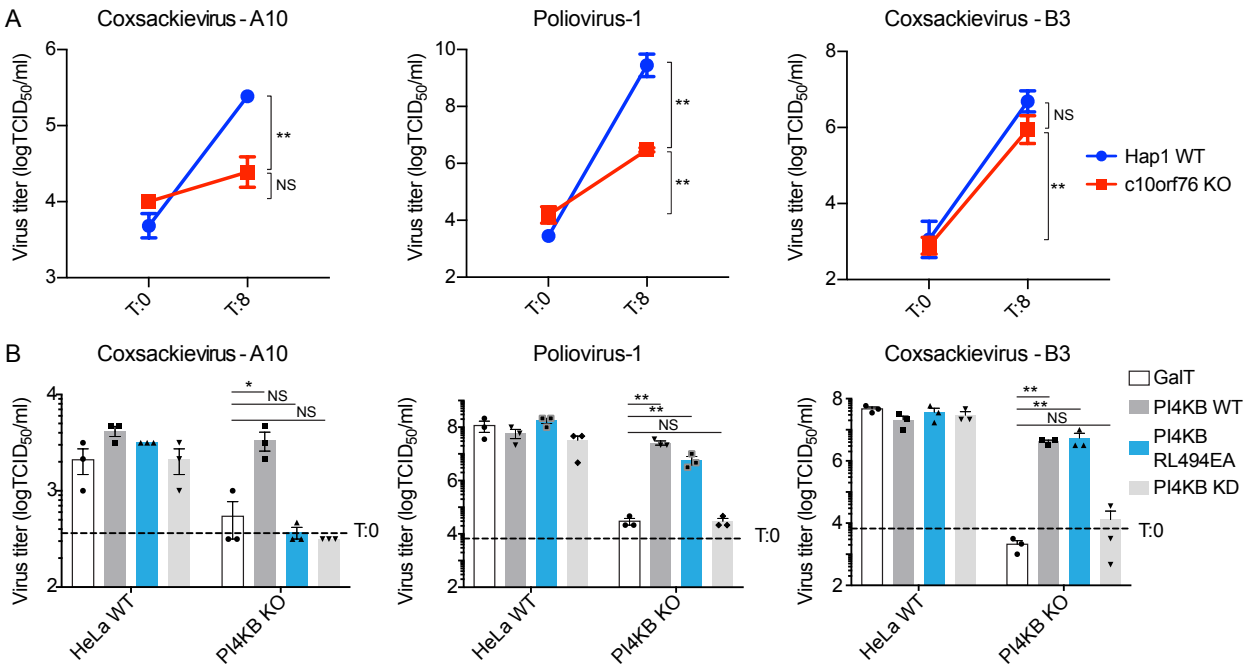

Figure 3.7. The c10orf76-PI4KB complex is essential for Coxsackievirus A10 replication.
(**A**) Viral infection assays determining viral titers by end-point titration at 0 hours and 8 hours in HAP1 wild-type or c10orf76 knockout cells. Left: Coxsackievirus A10 infection. Middle: Poliovirus-1 infection. Right: Coxsackievirus B3 infection. Titre values for c10orf76 knockout cells at 8 hours were statistically evaluated compared to c10orf76 knockout titres at 0 hours and wild-type titres at 8 hours using a one-way ANOVA. **, P<0.01; N.S., P>0.05. (**B**) Viral infection assays determining virus titers by end point titration at 8 hours in HeLa wild-type and PI4KB knockout cells upon transfection of wild-type PI4KB, the complex-disrupting RL494EA PI4KB mutant or the kinase dead D674A PI4KB mutant. Left: Coxsackievirus A10 infection. Middle: Poliovirus-1 infection. Right: Coxsackievirus B3 infection. Values were statistically evaluated compared to the GalT control using a one-way ANOVA. **, P<0.01; *, P<0.05; N.S., P>0.05. Data information: For all panels error bars represent standard error of biological replicates (n=3).

3.5 Discussion

Defining the full complement of cellular roles for PI4KB is an important objective in characterizing the integrated control of secretion and membrane trafficking at the Golgi, and also provides a framework for understanding how PI4P can be manipulated by viruses. We have identified the c10orf76-PI4KB interaction as an important Golgi signaling complex and a critical factor in the replication of specific enteroviruses. Multiple mechanisms have been previously described for how PI4KB participates in Golgi signaling and membrane trafficking, including detailed insights into protein binding partners, post-translational modifications, and regulated recruitment to specific membrane compartments. PI4KB was originally identified in yeast (yeast protein PIK1) as an essential gene (50), with its activity playing a key role in secretion from the Golgi (142). The mammalian isoform was identified soon afterwards through its sensitivity to

wortmannin (51, 52, 143). The first identified Golgi activator of PI4KB was the GTPase Arf1 (54). However, no direct interaction has been established, which indicates a potential indirect mechanism of activation. Phosphorylation of PI4KB by PKD at Ser294 mediates binding to 14-3-3 proteins, with this leading to an increase in PI4KB activity (71, 92), that has been suggested to correspond with an increase in PI4KB stability (69). The most well validated protein binding partner that regulates Golgi recruitment of PI4KB is ACBD3 (previously referred to as GCP60) (57). ACBD3 forms a direct, high-affinity interface with PI4KB that is mediated by a disorder-to-order transition in the N-terminus of PI4KB upon binding to the Q domain of ACBD3 (48, 49). The recruitment of PI4KB to the Golgi by ACBD3 is controlled through the direct interaction of the GOLD domain of ACBD3 with the Golgi resident transmembrane protein Giantin (112). In addition to regulatory protein interactions, PI4KB is predicted to contain an amphipathic lipid packing sensor (ALPS) motif at the C-terminus that mediates lipid binding to unsaturated membranes (46). PI4KB plays key non-catalytic roles through its interaction with the GTPase Rab11, with PI4KB required for localizing a pool of Rab11 to the Golgi and TGN (53). This interaction is mediated through a non-canonical, nucleotide-independent binding interface with the helical domain of PI4KB (38). However, there are still many unexplained aspects of PI4KB recruitment and regulation, highlighted by the increased recruitment of PI4KB to the Golgi following treatment with PI4KB inhibitors that is concomitant with a decrease in Golgi PI4P levels (95).

The protein c10orf76 was originally identified as a putative PI4KB interacting partner through co-immunoprecipitation experiments using tagged PI4KB (56, 88). Tests of genetic essentiality identified c10orf76 as a central molecular hub at the Golgi, with it being synthetically lethal in combination with the loss of several different Golgi-signaling proteins, and also showing a genetic link to PI4KB (68). That study also found that c10orf76 is essential in the KBM7 CML cells (near-haploid, human chronic myelogenous leukemia cells), but not in HAP1 cells (nonhematopoietic derivative of KBM7 CML cell line, haloid for all chromosomes), with this relationship also being true for PI4KB. Additional evidence on the essentiality of this protein is highlighted by the homozygous mutant of ARMH3, the mouse homolog of c10orf76, which is lethal at the pre-weaning stage (144). c10orf76 is highly conserved in vertebrates and we find a strong correlation between the conservation of the kinase linker region of PI4KB and the PI4KB-binding site in c10orf76, suggesting that a key role of c10orf76 is linked to its ability to form a

complex with PI4KB. PI4KB recruitment to the Golgi is not mediated by c10orf76, but instead it appears that PI4KB is responsible for the Golgi-recruitment of c10orf76. *In vitro,* c10orf76 led to decreased lipid kinase activity of PI4KB. However, knockout of c10orf76 in cells led to reduced PI4P levels. This discrepancy could be due to the lack of other PI4KB regulators *in vitro*, such as Arf1/GBF1 or ACBD3, as well as the potential for c10orf76 to alter phosphatidylinositol dynamics. Knockout of c10orf76 led to an increased cytosolic fraction of the Arf GEF GBF1 and active Arf1 effectors (COP-β or COP-α/γ), but not native coatomer, suggesting altered Arf1/GBF1 dynamics in the c10orf76 knockout may be responsible for the disruption of Golgi PI4P levels (54). This alteration was not due to Golgi disassembly, and despite perturbed Arf1 dynamics the presence of ACBD3 appeared to be sufficient for PI4KB recruitment to Golgi membranes as previously shown (48, 57). The activity of PI4KB is also regulated through the action of phosphatidylinositol transfer proteins (PITPs), which activate PI4KB activity, and c10orf76 may play a role in altering PI dynamics (145). It is also possible that while PI4KB drives c10orf76 recruitment to the Golgi, endogenous c10orf76 levels *in vivo* engage only a minor fraction of PI4KB, or that c10orf76 itself interacts with other Golgi factors that induce a non-inhibitory confirmation with PI4KB. While further studies will be needed to fully describe the role of the PI4KB/c10orf76 complex, our work reveals c10orf76 as a novel player in regulation of Arf1 dynamics and corresponding Golgi PI4P levels (**Fig 3.8A,B**).

Enteroviruses hijack numerous lipid signaling processes within infected cells to mediate their replication through the generation of replication organelles, with recruitment of PI4KB (58) and GBF1 (86) playing key roles in this process. Recruitment of these cellular host factors in enteroviruses is primarily mediated through the action of membrane-bound viral 3A proteins, which form either direct or indirect interactions that are important for facilitating replication organelle formation. One of the most well-conserved 3A binding partners in enteroviruses is the Golgi resident protein ACBD3, which interacts with the central part of 3A and recruits as well as activates PI4KB (49, 57, 79, 123, 124). The N-terminal part of the 3A proteins from several enteroviruses (*e.g.*, poliovirus and coxsackie virus B3) directly binds and recruits GBF1, but this interaction is less conserved, severely reduced, or even absent in the 3A proteins of rhinoviruses due to subtle amino acid differences in their N-terminus (79, 86). Recently, it has been found that there are multiple mechanisms of recruitment of GBF1 downstream of Poliovirus (146), with c10orf76 potentially being involved in this role. We find that c10orf76 is required for replication

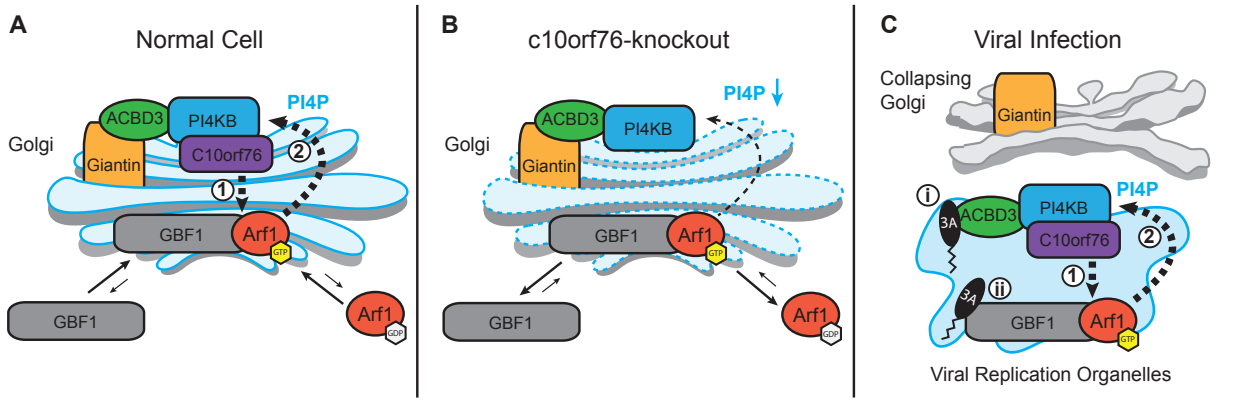

Figure 3.8. Summary of novel role of c10orf76 in modulating PI4P levels, active Arf1-GTP dynamics and viral replication.
(A) At the Golgi, the recruitment of PI4KB can be controlled through the action of ACBD3. PI4KB can recruit c10orf76 to the Golgi, with this playing a role in the dynamics and localization of GBF1 and active Arf1-GTP and their downstream effectors (1). Active, membrane localized Arf1-GTP can activate PI4KB (2). (**B**) In a c10orf76-knockout cell, there is decreased recruitment of GBF1 and active Arf1, with this potentially describing the decreased levels of PI4P. (**C**) In enterovirus infected cells there are multiple mechanisms that can alter PI4P levels and Arf1 activation. The 3A proteins from different viruses can activate PI4KB, primarily through hijacking ACBD3 (i), as well as directly binding to GBF1 (ii). Viruses that require c10orf76 to replicate rely on the PI4KB-c10orf76 interface, emphasising the importance of manipulating PI4KB-c10orf76 and GBF1/Arf1-GTP dynamics to facilitate viral replication

of coxsackie virus A10, and to a lesser extent poliovirus, and that c10orf76-dependent viruses rely on the c10orf76-PI4KB interface. Poliovirus is the causative agent of poliomyelitis, and coxsackie virus A10 is an important cause of outbreaks of hand-foot-and-mouth disease, but which is also associated with severe, and sometime fatal, clinical symptoms such as aseptic meningitis. Remarkably, replication of coxsackie virus B1 (68) and coxsackie virus B3 (this study) is independent of c10orf76. Why the c10orf76-PI4KB interface is necessary for replication of some enteroviruses, but not others, is unknown. The differential dependence on c10orf76 could possibly be explained by distinct affinity of 3A proteins from different viruses towards GBF1. Alternatively, each virus may require specific threshold PI4P level for efficient formation of its replication complexes or replication organelles. Together, viral 3A, ACBD3, GBF1 and c10orf76 play a role in viral replication organelle formation (**Fig. 3.8C**), although more research on the dependence of viral replication on either GBF1 or c10orf76-mediated alteration of PI4P levels is required to better understand how enteroviruses hijack these complex membrane trafficking processes.

Direct inhibition of PI4KB is likely not a useful antiviral strategy due to unexpected deleterious side effects of PI4KB inhibition in animal models (117). The targeting of other cellular host factors used to manipulate PI4KB signaling or feedback is a potential avenue for development of novel antiviral therapeutics. Identification of a direct high-affinity c10orf76-PI4KB complex that regulates the cellular localization of c10orf76 represents key insight into the multifaceted regulation of PI4KB signaling. The important role of the c10orf76-PI4KB complex in the replication of select enteroviruses represents a novel molecular platform which is targeted by viruses that hijack lipid signaling. The involvement of c10orf76 in Arf1 dynamics, as well as the dependence on PI4KB for Golgi localization of c10orf76, reveals a potential role of the c10orf76-PI4KB complex in Arf1 activation and subsequent PI4P production.

Chapter 4: Studying selective inhibition of human PI4KIIIβ and related lipid kinases to facilitate the development of novel therapeutics.

Adapted from:

1. Rageot, D., Bohnacker, T., Keles, E., McPhail, J.A., Hoffmann, R.M., Melone, A., Borsari, C., Sriramaratnam, R., Sele, A.M., Beufils, F., Hebeisen, P., Fabbro, D., Hillmann, P., Burke, J.E., Wymann, M.P. (2019). (S)-4-(Difluoromethyl)-5-(4-(3-methylmorpholino)-6-morpholino-1,3,5-triazin-2-yl)pyridin-2-amine (PQR530), a Potent, Orally Bioavailable, and Brain-Penetrable Dual Inhibitor of Class I PI3K and mTOR Kinase. Journal of Medicinal Chemistry. 62(13):6241-6261.
2. Fowler, M.L., McPhail, J.A., Jenkins, M.L., Masson, G.R., Rutaganira, F.U., Shokat, K.M., Williams, R.L., and Burke, J.E. (2016). Using hydrogen-deuterium exchange mass spectrometry to engineer optimized constructs for crystallization of protein complexes: case study of PI4KIIIβ. Protein Science. 25(4):826-39.
3. Rutaganira, F.U., Fowler, M.L., McPhail, J.A., Gelman, M.A., Nguyen, K., Xiong, A., Dornan, G.L., Tavshanjian, B., Glenn, J.S., Shokat, K.M., Burke, J.E. (2016). Design and Structural Characterization of Potent and Selective Inhibitors of Phosphatidylinositol 4 kinase IIIβ. Journal of Medicinal Chemistry. 59(5):1800-9.
4. Kato, N., Comer, E., Sakata-Kato, T., Sharma, A., Sharma, M., Maetani, M., Bastien, J., Brancucci, N.M., Bittker, J.A., Corey V., Clarke, D., Derbyshire, E.R., Dornan, G., Duffy, S., Eckley, S., Itoe, M.A., Koolen, K.M., Lewis, T.A., Lui P.S., Lukens, A.K., Lund, E., March, S., Meibalan, E., Meier, B.C., McPhail, J.A., Mitasev, B., Moss, E.L., Sayes, M., VanGessel, Y., Wawer, M.J., Yoshinaga, T., Zeeman, A., Avery, V.M., Bhatia, S.N., Burke, J.E., Cateruccia, F., Clardy, J.C., Clemons, P.A., Dechering, K.J., Duvall, J.R., Foley, M.A., Gusovsky, F., Kocken, C.H., Marti, M., Morningstar, M.L., Munoz, B., Neafsey, D.E., Sharma, A., Winzeler, E.A., Wirth, D.F., Scherer, C.A., Schreiber, S.L.. (2016). Diversity-oriented synthesis yields novel multistage antimalarial inhibitors. Nature. 538(7625):344-349.

Contributions:

I performed purification of the PIK3CA crystal construct and crystallographic setup with PQR530, which was synthesized by the laboratory of Matthias Wymann. I collected synchrotron data with John Burke (JEB) and assisted with co-crystal structure determination. HDX-MS on human PI4KIIIβ was performed by Meredith Jenkins (MLJ) in the laboratory of John Burke (JEB) and Glenn Masson in the laboratory of Roger Williams. I cloned all PI4KIIIβ constructs and assisted Melissa Fowler (MLF) with protein expression and purification. I performed all pulldown assays and the kinase assay of truncated PI4KIIIβ. BQR695, compound **9**, and KAI407 were synthesized by the laboratory of Kevan Shokat. BRD73842 was synthesized by the laboratory of Stuart Schreiber. I assisted Melissa Fowler with crystallographic setup and collection of synchrotron data with JEB, and JEB solved the co-crystal structures of Rab11-PI4KIIIβ with inhibitors. Cloning, expression, purification and HDX-MS analysis of *P. vivax* PI4K was performed by myself and Gillian Dornan. I performed all lipid kinase assays of human and *P. vivax* PI4K. Cloning, expression, purification and HDX-MS analysis of *C. parvium* PI4K was performed by myself with assistance from Reece Hoffmann and MLJ. I designed truncations in parasite PI4Ks with input from JEB, and performed expression, purification and crystallographic setup of these constructs myself.

4.1 Abstract

The lipid kinases that generate the lipid signalling phosphoinositides have been established as fundamental signalling enzymes that control numerous aspects of how cells respond to their extracellular environment. In addition, they play critical roles in regulating membrane trafficking and lipid transport within the cell. The class I phosphoinositide 3-kinases (PI3Ks), which generate the critical lipid signal PIP_3, are hyperactivated in numerous human pathologies including cancer, overgrowth syndromes, and primary immunodeficiencies. The evolutionally similar type III *beta* phosphatidylinositol 4-kinase isoform (PI4KIIIβ) is also implicated in disease as an essential host factor mediating the replication of numerous devastating pathogenic viruses. Additionally, the parasite PI4KIIIβ homologs play an essential role in the proliferation of the malaria and cryptosporidium parasites. Therefore, characterizing potent, isoform-selective inhibitors for PI3Ks and related PI4Ks is of paramount importance in developing therapeutic interventions for numerous diseases. Here we utilize crystallography-optimized constructs of class I PI3Kα

(PIK3CA) and PI4KIIIβ to co-crystalize these kinases with the novel, selective inhibitors PQR530, Compound **9** and BQR695 to define the molecular basis of their selectivity. We also engineer crystallography-optimized constructs of parasite PI4Ks, facilitating formation of the first microcrystals of malarial PI4K. Overall our findings will aid in the development of novel selective anti-cancer, anti-viral and anti-parasite compounds targeting PI3Ks and related PI4Ks.

4.2 Introduction

The class I phosphoinositide 3-kinases (PI3Ks) and related phosphatidylinositol 4-kinase type III *beta* (PI4KIIIβ) are two of the most clinically promising targets for drug development against lipid kinases. Class IA PI3Kα (PIK3CA) is one of the most frequently mutated oncogenes in human cancer (recently reviewed in (147)), with mutation rates of 24-46% in endometrial cancer (148, 149), 20-32% in breast cancer (150, 151), 20-27% in bladder cancer (152, 153), 14-23% in cervical cancer (154, 155), 13-28% in colorectal cancer (156), and 14-23% in head-and-neck cancers (157, 158). Inhibitors with both pan-PI3K (159), and PIK3CA-specific (160) activity have been recently approved as effective treatments for various cancers. PI3K inhibitor development continues, with dozens more compounds entering into clinical trials as potency, selectivity, and corresponding therapeutic index of lead compounds is further optimized. Successful crystallization of all four closely related isoforms of the class I PI3Ks – PIK3CA(36), PIK3CB(37), PIK3CD(39), PIK3CG(35) – have revealed the subtle isoform active site differences that mediate selectivity of inhibitors, and have provided a platform for studying inhibitor selectivity. Understanding the molecular mechanisms for selectivity of the next generation of PI3K inhibitors is critical for their development as cancer therapeutics, allowing for targeting of specific isoforms to reduce off target effects.

The lipid kinase PI4KIIIβ is related to class I PI3Ks, and plays a key role in both mediating viral replication (58), as well as in mediating proliferation of the *Plasmodium* (malaria) and *Cryptosporidium* parasites (59, 62). Small molecule inhibitors of human PI4KIIIβ are potent anti-viral agents (58, 118, 161). The potent PI4KIIIβ inhibitor PIK93 (27) has been used extensively to decipher the cellular roles of PI4KIIIβ (27, 55, 162) , and its role in mediating viral replication of pathogenic RNA viruses.(58, 79, 95, 163, 164). PIK93 potently inhibits PI4KIIIβ; however, it shows cross reactivity towards a number of other lipid kinases, including inhibition of several PI3Ks, which is associated with toxicity. Compared to PIK3CA inhibitors, molecular mechanisms

driving PI4KIIIβ selectivity are poorly understood The crystal structure of PI4KIIIβ bound to PIK93 was recently solved in complex with Rab11 (38), providing an opportunity for structure-guided drug design efforts towards novel inhibitors with greater selectivity over PI3Ks. However, the formation of diffraction quality crystals of PI4KIIIβ has thus far been dependent on the presence of PIK93, and the inability to crystalize PI4KIIIβ with other inhibitors has limited our understanding of the molecular mechanism of improved PI4KIIIβ inhibitor selectivity.

Considering anti-parasite PI4K inhibitors, the basis for *Plasmodium* and *Cryptosporidium* PI4K inhibitor selectivity over human PI4KIIIβ also remains poorly defined as the structures of parasite PI4Ks have yet to be elucidated. *P. vivax* PI4K (1525 residues) and *C. parvum* PI4K (1114 residues) are much larger than the human PI4KIIIβ homolog (801 residues for human isoform 2) although the parasite homologs maintain the canonical class I PI3K/ class III PI4K helical and kinase domain. A major impediment to generating constructs that are amenable to crystallography are dynamic regions within proteins with either no or limited secondary structure, which can contribute to protein flexibility and sample heterogeneity. These regions can prevent the ordered packing required for the formation of diffracting protein crystals. The larger parasite PI4K homologs are predicted to have many additional such disordered regions compared to human PI4KIIIβ, which have hindered efforts towards crystallization and structure determination. Intriguingly, inhibitors exist that potently target human and *Plasmodium* PI4KIIIβ, but not *Cryptosporidium* PI4KIIIβ (BQR695) – but inhibitors also exist that target *Plasmodium* and *Cryptosporidium* PI4Ks, but not human PI4KIIIβ (KDU-691) (59, 62). This suggests there are both conserved and non-conserved features within each homolog, and highlights the need for structural insights into parasite PI4K enzymes in order to define the molecular basis of PI4K inhibitor specificity to aid anti-parasite drug development.

To aid the development of anti-cancer, anti-viral and anti-parasitic therapeutics, we sought to determine the structural basis of selectivity for several novel phosphoinositide kinase inhibitors. First, we utilized inhibitor soaks, where inhibitor is added to pre-formed *apo* crystals, of a previously published crystallography-optimized construct of PIK3CA (165) to determine the co-structure of the novel anti-cancer agent PQR530. This structure reveals its enhanced PIK3CA selectivity is likely driven through a steric clash between PIK3CG Ile881 and the inhibitor methyl-morpholine group. Regarding the related kinase PI4KIIIβ, no such crystallography-optimized construct allowing for inhibitor soaks was available. To guide crystal construct design of PI4KIIIβ,

we utilized hydrogen-deuterium exchange mass spectrometry (HDX-MS), a technique successfully used as a preliminary step to produce truncated constructs optimized for crystallography (166, 167), including the original PI4KIIIβ crystal construct (38). HDX-MS measures the exchange rate of amide hydrogens, and is an excellent probe of secondary structure and solvent accessibility (168) (169, 170) – the dependence of H/D exchange rates on secondary structure makes HDX-MS a powerful tool to study and identify intrinsically disordered regions within proteins (171). Deletion of an additional disordered region identified using HDX-MS (residues 249-287) in the original PI4KIIIβ crystal construct facilitated crystallization in an apo state and soaking apo crystals with a variety of small molecule inhibitors led to successful determination of co-crystal structures of the anti-viral compound **9** and anti-malarial BQR695. These structures reveal that the less sterically hindered hydrophobic regions within the PI4KIIIβ active site are driving selectivity; bulkier substituents of compound **9** (relative to PIK93) likely encounter steric clashes in the active sites of related PI3Ks, with BQR695 also likely encountering clashes in related PI3Ks. We further utilize HDX-MS to define several extended dynamic regions within *P. vivax* and *C. parvum* PI4K and use this information to generate optimized constructs for X-ray crystallography, resulting in microcrystals of a truncated variant (Δ1-390 + Δ886-995 + Δ1055-1147) of *P. vivax* PI4K. In the absence of high resolution data, we show the anti-malarial compound BRD73842 shows remarkable selectivity for *P. vivax* PI4K (IC_{50} = 21 nM) over human PI4KIIIβ (IC_{50} >10 μM) in lipid kinase assays. Overall, we describe the molecular basis for human lipid kinase isoform selectivity of the anti-cancer compound PQR530, the anti-viral compound **9**, and the anti-malarial compound BQR695, and engineer truncated parasite PI4Ks to facilitate crystallization, representing the first step towards defining the molecular basis for parasite PI4K selectivity of anti-parasite compounds.

4.3 Methods

Protein Expression and Purification – PIK3CA

The crystal construct of PIK3CA (ΔABD-LBS p110α 105-1048) was expressed by recombinant baculovirus in Sf9 cells, purified, and initially crystallized as previously published (165). In brief, p110α was produced in *Spodoptera frugiperda* (Sf9) cells by infecting 1 L of cells at a density of 1.5×10^6 cells/mL with baculovirus encoding the kinase. After 65 h of infection at 27 °C, cells were harvested and washed with phosphate-buffered saline (PBS). The p110α

construct contained an N-terminal 2× Strep Tag followed by a 10× histidine tag and tobacco etch virus (TEV) protease cleavage site. Sf9 pellets were lysed in 50 mM Tris pH 8.0, 250 mm NaCl, 0.25 mM tris(2-carboxyethyl)phosphine (TCEP), 20 mM imidazole, protease inhibitor (Protease Inhibitor Cocktail Set III, Sigma) using sonication, Triton X-100 was added to 0.5% (v/v), and lysed material was centrifuged at 20 000g (Beckman J2-21, Beckman JA-20 rotor). Supernatant was passed through a 5 μm filter and onto a HisTrap FF Crude column preequilibrated in 50 mM Tris pH 8.0, 250 mm NaCl, 0.25 mM TCEP, and 20 mM imidazole. Protein was eluted from the column using 50 mM Tris pH 8.0, 200 mm NaCl, 0.25 mM TCEP, and 200 mM imidazole. Eluted protein was passed through a 5.0 mL StepTrapHP column preequilibrated in 50 mM Tris pH 8.0, 250 mm NaCl, 0.25 mM TCEP, and 20 mM imidazole. The column was washed with 5.0 mL of 50 mM Tris pH 8.0, 200 mm NaCl, 0.25 mM TCEP, and 40 mM imidazole, and 5.0 mL of TEV protease (0.01 mg/L) was added to the column for overnight cleavage at 4 °C. The protein was eluted with 7.0 mL of 50 mM Tris pH 8.0, 200 mm NaCl, 0.25 mM TCEP, and 40 mM imidazole and concentrated using an Amicon 50 kDa MWCO concentrator (MilliporeSigma) to 1.0 mL. The protein was loaded onto a Superdex 200 10/300 GL Increase (GE Healthcare) in 50 mM Tris pH 8.0, 100 mM NaCl, 2% ethylene glycol (EG), and 1 mM TCEP, and protein from a single peak was collected. Protein was concentrated using an Amicon 50 kDa MWCO concentrator to 6.5 mg/mL, flash-frozen as small aliquots in liquid nitrogen, and stored at −80 °C.

Protein Expression and Purification – human PI4KIIIβ-Rab11

Truncated human PI4KIIIβ and full-length human Rab11a (Q70L) were expressed in BL21 C41 (DE3) cells. For Rab11a (Q70L) expression, cultures were grown to an OD600 of 0.7 and induced with 0.5 mM IPTG for 3.5 h at 37°C. For truncated PI4KIIIβ expression, cultures were induced overnight at 16°C with 0.1 mM IPTG at an OD600 of 0.6. Cells were harvested by centrifugation, washed with cold phosphate-buffered saline (PBS), frozen in liquid nitrogen, and pellets were stored at −80°C. Full length PI4KIIIβ was expressed from *Spodoptera frugiperda* (Sf9) cells by infecting 1–4 L of cells at a density of 1.0 × 106 cells/mL with baculovirus encoding the kinase. All PI4K constructs had an N-terminal 6xhis-tag followed by a TEV protease site. After 48–65 h infection at 27°C, Sf9 cells were harvested and washed with ice-cold PBS.

Pellets of cells expressing PI4KIIIβ were resuspended in lysis buffer [20 mM Tris-HCl pH 8.0 (4°C), 100 mM NaCl, 10 mM imidazole, 5% (v/v) glycerol, 2 mM β-mercaptoethanol, protease

inhibitor cocktail (Millipore Protease Inhibitor Cocktail Set III, Animal-Free)], and were sonicated on ice for 5 min. Triton X-100 was then added to a final concentration of 0.2%, and the lysate was centrifuged for 45 min at 20,000g. The supernatant was then filtered through a 0.45 μm filter (Celltreat Scientific Products) and was loaded onto a 5 mL HisTrap FF column (GE Healthcare) equilibrated in buffer A [20 mM Tris-HCl pH 8.0 (4°C), 100 mM NaCl, 10 mM imidazole, 5% (v/v) glycerol, 2 mM β-mercaptoethanol]. The column was washed with 20 mL of buffer A, followed by 20 mL of 6% buffer B (20 mM Tris-HCl pH 8.0, 100 mM NaCl, 200 mM imidazole, 5% (v/v) glycerol, 2 mM β-mercaptoethanol), and was eluted with 100% buffer B. The His-affinity tagged protein was cleaved overnight at 4°C with TEV protease. The cleaved protein was then diluted to 50 mM NaCl (using 20 mM Tris-HCl pH 8.0, 10 mM imidazole, 5% (v/v) glycerol, 2 mM β-mercaptoethanol) and was loaded onto a 5 mL HiTrap Q HP column (GE Healthcare) equilibrated in buffer C (20 mM Tris-HCl pH 8.0, 50 mM NaCl, 5% (v/v) glycerol, 2 mM β-mercaptoethanol). Protein was eluted with a gradient elution using buffer D (20 mM Tris-HCl pH 8.0, 1.0M NaCl, 5% (v/v) glycerol, 2 mM β-mercaptoethanol). Fractions containing the cleaved PI4KIIIβ were pooled and concentrated to 700 μL in an Amicon 50 K centrifugal filter (Millipore). The protein was then loaded onto a HiPrep 16/60 Sephacryl S200 column equilibrated in buffer E [20 mM HEPES pH 7.2, 150 mM NaCl, 1 mM Tris Carboxyl Ethyl Phosphine (TCEP)]. The cleaved PI4KIIIβ was then concentrated to <15 mg/mL in an Amicon 50 K centrifugal filter (Millipore), and aliquots were frozen in liquid nitrogen and stored at −80°C.

Pellets of cells expressing Rab11 were resuspended in lysis buffer lacking imidazole [20 mM Tris-HCl pH 8.0, 100 mM NaCl, 5% (v/v) glycerol, 2 mM β-mercaptoethanol, protease inhibitor cocktail (Millipore Protease Inhibitor Cocktail Set III, Animal-Free)]. Cells were sonicated and centrifuged as described for PI4KIIIβ. The supernatant was filtered through a 0.45 μm filter (Celltreat Scientific Products) and incubated for 1 hour with 4 mL of Glutathione Sepharose 4B beads (GE Healthcare) equilibrated in buffer F (20 mM Tris-HCl pH 8.0, 100 mM NaCl, 5% (v/v) glycerol, 2 mM β-mercaptoethanol) followed by a 3 × 15 mL wash in buffer F. The GST tag was cleaved overnight on the beads with TEV protease. Anion-exchange chromatography was performed as outlined above for the truncated PI4KIIIβ. Cleaved and GST-tagged Rab11a(Q70L) were then concentrated to between 5 and 15 mg/mL and nucleotide loaded by adding EDTA to 10 mM followed by 1 U of phosphatase (Phosphatase, Alkaline-Agarose from calf intestine, Sigma P0762-100UN) per mg of protein. Proteins were then incubated for 1.5 h. The

phosphatase was removed using a 0.2 μm spin filter (Millipore); the flow-through was collected, and a 10-fold molar excess of GTPγS or GDP was added followed by MgCl2 to a final concentration of 20 mM. Proteins were incubated for 30 min. GST-tagged Rab11a(Q70L) was aliquoted and frozen in liquid nitrogen. Gel filtration was performed with cleaved GDP or GTPγS-loaded Rab11a(Q70L) as described above for PI4KIIIβ.

Protein Expression and Purification – P. vivax and C. parvum PI4K

The synthetic gene for full-length *P. vivax* PI4K (PVX_098050) was synthesized from GeneArt (ThermoScientific), and was expressed and purified as previously described (62). The synthetic gene for full-length *C. parvum* PI4K (cgd8_4500) was synthesized from GeneArt (ThermoScientific), and was expressed and purified as previously described (59). Both full-length and truncated PI4Ks were expressed from *Spodoptera frugiperda* (Sf9) cells by infecting 1–4 L of cells at a density of 1.0 × 106 cells/mL with baculovirus encoding the kinase. *P.vivax* PI4K had an N-terminal 6xhis-tag followed by a TEV protease site, while *C. parvum* PI4K had an N-terminal 10xhis-tag, followed by a 2X Strep-tag, followed by a TEV protease site. After 48–65 h infection at 27°C, Sf9 cells were harvested and washed with ice-cold PBS. Cell pellets were sonicated in NiNTA Buffer (20 mM Tris-HCl pH 8.0, 100 mM NaCl, 20 mM imidazole, 5% (v/v) glycerol, 2 mM β-mercaptoethanol) containing protease inhibitors (Millipore Protease Inhibitor Cocktail Set III, Animal-Free) for 5 minutes on ice. Triton X-100 (0.1% v/v) was added to the cell lysate and the lysed cell solution was centrifuged for 45 minutes at 20,000 x g at 2°C. Supernatant was filtered through a 5 μm filter and loaded onto a 5 mL HisTrap™ FF crude (GE) column in NiNTA buffer. The column was washed with 1.0 M NaCl and 20 mM imidazole in NiNTA buffer and protein was eluted with 200-250 mM imidazole in NiNTA buffer. Eluted *P.vivax* PI4K was pooled and concentrated onto a 5 mL HiTrap™ Q column (GE) equilibrated with Q buffer (20 mM Tris-HCl pH 8.0, 100 mM NaCl, 5% glycerol v/v, 2 mM β-mercaptoethanol) and eluted with an increasing concentration of NaCl. *P.vivax* PI4K was pooled and concentrated using an Amicon 30K concentrator and incubated overnight on ice with the addition of TEV protease. Eluted *C. parvum* PI4K was pooled and concentrated onto a 5 mL StrepTrap™ HP column (GE) equilibrated with Q buffer (20 mM Tris-HCl pH 8.0, 100 mM NaCl, 5% glycerol v/v, 2 mM β-mercaptoethanol) and was eluted by cleaving overnight on the column with the addition of TEV protease on ice. *C. parvum* PI4K was eluted with Q buffer and concentrated using an Amicon 30K concentrator and

incubated overnight on ice with the addition of TEV protease. Size exclusion chromatography (SEC) was performed using a Superdex™ 200 10/300 GL increase (GE) column equilibrated in SEC buffer (20 mM HEPES pH 7.5, 150 mM NaCl and 0.5 mM TCEP). Fractions containing the protein of interest were pooled, concentrated, spun down to remove potential aggregate and flash frozen in liquid nitrogen for storage at -80 ºC.

Protein expression and purification: P. falciparum Rab11a

Rab11a was expressed with an N-terminal GST tag in BL21 C-41(DE3) *E. coli* cells overnight at 16 ºC with 0.1 mM IPTG. Cell pellets were sonicated in Q Buffer (20 mM Tris-HCl pH 8.0, 100 mM NaCl, 5% (v/v) glycerol, 2 mM β-mercaptoethanol) containing protease inhibitors (Millipore Protease Inhibitor Cocktail Set III, Animal-Free) for 5 minutes on ice. Triton X-100 (0.1% v/v) was added to the cell lysate and the lysed cell solution was centrifuged for 45 minutes at 20,000 x g at 2ºC. Supernatant was filtered through a 5 μm filter and incubated with 1-4mL of Glutathione Sepharose™ 4B beads (GE) for 1-2 hours at 4ºC. Beads were washed with Q buffer, and GST-tagged proteins were eluted with 20 mM glutathione in Q buffer. Protein was further purified using anion exchange and size-exclusion chromatography as described above. Protein was spun down to remove potential aggregate, flash frozen in liquid nitrogen and stored at -80 ºC.

Crystallography - PIK3CA

Initial apo PIK3CA (ΔABD-LBS p110α 105-1048) crystallography hits were obtained from a grid of 1 μL hanging drops containing 0.5 μL of protein at 5.8 mg/mL (in 50 mM Tris pH 8.0, 100 mM NaCl, 2% EG, 1 mM TCEP pH 7.5) mixed 1:1 with 0.5 μL reservoir (poly(ethylene glycol)6000 (PEG6000) 6–12%, 0.6 M sodium formate, 0.1 M N-cyclohexyl-2-aminoethanesulfonic acid (CHES) pH 9.1–9.7, 5 mM TCEP pH 7.5) at a temperature of 18 °C. Crystals collected for diffraction were obtained from 1 μL hanging drop containing 0.5 μL of protein at 5.8 mg/mL with a 2-fold molar excess of inhibitor PQR530 mixed with 0.4 μL reservoir (8% PEG6000, 0.6 M Na formate, 0.1 M CHES pH 9.5, 5 mM TCEP pH 7.5) and 0.1 μL of 1/1000 diluted microseeds crushed from a drop of the original apo crystals. Crystals were flash-frozen in liquid nitrogen after transferring to 1 μL of reservoir solution containing 25% (v/v) glycerol as cryoprotectant and then stored in liquid nitrogen.

Diffraction data for the PIK3CA crystals were collected at 100 K at beamline BL14-1 of the Stanford Synchrotron Radiation Lightsource. Data were processed using XDS (172). Phases were initially obtained by molecular replacement using Phaser, (101) with the structure of truncated PI3Kα (PDB ID: 4TUU (165)). Iterative model building and refinement were performed in COOT (173) and phenix.refine (104), with a final Rwork = 24.2 and Rfree = 28.7 for the PI3Kα structure bound to PQR530. Refinement was carried out with rigid body refinement, followed by translation/libration/screw B-factor and xyz refinement. The final model was verified in Molprobity for the absence of both Ramachandran and Rotamer outliers (174). Data collection and refinement statistics are shown in **Table 4.1.**

Crystallography - PI4KIIIβ-Rab11

Crystals of the optimized PI4KIIIβ construct with Rab11a-GTPγS or Rab11a-GDP were obtained in vapor phase equilibration plates in sitting drops. The reservoir solution was 15% (w/v) PEG-4000, 100 mM sodium citrate pH 5.6, 200 mM ammonium sulfate and three volumes of protein were mixed with one volume in the crystallization drops, with a final drop volume of 2.5 µL. Refinement plates were set by gridding PEG-4000, ammonium sulfate, and glycerol. Optimized crystals were obtained by seeding using the Hampton Research Seed Bead Kit according to the manufacturer's instructions. The best crystals were obtained in 13–15% (w/v) PEG-4000, 100 mM sodium citrate pH 5.6, 250 mM ammonium sulfate, 2% glycerol with a 1/1000 or 1/10,000 seed solution dilution, a Rab11a-GTPγS final concentration of 4.51 mg/mL and a PI4K final concentration of 7.38 mg/mL. Crystals were frozen in liquid nitrogen using cryo buffer [15% PEG-4000 (w/v), 100 mM sodium citrate pH 5.6, 250 mM ammonium sulfate, 25% (v/v) glycerol] cryoprotectant. Inhibitor soaks were performed by incubating crystals with 0.5 µL of 10 µM inhibitor stocks in cryo buffer for 30 min, followed by a 30 min incubation with 0.5 µL of 100 µM inhibitor stock in cryo buffer, and a final 30 min incubation in 1 mM inhibitor stock in cryo buffer. Before the final addition, 1 µL was removed from the crystal drop and 1 µL of the 1 mM inhibitor in cryo buffer was added.

Data were collected at 100 K at the Canadian Macromolecular Crystallography Facility (Canadian Light Source, CLS) beamline 08ID-1. Data were integrated using iMosflm 7.1 (98) and scaled with AIMLESS (99). Phases were initially obtained by molecular replacement using Phaser (101) with the structure of PI4KIIIβ bound to PIK-93 and Rab11 (pdb code: 4D0L) used as the

search model. The final model of Apo PI4KIIIβ bound to Rab11 was built using iterative model building in COOT (103) and refinement using Phenix (104) to R work = 21.6 and R free = 24.6. The final model of PI4KIIIβ bound to BQR695 in complex with GDP loaded Rab11 was refined to R work =25.5 and R free = 28.6. The binding modes of BQR695 and compound **9** were unambiguous, and ligand geometry was generated using the elbow subset of Phenix.52 Full crystallographic statistics are shown in **Table 4.2**. Electron density corresponding to GTPγS and GDP in Rab11 was clear and the mode of binding was unambiguous.

Crystallography – P. vivax xtalPI4K-P. falciparum Rab11- KAI407

Microcrystals of the optimized *P. vivax* xtalPI4K construct with *P. falciparum* Rab11a and KAI407 were obtained in vapor phase equilibration plates in sitting drops. Prior to mixing with crystallization drops, protein solution was mixed containing 59 μM *P. vivax* xtalPI4K, 59 μM *P. falciparum* Rab11a and 120 μM KAI407 in Hepes pH 7.5, 150 mM NaCl and 1mM TCEP. The reservoir solution was 15% (w/v) PEG-8000, 100 mM MES pH 6.5, 200 mM Zinc Acetate; four volumes of protein were mixed with one volume of reservoir for a final drop volume of 0.5 μL.

GST Pulldown assay

Glutathione Sepharose 4B beads (GE Healthcare) were washed three times by centrifugation and resuspension in fresh buffer G (20 mM Hepes pH 7.0, 100 mM NaCl, 2 mM TCEP) at 4°C. GST-tagged bait protein [GST control or GST-Rab11a Q70L (GTPγS)] was then added to a concentration of 5 μM and incubated with the beads on ice for 30 min. Beads were then washed three times with buffer G at 4°C. Nontagged prey proteins (PI4KIIIβ or truncated PI4KIIIβ) were then added to a final concentration of 5 μM at which point the input was taken for SDS PAGE analysis. The mixture was incubated on ice for an additional 30 min and then washed four times with buffer G at 4°C, at which time an aliquot was taken for SDS PAGE analysis.

Lipid kinase assay of xtalPI4K

One hundred nanometer extruded PI vesicles were made with soybean phosphatidylinositol (Sigma) in lipid buffer [20 mM HEPES pH 7.5 (RT), 100 mM KCl, 0.5 mM EDTA] using the Avanti lipid mini-extruder. Lipid kinase assays were carried out using the Transcreener® ADP2 FI Assay (BellBrook Labs) following the published protocol as previously described (175); 4 μL

Reactions ran at 21°C for 30 min in a buffer containing 30 mM Hepes pH 7.5 (RT), 100 mM NaCl, 50 mM KCl, 5 mM MgCl2, 0.25 mM EDTA, 0.4% v/v Triton-X, 1 mM TCEP, 0.5 mg/mL PI vesicles and 10 μM ATP. Both full length human PI4KIIIB and the truncated PI4KIIIB crystal construct with the C-term were run at 200 nM. Fluorescence intensity was measured using a Spectramax M5 plate reader with λex = 590 nm and λem = 620 nm (20-nm bandwidth).

Lipid kinase assay of human PI4KIIIβ and P. vivax PI4K

One hundred nanometer extruded lipid vesicles were made to mimic Golgi organelle vesicles (20% phosphatidylinositol, 10% phosphatidylserine, 45% phosphatidylcholine and 25% phosphatidylethanolamine) in lipid buffer (20 mM HEPES pH 7.5 (room temperature), 100 mM KCl, 0.5 mM EDTA). Lipid kinase assays were carried out using the Transcreener ADP2 FI Assay (BellBrook Labs) following the published protocol as previously described61. 4-(μl reactions ran at 21 °C for 30 min in a buffer containing 30 mM HEPES pH 7.5, 100 mM NaCl, 50 mM KCl, 5 mM MgCl2, 0.25 mM EDTA, 0.4% (v/v) Triton X-100, 1 mM TCEP, 0.5 mg ml−1 Golgi-mimic vesicles and 10 μM ATP. *P. vivax* PI4K was used at 7.5 nM and human PI4KIIIβ was used at 200 nM. Fluorescence intensity was measured using a Spectramax M5 plate reader with excitation at 590 nm and emission at 620 nm (20-nm bandwidth). IC_{50} values were calculated from triplicate inhibitor curves using GraphPad Prism software.

Hydrogen deuterium exchange mass spectrometry

HDX reactions were conducted with 10 μL of protein in Dilution Buffer (20 mM HEPES pH 7.5, 150 mM NaCl, 2 mM TCEP), and initiated by the addition of 40 μL of D2O Buffer Solution (10 mM HEPES pH 7.5, 50 mM NaCl, 2 mM TCEP, 92% D2O), to give a final concentration of 74% D2O. Final protein concentrations were 1 μM. A fully deuterated sample was generated by incubating protein with 1M guanidine-HCl for 30 min, followed by overnight incubation with deuterated buffer at a final concentration of 74% D2O. Hydrogen exchange was terminated by the addition of a quench buffer (final concentration 0.6 M guanidine-HCl, 0.8% formic acid). Samples were rapidly frozen in liquid nitrogen and stored at −80°C until mass analysis.

Protein samples were rapidly thawed and injected onto a UPLC system immersed in ice. The protein was run over an immobilized pepsin column (Applied Biosystems; porosyme, 2-3131-00) at 130 μL/min for 3 min and the peptides were collected onto a VanGuard precolumn trap

(Waters). The trap was subsequently eluted in line with an Acquity 1.7 μm particle, 100 × 1 mm2 C18 UPLC column (Waters), using a gradient of 5-36% B (buffer A 0.1% formic acid, buffer B 100% acetonitrile) over 20 min. Mass spectrometry experiments were performed on both a Xevo QTOF (Waters) as well as an Impact II TOF (Bruker) acquiring over a mass range from 350 to 1500 m/z for 30 min, using an electrospray ionization source operated at 225°C, and a spray voltage of 2.5 kV (Xevo) or a temperature of 200°C, and a spray voltage of 4.5 kV (Impact).

Peptide identification was done by running tandem MS/MS experiments using a 5–36% B gradient over 120 min. This was supplemented with a 20 min MS/MS gradient separation to identify and correct the retention time for all samples. MS/MS was run in data dependent acquisition mode with a 1 s precursor scan from 350 to 1500 m/z, followed by three fragment scans from 50 to 2000 m/z of 2s (Xevo) or a 0.5 s precursor scan from 200-2000 m/z, followed by 12 fragment scans from 150 to 2000 m/z of 0.25 s (Impact). The resulting MS/MS datasets were analyzed with the Mascot search within Mascot distiller (Matrix Science). The MS tolerance in mascot was set to 3 ppm with an MS/MS tolerance at 0.1 Da. All peptides with a Mascot score >20 were analyzed using HD-Examiner Software (Sierra Analytics). The full list of peptides was manually validated by searching a non-deuterated protein sample's MS scan to test for the correct m/z state, and check for the presence of overlapping peptides. Ambiguously identified peptides were excluded from all subsequent analysis. Marker peptides identified in the 20 and 120 min samples were used to adjust the retention time of the long MS/MS gradient before analysis of deuterium exchange. Retention time adjustment was carried out using HD-Examiner Software (Sierra Analytics). The first round of analysis and identification were performed automatically by the HD-Examiner software, but all peptides (deuterated and non-deuterated) were manually verified at every state and time point for the correct charge state, m/z range, presence of overlapping peptides, and any deviation from the expected retention time. Any peptide that deviated from the expected mass by >5 ppm was excluded from analysis. Corrections for back exchange were generated from a fully deuterated sample. All experiments were done in triplicate.

4.4 Results

Molecular basis for selective PIK3CA inhibition by PQR530.

Class I PI3Ks are key drivers of cancer. PQR530 is a potent pre-clinical cancer therapeutic generated by the Mathias Wymann laboratory (176). PQR530 is a derivative of PQR309

(bimiralisib), a brain-penetrant pan-PI3K/mTOR inhibitor in phase II clinical trials (177, 178). PQR309 contains two morpholine moieties, with binding to class I PI3K mediated through a hydrogen bond of one of the morpholine O atoms with the hinge Val882 in PIK3CG (178), which corresponds to hinge Val851 in PIK3CA. In PQR530, one of these morpholine moieties is modified into an 3-methylmorpholine (**Fig. 4.1A**), which increases selectivity for PIK3CA (K_d = 0.84 nM) over PIK3CG (K_d = 10 nM (176), and also increases mTOR potency (0.33nM). Reducing PIK3CG inhibition is an ideal strategy for strategy for developing therapeutics against PIK3CA driven cancers, as inhibition of PIK3CG has adverse effects on immune function. To better understand the structural basis for selectivity of PQR530, we utilized a previously published crystallography-optimized PIK3CA p110α catalytic subunit construct (residues 105-1048, (165)) to co-crystalize p110α bound to PQR530. The core structure of PQR530 could be defined in the electron density, but distinct density for the methyl groups was not apparent. Fitting PQR530 to the obtained electron density map, the inhibitor was best accommodated with the methyl group in either one of the two hydrophobic interfaces formed by side chains of Tyr836, Ile848, Ile932 or Trp780, Ile800, and Val850 (numbering referring to PIK3CA) (**Fig 4.1 B,C**). Val850 in PIK3CA corresponds to Ile881 in PIK3CG, and the predicted steric clash at this position in PIK3CG could not be detected in PIK3CA. This potential clash may explain, in part, the preferred binding of PQR530 to PIK3CA versus PIK3CG – while PIK3CA facilitates binding of either potential orientation of the methyl group, PIK3CG only facilitates one.

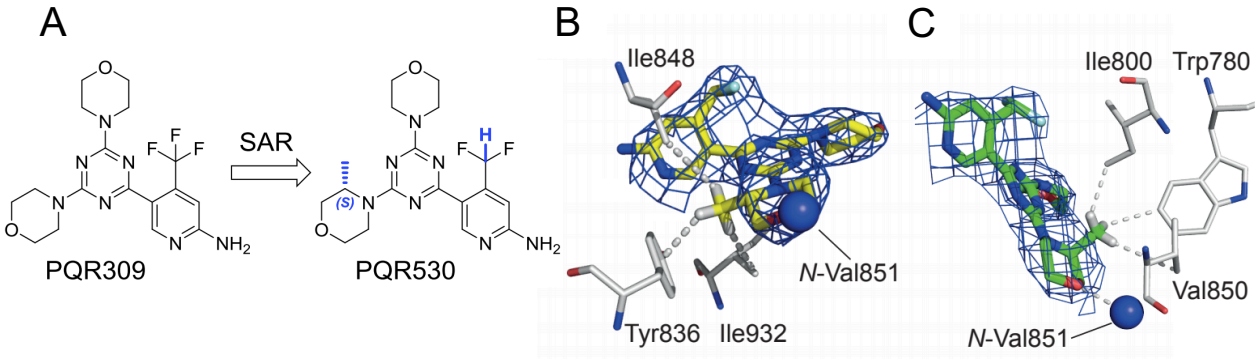

Figure 4.1. X-Ray crystal structure of PQR530 in the active site of PIK3CA to 3.15Å.
The electron density map of the inhibitor (2Fo-Fc map contoured at 1s, blue mesh) fits the core structure of PQR530, but did not provide clear density for placement of the C3-methyl during refinement in either orientation. Amino acids in proximity of the methylgroups are indicated in grey. **(A)** Structure of PQR530 (**B, C)** Two group preferred fits of PQR530 to the electron density map. Steric clashes predicted in the PIK3CG model for the conformation in **(B)** were not found in PIK3CA: residue Ile881 in PIK3CG corresponds to Val850 in PIK3CA. Full details of X-ray data collection and refinement are in **Table 4.1.**

Table 4.1 Data collection and refinement statistics for PI3K p110α bound to PQR530.

Data collection	**PIK3CA p110α-PQR530**
Space group	P 21 21 21
Unit Cell	58.93, 135.51, 144.50, 90, 90, 90
Resolution (Å)	38.3-3.15 (3.26-3.15)*
R_{merge}	0.145 (1.98)
Mean I/sigma(I)	9.1 (1.2)
CC(work)	0.935 (0.756)
CC(free)	0.908 (0.728)
Completeness (%)	99.5 (98.7)
Redundancy	8.3 (8.5)
Refinement	
Resolution (Å)	39.3-3.15 (3.36-3.15)
No. reflections	20690 (3642)
R_{work}/R_{free}	24.2/28.7
No. of hydrogen atoms	6385
Macromolecules	6356
Ligands	29
Water	0
Protein residues	847
RMS(bonds)	0.002
RMS(angles)	0.41
Ramachandran favored (%)	91.78
Ramachandran allowed (%)	7.50
Ramachandran outliers (%)	0.73
Rotamer outliers	1.00
Clashscore	17.26
Average B-factor	121.71
Macromolecules	121.69
Ligand/Ion	125.67
Water	0

**Values in parentheses are for highest resolution shell.*

Truncations in PI4KIIIβ identified by HDX-MS facilitate characterization of specific inhibitors

PI4KIIIβ is a key enzyme mediating the replication of enteroviruses and the proliferation of the malaria parasite. Compound **9** is a potent anti-viral compound with excellent selectivity for

human PI4KIIIβ (116), and BQR695 is a recently reported highly potent PI4KIIIβ inhibitor that targets both the human and *Plasmodium vivax* variants of PI4KIIIβ (62). To better understand the structural basis for selectivity of these compounds, we sought to determine their co-crystal structures with PI4KIIIβ. Hampering these efforts has been the requirement of PIK93 for crystallization of PI4KIIIβ, an inhibitor with limited selectivity over class I PI3Ks. To facilitate crystallization of the apo-state of PI4KIIIβ for inhibitor studies, we sought to optimize the original crystallography construct of PI4KIIIβ (38) by identifying regions of disorder using HDX-MS. Dynamic regions (either no or very transient secondary structure) in PI4KIIIβ were identified using HDX-MS (**Appendix L**) (97, 116). A truncated PI4KIIIβ construct was designed using the HDX information describing dynamic regions, and included an N-terminal deletion from 1 to 120, two internal truncations (one from 249 to 287, and one from 408 to 507), and a C-terminal deletion from 785 to 801 **(Fig. 4.1A)**. This construct, referred to from now on as xtalPI4K (HsPI4KIIIβ S294A 121–784, Δ249–287, Δ408–507), enabled us to generate crystals of apo PI4KIIIβ in complex with full length Rab11 (**Fig 4.1A).**

A major concern when engineering proteins for structural studies is that the introduction of truncations may disrupt the native conformation, as well as the function of the enzyme. To verify that the HDX optimized construct was not structurally perturbed by the engineered truncations we carried out tests on both the structure and function of this enzyme compared with the full-length enzyme. HDX-MS experiments were carried out on both full length PI4KIIIβ and xtalPI4K, and these revealed that levels of deuterium incorporation for xtalPI4K were similar to full length PI4KIIIβ **(Fig. 4.2B).** Importantly, there was no difference in dynamics within or around the active site of the enzyme. To verify that truncations did not change the activity or ability to bind protein partners, we carried out lipid kinase assays as well as GST pulldowns with GST-tagged Rab11. Binding assays were carried out with the PI4KIIIβ binding partner Rab11 **(Fig. 4.2C)** and GST pull downs indicated that there was no qualitative difference in the ability of the xtalPI4K to bind to Rab11 compared with full length PI4KIIIβ. It was previously shown that the C-termini of both PI4K and PI3Ks are essential for their activity (38, 179). For this reason, we made a construct containing the N-terminal and internal truncations, but with an intact C-terminus (referred to as xtal PI4KIIIβ +cterm). This construct showed a slightly reduced (~70%) lipid kinase activity on pure PI vesicles compared to WT full length PI4KIIIβ **(Fig 4.2D)**.

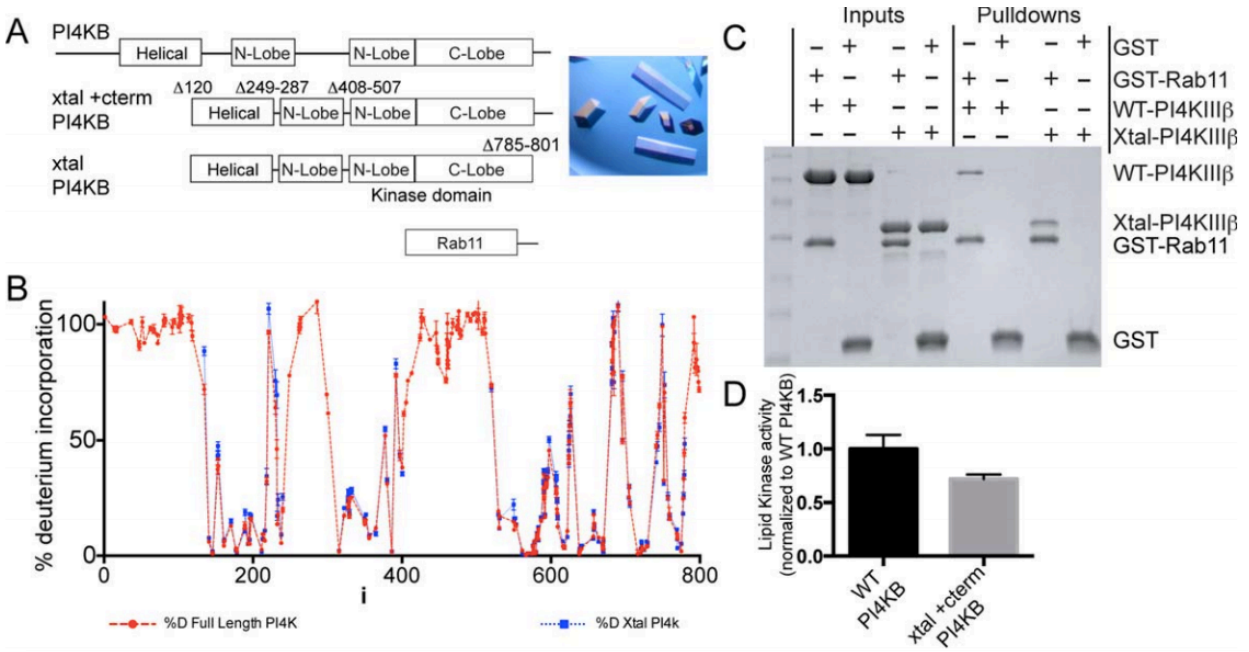

Figure 4.2. HDX-MS facilitated design of crystallography-optimized constructs of human PI4KIIIβ (refers to Appendix L).
(A) Four truncations were made in PI4KIIIβ (1-120, 249-287, 408-507, and 785-801, referred to as xtal-PI4KIIIβ), and Rab11 was full-length. Representative crystals of GTPγS Rab11 with Apo xtal-PI4KIIIβ, best crystals diffracted to 2.65 Å. (**B**) HDX levels for the full length and truncated versions of PI4KIIIβ after 3 seconds of deuterium exposure at 0°. (**C**) Pulldown assays with GST-tagged Rab11 Q70L loaded with GTPγS for both the full-length wild-type PI4KIIIβ and xtal-PI4KIIIβ constructs. The inputs and the bound proteins were analysed on SDS gels stained with Instant Blue. D: Lipid kinase assay of full-length wild-type PI4KIIIβ and xtal + cterm PI4KIIIβ constructs. Assays were carried out with 200 n*M* PI4KIIIβ in the presence of 0.5 mg/mL phosphatidylinositol vesicles with 10 μM ATP. Enzyme activity is normalized to the activity of the full length wild-type enzyme. Substrate conversion of ATP was ~15% for the wild type PI4KIIIβ.

Molecular basis for selective PI4KIIIβ inhibition by anti-viral compound 9.

Compound **9** is a bulkier derivative of PIK93 with a methoxy substituent off the central phenyl, a para-hydroxy phenol off the sulfonamide, and a cyclopentyl group at the acetamide position off of the central thiazole generated by Florentine Rutaganira in the Kevan Shokat Lab (116). Compared to PIK93, Compound **9** is a more potent PI4KIIIβ inhibitor with >140 fold selectivity over PIK3CG, >20 fold selectivity over PIK3CD, and no inhibition of VPS34 (a class III PI3K) at concentrations up to 20 μM (116). Compound **9** displayed >7-fold antiviral activity against Hepatitus C virus with reduced cell toxicity (116). To determine the molecular basis for the potency and specificity towards PI4KIIIβ, we set out to crystallize it bound to PI4KIIIβ. Utilizing soaks of compound **9** with pre-formed crystals of apo xtalPI4K bound to GDP loaded Rab11 allowed us to solve the co-crystal structure at 3.2 angstrom resolution.

Compound **9** forms a crescent shape that conforms to the active site of PI4KIIIβ. This molecule makes extensive contacts with PI4KIIIβ (**Fig. 4.3A**) (116). There are two putative hydrogen bonds formed between the thiazole and the acetamide of compound **9** with both the amide and carbonyl group of V598. The sulfonamide group also forms a hydrogen bond with Lys549. All of these hydrogen bonds are similar to those reported in the structure of PIK93 bound to PI4KIIIβ (38). Intriguingly the para-hydoxy group on the N-phenol sulfonamide also makes a putative hydrogen bond with the carbonyl of G660 (116). The structure of compound **9** also reveals the molecular mechanism for how the acetamide and methoxy substituent mediate inhibitor selectivity over PI3Kγ and vps34. Aligning the structure of PI4KIIIβ bound to compound **9** with structures of PIK93 bound to PIK3CG and VPS34 **(Fig. 4.3B-D)** reveals a number of steric clashes that explain the lack of potency of compound **9** against the PI3K family kinases. The acetamide group clashes with residues W812 and M953 in PIK3CG, and residues Y746 and F673 in vps34. The methoxy group off the central phenyl group clashes with the aspartic acid from the DFG motif in the activation loop (D964 in PI3Kγ and D823 in vps34).

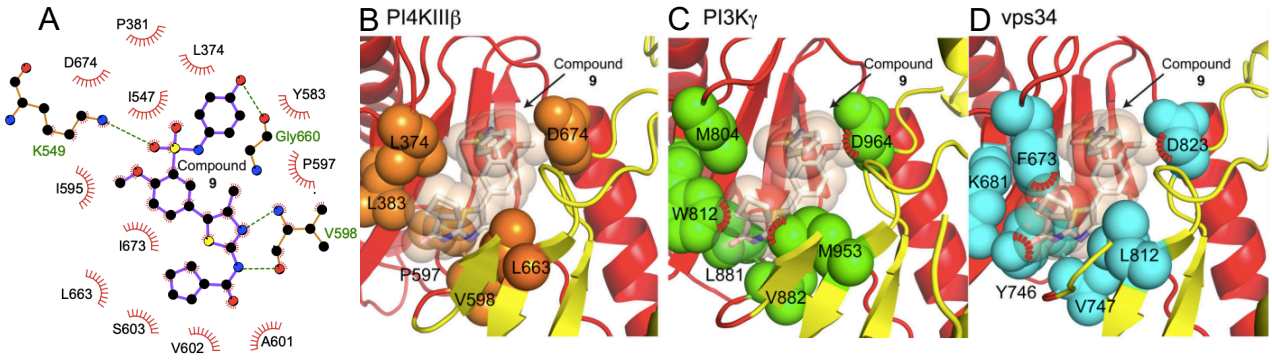

Figure 4.3. X-ray crystal structure of PI4KIIIβ bound to compound 9 to 3.2 Å reveals the structural basis for its selectivity.
(A) Residues mediating the interaction of PI4KIIIβ with compound 9, with putative hydrogen bonds indicated by dotted lines; figure generated using ligplot (180). **(B)** The structure of compound 9 bound to PI4KIIIβ, with selected residues colored in orange and shown as spheres. **(C)** A model of compound 9 in the active site of PI3Kγ. The model was generated by aligning the active site of the structure of compound 9 bound to PI4KIIIβ to the structure of PI3Kγ bound to compound 1 (PDB: 2CHZ). The equivalent residues shown in panel A are colored in green and shown as spheres, with steric clashes highlighted in red. **(D)** A model of compound 9 in the active site of vps34. The model was generated by aligning the active site of the structure of compound 9 bound to PI4KIIIβ to the structure of vps34 bound to PIK93 (PDB: 2X6J). The equivalent residues shown in panel A are colored in cyan and shown as spheres, with steric clashes highlighted in red. Full details of X-ray data collection and refinement are in **Table 4.2.**

Molecular basis for selective PI4KIIIβ inhibition by anti-malarial BQR695.

The compound BQR695 is a recently reported highly potent PI4KIIIβ inhibitor that has high potency against both the human (IC_{50} = 80 nM) and *Plasmodium vivax* (~3.5 nM) variants of PI4KIIIβ (62). Soaking apo xtalPI4K-Rab11 GDP crystals with the potent anti-malarial compound BQR695 allowed for determination of the structure of human PI4KIIIβ bound to BQR695 refined to a resolution of 3.2 Å. This compound makes two putative hydrogen bonds with PI4KIIIβ, one between the nitrogen of the central quinoxaline and the amide hydrogen of V598, and one between the hydrogen on the amino group off the central quinoxaline with the carbonyl of A601 (**Fig. 4.4A**). The hydrogen bond between V598 and the central quinoxaline is characteristic of many protein and lipid kinase inhibitors (181) as this mimics the hydrogen bond made with the N1 of the ATP adenine. This compound has been shown to be specific over PI3K kinases (10 fold more potent against PI4KIIIβ over PIK3CA, and >100 fold more potent against PI4KIIIβ compared to all other class I and class III PI3K isoforms) (62). Comparing the structure of PI4KIIIβ bound to BQR695 with PI3K structures (104, 173, 182, 183) reveals the molecular basis for this specificity; PI4KIIIβ has a larger binding pocket to accommodate the glycyl methyl amide group compared to the class I and class III PI3Ks. The wall of this pocket is composed of L383 in PI4KIIIβ, which corresponds to a tryptophan in class I PI3Ks, and a phenylalanine in class III PI3Ks (**Fig. 4.4B,C**). The clash at this position is likely to interfere with the ability of the central quinoxaline of BQR695 to properly hydrogen bond with V598 of PI4KIIIβ.

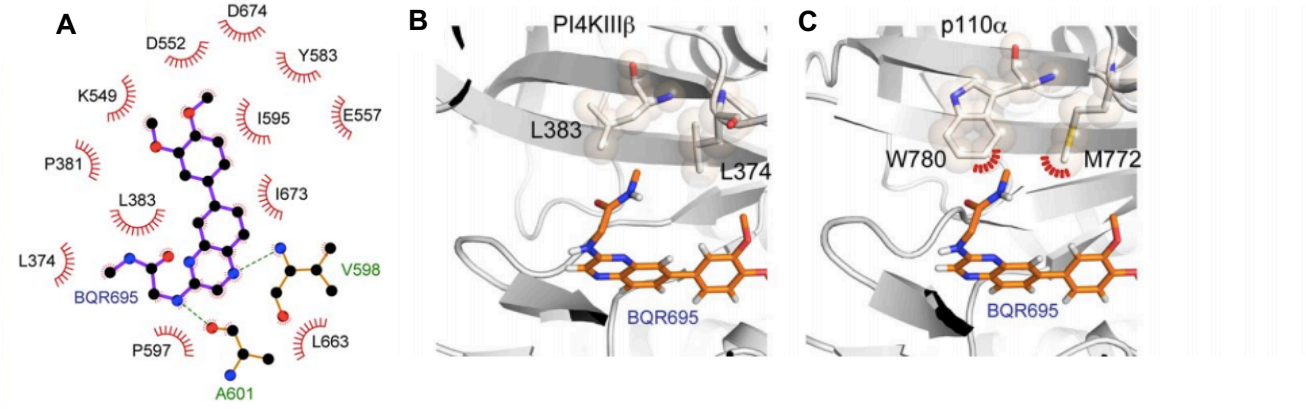

Figure 4.4. X-ray crystal structure of PI4KIIIβ bound to BQR695 to 3.2 Å reveals the structural basis for its selectivity.
(**A**) Residues mediating the interaction of PI4KIIIβ with BQR695, with putative hydrogen bonds indicated by dotted lines; figure generated using ligplot (180). **(B, C)** Comparison of the PI4KIIIβ and class I PI3K (p110 α) active site. Shown are the PI4KIIIβ structure with BQR695, and a model of p110α (derived from PDB: 4JPS54) with BQR695. Residues in similar position in PI4KIIIβ and p110α are highlighted (L373 and L384 in PI4KIIIβ) and (M772 and W780 in p110a) are shown as sticks. Potential clashes in the p110α are highlighted in red. Full details of X-ray data collection and refinement are in **Table 4.2.**

Table 4.2 Data collection and refinement statistics for PI4KIIIβ bound to compound 9 or BQR695.

Data collection	**PI4K-compound 9-Rab11-GDP**	**PI4K-BQR695-Rab11-GDP**
Wavelength (Å)	0.9797	0.9797
Space group	P 21 21 21	P 21 21 21
Unit cell	48.9, 103.5, 188.9, 90, 90, 90	48.82, 105.4, 188.85, 90, 90, 90
Total reflections	67660 (6441)	62,007 (5729)
Unique reflections	16316 (1611)	16,065 (1499)
Multiplicity	4.1 (4.0)	3.9 (3.8)
Completeness (%)	98.63 (99.44)	95.56 (90.96)
Mean I/sigma(I)	8.93 (2.11)	8.12 (1.64)
Wilson B-factor	82.35	91.96
R-merge	0.1092 (0.7019)	0.1008 (0.7039)
R-meas	0.1249	0.1164
CC1/2	0.933 (0.375)	0.996 (0.815)
CC*	0.988 (0.738)	0.999 (0.948)
Refinement		
Resolution range (Å)	47.34–3.2 (3.31-3.2)	54.05-3.2 (3.314-3.2)
Reflections used for R-free	5%	5%
R-work	0.2291 (0.3328)	0.2553 (0.3936)
R-free	0.2616 (0.3660)	0.2864 (0.3915)
Number of non-hydrogen atoms	5058	5059
Macromolecules	4987	5020
Ligands	71	39
Water	0	0
Protein residues	621	622
RMS(bonds)	0.003	0.002
RMS(angles)	0.69	0.40
Ramachandran favored (%)	96	95
Ramachandran outliers (%)	0.3	0.17
Clashscore	5.73	21.10
Average B-factor	96	110.80
Macromolecules	96.1	110.80
Ligands	93.9	119.20
Solvent	N.A.	N.A.

Optimization of parasite PI4K constructs for crystallography using HDX-MS

In the absence of the *Plasmodium* or *Cryptosporidium* PI4K structure, the structural basis for specificity of anti-parasitic PI4K inhibitors over human PI4KIIIβ remains poorly defined. Crystallization and structure determination of the human PI4KIIIβ homolog is so far only possible through the removal of disordered regions of the protein that impede crystallization (38, 97, 115, 116). The larger *Plasmodium* PI4K homolog (172 kDa) and *Cryptosporidium* PI4K homolog (129 kDa) are predicted to have many additional such disordered regions, which have hindered efforts towards crystallization and structure determination. To identify dynamic regions within *Plasmodium PI4K,* we subjected recombinant protein to a short 0.3 second pulse of deuterium (3 sec on ice) so that only amides with low secondary structure would become deuterated. We identified four key regions within the protein with rapid exchange profiles: the N-terminus (~1-400), C-terminal to the predicted helical domain (~550-700), and two regions in the N-lobe of the kinase domain (~900-100 and 1100-1200) (**Fig 4.5A)**. Using the HDX-MS dynamics information, several truncated constructs were designed to reduce overall disorder and potentially facilitate crystallization, and expressed in *Sf9* cells (all constructs are summarized in **Table 4.3)**. The most promising construct, *P. vivax* xtalPI4K (Δ1-390 + Δ886-995 + Δ1055-1147), contained three truncations **(Fig 4.5B)** and eluted from gel filtration in the void as a potential soluble aggregate **(Fig. 4.5C**) with moderately pure yields of 0.9 mg per 1.0 L *Sf9* cells after purification (**Fig 4.5D**). Despite presentation as a potentially soluble aggregate, *P. vivax* xtalPI4K formed microcrystals in the presence of *P. falciparum* Rab11a and the anti-malarial inhibitor KAI-407 **(Fig 4.5E**).

We then utilized the short D_2O pulse experiment to identify dynamic regions within the smaller *Cryptosporidium PI4K.* We identified four key regions within the protein with rapid exchange profiles, albeit these were shorter than the *Plasmodium* PI4K disordered regions: the N-terminus (~1-75), two regions c-terminal the predicted helical domain (~200-300, 425-525), and one region within the N-lobe of the kinase domain (~775-825) (**Fig 4.5F)**. Again, several truncated constructs were designed to reduce overall disorder and potentially facilitate crystallization, and expressed in *Sf9* cells (all constructs are summarized in **Table 4.3)**. The most promising construct, *C. parvum* xtalPI4K (Δ1-68 + Δ217-290+ Δ782-817), contained three truncations **(Fig 4.5G)** and eluted from gel filtration at a volume consistent with a monomer **(Fig. 4.5H**). After purification, *C. parvum* xtalPI4K was extremely pure (**Fig 4.5I**); however, yields of 150 μg per 1.0 L *Sf9* cells after purification were too low to continue with crystallography.

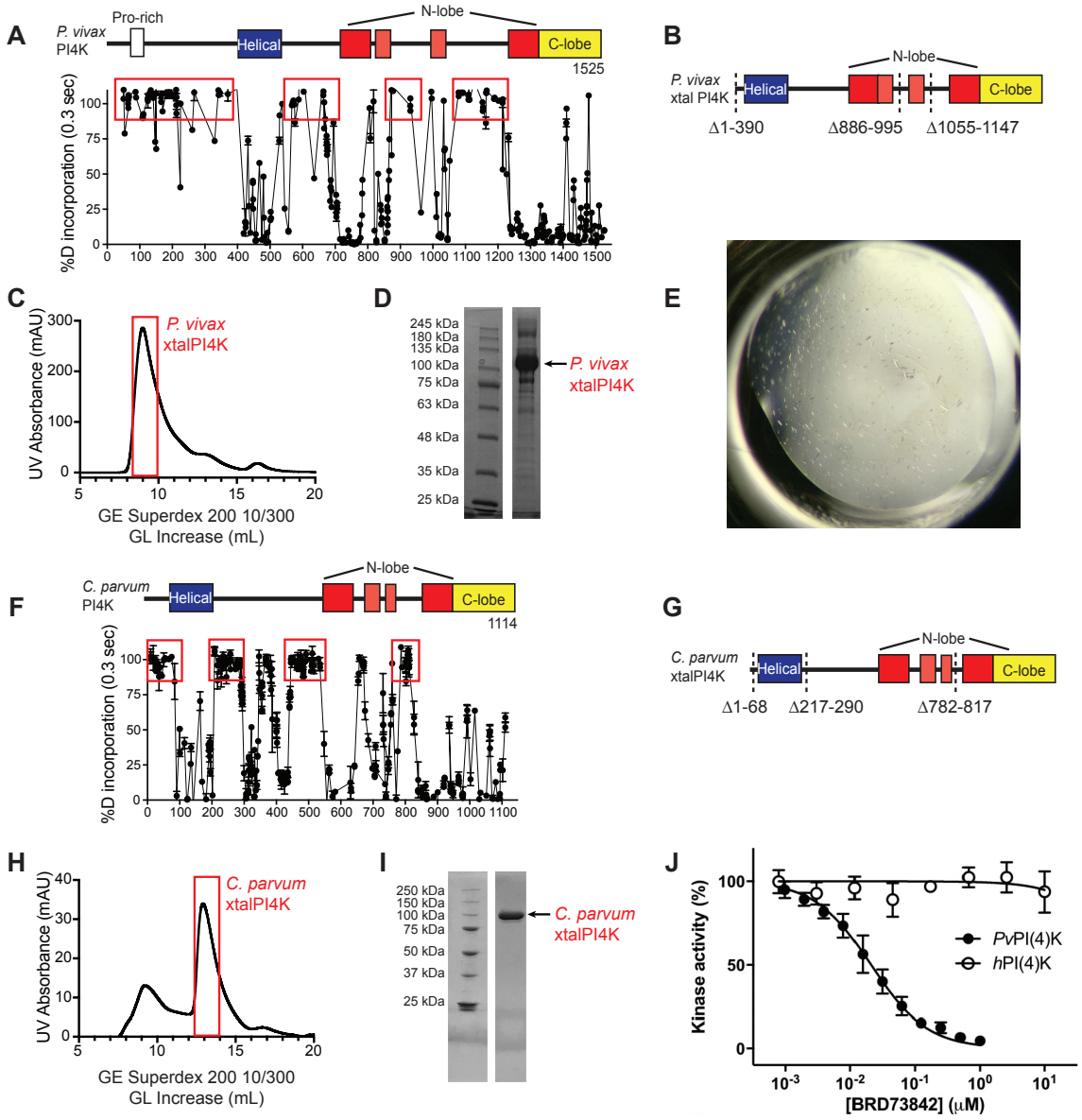

Figure 4.5. Identification of dynamic regions within parasite PI4Ks using HDX-MS facilitates engineering of crystallography optimized constructs.

(A) The deuterium incorporation of *P. vivax* PI4K at 0.3 s D_2O exposure (i.e. 3 s D_2O exposure at 0°C) is mapped according to the central residue, with putative domain architechture shown above. Every point represents a single peptide. Experiments were carried out in triplicate, and error bars represent SD. Most are smaller than the size of the point. Red boxes highlight rapidly exchanging regions with limited secondary structure. **(B)** *P.vivax xtalPI4K* (Δ1-390 + Δ886-995 + Δ1055-1147) optimized crystallography construct engineered to remove disordered regions identified using HDX-MS. **(C)** Recombinant *P.vivax xtalPI4K* (103kDa) elutes from a S200 Superdex 10/300 GL increase gel filtration column (GE) at a volume consistent with a soluble aggregate (in the void). SDS-Page Gel of purified *P.vivax xtalPI4K* peak marked with a red box is shown in **(D)**. **(E)** Microcrystals formed by *P.vivax xtalPI4K* in complex with *P. falciparum* Rab11a and the anti-malarial inhibitor KAI-407. **(F)** The deuterium incorporation of *P. vivax* PI4K at 0.3 s D_2O exposure (i.e. 3 s D_2O exposure at 0°C) is mapped according to the central residue, with putative domain architecture shown above. Every point represents a single peptide. Experiments were carried out in triplicate, and error bars represent SD. Most are smaller than the size of the point. Red boxes highlight rapidly exchanging regions with limited secondary structure. **(G)** *C. parvum* xtalPI4K (Δ1-68 + Δ217-290 + Δ782-817) optimized crystallography construct engineered to remove disordered

regions identified using HDX-MS. **(H)** Recombinant *C. parvum* xtalPI4K (109kDa) elutes from a S200 Superdex 10/300 GL increase gel filtration column (GE) at a volume consistent with a monomer. SDS-Page Gel of purified *C. parvum* xtalPI4K peak marked with a red box is shown in **(I)**. **(J)** *Plasmodium* PI4K, but not human PI4KIIIβ, is potently inhibited by the anti-malarial BRD73842. Kinase assays of *Plasmodium* PI4K (7.5 nM) and human PI4KIIIβ (200 nM) in the presence of varying concentrations of BRD73842 were carried out on Golgi-mimic vesicles (0.5 mg/L) in the presence of 10 μM ATP. The data was normalized to the kinase activity of each enzyme alone. IC_{50} values were determined by one binding site, nonlinear regression (curve fit) using Graphpad. Error bars represent standard deviation of independent technical replicates (n=3).

Table 4.3 Summary of engineered crystallography-optimized parasite PI4K constructs.

Protein	Truncation(s)	Soluble *Sf9* expression	Further Characterization
P. vivax PI4K	Δ1-390	yes	-
	Δ1-390 + Δ573-660	yes	-
	Δ1-390 + Δ866-955	yes	-
	Δ1-390 + Δ937-1222	no	-
	Δ1-390 + Δ1051-1205	no	-
	Δ1-390 + Δ1065-1200	yes	-
	Δ1-390 + Δ573-660 + Δ886-995	yes	-
	Δ1-390 + Δ886-995 + Δ1065-1151	yes	-
	Δ1-390 + Δ886-995 + Δ1055-1098	yes	-
	Δ1-390 + Δ886-995 + Δ1055-1147	yes	potentially soluble aggregate; resulted in microcrystals
	Δ1-390 + Δ573-660 + Δ866-995 + Δ1055-1147	yes	potentially soluble aggregate; low yield
C. parvum PI4K	Precision Protease cut site at 531	no	unstable after cleavage
	Δ1-68	yes	-
	Δ217-290	yes	-
	Δ448-535	no	-
	Δ452-518	yes	-
	Δ782-817	yes	-
	Δ1098-1114	no	-
	Δ1-68 + Δ217-290	yes	-
	Δ1-68 + Δ217-290 + Δ782-817	yes	monomeric; low yield
	Δ1-68 + Δ217-290 + Δ452-518 + Δ782-817	yes	unstable

In the absence of a high resolution structure of *Plasmodium* PI4K, we utilized kinase assays of human PI4KIIIβ and *Plasmodium* PI4K on Golgi-mimic vesicles to determine the mechanism of action and selectivity of BRD73842, a novel anti-malarial (61). BRD73842 was a potent inhibitor of *Plasmodium* PI4K (IC_{50} = 21 nM) and showed no inhibition of human PI4KIIIβ at concentrations up to 10 μM **(Fig 4.5J)**.

4.5 Discussion

Recent years have seen an explosion in the development of potent and selective small molecules targeting the class I PI3Ks and PI4KIIIβ. The class I PI3K inhibitors are now quite advanced in the clinic, with multiple being approved for treatment of blood cancers. There has been a number of failed trials of PI3K inhibitors in solid tumors, with many complications from dose-limiting toxicity. As the next generation of preclinical cancer therapeutics targeting class I PI3Ks is optimized to increase potency and tune selectivity, understanding the molecular basis of inhibition by these compounds will provide key insight in optimizing isoform selectivity. PQR530, a novel anti-cancer compound derived from PQR309, is modified into a 3-methylmorpholine, which increases selectivity for PIK3CA over PIK3CG. We were able to determine the co-crystal structure of PIK3CA bound to PQR530. While the core structure of PQR530 could be defined in the electron density, clear density for the methyl group on the modified morpholine was not apparent, which was best accommodated in one of two hydrophobic interfaces in PIK3CA. The lack of distinct density for the methyl group may be due to binding of PQR530 in both methyl orientations within the co-crystal structure. One of these potential inhibitor orientations in PIK3CA shows the additional methyl group packs against Val850 in PIK3CA. This residue corresponds to Ile881 in PIK3CG, which would exhibit an expected steric clash that could not be detected in PIK3CA. This structure explains the preferred binding of PQR530 to PIK3CA versus PIK3CG, in which it would be unable to bind in one of the potential orientations. It should be noted that the lack of a distinct signal for the methyl group in the X-ray structure may also suggest that PQR530 can bind to PI3Ks in multiple ways, with the substituted morpholine pointing toward either the hinge region or the solvent exposed space.

The related lipid kinase PI4KIIIβ plays both key physiological and pathological roles, and the design of novel potent and selective inhibitors will be essential both in deciphering the cellular functions of this enzyme, as well as in the development of potential future therapeutic agents in diseases dependent on PI4KIIIβ activity. In addition to playing an essential role in the replication of the malaria parasite (62), PI4KIIIβ mediates the replication of a variety of pathogenic RNA viruses. Along with this critical role in mediating pathological conditions, PI4KIIIβ also plays key roles in a number of physiological processes including membrane trafficking (88), lipid transport (184), and cytokinesis (53), and the development of potent and selective molecules will be essential in deciphering the isoform specific functions of this enzyme. Since PI4KIIIβ plays an

essential role in mediating viral replication for a variety of pathogenic viruses, the development of PI4KIIIβ inhibitors has been an attractive target for pan anti-viral agents. A number of potent PI4KIIIβ inhibitors have recently been discovered (62, 95, 114, 115, 117, 118, 185, 186), and experiments on a variety of RNA viruses show they are potent anti-viral agents. However, a complication of this work has been the toxic effects of some of these inhibitors on host function. There are conflicting results of the toxicity of PI4KIIIβ inhibitors *in vivo*, with some showing immunosuppressive effects (114), some showing lethality in mice (117), and others being well tolerated (118). Deciphering if these effects are dependent on the inhibition of PI4KIIIβ, or through other off target effects requires the generation of more potent and specific PI4KIIIβ inhibitors. Further, in recent years, non-polio enteroviruses, particularly Enterovirus D68, have emerged as a threat to public health with outbreak sizes increasing and no targeted anti-viral therapy available (81). Particularly in children, EV-D68 causes devastating polio-like symptoms including acute flaccid myelitis, which can result in debilitating paralysis and even death. The potential anti-viral benefit of human PI4KIIIβ inhibitors in these cases may outweigh the risk of immunosuppressive effects. A specific goal for the development of antivirals is to avoid off target effects on both PIK3CG and PIK3CD as both of these enzymes play key roles in the immune system (33).

A prominent challenge in deciphering the molecular basis of PI4KIIIβ inhibitor specificity has been the inability to crystalize the kinase in the absence of PIK93, an inhibitor with several off-target effects. Using HDX-MS to identify disordered regions in PI4KIIIβ permitted us to generate crystals of PI4KIIIβ in the absence of small molecule inhibitors, enabling us to soak these crystals with the potent inhibitors compound **9** and BQR695, and solve the co-crystal structure with these compounds. These structures have revealed novel molecular details about the mechanism of specificity of PI4KIIIβ inhibitors. Differences in the pocket accommodating the acetamide group of compound 9 in PI4KIIIβ compared to PIK3CG and vps34 explains why compound **9**, the bulkier derivative of PIK93, was a more effective antiviral compound in a cellular model of Hepatitis C virus replication, with lower cellular toxicity. The acetamide group mediating specificity of PI4KIIIβ compound **9** strongly correlates with previous studies on compounds very similar to PIK93, where addition of a bulky substituent in a similar position to the acetamide group in PIK93 greatly enhanced specificity (186, 187). The larger binding pocket of PI4KIIIβ is also key in accommodating the glycyl methyl amide group of the anti-malarial BQR695 compared to the class I and class III PI3Ks.The structural details of these compounds bound in the active site

pocket will provide a future framework for the optimization of PI4KIIIβ inhibitors to enhance potency and specificity, reducing off-target effects against PI3Ks.

Finally, PI4KIIIβ also plays a critical role in the replication of the malaria and cryptosporidiosis parasites (59, 62). While several novel anti-parasitic compounds target *Plasmodium* and *Cryptosporidium* PI4Ks, the molecular basis for their potency and specificity is poorly understood. Both parasite homologs of PI4KIIIβ are significantly larger than the human variant, and contain several key differences in residues lining the active site. As such, structural information from human PI4KIIIβ has limited use in facilitating structure-guided drug design against parasite PI4Ks. Using HDX-MS we were able to show significantly longer stretches of disorder are present in the *P. vivax* and *C. parvum* PI4Ks, which may explain the failure to obtain diffraction quality crystals of either enzyme to this point. Removal of these disordered regions allowed us to purify engineered protein constructs more likely to crystalize, resulting in microcrystals of *P. vivax* PI4K in complex with *P. falciparum* Rab11a and the potent anti-malarial KAI407. While these crystals were too small to attempt diffraction experiments, future optimization of crystallization conditions and eventual determination of *P. vivax* PI4K with this construct remains a possibility. Engineering attempts in *C. parvum* PI4K generated well-behaved, monomeric protein, but significantly impaired total yield. Future optimizations should include scaling-up expressions, co-expressions with a binding partner such as Rab11a, and/or optimization of purification conditions, which may ultimately lead to viability of this construct for crystallography experiments. In the absence of parasite PI4K structures, recombinant lipid kinase assays on Golgi mimic vesicles have allowed for the characterization of potency and specific anti-malarial and anti-cryptosporidium compounds targeting PI4K. Identification of BRD73842 as a potent *Plasmodium* PI4K inhibitor with no activity against human PI4KIIIβ highlights the possibility of taking advantage of subtle isoform differences in developing novel anti-parasitic therapeutics.

Chapter 5: Discussion and Future Directions

5.1 Summary of Research Objectives

PI4KIIIβ is a key generator of PI4P at the Golgi that is essential for proper Golgi formation and function and plays crucial roles in lipid transport, membrane trafficking and cytokinesis. Further, PI4KIIIβ plays critical roles in the proliferation of many viruses and the malaria and cryptosporidium parasites, and is a prominent target for the development of novel therapeutics against these pathogens. Since mammalian PI4KIIIβ was identified in the late 90s, several important regulatory proteins have been identified, including GBF1/Arf1, ACBD3 and the protein c10orf76. Additionally, viral 3A proteins manipulate host PI4KIIIβ during infection to drive viral replication. Despite the identification of numerous regulatory proteins, molecular mechanisms involved in both the normal regulation of PI4KIIIβ and its hijacking during viral infection have remained undefined.

During the course of this dissertation, I set out to define key molecular mechanisms regulating PI4KIIIβ activity. To this end, I have used various biochemistry techniques to reveal mechanisms of PI4KIIIβ regulation by protein binding partners and small molecule inhibitors. The primary objective of this dissertation has been to define the molecular basis of PI4KIIIβ protein complexes required for normal Golgi PI4P levels and viral replication. In Chapter 2, I described the molecular basis of PI4KIIIβ activation by the Aichivirus 3A protein through ACBD3. In Chapter 3, I discovered a direct complex between PI4KIIIβ and c10orf76, defined crucial interfaces of this interaction, and utilized complex-disrupting mutations to study the critical role of this complex in normal Golgi PI4P production and the replication of enteroviruses. In Chapter 4, I studied the molecular basis for selective inhibition of human PI4KIIIβ and related lipid kinases by novel anti-cancer, anti-viral and anti-parasitic compounds.

In this final chapter, I will first discuss the implications of the results from Chapter 2 and Chapter 3 pertaining to both normal PI4KIIIβ signalling, and its manipulation during viral infection. I will also discuss the significance of the results from Chapter 4 regarding selective inhibition of human PI4KIIIβ and related lipid kinases as therapeutics. Finally, I will summarize future directions to further probe human PI4KIIIβ regulation by host and viral proteins, and characterize parasite PI4Ks.

5.2 Regulation of PI4KIIIβ and Golgi PI4P

PI4KIIIβ was first recognized as a key signalling protein when the yeast homolog, Pik1p, was identified as an essential gene in *Saccharomyces cerevisiae* (50). The eventual characterization of mammalian PI4KIIIβ revealed its Golgi localization and distinct similarity to PI3Ks (52, 188). PI4P generated by PI4KIIIβ at the Golgi is recognized by several proteins including OSBP, FAPP, CERT, and GOLPH3 which are important for Golgi stability and lipid transport (55, 63–66). The activity of PI4KIIIβ is regulated by multiple protein-protein interactions with its various domains, as well as phosphorylation. The small GTPase Arf1 was the first identified regulator of human PI4KIIIβ at the Golgi and acts to drive PI4KIIIβ-dependent PI4P generation through a yet unknown mechanism (54). In turn, PI4KIIIβ plays a critical role in recruitment of the small GTPase Rab11 to the Golgi, through its helical domain (38, 67). Experiments utilizing the *Drosophila melanogaster* PI4KIIIβ homolog, "four-wheel drive" (FWD), have shown that PI4KIIIβ-mediated Rab11 recruitment is independent of kinase activity, with formation of this complex essential for spermatogenesis in the fly (53). PI4KIIIβ is phosphorylated at Ser294 by the protein kinase PKD, which directly drives binding of 14-3-3 and leads to an activation of PI4P production at the Golgi (69–71, 92). Less well understood are interactions involving the proteins ACBD3 and c10orf76, which have recently been implicated in PI4KIIIβ regulation (56, 57, 68). Defining the molecular mechanisms of all regulatory partner interactions with PI4KIIIβ is a key goal in deciphering the complexity of its regulation, and understanding its catalytic and non-catalytic roles.

PI4KIIIβ-ACBD3 complex

ACBD3 has been implicated in PI4KIIIβ regulation since several studies showed their co-localization to viral replication organelles during viral infection (56, 57, 76, 79). ACBD3 is a multi-domain adaptor protein, containing an acyl-CoA binding domain (ACBD), glutamine-rich region (Q) and Golgi-dynamics domain (GOLD). ACBD3 is normally localized to the Golgi via an interaction with its GOLD domain and the large transmembrane Golgi-resident protein Giantin (112). Our HDX-MS experiments probing the PI4KIIIβ-ACBD3 interface show that the normally disordered N-terminus of PI4KIIIβ undergoes a disorder-to-order transition to bind to the Q region of ACBD3. Mutations in these regions of PI4KIIIβ (I43A, D44A) or ACBD3 (FQ258AA) successfully disrupted complex formation, confirming the putative interface. Concurrent to these

initial experiments, another group published the NMR structure of the PI4KIIIβ N-terminus bound to the ACBD3 Q region (48). Further, by locking the ACBD3 GOLD domain onto membranes to mimic Giantin recruitment, they showed that ACBD3 alone is able to activate PI4KIIIβ by directly recruiting it to membranes. (48). In our studies we were unable to show an activation of PI4KIIIβ by freely soluble ACBD3 even in the presence of membranes. Taken together, these findings reveal a mechanism by which Giantin localizes ACBD3 to the Golgi, where it subsequently recruits PI4KIIIβ via a disorder-to-order transition of the N-terminus, activating its kinase activity on Golgi membranes.

PI4KIIIβ-c10orf76 complex

c10orf76 was originally identified as a PI4KIIIβ-associated protein through co-immunoprecipitation experiments using tagged PI4KIIIβ (56, 88). Recent experiments probing genetic essentiality identified c10orf76 as a key molecular hub at the Golgi. c10orf76 in HAP1 cells was identified as synthetically lethal in combination with the loss of several different Golgi-signaling proteins, and genetically linked to PI4KIIIβ (68). c10orf76 is highly conserved in vertebrates, and homozygous knockout of the mouse homolog of c10orf76 (ARMH3) is lethal in the pre-weaning stage (144).

Our work provides the first evidence of a direct PI4KIIIβ-c10orf76 complex, which is mediated through the kinase linker region of PI4KIIIβ, and functions to recruit c10orf76 to the Golgi. In vertebrates, there is a strong correlation between the conservation of the kinase linker region of PI4KIIIβ and the PI4KIIIβ-binding site in c10orf76, suggesting that a critical role of c10orf76 is linked to its ability to form a complex with PI4KIIIβ. While the majority of PI4KIIIβ is normally localized to the Golgi, phosphorylation of Ser496, located in the binding interface for c10orf76, has been shown to drive the kinase to nuclear speckles through a yet unknown mechanism (122). The role of PI4KIIIβ in the nucleus remains unexplained. While phosphorylation of Ser496 was recently shown to be driven by PKA *in vivo* (121), we show PKA directly and specifically phosphorylates this site *in vitro*, which in turn modulates the affinity of PI4KIIIβ for c10orf76. Due to the number of signalling pathways affected by PKA activation/inhibition, studying the direct effect of this protein kinase on PI4KIIIβ *in vivo* is challenging. As expected, the non-phosphorylatable S496A mutant showed no distinct changes in Golgi localization or its ability to recruit c10orf76. Unfortunately, the inability of either S496D or

S496E mutants to mimic phosphorylation limited our ability to further study the effect of PKA phosphorylation on PI4KIIIβ signalling. It is possible phosphorylation of PI4KIIIβ Ser496 modulates the PI4KIIIβ-c10orf76 complex *in vivo,* facilitating binding of another protein associated with re-localization of PI4KIIIβ from the Golgi to the nucleus, though further investigation is required.

We show that PI4KIIIβ is able to bind both ACBD3 and c10orf76 simultaneously, and PI4KIIIβ is both necessary and sufficient for Golgi membrane recruitment of c10orf76, indicating ACBD3 recruitment of PI4KIIIβ to the Golgi in turn recruits c10orf76 to the Golgi. Intriguingly, c10orf76 causes a decrease of PI4KIIIβ kinase activity *in vitro*, yet knockout of c10orf76 leads to reduced PI4P levels *in vivo*. This discrepancy between could be due to the lack of other PI4KIIIβ activators *in vitro*, such as ACBD3 or Arf1/GBF1, as well as the potential of c10orf76 to alter phosphatidylinositol dynamics, possibly through phosphatidylinositol transfer proteins (PITPs) that activate PI4KIIIβ (145). Significant attempts at crystalizing the PI4KIIIβ-c10orf76 complex to explain the direct inhibitory effect *in vitro* were unsuccessful, yet nanobodies (189) we raised against this complex (data not shown) may facilitate future high resolution structural studies. *In vivo*, knockout of c10orf76 led to an increased cytosolic fraction of GBF1 and the active Arf1 effectors (COP-β or COP-α/γ) but not native coatomer, indeed suggesting altered Arf1/GBF1 dynamics are responsible for disruption of Golgi PI4P levels (54). During the publication process of our findings, another group published proximity-dependent biotinylation (BioID) experiments with GBF1, identifying an interaction with c10orf76 (190). Taken together with our findings, there is a clear link between c10orf76 and GBF1. Perhaps c10orf76, when recruited to the Golgi by PI4KIIIβ, directly recruits GBF1 to Golgi membranes, driving Arf1 activation which in turn positively regulates PI4KIIIβ. Additional study into the potential of a direct c10orf76-GBF1 complex will be necessary to define how c10orf76 affects GBF1/Arf1 dynamics downstream of PI4KIIIβ.

That concurrent study also shows c10orf76 siRNA knockdown causes Golgi fragmentation and impairs cellular secretion in HeLa cells (190). In HAP1 cells we do not observe Golgi fragmentation, and ACBD3-PI4KIIIβ recruitment to the Golgi is normal. This discrepancy may be due to utilization of different cell types: HAP1 cells are fully haploid (1n), while HeLa cells are hypertriploid (3n+), carrying a different genetic complement (191). Potential genetic compensation mechanisms in these HAP1 c10orf76 knockout cells may also contribute to these

differences. Considering the observed essentiality of c10orf76 in KBM7 cells (68), it is clear a precise coordination of cellular c10orf76 protein levels is required for proper Golgi maintenance and cell viability.

5.3 Hijacking of PI4KIIIβ during viral infection

Picornaviruses cause a host of human diseases including gastroenteritis, poliomyelitis, aseptic meningitis and acute flaccid paralysis. Despite the impact of these viruses on human health, no targeted anti-viral therapy is available. Picornaviruses hijack numerous lipid signaling processes within infected cells, manipulating lipid composition to generate replication organelles, which are essential for the proper formation of viral replication machinery (75). The recruitment of PI4KIIIβ and GBF1/Arf1 to replication organelles plays a critical role in this process (58, 86). Central to recruitment of these host factors are interactions with virus encoded membrane-bound 3A proteins, which are required for viral replication organelle formation. While the recruitment of ACBD3, PI4KIIIβ, and GBF1 to replication organelles has been well established, the exact complement of necessary components is not well understood. Defining the molecular mechanisms of viral PI4KIIIβ hijacking is an important goal in understanding viral replication and could potentially lead to novel therapeutic strategies.

PI4KIIIβ and ACBD3

ACBD3 has been heavily implicated in mediating PI4KIIIβ activation by many picornaviruses, with the viral 3A proteins from Aichivirus, rhinovirus, poliovirus and coxsackieviruses exhibiting direct interactions with ACBD3 (79). However, initial studies examining the effect of ACBD3 siRNA knockdowns on viral replication are ambiguous: ACBD3 is essential for Aichivirus replication (57, 76), non-essential for rhinovirus 14 and coxsackievirus B3 (83, 87), and results are conflicting for poliovirus (77, 79). Our discovery that Aichvirus 3A protein is able to directly activate PI4KIIIβ *in vitro* may explain some of the discrepancies on the role of ACBD3 in viral infection – while our experiments and those previous have not been able to identify a direct interaction, perhaps the presence of viral 3A affects local membrane dynamics or lipid presentation in a manner that enhances catalysis by PI4KIIIβ. It is possible this direct activation does not occur in all picornaviruses, as the sequence of viral 3A proteins does differ even between viral serotypes, which could contribute to the discrepancies in ACBD3 requirement.

Regardless of direct activation, we show a significantly stronger activation of PI4KIIIβ by viral 3A in the presence of ACBD3, which would be present with PI4KIIIβ during infection *in vivo*. Our discovery of the role of the GOLD domain mediating the interaction between viral 3A and ACBD3 in intriguing, as this domain also mediates the recruitment of ACBD3 to the Golgi through an interaction with Giantin (112). The replacement of the normal Giantin interaction provides a potential mechanism of ACBD3 redistribution, and synchronous PI4KIIIβ redistribution, from the Golgi to replication organelles. The non-conserved N-terminal extension of the ACBD3 GOLD domain, which mediates the 3A interaction, explains the specificity of 3A for ACBD3 over other GOLD domain containing proteins.

Recent determination of the X-ray crystal structures of 3A proteins from Aichivirus, rhinovirus 14, poliovirus, enterovirus D68 and enterovirus A71 bound to ACBD3 show that 3A forms a molecular harness around the unique N-terminal extension of the GOLD domain, supporting our initial characterization of this interface (124, 192). Utilizing the PI4KIIIβ-ACBD3 complex disrupting mutants we identified, another group recently showed that the PI4KIIIβ-ACBD3 interaction is required for PI4KIIIβ recruitment to replication organelles and efficient viral replication (123). Further, using full ACBD3 knockout cell lines, they showed that ACBD3 was required for viral replication in all enteroviruses tested – previous ambiguity in the requirement for ACBD3 was in fact due to an incomplete, yet still potent (>90%) siRNA knockdown, with levels still sufficient to facilitate viral replication (123). While our research has contributed to the understanding of the essential role of the viral 3A-ACBD3-PI4KIIIβ complex in mediating picornavirus replication, the binding interfaces of this complex involve flexible regions of proteins and disorder-to-order transitions, and will be challenging to disrupt pharmacologically as an anti-viral strategy.

PI4KIIIβ and c10orf76

While the ACBD3 is required by all enteroviruses for replication, we find that c10orf76 is required for the replication of coxsackievirus A10, and to a lesser extent poliovirus. Our data show coxsackievirus B3 does not depend on c10orf76, which is also observed in coxsackievirus B1 (68).We find that c10orf76-dependent viruses rely on formation of the PI4KIIIβ-c10orf76 complex. Since PI4KIIIβ drives recruitment of c10orf76, and not the reciprocal, the role of this complex in viral replication is unlikely a PI4KIIIβ recruitment mechanism, as is the case with

ACBD3. Intriguingly, GBF1 also plays an important role in the replication of select viruses, namely coxsackievirus B3 and to a lesser extent poliovirus (125, 193). The GBF1-dependence of specific viruses is thought to correlate with the affinity of the specific viral 3A protein for GBF1, with those of high affinity requiring GBF1 (85, 86, 125, 193). The N-terminal part of the 3A proteins from coxsackievirus B3 and poliovirus directly bind to and recruit GBF1 (in addition to ACBD3) but this interaction appears absent in the 3A proteins of rhinoviruses due to subtle amino acid differences (79, 85). Excitingly, our demonstration of the role of the PI4KIIIβ-c10orf76 complex in GBF1 dynamics suggests enterovirus 3A proteins of low GBF1 affinity could still regulate GBF1 on replication organelles by recruiting only the PI4KIIIβ-c10orf76 complex. Essentially, it is possible that all enterovirus 3A proteins bind ACBD3, and some also bind GBF1, recruiting these proteins along with PI4KIIIβ to replication organelles. Enteroviruses with a low 3A-GBF1 affinity cannot recruit GBF1 directly, and instead rely on recruitment of the intact PI4KIIIβ-c10or76 complex to regulate GBF1 at replication organelles. Alternatively, each virus may require a specific threshold level of PI4P for efficient formation of replication complexes or replication organelles, which is disrupted in the absence of the PI4KIIIβ-c10orf76 complex. Further experiments are needed to probe potential recruitment of c10orf76 to replication organelles and its effect on GBF1 activity during viral replication.

5.4 Selective inhibition of human PI4KIIIβ and related lipid kinases

In addition to studying the molecular mechanisms of PI4KIIIβ signalling and hijacking by viruses, directly targeting human and parasite PI4KIIIβs pharmacologically remains an active area of potential therapeutic development. Class I PI3Ks, which are evolutionarily related to PI4KIIIβ, are key targets of cancer therapeutics, and represent the best studied of the lipid kinases in terms of inhibition by small molecules. Successful crystallization of all four class I PI3K isoforms (35–37, 39), together with the recently solved crystal structure of human PI4KIIIβ (38), has revealed the subtle isoform differences mediating inhibitor selectivity and have provided a framework for developing potent and selective PI4KIIIβ inhibitors with anti-viral and anti-parasite potential.

Class I PI3K

Class I PI3Ks play critical roles in cancer, and the first generation of cancer therapeutics targeting these enzymes have recently gained FDA approval (159, 160, 194, 195). PIK3CA is one

of the most frequently mutated oncogenes in human cancer, with high mutation rates observed in several types of cancer including endometrial, breast, bladder, cervical, colorectal and head-and-neck cancers (147). Therefore, understanding the molecular basis of PIK3CA inhibition by novel anti-cancer compounds is a critical goal for cancer therapeutic development. PQR530, a novel anti-cancer compound derived from the phase II drug bimirilisib, contains an additional methyl group that reduces off-target inhibition of PIK3CG (176). Through determination of the co-crystal structure of PIK3CA bound to PQR530, we provide insight into its mechanism of inhibition and specificity. We find PQR530 likely binds with two distinct methyl orientations within PIK3CA. A steric clash in one of these potential binding orientations within PIK3CG caused by Ile881 (V850 in PIK3CA) could not be detected in PIK3CA, suggesting only one potential binding orientation is possible within PIK3CG, which explains the reduced inhibition observed for this isoform.

Human PI4KIIIβ

PI4KIIIβ is closely related to class I PI3Ks, and plays critical roles in viral replication and parasite proliferation. While potent PI4KIIIβ inhibitors have been discovered that act as potent anti-viral agents on numerous RNA viruses (58, 115, 117, 118, 185), development has been limited due to potential immune suppression (114) and toxicity in mice (117). However, some PI4KIIIβ inhibitors are well tolerated in mice (118), and in recent years non-polio enteroviruses have emerged as a threat to public health (81) with no targeted anti-viral treatment available. Key to exploring the potential of PI4KIIIβ inhibitors as anti-viral therapeutics is the development and characterization of more potent and specific inhibitors. Our HDX-MS-aided design of optimized PI4KIIIβ constructs promoted crystallization of the kinase in the absence of an inhibitor, which was only possible with an additional deletion of the disordered 249-287 region present in the original PI4KIIIβ crystal construct (38). We also demonstrated that these engineered truncations do not affect overall PI4KIIIβ structure, as catalytic activity is maintained. Apo PI4KIIIβ crystals allowed for inhibitor soaks and facilitated the determination of the co-crystal structures of PI4KIIIβ bound to either the anti-viral compound **9** or anti-malarial BQR695. Together, these structures reveal that PI4KIIIβ has a more accommodating active site than related PI3Ks, and that PI4KIIIβ selectivity can generally be driven with bulkier inhibitors. Future investigation is necessary to determine whether highly selective inhibitors, such as compound **9**, still elicit toxicity and/or

immunosuppressive effects *in vivo*. Our engineered PI4KIIIβ construct will provide an excellent tool for future characterization of novel PI4KIIIβ inhibitors moving forward.

Parasite PI4Ks

The parasite homologs of PI4KIIIβ are essential for the replication of the malaria and cryptosporidiosis parasites, and are prominent targets for drug development (59, 62). Despite the effectiveness of parasite PI4KIIIβ inhibitors, the molecular basis for their potency and specificity is poorly understood. The anti-malarial BQR695 is a potent *Plasmodium* PI4K inhibitor, however it also inhibits human PI4KIIIβ, indicating the human PI4KIIIβ structure is of limited utility in designing specific anti-parasite compounds. Structural characterization of either the *Plasmodium* or *Cryptosporidium* PI4K active site is a key goal in developing potent parasite PI4K inhibitors that avoid inhibition of human PI4KIIIβ and related PI3Ks. Our HDX-MS analysis reveals significantly longer stretches of disorder in the *P. vivax* and *C. parvum* PI4Ks, which likely explains the failure to obtain diffraction quality crystals of either enzyme thus far. Truncations in disordered regions of *P. vivax* PI4K facilitated the formation of microcrystals bound to the potent anti-malarial KAI407 in complex with *P. falciparum* Rab11. However, these microcrystals were too small to attempt diffraction experiments, and further optimization of crystallization conditions failed to improve crystal quality. In the absence of parasite PI4K structures, we demonstrate our recombinant lipid kinase assays provide an excellent platform for characterizing anti-parasite PI4K inhibitors, evident through our identification of the potent anti-malarial compound BRD73842 as a potent, selective *Plasmodium* PI4K inhibitor. Our initial *P. vivax* PI4K crystals represent progress towards *Plasmodium* PI4K structure determination, and optimization efforts continue in collaboration with Novartis.

5.5 Future Directions

PI4KIIIβ is a critical signalling molecule that exhibits key catalytic and non-catalytic roles through interactions with several protein binding partners at the Golgi. The work of this dissertation has elucidated the molecular mechanisms by which ACBD3 and c10orf76 mediate fundamental PI4KIIIβ functions at the Golgi. Our data, along with others (190), have identified a clear link between PI4KIIIβ recruitment of c10orf76 to the Golgi, and GBF1/Arf1 regulation. Whether c10orf76 indeed forms a direct interaction with GBF1, or this interaction is mediated

through an intermediate factor, remains a prominent question in deciphering the role of c10orf76 in GBF1 regulated Arf1 dynamics. Additionally, while active Arf1 in turn activates PI4KIIIβ at the Golgi to drive PI4P generation (54), a direct interaction has yet to be determined, indicating this regulatory mechanism may be more complex. Further investigation into the mechanisms of the c10orf76-GBF1 and GBF1/Arf1-PI4KIIIβ interactions are required to fully define this signalling axis. Future experiments probing the c10orf76-GBF1 and GBF1/Arf1-PI4KIIIβ interactions could utilize recombinant proteins and HDX-MS analysis, in a similar manner as the work of this dissertation, to identify potential protein-protein interfaces. Engineered complex-disrupting mutations at these interfaces could then be utilized to study the role of these complexes in Golgi homeostasis and PI4P levels *in vivo*.

Host PI4KIIIβ also plays an essential role in the replication of numerous viruses. Our studies have contributed to the understanding that all enteroviruses rely on a direct interaction between the viral 3A protein and host ACBD3 to recruit PI4KIIIβ to replication organelles, a process necessary for viral replication (123, 192). The GBF1 protein is also required for replication in a subset of picornaviruses thought to have high affinity of viral 3A protein for GBF1 (85, 86, 125, 193). The work of this dissertation has revealed that a subset of picornaviruses also require an intact PI4KIIIβ-c10orf76 complex for replication. Taken together with the notion that c10orf76 regulates GBF1, it is possible that picornaviruses with viral 3A proteins that do not bind GBF1 with high affinity require the PI4KIIIβ-c10orf76 complex to elicit GBF1 manipulation. In addition to characterizing affinities of distinct viral 3A proteins for GBF1, future experiments probing c10orf76 recruitment to replication organelles, and the role of c10orf76-GBF1 dynamics on viral replication are necessary to thoroughly explain viral 3A-mediated mechanisms of host protein hijacking.

Finally, the *Plasmodium* and *Cryptosporidium* PI4KIIIβ homologs are prominent targets for pharmaceutical development, and determination of their high-resolution structures would significantly aid medicinal chemistry efforts towards inhibiting these enzymes. Microcrystals of the truncated *Plasmodium* PI4KIIIβ designed with HDX-MS data provide some promise in this endeavor, yet protein stability and yield were limitations for our crystallography-optimized constructs. Future experiments utilizing different expression systems, such as human embryonic kidney (HEK) cells, optimization purification conditions, or even or raising specific nanobodies

as crystallization chaperones (189) could be explored to improve these limitations and potentially lead to high-resolution structure determination of parasite PI4KIIIβs.

5.6 Conclusion

PI4KIIIβ is a critical signalling molecule at the Golgi which regulates PI4P levels and subsequent membrane trafficking, lipid transport, and cell division processes. Understanding the regulation of this kinase thus has significant implications in basic cell biology. The essential role of PI4KIIIβ in the replication of several prominent human viruses and parasites emphasises the importance of also understanding its role in disease to facilitate novel therapeutics. This dissertation has elucidated the molecular basis for the viral 3A-ACBD3-PI4KIIIβ and c10orf76-PI4KIIIβ complexes, and provided insight into their roles in both normal Golgi signalling and the replication of viruses. In addition, characterization of the molecular basis of selective inhibitors of PI4KIIIβ has provided invaluable information to support the future development of novel anti-viral and anti-parasite therapeutics.

Bibliography

1. Di Paolo G, De Camilli P. 2006. Phosphoinositides in cell regulation and membrane dynamics. Nature 443:651–657.
2. Balla T. 2013. Phosphoinositides: Tiny Lipids With Giant Impact on Cell Regulation. Physiological Reviews 93:1019–1137.
3. Sugimoto Y, Whitman M, Cantley LC, Erikson RL. 1984. Evidence that the Rous sarcoma virus transforming gene product phosphorylates phosphatidylinositol and diacylglycerol. Proc Natl Acad Sci U S A 81:2117–2121.
4. Whitman M, Kaplan DR, Schaffhausen B, Cantley L, Roberts TM. 1985. Association of phosphatidylinositol kinase activity with polyoma middle-T competent for transformation. Nature 315:239–242.
5. Hawkins PT, Jackson TR, Stephens LR. 1992. Platelet-derived growth factor stimulates synthesis of Ptdlns(3,4,5)P 3 by activating a Ptdlns(4,5)P 2 3-OH kinase. Nature 358:157–159.
6. Auger KR, Serunian LA, Soltoff SP, Libby P, Cantley LC. 1989. PDGF-dependent tyrosine phosphorylation stimulates production of novel polyphosphoinositides in intact cells. Cell 57:167–175.
7. Stephens LR, Hughes KT, Irvine RF. 1991. Pathway of phosphatidylinositol(3,4,5)-trisphosphate synthesis in activated neutrophils. Nature 351:33–39.
8. Ruderman NB, Kapeller R, White MF, Cantley LC. 1990. Activation of phosphatidylinositol 3-kinase by insulin. Proc Natl Acad Sci U S A 87:1411–1415.
9. Backer JM, Myers MG, Shoelson SE, Chin DJ, Sun XJ, Miralpeix M, Hu P, Margolis B, Skolnik EY, Schlessinger J. 1992. Phosphatidylinositol 3’-kinase is activated by association with IRS-1 during insulin stimulation. EMBO J 11:3469–3479.
10. Cantley LC. 2002. The Phosphoinositide 3-Kinase Pathway. Science 296:1655–1657.
11. Fruman DA, Chiu H, Hopkins BD, Bagrodia S, Cantley LC, Abraham RT. 2017. The PI3K pathway in human disease. Cell 170:605–635.
12. Burke JE, Williams RL. 2015. Synergy in activating class I PI3Ks. Trends in Biochemical Sciences 40:88–100.
13. Ebner M, Lučić I, Leonard TA, Yudushkin I. 2017. PI(3,4,5)P3 Engagement Restricts Akt Activity to Cellular Membranes. Molecular Cell 65:416-431.e6.
14. Bilanges B, Posor Y, Vanhaesebroeck B. 2019. PI3K isoforms in cell signalling and vesicle trafficking. Nature Reviews Molecular Cell Biology 20:515–534.
15. Yu J, Wjasow C, Backer JM. 1998. Regulation of the p85/p110α Phosphatidylinositol 3′-Kinase. Distinct roles for the n-terminal and c-terminal sh2 domains. J Biol Chem 273:30199–30203.

16. Yu J, Zhang Y, McIlroy J, Rordorf-Nikolic T, Orr GA, Backer JM. 1998. Regulation of the p85/p110 Phosphatidylinositol 3′-Kinase: Stabilization and Inhibition of the p110α Catalytic Subunit by the p85 Regulatory Subunit. Mol Cell Biol 18:1379–1387.

17. Miled N, Yan Y, Hon W-C, Perisic O, Zvelebil M, Inbar Y, Schneidman-Duhovny D, Wolfson HJ, Backer JM, Williams RL. 2007. Mechanism of Two Classes of Cancer Mutations in the Phosphoinositide 3-Kinase Catalytic Subunit. Science 317:239–242.

18. Songyang et al. 1993. SH2 domains recognize specific phosphopeptide sequences. Cell 72:767–768.

19. Mandelker D, Gabelli SB, Schmidt-Kittler O, Zhu J, Cheong I, Huang C-H, Kinzler KW, Vogelstein B, Amzel LM. 2009. A frequent kinase domain mutation that changes the interaction between PI3Kα and the membrane. Proc Natl Acad Sci U S A 106:16996–17001.

20. Pacold ME, Suire S, Perisic O, Lara-Gonzalez S, Davis CT, Walker EH, Hawkins PT, Stephens L, Eccleston JF, Williams RL. 2000. Crystal Structure and Functional Analysis of Ras Binding to Its Effector Phosphoinositide 3-Kinase γ. Cell 103:931–944.

21. Siempelkamp BD, Rathinaswamy MK, Jenkins ML, Burke JE. 2017. Molecular mechanism of activation of class IA phosphoinositide 3-kinases (PI3Ks) by membrane-localized HRas. J Biol Chem 292:12256–12266.

22. Fritsch R, de Krijger I, Fritsch K, George R, Reason B, Kumar MS, Diefenbacher M, Stamp G, Downward J. 2013. RAS and RHO Families of GTPases Directly Regulate Distinct Phosphoinositide 3-Kinase Isoforms. Cell 153:1050–1063.

23. Suire S, Coadwell J, Ferguson GJ, Davidson K, Hawkins P, Stephens L. 2005. p84, a New Gβγ-Activated Regulatory Subunit of the Type IB Phosphoinositide 3-Kinase p110γ. Current Biology 15:566–570.

24. Stephens LR, Eguinoa A, Erdjument-Bromage H, Lui M, Cooke F, Coadwell J, Smrcka AS, Thelen M, Cadwallader K, Tempst P, Hawkins PT. 1997. The Gβγ Sensitivity of a PI3K Is Dependent upon a Tightly Associated Adaptor, p101. Cell 89:105–114.

25. Kurig B, Shymanets A, Bohnacker T, Prajwal, Brock C, Ahmadian MR, Schaefer M, Gohla A, Harteneck C, Wymann MP, Jeanclos E, Nürnberg B. 2009. Ras is an indispensable coregulator of the class IB phosphoinositide 3-kinase p87/p110γ. Proc Natl Acad Sci U S A 106:20312–20317.

26. Maier U, Babich A, Nürnberg B. 1999. Roles of Non-catalytic Subunits in Gβγ-induced Activation of Class I Phosphoinositide 3-Kinase Isoforms β and γ. J Biol Chem 274:29311–29317.

27. Knight ZA, Gonzalez B, Feldman ME, Zunder ER, Goldenberg DD, Williams O, Loewith R, Stokoe D, Balla A, Toth B, Balla T, Weiss WA, Williams RL, Shokat KM. 2006. A Pharmacological Map of the PI3-K Family Defines a Role for p110α in Insulin Signaling. Cell 125:733–747.

28. Jackson SP, Schoenwaelder SM, Goncalves I, Nesbitt WS, Yap CL, Wright CE, Kenche V, Anderson KE, Dopheide SM, Yuan Y, Sturgeon SA, Prabaharan H, Thompson PE,

Smith GD, Shepherd PR, Daniele N, Kulkarni S, Abbott B, Saylik D, Jones C, Lu L, Giuliano S, Hughan SC, Angus JA, Robertson AD, Salem HH. 2005. PI 3-kinase p110β: a new target for antithrombotic therapy. Nature Medicine 11:507–514.

29. Okkenhaug K, Bilancio A, Farjot G, Priddle H, Sancho S, Peskett E, Pearce W, Meek SE, Salpekar A, Waterfield MD, Smith AJH, Vanhaesebroeck B. 2002. Impaired B and T Cell Antigen Receptor Signaling in p110δ PI 3-Kinase Mutant Mice. Science 297:1031–1034.

30. Ji H, Rintelen F, Waltzinger C, Bertschy Meier D, Bilancio A, Pearce W, Hirsch E, Wymann MP, Rückle T, Camps M, Vanhaesebroeck B, Okkenhaug K, Rommel C. 2007. Inactivation of PI3Kγ and PI3Kδ distorts T-cell development and causes multiple organ inflammation. Blood 110:2940–2947.

31. Kim M-S, Rådinger M, Gilfillan AM. 2008. The multiple roles of phosphoinositide 3-kinase in mast cell biology. Trends Immunol 29:493–501.

32. Li Z. 2000. Roles of PLC-2 and -3 and PI3K in Chemoattractant-Mediated Signal Transduction. Science 287:1046–1049.

33. Okkenhaug K. 2013. Signaling by the Phosphoinositide 3-Kinase Family in Immune Cells. Annu Rev Immunol 31:675–704.

34. Walker EH, Perisic O, Ried C, Stephens L, Williams RL. 1999. Structural insights into phosphoinositide 3-kinase catalysis and signalling. Nature 402:313–320.

35. Walker EH, Pacold ME, Perisic O, Stephens L, Hawkins PT, Wymann MP, Williams RL. 2000. Structural Determinants of Phosphoinositide 3-Kinase Inhibition by Wortmannin, LY294002, Quercetin, Myricetin, and Staurosporine. Molecular Cell 6:909–919.

36. Huang C-H, Mandelker D, Schmidt-Kittler O, Samuels Y, Velculescu VE, Kinzler KW, Vogelstein B, Gabelli SB, Amzel LM. 2007. The Structure of a Human p110α/p85α Complex Elucidates the Effects of Oncogenic PI3Kα Mutations. Science 318:1744–1748.

37. Zhang X, Vadas O, Perisic O, Anderson KE, Clark J, Hawkins PT, Stephens LR, Williams RL. 2011. Structure of Lipid Kinase p110β/p85β Elucidates an Unusual SH2-Domain-Mediated Inhibitory Mechanism. Molecular Cell 41:567–578.

38. Burke JE, Inglis AJ, Perisic O, Masson GR, McLaughlin SH, Rutaganira F, Shokat KM, Williams RL. 2014. Structures of PI4KIIIβ complexes show simultaneous recruitment of Rab11 and its effectors. Science 344:1035–1038.

39. Berndt A, Miller S, Williams O, Le DD, Houseman BT, Pacold JI, Gorrec F, Hon W-C, Liu Y, Rommel C, Gaillard P, Ruckle T, Schwarz MK, Shokat KM, Shaw JP, Williams RL. 2010. The p110δ crystal structure uncovers mechanisms for selectivity and potency of novel PI3K inhibitors. Nat Chem Biol 6:117–124.

40. Lees JA, Zhang Y, Oh MS, Schauder CM, Yu X, Baskin JM, Dobbs K, Notarangelo LD, De Camilli P, Walz T, Reinisch KM. 2017. Architecture of the human PI4KIIIα lipid kinase complex. Proc Natl Acad Sci U S A 114:13720–13725.

41. Vadas O, Burke JE, Zhang X, Berndt A, Williams RL. 2011. Structural Basis for Activation and Inhibition of Class I Phosphoinositide 3-Kinases. Sci Signal 4:re2–re2.

42. Miller S, Tavshanjian B, Oleksy A, Perisic O, Houseman BT, Shokat KM, Williams RL. 2010. Shaping Development of Autophagy Inhibitors with the Structure of the Lipid Kinase Vps34. Science 327:1638–1642.

43. Boura E, Nencka R. 2015. Phosphatidylinositol 4-kinases: Function, structure, and inhibition. Experimental Cell Research 337:136–145.

44. Dornan GL, McPhail JA, Burke JE. 2016. Type III phosphatidylinositol 4 kinases: structure, function, regulation, signalling and involvement in disease. Biochem Soc Trans 44:260–266.

45. Burke JE. 2018. Structural Basis for Regulation of Phosphoinositide Kinases and Their Involvement in Human Disease. Molecular Cell 71:653–673.

46. Mesmin B, Bigay J, Polidori J, Jamecna D, Lacas-Gervais S, Antonny B. 2017. Sterol transfer, PI4P consumption, and control of membrane lipid order by endogenous OSBP. EMBO J 36:3156–3174.

47. Lu D, Sun H, Wang H, Barylko B, Fukata Y, Fukata M, Albanesi JP, Yin HL. 2012. Phosphatidylinositol 4-kinase IIα is palmitoylated by Golgi-localized palmitoyltransferases in cholesterol-dependent manner. J Biol Chem 287:21856–21865.

48. Klima M, Tóth DJ, Hexnerova R, Baumlova A, Chalupska D, Tykvart J, Rezabkova L, Sengupta N, Man P, Dubankova A, Humpolickova J, Nencka R, Veverka V, Balla T, Boura E. 2016. Structural insights and in vitro reconstitution of membrane targeting and activation of human PI4KB by the ACBD3 protein. Scientific Reports 6:23641.

49. McPhail JA, Ottosen EH, Jenkins ML, Burke JE. 2017. The Molecular Basis of Aichi Virus 3A Protein Activation of Phosphatidylinositol 4 Kinase IIIβ, PI4KB, through ACBD3. Structure 25:121–131.

50. Flanagan CA, Schnieders EA, Emerick AW, Kunisawa R, Admon A, Thorner J. 1993. Phosphatidylinositol 4-kinase: gene structure and requirement for yeast cell viability. Science 262:1444–1448.

51. Balla T, Downing GJ, Jaffe H, Kim S, Zólyomi A, Catt KJ. 1997. Isolation and Molecular Cloning of Wortmannin-sensitive Bovine Type III Phosphatidylinositol 4-Kinases. J Biol Chem 272:18358–18366.

52. Meyers R, Cantley LC. 1997. Cloning and Characterization of a Wortmannin-sensitive Human Phosphatidylinositol 4-Kinase. J Biol Chem 272:4384–4390.

53. Polevoy G, Wei H-C, Wong R, Szentpetery Z, Kim YJ, Goldbach P, Steinbach SK, Balla T, Brill JA. 2009. Dual roles for the Drosophila PI 4-kinase Four wheel drive in localizing Rab11 during cytokinesis. The Journal of Cell Biology 187:847–858.

54. Godi A, Pertile P, Meyers R, Marra P, Tullio GD, Iurisci C, Luini A, Corda D, Matteis MAD. 1999. ARF mediates recruitment of PtdIns-4-OH kinase- β and stimulates synthesis of PtdIns(4,5)P 2 on the Golgi complex. Nat Cell Biol 1:280–287.

55. Tóth B, Balla A, Ma H, Knight ZA, Shokat KM, Balla T. 2006. Phosphatidylinositol 4-Kinase IIIβ Regulates the Transport of Ceramide between the Endoplasmic Reticulum and Golgi. J Biol Chem 281:36369–36377.

56. Greninger AL, Knudsen GM, Betegon M, Burlingame AL, DeRisi JL. 2013. ACBD3 Interaction with TBC1 Domain 22 Protein Is Differentially Affected by Enteroviral and Kobuviral 3A Protein Binding. mBio 4:e00098-13.

57. Sasaki J, Ishikawa K, Arita M, Taniguchi K. 2012. ACBD3-mediated recruitment of PI4KB to picornavirus RNA replication sites. The EMBO Journal 31:754–766.

58. Hsu N-Y, Ilnytska O, Belov G, Santiana M, Chen Y-H, Takvorian PM, Pau C, van der Schaar H, Kaushik-Basu N, Balla T, Cameron CE, Ehrenfeld E, van Kuppeveld FJM, Altan-Bonnet N. 2010. Viral Reorganization of the Secretory Pathway Generates Distinct Organelles for RNA Replication. Cell 141:799–811.

59. Manjunatha UH, Vinayak S, Zambriski JA, Chao AT, Sy T, Noble CG, Bonamy GMC, Kondreddi RR, Zou B, Gedeck P, Brooks CF, Herbert GT, Sateriale A, Tandel J, Noh S, Lakshminarayana SB, Lim SH, Goodman LB, Bodenreider C, Feng G, Zhang L, Blasco F, Wagner J, Leong FJ, Striepen B, Diagana TT. 2017. A Cryptosporidium PI(4)K inhibitor is a drug candidate for cryptosporidiosis. Nature 546:376–380.

60. Paquet T, Le Manach C, Cabrera DG, Younis Y, Henrich PP, Abraham TS, Lee MCS, Basak R, Ghidelli-Disse S, Lafuente-Monasterio MJ, Bantscheff M, Ruecker A, Blagborough AM, Zakutansky SE, Zeeman A-M, White KL, Shackleford DM, Mannila J, Morizzi J, Scheurer C, Angulo-Barturen I, Martínez MS, Ferrer S, Sanz LM, Gamo FJ, Reader J, Botha M, Dechering KJ, Sauerwein RW, Tungtaeng A, Vanachayangkul P, Lim CS, Burrows J, Witty MJ, Marsh KC, Bodenreider C, Rochford R, Solapure SM, Jiménez-Díaz MB, Wittlin S, Charman SA, Donini C, Campo B, Birkholtz L-M, Hanson KK, Drewes G, Kocken CHM, Delves MJ, Leroy D, Fidock DA, Waterson D, Street LJ, Chibale K. 2017. Antimalarial efficacy of MMV390048, an inhibitor of Plasmodium phosphatidylinositol 4-kinase. Sci Transl Med 9.

61. Kato N, Comer E, Sakata-Kato T, Sharma A, Sharma M, Maetani M, Bastien J, Brancucci NM, Bittker JA, Corey V, Clarke D, Derbyshire ER, Dornan GL, Duffy S, Eckley S, Itoe MA, Koolen KMJ, Lewis TA, Lui PS, Lukens AK, Lund E, March S, Meibalan E, Meier BC, McPhail JA, Mitasev B, Moss EL, Sayes M, Van Gessel Y, Wawer MJ, Yoshinaga T, Zeeman A-M, Avery VM, Bhatia SN, Burke JE, Catteruccia F, Clardy JC, Clemons PA, Dechering KJ, Duvall JR, Foley MA, Gusovsky F, Kocken CHM, Marti M, Morningstar ML, Munoz B, Neafsey DE, Sharma A, Winzeler EA, Wirth DF, Scherer CA, Schreiber SL. 2016. Diversity-oriented synthesis yields novel multistage antimalarial inhibitors. Nature 538:344–349.

62. McNamara CW, Lee MCS, Lim CS, Lim SH, Roland J, Nagle A, Simon O, Yeung BKS, Chatterjee AK, McCormack SL, Manary MJ, Zeeman A-M, Dechering KJ, Kumar TRS, Henrich PP, Gagaring K, Ibanez M, Kato N, Kuhen KL, Fischli C, Rottmann M, Plouffe DM, Bursulaya B, Meister S, Rameh L, Trappe J, Haasen D, Timmerman M, Sauerwein RW, Suwanarusk R, Russell B, Renia L, Nosten F, Tully DC, Kocken CHM, Glynne RJ, Bodenreider C, Fidock DA, Diagana TT, Winzeler EA. 2013. Targeting Plasmodium PI(4)K to eliminate malaria. Nature 504:248–253.

63. D'Angelo G, Uemura T, Chuang C-C, Polishchuk E, Santoro M, Ohvo-Rekilä H, Sato T, Di Tullio G, Varriale A, D'Auria S, Daniele T, Capuani F, Johannes L, Mattjus P, Monti M, Pucci P, Williams RL, Burke JE, Platt FM, Harada A, De Matteis MA. 2013. Vesicular

and non-vesicular transport feed distinct glycosylation pathways in the Golgi. Nature 501:116–120.

64. Mesmin B, Bigay J, Moser von Filseck J, Lacas-Gervais S, Drin G, Antonny B. 2013. A Four-Step Cycle Driven by PI(4)P Hydrolysis Directs Sterol/PI(4)P Exchange by the ER-Golgi Tether OSBP. Cell 155:830–843.

65. Rahajeng J, Kuna RS, Makowski SL, Tran TTT, Buschman MD, Li S, Cheng N, Ng MM, Field SJ. 2019. Efficient Golgi Forward Trafficking Requires GOLPH3-Driven, PI4P-Dependent Membrane Curvature. Developmental Cell 50:573-585.e5.

66. Dippold HC, Ng MM, Farber-Katz SE, Lee S-K, Kerr ML, Peterman MC, Sim R, Wiharto PA, Galbraith KA, Madhavarapu S, Fuchs GJ, Meerloo T, Farquhar MG, Zhou H, Field SJ. 2009. GOLPH3 Bridges Phosphatidylinositol-4- Phosphate and Actomyosin to Stretch and Shape the Golgi to Promote Budding. Cell 139:337–351.

67. de Graaf P, Zwart WT, van Dijken RAJ, Deneka M, Schulz TKF, Geijsen N, Coffer PJ, Gadella BM, Verkleij AJ, van der Sluijs P, van Bergen en Henegouwen PMP. 2004. Phosphatidylinositol 4-Kinaseβ Is Critical for Functional Association of rab11 with the Golgi Complex. MBoC 15:2038–2047.

68. Blomen VA, Májek P, Jae LT, Bigenzahn JW, Nieuwenhuis J, Staring J, Sacco R, Diemen FR van, Olk N, Stukalov A, Marceau C, Janssen H, Carette JE, Bennett KL, Colinge J, Superti-Furga G, Brummelkamp TR. 2015. Gene essentiality and synthetic lethality in haploid human cells. Science 350:1092–1096.

69. Chalupska D, Eisenreichova A, Różycki B, Rezabkova L, Humpolickova J, Klima M, Boura E. 2017. Structural analysis of phosphatidylinositol 4-kinase IIIβ (PI4KB) – 14-3-3 protein complex reveals internal flexibility and explains 14-3-3 mediated protection from degradation in vitro. Journal of Structural Biology 200:36–44.

70. Valente C, Turacchio G, Mariggiò S, Pagliuso A, Gaibisso R, Di Tullio G, Santoro M, Formiggini F, Spanò S, Piccini D, Polishchuk RS, Colanzi A, Luini A, Corda D. 2012. A 14-3-3γ dimer-based scaffold bridges CtBP1-S/BARS to PI(4)KIIIβ to regulate post-Golgi carrier formation. Nature Cell Biology 14:343–354.

71. Hausser A, Storz P, Märtens S, Link G, Toker A, Pfizenmaier K. 2005. Protein kinase D regulates vesicular transport by phosphorylating and activating phosphatidylinositol-4 kinase IIIβ at the Golgi complex. Nat Cell Biol 7:880–886.

72. Ile KE, Schaaf G, Bankaitis VA. 2006. Phosphatidylinositol transfer proteins and cellular nanoreactors for lipid signaling. Nature Chemical Biology 2:576–583.

73. Schaaf G, Ortlund EA, Tyeryar KR, Mousley CJ, Ile KE, Garrett TA, Ren J, Woolls MJ, Raetz CRH, Redinbo MR, Bankaitis VA. 2008. Functional Anatomy of Phospholipid Binding and Regulation of Phosphoinositide Homeostasis by Proteins of the Sec14 Superfamily. Molecular Cell 29:191–206.

74. Altan-Bonnet N, Balla T. 2012. Phosphatidylinositol 4-kinases: hostages harnessed to build panviral replication platforms. Trends in Biochemical Sciences 37:293–302.

75. van der Schaar HM, Dorobantu CM, Albulescu L, Strating JRPM, van Kuppeveld FJM. 2016. Fat(al) attraction: Picornaviruses Usurp Lipid Transfer at Membrane Contact Sites to Create Replication Organelles. Trends in Microbiology 24:535–546.

76. Ishikawa-Sasaki K, Sasaki J, Taniguchi K. 2014. A Complex Comprising Phosphatidylinositol 4-Kinase III , ACBD3, and Aichi Virus Proteins Enhances Phosphatidylinositol 4-Phosphate Synthesis and Is Critical for Formation of the Viral Replication Complex. Journal of Virology 88:6586–6598.

77. Téoulé F, Brisac C, Pelletier I, Vidalain P-O, Jégouic S, Mirabelli C, Bessaud M, Combelas N, Autret A, Tangy F, Delpeyroux F, Blondel B. 2013. The Golgi Protein ACBD3, an Interactor for Poliovirus Protein 3A, Modulates Poliovirus Replication. Journal of Virology 87:11031–11046.

78. Tapparel C, Siegrist F, Petty TJ, Kaiser L. 2013. Picornavirus and enterovirus diversity with associated human diseases. Infection, Genetics and Evolution 14:282–293.

79. Greninger AL, Knudsen GM, Betegon M, Burlingame AL, DeRisi JL. 2012. The 3A Protein from Multiple Picornaviruses Utilizes the Golgi Adaptor Protein ACBD3 To Recruit PI4KIIIβ. Journal of Virology 86:3605–3616.

80. Ilnytska O, Santiana M, Hsu N-Y, Du W-L, Chen Y-H, Viktorova EG, Belov G, Brinker A, Storch J, Moore C, Dixon JL, Altan-Bonnet N. 2013. Enteroviruses Harness the Cellular Endocytic Machinery to Remodel the Host Cell Cholesterol Landscape for Effective Viral Replication. Cell Host & Microbe 14:281–293.

81. CDC. 2019. Acute Flaccid Myelitis (AFM) Cases in the U.S. Centers for Disease Control and Prevention.

82. Xiao X, Lei X, Zhang Z, Ma Y, Qi J, Wu C, Xiao Y, Li L, He B, Wang J. 2017. Enterovirus 3A Facilitates Viral Replication by Promoting Phosphatidylinositol 4-Kinase IIIβ-ACBD3 Interaction. J Virol 91.

83. Dorobantu CM, van der Schaar HM, Ford LA, Strating JRPM, Ulferts R, Fang Y, Belov G, van Kuppeveld FJM, Sandri-Goldin RM. 2014. Recruitment of PI4KIIIβ to Coxsackievirus B3 Replication Organelles Is Independent of ACBD3, GBF1, and Arf1. Journal of Virology 88:2725–2736.

84. Dorobantu CM, Albulescu L, Harak C, Feng Q, Kampen M van, Strating JRPM, Gorbalenya AE, Lohmann V, Schaar HM van der, Kuppeveld FJM van. 2015. Modulation of the Host Lipid Landscape to Promote RNA Virus Replication: The Picornavirus Encephalomyocarditis Virus Converges on the Pathway Used by Hepatitis C Virus. PLOS Pathogens 11:e1005185.

85. Wessels E, Duijsings D, Lanke KHW, Dooren SHJ van, Jackson CL, Melchers WJG, Kuppeveld FJM van. 2006. Effects of Picornavirus 3A Proteins on Protein Transport and GBF1-Dependent COP-I Recruitment. Journal of Virology 80:11852–11860.

86. Wessels E, Duijsings D, Niu T-K, Neumann S, Oorschot VM, de Lange F, Lanke KHW, Klumperman J, Henke A, Jackson CL, Melchers WJG, van Kuppeveld FJM. 2006. A Viral Protein that Blocks Arf1-Mediated COP-I Assembly by Inhibiting the Guanine Nucleotide Exchange Factor GBF1. Developmental Cell 11:191–201.

87. Dorobantu CM, Ford-Siltz LA, Sittig SP, Lanke KHW, Belov GA, Kuppeveld FJM van, Schaar HM van der. 2015. GBF1- and ACBD3-Independent Recruitment of PI4KIIIβ to Replication Sites by Rhinovirus 3A Proteins. Journal of Virology 89:1913–1918.

88. Jović M, Kean MJ, Szentpetery Z, Polevoy G, Gingras A-C, Brill JA, Balla T. 2012. Two phosphatidylinositol 4-kinases control lysosomal delivery of the Gaucher disease enzyme, β-glucocerebrosidase. MBoC 23:1533–1545.

89. Ashley EA, Dhorda M, Fairhurst RM, Amaratunga C, Lim P, Suon S, Sreng S, Anderson JM, Mao S, Sam B, Sopha C, Chuor CM, Nguon C, Sovannaroth S, Pukrittayakamee S, Jittamala P, Chotivanich K, Chutasmit K, Suchatsoonthorn C, Runcharoen R, Hien TT, Thuy-Nhien NT, Thanh NV, Phu NH, Htut Y, Han K-T, Aye KH, Mokuolu OA, Olaosebikan RR, Folaranmi OO, Mayxay M, Khanthavong M, Hongvanthong B, Newton PN, Onyamboko MA, Fanello CI, Tshefu AK, Mishra N, Valecha N, Phyo AP, Nosten F, Yi P, Tripura R, Borrmann S, Bashraheil M, Peshu J, Faiz MA, Ghose A, Hossain MA, Samad R, Rahman MR, Hasan MM, Islam A, Miotto O, Amato R, MacInnis B, Stalker J, Kwiatkowski DP, Bozdech Z, Jeeyapant A, Cheah PY, Sakulthaew T, Chalk J, Intharabut B, Silamut K, Lee SJ, Vihokhern B, Kunasol C, Imwong M, Tarning J, Taylor WJ, Yeung S, Woodrow CJ, Flegg JA, Das D, Smith J, Venkatesan M, Plowe CV, Stepniewska K, Guerin PJ, Dondorp AM, Day NP, White NJ. 2014. Spread of Artemisinin Resistance in Plasmodium falciparum Malaria. N Engl J Med 371:411–423.

90. Vale N, Moreira R, Gomes P. 2009. Primaquine revisited six decades after its discovery. European Journal of Medicinal Chemistry 44:937–953.

91. Robert X, Gouet P. 2014. Deciphering key features in protein structures with the new ENDscript server. Nucleic Acids Res 42:W320–W324.

92. Hausser A, Link G, Hoene M, Russo C, Selchow O, Pfizenmaier K. 2006. Phospho-specific binding of 14-3-3 proteins to phosphatidylinositol 4-kinase III β protects from dephosphorylation and stabilizes lipid kinase activity. J Cell Sci 119:3613–3621.

93. Reiss S, Rebhan I, Backes P, Romero-Brey I, Erfle H, Matula P, Kaderali L, Poenisch M, Blankenburg H, Hiet M-S, Longerich T, Diehl S, Ramirez F, Balla T, Rohr K, Kaul A, Bühler S, Pepperkok R, Lengauer T, Albrecht M, Eils R, Schirmacher P, Lohmann V, Bartenschlager R. 2011. Recruitment and Activation of a Lipid Kinase by Hepatitis C Virus NS5A Is Essential for Integrity of the Membranous Replication Compartment. Cell Host & Microbe 9:32–45.

94. Arita M. 2016. Mechanism of Poliovirus Resistance to Host Phosphatidylinositol-4 Kinase III β Inhibitor. ACS Infect Dis 2:140–148.

95. van der Schaar HM, van der Linden L, Lanke KHW, Strating JRPM, Pürstinger G, de Vries E, de Haan CAM, Neyts J, van Kuppeveld FJM. 2012. Coxsackievirus mutants that can bypass host factor PI4KIIIβ and the need for high levels of PI4P lipids for replication. Cell Res 22:1576–1592.

96. Burke JE, Perisic O, Masson GR, Vadas O, Williams RL. 2012. Oncogenic mutations mimic and enhance dynamic events in the natural activation of phosphoinositide 3-kinase p110α (PIK3CA). PNAS 109:15259–15264.

97. Fowler ML, McPhail JA, Jenkins ML, Masson GR, Rutaganira FU, Shokat KM, Williams RL, Burke JE. 2016. Using hydrogen deuterium exchange mass spectrometry to engineer optimized constructs for crystallization of protein complexes: Case study of PI4KIIIβ with Rab11. Protein Science 25:826–839.

98. Battye TGG, Kontogiannis L, Johnson O, Powell HR, Leslie AGW. 2011. iMOSFLM: a new graphical interface for diffraction-image processing with MOSFLM. Acta Cryst D 67:271–281.

99. Evans PR, Murshudov GN. 2013. How good are my data and what is the resolution? Acta Cryst D 69:1204–1214.

100. Strong M, Sawaya MR, Wang S, Phillips M, Cascio D, Eisenberg D. 2006. Toward the structural genomics of complexes: Crystal structure of a PE/PPE protein complex from Mycobacterium tuberculosis. PNAS 103:8060–8065.

101. McCoy AJ, Grosse-Kunstleve RW, Adams PD, Winn MD, Storoni LC, Read RJ. 2007. Phaser crystallographic software. J Appl Cryst 40:658–674.

102. Zwart PH, Afonine PV, Grosse-Kunstleve RW, Hung L-W, Ioerger TR, McCoy AJ, McKee E, Moriarty NW, Read RJ, Sacchettini JC, Sauter NK, Storoni LC, Terwilliger TC, Adams PD. 2008. Automated Structure Solution with the PHENIX Suite, p. 419–435. *In* Kobe, B, Guss, M, Huber, T (eds.), Structural Proteomics: High-Throughput Methods. Humana Press, Totowa, NJ.

103. Emsley P, Cowtan K. 2004. Coot: model-building tools for molecular graphics. Acta Cryst D 60:2126–2132.

104. Afonine PV, Grosse-Kunstleve RW, Echols N, Headd JJ, Moriarty NW, Mustyakimov M, Terwilliger TC, Urzhumtsev A, Zwart PH, Adams PD. 2012. Towards automated crystallographic structure refinement with phenix.refine. Acta Cryst D 68:352–367.

105. McDonold CM, Fromme JC. 2014. Four GTPases Differentially Regulate the Sec7 Arf-GEF to Direct Traffic at the trans-Golgi Network. Developmental Cell 30:759–767.

106. Harrison RA, Engen JR. 2016. Conformational insight into multi-protein signaling assemblies by hydrogen–deuterium exchange mass spectrometry. Current Opinion in Structural Biology 41:187–193.

107. Vadas O, Burke JE. 2015. Probing the dynamic regulation of peripheral membrane proteins using hydrogen deuterium exchange–MS (HDX–MS). Biochem Soc Trans 43:773–786.

108. Gallagher ES, Hudgens JW. 2016. Chapter Fourteen - Mapping Protein–Ligand Interactions with Proteolytic Fragmentation, Hydrogen/Deuterium Exchange-Mass Spectrometry, p. 357–404. *In* Kelman, Z (ed.), Methods in Enzymology. Academic Press.

109. Masson GR, Perisic O, Burke JE, Williams RL. 2016. The intrinsically disordered tails of PTEN and PTEN-L have distinct roles in regulating substrate specificity and membrane activity. Biochem J 473:135–144.

110. Christen M, Marcaida MJ, Lamprakis C, Aeschimann W, Vaithilingam J, Schneider P, Hilbert M, Schneider G, Cascella M, Stocker A. 2015. Structural insights on cholesterol

endosynthesis: Binding of squalene and 2,3-oxidosqualene to supernatant protein factor. Journal of Structural Biology 190:261–270.

111. Anantharaman V, Aravind L. 2002. The GOLD domain, a novel protein module involved in Golgi function and secretion. Genome Biology 3:research0023.1.

112. Sohda M, Misumi Y, Yamamoto A, Yano A, Nakamura N, Ikehara Y. 2001. Identification and Characterization of a Novel Golgi Protein, GCP60, That Interacts with the Integral Membrane Protein Giantin. J Biol Chem 276:45298–45306.

113. Fan J, Liu J, Culty M, Papadopoulos V. 2010. Acyl-coenzyme A binding domain containing 3 (ACBD3; PAP7; GCP60): An emerging signaling molecule. Progress in Lipid Research 49:218–234.

114. LaMarche MJ, Borawski J, Bose A, Capacci-Daniel C, Colvin R, Dennehy M, Ding J, Dobler M, Drumm J, Gaither LA, Gao J, Jiang X, Lin K, McKeever U, Puyang X, Raman P, Thohan S, Tommasi R, Wagner K, Xiong X, Zabawa T, Zhu S, Wiedmann B. 2012. Anti-Hepatitis C Virus Activity and Toxicity of Type III Phosphatidylinositol-4-Kinase Beta Inhibitors. Antimicrobial Agents and Chemotherapy 56:5149–5156.

115. Mejdrová I, Chalupská D, Kögler M, Šála M, Plačková P, Baumlová A, Hřebabecký H, Procházková E, Dejmek M, Guillon R, Strunin D, Weber J, Lee G, Birkus G, Mertlíková-Kaiserová H, Boura E, Nencka R. 2015. Highly Selective Phosphatidylinositol 4-Kinase IIIβ Inhibitors and Structural Insight into Their Mode of Action. J Med Chem 58:3767–3793.

116. Rutaganira FU, Fowler ML, McPhail JA, Gelman MA, Nguyen K, Xiong A, Dornan GL, Tavshanjian B, Glenn JS, Shokat KM, Burke JE. 2016. Design and Structural Characterization of Potent and Selective Inhibitors of Phosphatidylinositol 4 Kinase IIIβ. J Med Chem 59:1830–1839.

117. Spickler C, Lippens J, Laberge M-K, Desmeules S, Bellavance É, Garneau M, Guo T, Hucke O, Leyssen P, Neyts J, Vaillancourt FH, Décor A, O'Meara J, Franti M, Gauthier A. 2013. Phosphatidylinositol 4-Kinase III Beta Is Essential for Replication of Human Rhinovirus and Its Inhibition Causes a Lethal Phenotype In Vivo. Antimicrobial Agents and Chemotherapy 57:3358–3368.

118. van der Schaar HM, Leyssen P, Thibaut HJ, Palma A de, Linden L van der, Lanke KHW, Lacroix C, Verbeken E, Conrath K, MacLeod AM, Mitchell DR, Palmer NJ, Poël H van de, Andrews M, Neyts J, Kuppeveld FJM van. 2013. A Novel, Broad-Spectrum Inhibitor of Enterovirus Replication That Targets Host Cell Factor Phosphatidylinositol 4-Kinase IIIβ. Antimicrobial Agents and Chemotherapy 57:4971–4981.

119. Tan J, Brill JA. 2014. Cinderella story: PI4P goes from precursor to key signaling molecule. Critical Reviews in Biochemistry and Molecular Biology 49:33–58.

120. Weber SS, Ragaz C, Reus K, Nyfeler Y, Hilbi H. 2006. Legionella pneumophila Exploits PI(4)P to Anchor Secreted Effector Proteins to the Replicative Vacuole. PLOS Pathogens 2:e46.

121. Isobe K, Jung HJ, Yang C-R, Claxton J, Sandoval P, Burg MB, Raghuram V, Knepper MA. 2017. Systems-level identification of PKA-dependent signaling in epithelial cells. Proc Natl Acad Sci USA 114:E8875–E8884.

122. Szivak I, Lamb N, Heilmeyer LMG. 2006. Subcellular Localization and Structural Function of Endogenous Phosphorylated Phosphatidylinositol 4-Kinase (PI4K92). J Biol Chem 281:16740–16749.

123. Lyoo H, Schaar HM van der, Dorobantu CM, Rabouw HH, Strating JRPM, Kuppeveld FJM van. 2019. ACBD3 Is an Essential Pan-enterovirus Host Factor That Mediates the Interaction between Viral 3A Protein and Cellular Protein PI4KB. mBio 10.

124. Klima M, Chalupska D, Różycki B, Humpolickova J, Rezabkova L, Silhan J, Baumlova A, Dubankova A, Boura E. 2017. Kobuviral Non-structural 3A Proteins Act as Molecular Harnesses to Hijack the Host ACBD3 Protein. Structure 25:219–230.

125. Lanke KHW, van der Schaar HM, Belov GA, Feng Q, Duijsings D, Jackson CL, Ehrenfeld E, van Kuppeveld FJM. 2009. GBF1, a guanine nucleotide exchange factor for Arf, is crucial for coxsackievirus B3 RNA replication. J Virol 83:11940–11949.

126. Slice LW, Taylor SS. 1989. Expression of the catalytic subunit of cAMP-dependent protein kinase in Escherichia coli. J Biol Chem 264:20940–20946.

127. Sievers F, Wilm A, Dineen D, Gibson TJ, Karplus K, Li W, Lopez R, McWilliam H, Remmert M, Söding J, Thompson JD, Higgins DG. 2011. Fast, scalable generation of high-quality protein multiple sequence alignments using Clustal Omega. Molecular Systems Biology 7:539.

128. Gibson DG, Young L, Chuang R-Y, Venter JC, Hutchison CA, Smith HO. 2009. Enzymatic assembly of DNA molecules up to several hundred kilobases. Nature Methods 6:343–345.

129. Varnai P, Thyagarajan B, Rohacs T, Balla T. 2006. Rapidly inducible changes in phosphatidylinositol 4,5-bisphosphate levels influence multiple regulatory functions of the lipid in intact living cells. J Cell Biol 175:377–382.

130. Csordás G, Várnai P, Golenár T, Roy S, Purkins G, Schneider TG, Balla T, Hajnóczky G. 2010. Imaging Interorganelle Contacts and Local Calcium Dynamics at the ER-Mitochondrial Interface. Molecular Cell 39:121–132.

131. Hunyady L, Baukal AJ, Gáborik Z, Olivares-Reyes JA, Bor M, Szaszák M, Lodge R, Catt KJ, Balla T. 2002. Differential PI 3-kinase dependence of early and late phases of recycling of the internalized AT1 angiotensin receptor. The Journal of Cell Biology 157:1211–1222.

132. Schindelin J, Arganda-Carreras I, Frise E, Kaynig V, Longair M, Pietzsch T, Preibisch S, Rueden C, Saalfeld S, Schmid B, Tinevez J-Y, White DJ, Hartenstein V, Eliceiri K, Tomancak P, Cardona A. 2012. Fiji: an open-source platform for biological-image analysis. Nature Methods 9:676–682.

133. Wessels E, Duijsings D, Notebaart RA, Melchers WJG, Kuppeveld FJM van. 2005. A Proline-Rich Region in the Coxsackievirus 3A Protein Is Required for the Protein To Inhibit Endoplasmic Reticulum-to-Golgi Transport. Journal of Virology 79:5163–5173.

134. Hammond GRV, Schiavo G, Irvine RF. 2009. Immunocytochemical techniques reveal multiple, distinct cellular pools of PtdIns4P and PtdIns(4,5)P2. Biochem J 422:23–35.

135. Hornbeck PV, Zhang B, Murray B, Kornhauser JM, Latham V, Skrzypek E. 2015. PhosphoSitePlus, 2014: mutations, PTMs and recalibrations. Nucleic Acids Res 43:D512–D520.

136. Ward DG, Ashton PR, Trayer HR, Trayer IP. 2001. Additional PKA phosphorylation sites in human cardiac troponin I. European Journal of Biochemistry 268:179–185.

137. Marx SO, Reiken S, Hisamatsu Y, Jayaraman T, Burkhoff D, Rosemblit N, Marks AR. 2000. PKA Phosphorylation Dissociates FKBP12.6 from the Calcium Release Channel (Ryanodine Receptor): Defective Regulation in Failing Hearts. Cell 101:365–376.

138. Zhu MM, Rempel DL, Du Z, Gross ML. 2003. Quantification of Protein−Ligand Interactions by Mass Spectrometry, Titration, and H/D Exchange: PLIMSTEX. J Am Chem Soc 125:5252–5253.

139. Hammond GRV, Fischer MJ, Anderson KE, Holdich J, Koteci A, Balla T, Irvine RF. 2012. PI4P and PI(4,5)P2 are essential but independent lipid determinants of membrane identity. Science 337:727–730.

140. Palmer DJ, Helms JB, Beckers CJ, Orci L, Rothman JE. 1993. Binding of coatomer to Golgi membranes requires ADP-ribosylation factor. J Biol Chem 268:12083–12089.

141. Staring J, von Castelmur E, Blomen VA, van den Hengel LG, Brockmann M, Baggen J, Thibaut HJ, Nieuwenhuis J, Janssen H, van Kuppeveld FJM, Perrakis A, Carette JE, Brummelkamp TR. 2017. PLA2G16 represents a switch between entry and clearance of Picornaviridae. Nature 541:412–416.

142. Walch-Solimena C, Novick P. 1999. The yeast phosphatidylinositol-4-OH kinase Pik1 regulates secretion at the Golgi. Nature Cell Biology 1:523–525.

143. Nakanishi S, Catt KJ, Balla T. 1995. A wortmannin-sensitive phosphatidylinositol 4-kinase that regulates hormone-sensitive pools of inositolphospholipids. Proc Natl Acad Sci U S A 92:5317–5321.

144. Dickinson ME, Flenniken AM, Ji X, Teboul L, Wong MD, White JK, Meehan TF, Weninger WJ, Westerberg H, Adissu H, Baker CN, Bower L, Brown JM, Caddle LB, Chiani F, Clary D, Cleak J, Daly MJ, Denegre JM, Doe B, Dolan ME, Edie SM, Fuchs H, Gailus-Durner V, Galli A, Gambadoro A, Gallegos J, Guo S, Horner NR, Hsu C-W, Johnson SJ, Kalaga S, Keith LC, Lanoue L, Lawson TN, Lek M, Mark M, Marschall S, Mason J, McElwee ML, Newbigging S, Nutter LMJ, Peterson KA, Ramirez-Solis R, Rowland DJ, Ryder E, Samocha KE, Seavitt JR, Selloum M, Szoke-Kovacs Z, Tamura M, Trainor AG, Tudose I, Wakana S, Warren J, Wendling O, West DB, Wong L, Yoshiki A, Wurst W, MacArthur DG, Tocchini-Valentini GP, Gao X, Flicek P, Bradley A, Skarnes WC, Justice MJ, Parkinson HE, Moore M, Wells S, Braun RE, Svenson KL, Angelis MH de, Herault Y, Mohun T, Mallon A-M, Henkelman RM, Brown SDM, Adams DJ, Lloyd KCK, McKerlie C, Beaudet AL, Bućan M, Murray SA. 2016. High-throughput discovery of novel developmental phenotypes. Nature 537:508–514.

145. Wang Y, Mousley CJ, Lete MG, Bankaitis VA. 2019. An equal opportunity collaboration between lipid metabolism and proteins in the control of membrane trafficking in the trans-Golgi and endosomal systems. Current Opinion in Cell Biology 59:58–72.

146. Viktorova EG, Gabaglio S, Meissner JM, Lee E, Moghimi S, Sztul E, Belov GA. 2019. A Redundant Mechanism of Recruitment Underlies the Remarkable Plasticity of the Requirement of Poliovirus Replication for the Cellular ArfGEF GBF1. Journal of Virology 93.

147. Arafeh R, Samuels Y. 2019. PIK3CA in cancer: The past 30 years. Seminars in Cancer Biology 59:36–49.

148. Levine DA. 2013. Integrated genomic characterization of endometrial carcinoma. Nature 497:67–73.

149. Le Gallo M, Bell DW. 2014. The Emerging Genomic Landscape of Endometrial Cancer. Clin Chem 60:98–110.

150. Koboldt DC, Fulton RS, McLellan MD, Schmidt H, Kalicki-Veizer J, McMichael JF, Fulton LL, Dooling DJ, Ding L, Mardis ER, Wilson RK, Ally A, Balasundaram M, Butterfield YSN, Carlsen R, Carter C, Chu A, Chuah E, Chun H-JE, Coope RJN, Dhalla N, Guin R, Hirst C, Hirst M, Holt RA, Lee D, Li HI, Mayo M, Moore RA, Mungall AJ, Pleasance E, Gordon Robertson A, Schein JE, Shafiei A, Sipahimalani P, Slobodan JR, Stoll D, Tam A, Thiessen N, Varhol RJ, Wye N, Zeng T, Zhao Y, Birol I, Jones SJM, Marra MA, Cherniack AD, Saksena G, Onofrio RC, Pho NH, Carter SL, Schumacher SE, Tabak B, Hernandez B, Gentry J, Nguyen H, Crenshaw A, Ardlie K, Beroukhim R, Winckler W, Getz G, Gabriel SB, Meyerson M, Chin L, Park PJ, Kucherlapati R, Hoadley KA, Todd Auman J, Fan C, Turman YJ, Shi Y, Li L, Topal MD, He X, Chao H-H, Prat A, Silva GO, Iglesia MD, Zhao W, Usary J, Berg JS, Adams M, Booker J, Wu J, Gulabani A, Bodenheimer T, Hoyle AP, Simons JV, Soloway MG, Mose LE, Jefferys SR, Balu S, Parker JS, Neil Hayes D, Perou CM, Malik S, Mahurkar S, Shen H, Weisenberger DJ, Triche Jr T, Lai PH, Bootwalla MS, Maglinte DT, Berman BP, Van Den Berg DJ, Baylin SB, Laird PW, Creighton CJ, Donehower LA, Getz G, Noble M, Voet D, Saksena G, Gehlenborg N, DiCara D, Zhang J, Zhang H, Wu C-J, Yingchun Liu S, Lawrence MS, Zou L, Sivachenko A, Lin P, Stojanov P, Jing R, Cho J, Sinha R, Park RW, Nazaire M-D, Robinson J, Thorvaldsdottir H, Mesirov J, Park PJ, Chin L, Reynolds S, Kreisberg RB, Bernard B, Bressler R, Erkkila T, Lin J, Thorsson V, Zhang W, Shmulevich I, Ciriello G, Weinhold N, Schultz N, Gao J, Cerami E, Gross B, Jacobsen A, Sinha R, Arman Aksoy B, Antipin Y, Reva B, Shen R, Taylor BS, Ladanyi M, Sander C, Anur P, Spellman PT, Lu Y, Liu W, Verhaak RRG, Mills GB, Akbani R, Zhang N, Broom BM, Casasent TD, Wakefield C, Unruh AK, Baggerly K, Coombes K, Weinstein JN, Haussler D, Benz CC, Stuart JM, Benz SC, Zhu J, Szeto CC, Scott GK, Yau C, Paull EO, Carlin D, Wong C, Sokolov A, Thusberg J, Mooney S, Ng S, Goldstein TC, Ellrott K, Grifford M, Wilks C, Ma S, Craft B, Yan C, Hu Y, Meerzaman D, Gastier-Foster JM, Bowen J, Ramirez NC, Black AD, Pyatt RE, White P, Zmuda EJ, Frick J, Lichtenberg TM, Brookens R, George MM, Gerken MA, Harper HA, Leraas KM, Wise LJ, Tabler TR, McAllister C, Barr T, Hart-Kothari M, Tarvin K, Saller C, Sandusky G, Mitchell C, Iacocca MV, Brown J, Rabeno B, Czerwinski C, Petrelli N, Dolzhansky O, Abramov M, Voronina O, Potapova O, Marks JR, Suchorska WM, Murawa D, Kycler W, Ibbs M, Korski K, Spychała A,

Murawa P, Brzeziński JJ, Perz H, Łaźniak R, Teresiak M, Tatka H, Leporowska E, Bogusz-Czerniewicz M, Malicki J, Mackiewicz A, Wiznerowicz M, Van Le X, Kohl B, Viet Tien N, Thorp R, Van Bang N, Sussman H, Duc Phu B, Hajek R, Phi Hung N, Viet The Phuong T, Quyet Thang H, Zaki Khan K, Penny R, Mallery D, Curley E, Shelton C, Yena P, Ingle JN, Couch FJ, Lingle WL, King TA, Maria Gonzalez-Angulo A, Mills GB, Dyer MD, Liu S, Meng X, Patangan M, The Cancer Genome Atlas Network, Genome sequencing centres: Washington University in St Louis, Genome characterization centres: BC Cancer Agency, Broad Institute, Brigham & Women's Hospital & Harvard Medical School, University of North Carolina CH, University of Southern California/Johns Hopkins, Genome data analysis: Baylor College of Medicine, Institute for Systems Biology, Memorial Sloan-Kettering Cancer Center, Oregon Health & Science University, The University of Texas MD Anderson Cancer Center, University of California SCI, NCI, Biospecimen core resource: Nationwide Children's Hospital Biospecimen Core Resource, Tissue source sites: ABS-IUPUI, Christiana, Cureline, Duke University Medical Center, The Greater Poland Cancer Centre, ILSBio, International Genomics Consortium, Mayo Clinic, MSKCC, MD Anderson Cancer Center. 2012. Comprehensive molecular portraits of human breast tumours. Nature 490:61–70.

151. Pereira B, Chin S-F, Rueda OM, Vollan H-KM, Provenzano E, Bardwell HA, Pugh M, Jones L, Russell R, Sammut S-J, Tsui DWY, Liu B, Dawson S-J, Abraham J, Northen H, Peden JF, Mukherjee A, Turashvili G, Green AR, McKinney S, Oloumi A, Shah S, Rosenfeld N, Murphy L, Bentley DR, Ellis IO, Purushotham A, Pinder SE, Børresen-Dale A-L, Earl HM, Pharoah PD, Ross MT, Aparicio S, Caldas C. 2016. The somatic mutation profiles of 2,433 breast cancers refine their genomic and transcriptomic landscapes. Nature Communications 7:1–16.

152. Weinstein JN, Akbani R, Broom BM, Wang W, Verhaak RGW, McConkey D, Lerner S, Morgan M, Creighton CJ, Smith C, Kwiatkowski DJ, Cherniack AD, Kim J, Sekhar Pedamallu C, Noble MS, Al-Ahmadie HA, Reuter VE, Rosenberg JE, Bajorin DF, Bochner BH, Solit DB, Koppie T, Robinson B, Gordenin DA, Fargo D, Klimczak LJ, Roberts SA, Au J, Laird PW, Hinoue T, Schultz N, Ramirez R, Hansel D, Hoadley KA, Kim WY, Damrauer JS, Baylin SB, Mungall AJ, Gordon Robertson A, Chu. A, Kwiatkowski DJ, Sougnez C, Cibulskis K, Lichtenstein L, Sivachenko A, Stewart C, Lawrence MS, Getz G, Lander E, Gabriel. SB, Creighton CJ, Donehower L, Cherniack AD, Kim J, Carter SL, Saksena G, Schumacher SE, Sougnez C, Freeman SS, Jung J, Sekhar Pedamallu C, Bhatt AS, Pugh T, Getz G, Beroukhim R, Gabriel SB, Meyerson M, Mungall AJ, Gordon Robertson A, Chu A, Ally A, Balasundaram M, Butterfield YSN, Dhalla N, Hirst C, Holt RA, Jones SJM, Lee D, Li HI, Marra MA, Mayo M, Moore RA, Schein JE, Sipahimalani P, Tam A, Thiessen N, Wong T, Wye N, Bowlby R, Chuah E, Guin R, Jones SJM, Marra MA, Hinoue T, Shen H, Bootwalla MS, Triche Jr T, Lai PH, Van Den Berg DJ, Weisenberger DJ, Laird PW, Hansel D, Hoadley KA, Balu S, Bodenheimer T, Damrauer Alan P. Hoyle JS, Jefferys SR, Meng S, Mose LE, Simons JV, Soloway MG, Wu J, Kim WY, Parker JS, Neil Hayes D, Roach J, Buda E, Jones CD, Mieczkowski PA, Tan D, Veluvolu U, Waring S, Todd Auman J, Perou CM, Wilkerson MD, Santoso N, Parfenov M, Ren X, Pantazi A, Hadjipanayis A, Seidman J, Kucherlapati R, Lee S, Yang L, Park PJ, Baylin SB, Wei Xu A, Protopopov A, Zhang J, Bristow C, Mahadeshwar HS, Seth S, Song X, Tang J, Zeng D, Chin L, Guo C, Weinstein JN, Akbani R, Broom BM, McConkey D,

Casasent TD, Liu W, Ju Z, Motter T, Peng B, Ryan M, Wang W, Verhaak RGW, Su X, Yang J-Y, Lorenzi PL, Yao H, Zhang N, Zhang J, Mills GB, Kim J, Noble MS, Cho J, DiCara D, Frazer S, Gehlenborg N, Heiman DI, Lin P, Liu Y, Stojanov P, Voet D, Zhang H, Zou L, Chin L, Getz G, Bernard B, Kreisberg D, Reynolds S, Rovira H, Shmulevich I, Ramirez R, Schultz N, Gao J, Jacobsen A, Arman Aksoy B, Antipin Y, Ciriello G, Dresdner G, Gross B, Lee W, Reva B, Shen R, Sinha R, Onur Sumer S, Weinhold N, Ladanyi M, Sander C, Benz C, Carlin D, Haussler D, Ng S, Paull EO, Stuart J, Zhu J, Liu Y, Zhang W, Taylor BS, Lichtenberg TM, Zmuda E, Barr T, Black AD, George M, Hanf B, Helsel C, McAllister C, Ramirez NC, Tabler TR, Weaver S, Wise L, Bowen J, Gastier-Foster JM, Weinstein JN, Lerner S, Jian W, Tello S, Ittman M, Castro P, McClenden WD, Morgan M, Gibbs R, Liu Y, Saller C, Tarvin K, DiPiero JM, Owens J, Bollag R, Li Q, Weinberger P, Czerwinski C, Huelsenbeck-Dill L, Iacocca M, Petrelli N, Rabeno B, The Cancer Genome Atlas Research Network, Analysis working group: The University of Texas MD Anderson Cancer Center, Baylor College of Medicine, Broad Institute, Memorial Sloan-Kettering Cancer Center, Oregon Health and Science University D of U, Weill Medical College of Cornell University, National Institute of Environmental Health Sciences, Optimum Therapeutics LLC, University of Southern California Epigenome Center, Computational Biology Center MS-KCC, UCSD Department of Pathology, Lineberger Comprehensive Cancer Center U of NC at CH, Department of Genetics U of NC at CH, The Sidney Kimmel Comprehensive Cancer Center at Johns Hopkins University, Canada's Michael Smith Genome Sciences Centre BCA, Genome Sequencing Center: Broad Institute, Genome characterization centres: Dan L. Duncan Cancer Center HGSC Baylor College of Medicine, Canada's Michael Smith Genome Sciences Centre BCA, Research Computing Center U of NC at CH, Carolina Center for Genome Sciences U of NC at CH, Department of Biology U of NC at CH, Eshelman School of Pharmacy U of NC at CH, Department of Genetics HMS, The Center for Biomedical Informatics HMS, Cancer Biology Division TSKCCC at JHU, Division of Genetics B and WH, Institute for Applied Cancer Science D of GM The University of Texas MD Anderson Cancer Center, The University of Texas MD Anderson Cancer Center D of P, Genome data analysis centres: The University of Texas M.D. Anderson Cancer Center, Institute for Systems Biology, Buck Institute for Research on Aging, University of California Santa Cruz, Department of Pathology MACC, Helen Diller Family Comprehensive Cancer Center U of C, Biospecimen core resource: The Research Institute at Nationwide Children's Hospital, Tissue source sites: The University of Texas MD Anderson Cancer Center, Scott Department of Urology BC of M, Texas Cancer Research Biobank (TCRB) BC of M, Analytical Biological Services Inc, Cleveland Clinic Foundation, Georgia Regents University Cancer Center, Helen F. Graham Cancer Center at Christiana Care. 2014. Comprehensive molecular characterization of urothelial bladder carcinoma. Nature 507:315–322.

153. Dueñas M, Martínez-Fernández M, García-Escudero R, Villacampa F, Marqués M, Saiz-Ladera C, Duarte J, Martínez V, Gómez MJ, Martín ML, Fernández M, Castellano D, Real FX, Rodriguez-Peralto JL, De La Rosa F, Paramio JM. 2015. PIK3CA gene alterations in bladder cancer are frequent and associate with reduced recurrence in non-muscle invasive tumors. Mol Carcinog 54:566–576.

154. Ojesina AI, Lichtenstein L, Freeman SS, Pedamallu CS, Imaz-Rosshandler I, Pugh TJ, Cherniack AD, Ambrogio L, Cibulskis K, Bertelsen B, Romero-Cordoba S, Treviño V, Vazquez-Santillan K, Guadarrama AS, Wright AA, Rosenberg MW, Duke F, Kaplan B, Wang R, Nickerson E, Walline HM, Lawrence MS, Stewart C, Carter SL, McKenna A, Rodriguez-Sanchez IP, Espinosa-Castilla M, Woie K, Bjorge L, Wik E, Halle MK, Hoivik EA, Krakstad C, Gabiño NB, Gómez-Macías GS, Valdez-Chapa LD, Garza-Rodríguez ML, Maytorena G, Vazquez J, Rodea C, Cravioto A, Cortes ML, Greulich H, Crum CP, Neuberg DS, Hidalgo-Miranda A, Escareno CR, Akslen LA, Carey TE, Vintermyr OK, Gabriel SB, Barrera-Saldaña HA, Melendez-Zajgla J, Getz G, Salvesen HB, Meyerson M. 2014. Landscape of genomic alterations in cervical carcinomas. Nature 506:371–375.

155. Burk RD, Chen Z, Saller C, Tarvin K, Carvalho AL, Scapulatempo-Neto C, Silveira HC, Fregnani JH, Creighton CJ, Anderson ML, Castro P, Wang SS, Yau C, Benz C, Robertson AG, Mungall K, Lim L, Bowlby R, Sadeghi S, Brooks D, Sipahimalani P, Mar R, Ally A, Clarke A, Mungall AJ, Tam A, Lee D, Chuah E, Schein JE, Tse K, Kasaian K, Ma Y, Marra MA, Mayo M, Balasundaram M, Thiessen N, Dhalla N, Carlsen R, Moore RA, Holt RA, Jones SJM, Wong T, Pantazi A, Parfenov M, Kucherlapati R, Hadjipanayis A, Seidman J, Kucherlapati M, Ren X, Xu AW, Yang L, Park PJ, Lee S, Rabeno B, Huelsenbeck-Dill L, Borowsky M, Cadungog M, Iacocca M, Petrelli N, Swanson P, Ojesina AI, Le X, Sandusky G, Adebamowo SN, Akeredolu T, Adebamowo C, Reynolds SM, Shmulevich I, Shelton C, Crain D, Mallery D, Curley E, Gardner J, Penny R, Morris S, Shelton T, Liu J, Lolla L, Chudamani S, Wu Y, Birrer M, McLellan MD, Bailey MH, Miller CA, Wyczalkowski MA, Fulton RS, Fronick CC, Lu C, Mardis ER, Appelbaum EL, Schmidt HK, Fulton LA, Cordes MG, Li T, Ding L, Wilson RK, Rader JS, Behmaram B, Uyar D, Bradley W, Wrangle J, Pastore A, Levine DA, Dao F, Gao J, Schultz N, Sander C, Ladanyi M, Einstein M, Teeter R, Benz S, Wentzensen N, Felau I, Zenklusen JC, Bodelon C, Demchok JA, Yang L, Sheth M, Ferguson ML, Tarnuzzer R, Yang H, Schiffman M, Zhang J, Wang Z, Davidsen T, Olaniyan O, Hutter CM, Sofia HJ, Gordenin DA, Chan K, Roberts SA, Klimczak LJ, Van Waes C, Chen Z, Saleh AD, Cheng H, Parfitt J, Bartlett J, Albert M, Arnaout A, Sekhon H, Gilbert S, Peto M, Myers J, Harr J, Eckman J, Bergsten J, Tucker K, Zach LA, Karlan BY, Lester J, Orsulic S, Sun Q, Naresh R, Pihl T, Wan Y, Zaren H, Sapp J, Miller J, Drwiega P, Ojesina AI, Murray BA, Zhang H, Cherniack AD, Sougnez C, Pedamallu CS, Lichtenstein L, Meyerson M, Noble MS, Heiman DI, Voet D, Getz G, Saksena G, Kim J, Shih J, Cho J, Lawrence MS, Gehlenborg N, Lin P, Beroukhim R, Frazer S, Gabriel SB, Schumacher SE, Leraas KM, Lichtenberg TM, Zmuda E, Bowen J, Frick J, Gastier-Foster JM, Wise L, Gerken M, Ramirez NC, Danilova L, Cope L, Baylin SB, Salvesen HB, Vellano CP, Ju Z, Diao L, Zhao H, Chong Z, Ryan MC, Martinez-Ledesma E, Verhaak RG, Averett Byers L, Yuan Y, Chen K, Ling S, Mills GB, Lu Y, Akbani R, Seth S, Liang H, Wang J, Han L, Weinstein JN, Bristow CA, Zhang W, Mahadeshwar HS, Sun H, Tang J, Zhang J, Song X, Protopopov A, Shaw KRM, Chin L, Olabode O, Ojesina AI, DiSaia P, Radenbaugh A, Haussler D, Zhu J, Stuart J, Chalise P, Koestler D, Fridley BL, Godwin AK, Madan R, Ciriello G, Martinez C, Higgins K, Bocklage T, Auman JT, Perou CM, Tan D, Parker JS, Hoadley KA, Wilkerson MD, Mieczkowski PA, Skelly T, Veluvolu U, The Cancer Genome Atlas Research Network, Albert Einstein College of Medicine, Analytical Biological Services, Barretos Cancer Hospital, Baylor College of Medicine, Beckman Research Institute of City of Hope, Buck Institute for Research on Aging, Canada's Michael Smith Genome Sciences Centre,

Harvard Medical School, Helen F. Graham Cancer Center & Research Institute at Christiana Care Health Services, HudsonAlpha Institute for Biotechnology, ILSbio L, Indiana University School of Medicine, Institute of Human Virology, Institute for Systems Biology, International Genomics Consortium, Leidos Biomedical, Massachusetts General Hospital, McDonnell Genome Institute at Washington University, Medical College of Wisconsin, Medical University of South Carolina, Memorial Sloan Kettering Cancer Center, Montefiore Medical Center, NantOmics, National Cancer Institute, National Hospital A Nigeria, National Human Genome Research Institute, National Institute of Environmental Health Sciences, National Institute on Deafness & Other Communication Disorders, Ontario Tumour Bank LHSC, Ontario Tumour Bank OI for CR, Ontario Tumour Bank TOH, Oregon Health & Science University, Samuel Oschin Comprehensive Cancer Institute C-SMC, SRA International, St Joseph's Candler Health System, The Eli & Edythe L. Broad Institute of Massachusetts Institute of Technology & Harvard University, The Research Institute at Nationwide Children's Hospital, The Sidney Kimmel Comprehensive Cancer Center at Johns Hopkins University, The University of Bergen, The University of Texas MD Anderson Cancer Center, University of Abuja Teaching Hospital, University of Alabama at Birmingham, University of California I, University of California Santa Cruz, University of Kansas Medical Center, University of Lausanne, University of New Mexico Health Sciences Center, University of North Carolina at Chapel Hill. 2017. Integrated genomic and molecular characterization of cervical cancer. Nature 543:378–384.

156. Samuels Y, Wang Z, Bardelli A, Silliman N, Ptak J, Szabo S, Yan H, Gazdar A, Powell SM, Riggins GJ, Willson JKV, Markowitz S, Kinzler KW, Vogelstein B, Velculescu VE. 2004. High Frequency of Mutations of the PIK3CA Gene in Human Cancers. Science 304:554–554.

157. Kozaki K, Imoto I, Pimkhaokham A, Hasegawa S, Tsuda H, Omura K, Inazawa J. 2006. PIK3CA mutation is an oncogenic aberration at advanced stages of oral squamous cell carcinoma. Cancer Science 97:1351–1358.

158. Murugan AK, Munirajan AK, Tsuchida N. 2013. Genetic deregulation of the PIK3CA oncogene in oral cancer. Cancer Letters 338:193–203.

159. Liu N, Rowley BR, Bull CO, Schneider C, Haegebarth A, Schatz CA, Fracasso PR, Wilkie DP, Hentemann M, Wilhelm SM, Scott WJ, Mumberg D, Ziegelbauer K. 2013. BAY 80-6946 Is a Highly Selective Intravenous PI3K Inhibitor with Potent p110α and p110δ Activities in Tumor Cell Lines and Xenograft Models. Mol Cancer Ther 12:2319–2330.

160. André F, Ciruelos E, Rubovszky G, Campone M, Loibl S, Rugo HS, Iwata H, Conte P, Mayer IA, Kaufman B, Yamashita T, Lu Y-S, Inoue K, Takahashi M, Pápai Z, Longin A-S, Mills D, Wilke C, Hirawat S, Juric D. 2019. Alpelisib for PIK3CA-Mutated, Hormone Receptor–Positive Advanced Breast Cancer. New England Journal of Medicine 380:1929–1940.

161. Arita M, Kojima H, Nagano T, Okabe T, Wakita T, Shimizu H. 2011. Phosphatidylinositol 4-Kinase III Beta Is a Target of Enviroxime-Like Compounds for Antipoliovirus Activity. Journal of Virology 85:2364–2372.

162. Balla A, Kim YJ, Varnai P, Szentpetery Z, Knight Z, Shokat KM, Balla T. 2007. Maintenance of Hormone-sensitive Phosphoinositide Pools in the Plasma Membrane Requires Phosphatidylinositol 4-Kinase IIIα. MBoC 19:711–721.

163. Mello C, Aguayo E, Rodriguez M, Lee G, Jordan R, Cihlar T, Birkus G. 2014. Multiple Classes of Antiviral Agents Exhibit In Vitro Activity against Human Rhinovirus Type C. Antimicrobial Agents and Chemotherapy 58:1546–1555.

164. Borawski J, Troke P, Puyang X, Gibaja V, Zhao S, Mickanin C, Leighton-Davies J, Wilson CJ, Myer V, CornellaTaracido I, Baryza J, Tallarico J, Joberty G, Bantscheff M, Schirle M, Bouwmeester T, Mathy JE, Lin K, Compton T, Labow M, Wiedmann B, Gaither LA. 2009. Class III Phosphatidylinositol 4-Kinase Alpha and Beta Are Novel Host Factor Regulators of Hepatitis C Virus Replication. Journal of Virology 83:10058–10074.

165. Chen P, Deng Y-L, Bergqvist S, Falk MD, Liu W, Timofeevski S, Brooun A. 2014. Engineering of an isolated p110α subunit of PI3Kα permits crystallization and provides a platform for structure-based drug design. Protein Sci 23:1332–1340.

166. Spraggon G, Pantazatos D, Klock HE, Wilson IA, Woods VL, Lesley SA. 2004. On the use of DXMS to produce more crystallizable proteins: Structures of the T. maritima proteins TM0160 and TM1171. Protein Science 13:3187–3199.

167. Pantazatos D, Kim JS, Klock HE, Stevens RC, Wilson IA, Lesley SA, Woods VL. 2004. Rapid refinement of crystallographic protein construct definition employing enhanced hydrogen/deuterium exchange MS. PNAS 101:751–756.

168. Engen JR. 2009. Analysis of Protein Conformation and Dynamics by Hydrogen/Deuterium Exchange MS. Anal Chem 81:7870–7875.

169. Skinner JJ, Lim WK, Bédard S, Black BE, Englander SW. 2012. Protein hydrogen exchange: Testing current models. Protein Science 21:987–995.

170. Skinner JJ, Lim WK, Bédard S, Black BE, Englander SW. 2012. Protein dynamics viewed by hydrogen exchange. Protein Science 21:996–1005.

171. Balasubramaniam D, Komives EA. 2013. Hydrogen-exchange mass spectrometry for the study of intrinsic disorder in proteins. Biochimica et Biophysica Acta (BBA) - Proteins and Proteomics 1834:1202–1209.

172. Kabsch W. 2010. XDS. Acta Crystallogr D Biol Crystallogr 66:125–132.

173. Emsley P, Lohkamp B, Scott WG, Cowtan K. 2010. Features and development of Coot. Acta Cryst D 66:486–501.

174. Chen VB, Arendall WB, Headd JJ, Keedy DA, Immormino RM, Kapral GJ, Murray LW, Richardson JS, Richardson DC. 2010. MolProbity: all-atom structure validation for macromolecular crystallography. Acta Crystallogr D Biol Crystallogr 66:12–21.

175. Burke JE, Williams RL. 2013. Dynamic steps in receptor tyrosine kinase mediated activation of class IA phosphoinositide 3-kinases (PI3K) captured by H/D exchange (HDX-MS). Advances in Biological Regulation 53:97–110.

176. Rageot D, Bohnacker T, Keles E, McPhail JA, Hoffmann RM, Melone A, Borsari C, Sriramaratnam R, Sele AM, Beaufils F, Hebeisen P, Fabbro D, Hillmann P, Burke JE, Wymann MP. 2019. (S)-4-(Difluoromethyl)-5-(4-(3-methylmorpholino)-6-morpholino-1,3,5-triazin-2-yl)pyridin-2-amine (PQR530), a Potent, Orally Bioavailable, and Brain-Penetrable Dual Inhibitor of Class I PI3K and mTOR Kinase. J Med Chem 62:6241–6261.

177. Bohnacker T, Prota AE, Beaufils F, Burke JE, Melone A, Inglis AJ, Rageot D, Sele AM, Cmiljanovic V, Cmiljanovic N, Bargsten K, Aher A, Akhmanova A, Díaz JF, Fabbro D, Zvelebil M, Williams RL, Steinmetz MO, Wymann MP. 2017. Deconvolution of Buparlisib's mechanism of action defines specific PI3K and tubulin inhibitors for therapeutic intervention. Nat Commun 8.

178. Beaufils F, Cmiljanovic N, Cmiljanovic V, Bohnacker T, Melone A, Marone R, Jackson E, Zhang X, Sele A, Borsari C, Mestan J, Hebeisen P, Hillmann P, Giese B, Zvelebil M, Fabbro D, Williams RL, Rageot D, Wymann MP. 2017. 5-(4,6-Dimorpholino-1,3,5-triazin-2-yl)-4-(trifluoromethyl)pyridin-2-amine (PQR309), a Potent, Brain-Penetrant, Orally Bioavailable, Pan-Class I PI3K/mTOR Inhibitor as Clinical Candidate in Oncology. J Med Chem 60:7524–7538.

179. Burke JE, Vadas O, Berndt A, Finegan T, Perisic O, Williams RL. 2011. Dynamics of the Phosphoinositide 3-Kinase p110δ Interaction with p85α and Membranes Reveals Aspects of Regulation Distinct from p110α. Structure 19:1127–1137.

180. Laskowski RA, Swindells MB. 2011. LigPlot+: Multiple Ligand–Protein Interaction Diagrams for Drug Discovery. J Chem Inf Model 51:2778–2786.

181. Wang Q, Zorn JA, Kuriyan J. 2014. Chapter Two - A Structural Atlas of Kinases Inhibited by Clinically Approved Drugs, p. 23–67. *In* Shokat, KM (ed.), Methods in Enzymology. Academic Press.

182. Adams PD, Afonine PV, Bunkóczi G, Chen VB, Echols N, Headd JJ, Hung L-W, Jain S, Kapral GJ, Grosse Kunstleve RW, McCoy AJ, Moriarty NW, Oeffner RD, Read RJ, Richardson DC, Richardson JS, Terwilliger TC, Zwart PH. 2011. The Phenix software for automated determination of macromolecular structures. Methods 55:94–106.

183. Moriarty NW, Grosse-Kunstleve RW, Adams PD. 2009. electronic Ligand Builder and Optimization Workbench (eLBOW): a tool for ligand coordinate and restraint generation. Acta Cryst D 65:1074–1080.

184. D'Angelo G, Vicinanza M, Wilson C, De Matteis MA. 2012. Phosphoinositides in Golgi Complex Function, p. 255–270. *In* Balla, T, Wymann, M, York, JD (eds.), Phosphoinositides II: The Diverse Biological Functions. Springer Netherlands, Dordrecht.

185. Arita M, Philipov S, Galabov AS. 2015. Phosphatidylinositol 4-kinase III beta is the target of oxoglaucine and pachypodol (Ro 09-0179) for their anti-poliovirus activities, and is located at upstream of the target step of brefeldin A. Microbiology and Immunology 59:338–347.

186. Waring MJ, Andrews DM, Faulder PF, Flemington V, McKelvie JC, Maman S, Preston M, Raubo P, Robb GR, Roberts K, Rowlinson R, Smith JM, Swarbrick ME, Treinies I, Winter JJG, Wood RJ. 2014. Potent, selective small molecule inhibitors of type III

phosphatidylinositol-4-kinase α- but not β-inhibit the phosphatidylinositol signaling cascade and cancer cell proliferation. Chem Commun 50:5388–5390.

187. Keaney EP, Connolly M, Dobler M, Karki R, Honda A, Sokup S, Karur S, Britt S, Patnaik A, Raman P, Hamann LG, Wiedmann B, LaMarche MJ. 2014. 2-Alkyloxazoles as potent and selective PI4KIIIβ inhibitors demonstrating inhibition of HCV replication. Bioorganic & Medicinal Chemistry Letters 24:3714–3718.

188. Wong K, Meyers R, Cantley LC. 1997. Subcellular Locations of Phosphatidylinositol 4-Kinase Isoforms. J Biol Chem 272:13236–13241.

189. Pardon E, Laeremans T, Triest S, Rasmussen SGF, Wohlkönig A, Ruf A, Muyldermans S, Hol WGJ, Kobilka BK, Steyaert J. 2014. A general protocol for the generation of Nanobodies for structural biology. Nat Protoc 9:674–693.

190. Chan CJ, Le R, Burns K, Ahmed K, Coyaud E, Laurent EMN, Raught B, Melançon P. 2019. BioID Performed on Golgi Enriched Fractions Identify C10orf76 as a GBF1 Binding Protein Essential for Golgi Maintenance and Secretion. Molecular & Cellular Proteomics 18:2285–2297.

191. Macville M, Schröck E, Padilla-Nash H, Keck C, Ghadimi BM, Zimonjic D, Popescu N, Ried T. 1999. Comprehensive and Definitive Molecular Cytogenetic Characterization of HeLa Cells by Spectral Karyotyping. Cancer Res 59:141–150.

192. Horova V, Lyoo H, Różycki B, Chalupska D, Smola M, Humpolickova J, Strating JRPM, Kuppeveld FJM van, Boura E, Klima M. 2019. Convergent evolution in the mechanisms of ACBD3 recruitment to picornavirus replication sites. PLOS Pathogens 15:e1007962.

193. Belov GA, Feng Q, Nikovics K, Jackson CL, Ehrenfeld E. 2008. A Critical Role of a Cellular Membrane Traffic Protein in Poliovirus RNA Replication. PLOS Pathogens 4:e1000216.

194. Gopal AK, Kahl BS, de Vos S, Wagner-Johnston ND, Schuster SJ, Jurczak WJ, Flinn IW, Flowers CR, Martin P, Viardot A, Blum KA, Goy AH, Davies AJ, Zinzani PL, Dreyling M, Johnson D, Miller LL, Holes L, Li D, Dansey RD, Godfrey WR, Salles GA. 2014. PI3Kδ inhibition by idelalisib in patients with relapsed indolent lymphoma. N Engl J Med 370:1008–1018.

195. Winkler DG, Faia KL, DiNitto JP, Ali JA, White KF, Brophy EE, Pink MM, Proctor JL, Lussier J, Martin CM, Hoyt JG, Tillotson B, Murphy EL, Lim AR, Thomas BD, MacDougall JR, Ren P, Liu Y, Li L-S, Jessen KA, Fritz CC, Dunbar JL, Porter JR, Rommel C, Palombella VJ, Changelian PS, Kutok JL. 2013. PI3K-δ and PI3K-γ Inhibition by IPI-145 Abrogates Immune Responses and Suppresses Activity in Autoimmune and Inflammatory Disease Models. Chemistry & Biology 20:1364–1374.

196. Masson GR, Burke JE, Ahn NG, Anand GS, Borchers C, Brier S, Bou-Assaf GM, Engen JR, Englander SW, Faber J, Garlish R, Griffin PR, Gross ML, Guttman M, Hamuro Y, Heck AJR, Houde D, Iacob RE, Jørgensen TJD, Kaltashov IA, Klinman JP, Konermann L, Man P, Mayne L, Pascal BD, Reichmann D, Skehel M, Snijder J, Strutzenberg TS, Underbakke ES, Wagner C, Wales TE, Walters BT, Weis DD, Wilson DJ, Wintrode PL, Zhang Z, Zheng J, Schriemer DC, Rand KD. 2019. Recommendations for performing,

interpreting and reporting hydrogen deuterium exchange mass spectrometry (HDX-MS) experiments. Nature Methods 16:595–602.

Copyright Permissions

For manuscripts adapted in this dissertation:

(1) McPhail, J.A. and Burke, J.E. (accepted). Drugging the phosphoinositide 3-kinase (PI3K) and phosphatidylinositol 4-kinase (PI4K family of enzymes for treatment of cancer, immune disorders, and viral/parasitic infections. Advances in Experimental Medicine and Biology. Invited Review.

- Springer Nature's website (https://www.springer.com/gp/rights-permissions/obtaining-permissions/882) states authors have permission for inclusion of articles in thesis/dissertation. Adapted with permission from the authors. Copyright Springer.

(2) Dornan, G.L., McPhail, J.A. and Burke, J.E. (2016). Type III phosphatidylinositol 4 kinases: structure, function, regulation, signalling and involvement in disease. Biochemical Society Transactions. Invited Review. 44(1):260-6.

- Portland Press' website (https://portlandpress.com/pages/copyright_and_permissions) states authors have permission for inclusion of articles in thesis/dissertation. Adapted with permission from the authors. Copyright Portland Press.

(3) McPhail, J.A., Ottosen, E.H., Jenkins, M.L., and Burke, J.E. (2017). The Molecular Basis of Aichi Virus 3A Protein Activation of Phosphatidylinositol 4 Kinase IIIβ, PI4KB, through ACBD3. Structure. 2017 Jan 3; 25(1):121-131. https://doi.org/10.1016/j.str.2016.11.016

- From Elsevier's website (https://www.elsevier.com/about/policies/copyright) on copyright permissions: "Authors can use their articles, in full or in part, for … inclusion in a thesis or dissertation (provided that this is not to be published commercially)."

(4) McPhail, J.A., Lyoo, H.R., Pemberton, J.G, Hoffmann, R.M., van Elst, W., Strating J.R.P.M., Jenkins, M.L., Stariha J.T.B., Powell, C.J., Boulanger, M.J., Balla, T., van Kuppeveld, F.J.M., and Burke, J.E. (2019). Characterization of the c10orf76-PI4KB complex, and its necessity for Golgi PI4P levels and enterovirus replication. EMBO Reports. 2019. e48441.

- From EMBO Press' website (https://www.embopress.org/page/journal/14693178/authorguide#chargesguide) on copyright permissions: "Authors grant EMBO Press and its publishers an exclusive license to publish, in return for which they can re-use their papers in their future printed work."
- Publication is under Creative Commons license CC BY-NC-ND 4.0, meaning users are free to share (copy, distribute and transmit) the contribution; see full legal code at (https://creativecommons.org/licenses/by-nc-nd/4.0/) Attribution: © 2019 The Authors, EMBO Reports. Some appendix figures have been integrated into main text figures. (https://www.embopress.org/doi/10.15252/embr.201948441)

(5) Rageot, D., Bohnacker, T., Keles, E., McPhail, J.A., Hoffmann, R.M., Melone, A., Borsari, C., Sriramaratnam, R., Sele, A.M., Beufils, F., Hebeisen, P., Fabbro, D., Hillmann, P., Burke, J.E., Wymann, M.P. (2019). (S)-4-(Difluoromethyl)-5-(4-(3-methylmorpholino)-6-morpholino-1,3,5-triazin-2-yl)pyridin-2-amine (PQR530), a Potent, Orally Bioavailable, and Brain-Penetrable Dual Inhibitor of Class I PI3K and mTOR Kinase. Journal of Medicinal Chemistry. 62(13):6241-6261.

- From ACS Publications' website (https://www.springer.com/gp/rights-permissions/obtaining-permissions/882) for inclusion in thesis/dissertation: "Permission is granted for your request in both print and electronic formats, and translations". Adapted with permission from the authors. Copyright (2019) American Chemical Society.

(6) Fowler, M.L., McPhail, J.A., Jenkins, M.L., Masson, G.R., Rutaganira, F.U., Shokat, K.M., Williams, R.L., and Burke, J.E. (2016). Using hydrogen-deuterium exchange mass spectrometry to engineer optimized constructs for crystallization of protein complexes: case study of PI4KIIIβ. Protein Science. 25(4):826-39.

- Publication is under Creative Commons license CC BY 4.0, meaning users are free to share and adapt the contribution; see full legal code at (https://creativecommons.org/licenses/by/4.0/) Attribution: © 2016 The Authors,

Protein Science. The only change made is the Figure numbering scheme. https://onlinelibrary.wiley.com/doi/full/10.1002/pro.2879

(7) Rutaganira, F.U., Fowler, M.L., McPhail, J.A., Gelman, M.A., Nguyen, K., Xiong, A., Dornan, G.L., Tavshanjian, B., Glenn, J.S., Shokat, K.M., Burke, J.E. (2016). Design and Structural Characterization of Potent and Selective Inhibitors of Phosphatidylinositol 4 kinase IIIβ. Journal of Medicinal Chemistry. 59(5):1800-9.

- From ACS Publications' website (https://s100.copyright.com/AppDispatchServlet#formTop) for inclusion in thesis/dissertation: "Permission is granted for your request in both print and electronic formats, and translations". Adapted with permission from the authors. Copyright (2016) American Chemical Society.

(8) Kato, N., Comer, E., Sakata-Kato, T., Sharma, A., Sharma, M., Maetani, M., Bastien, J., Brancucci, N.M., Bittker, J.A., Corey V., Clarke, D., Derbyshire, E.R., Dornan, G., Duffy, S., Eckley, S., Itoe, M.A., Koolen, K.M., Lewis, T.A., Lui P.S., Lukens, A.K., Lund, E., March, S., Meibalan, E., Meier, B.C., McPhail, J.A., Mitasev, B., Moss, E.L., Sayes, M., VanGessel, Y., Wawer, M.J., Yoshinaga, T., Zeeman, A., Avery, V.M., Bhatia, S.N., Burke, J.E., Cateruccia, F., Clardy, J.C., Clemons, P.A., Dechering, K.J., Duvall, J.R., Foley, M.A., Gusovsky, F., Kocken, C.H., Marti, M., Morningstar, M.L., Munoz, B., Neafsey, D.E., Sharma, A., Winzeler, E.A., Wirth, D.F., Scherer, C.A., Schreiber, S.L.. (2016). Diversity-oriented synthesis yields novel multistage antimalarial inhibitors. Nature. 538(7625):344-349.

- From Springer Nature's website (https://s100.copyright.com/AppDispatchServlet#formTop) for inclusion in thesis/dissertation: "Permission is granted for your request in both print and electronic formats, and translations". Adapted with permission from the authors. Copyright (2016) American Chemical Society.

Appendix

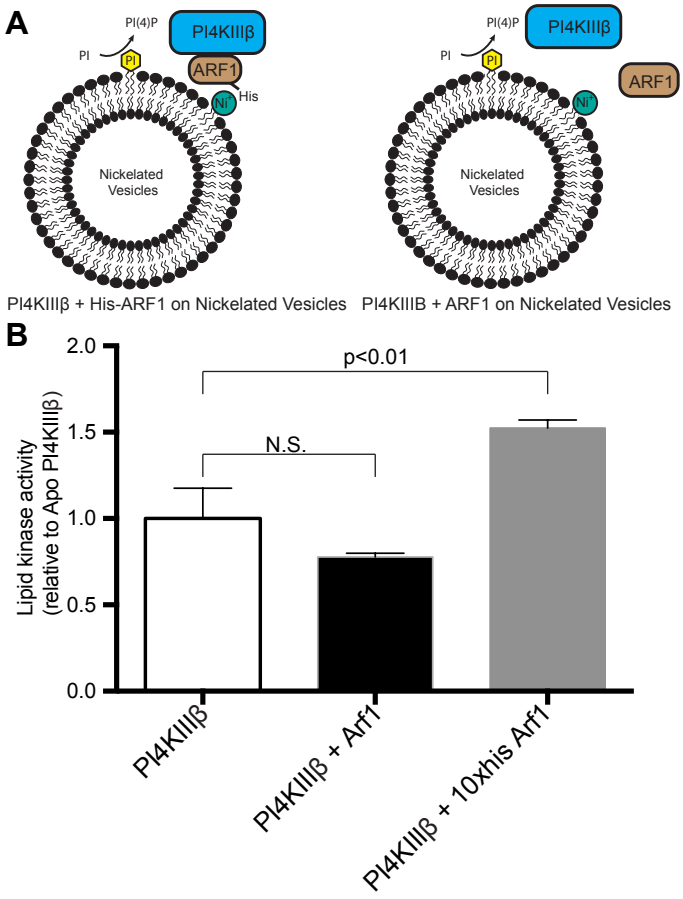

Appendix A. In vitro lipid kinase assay shows membrane-bound Arf1 activates PI4KIIIβ (refers to Fig 2.1).
(A) Schematic – Arf1 with a His-Tag binds to Nickelated Vesicles (5% DGS-NTA(Ni), 10% PS, 20% PE, 20% PI, 45% PC) and recruits PI4KIIIβ to the membrane, while free Arf1 lacking a His-Tag no longer binds Nickelated Vesicles. **(B)** Lipid kinase assays monitoring the production of ADP in the presence of Golgi mimicking vesicles containing 5% NGS-NTA(Ni) were carried out with 150 nM PI4KIIIβ for 60 minutes. Arf1 was present at 750 nM. Free Arf1 shows no significant activation of PI4KIIIβ, while membrane-bound Arf1 with a His-Tag activates PI4KIIIβ.

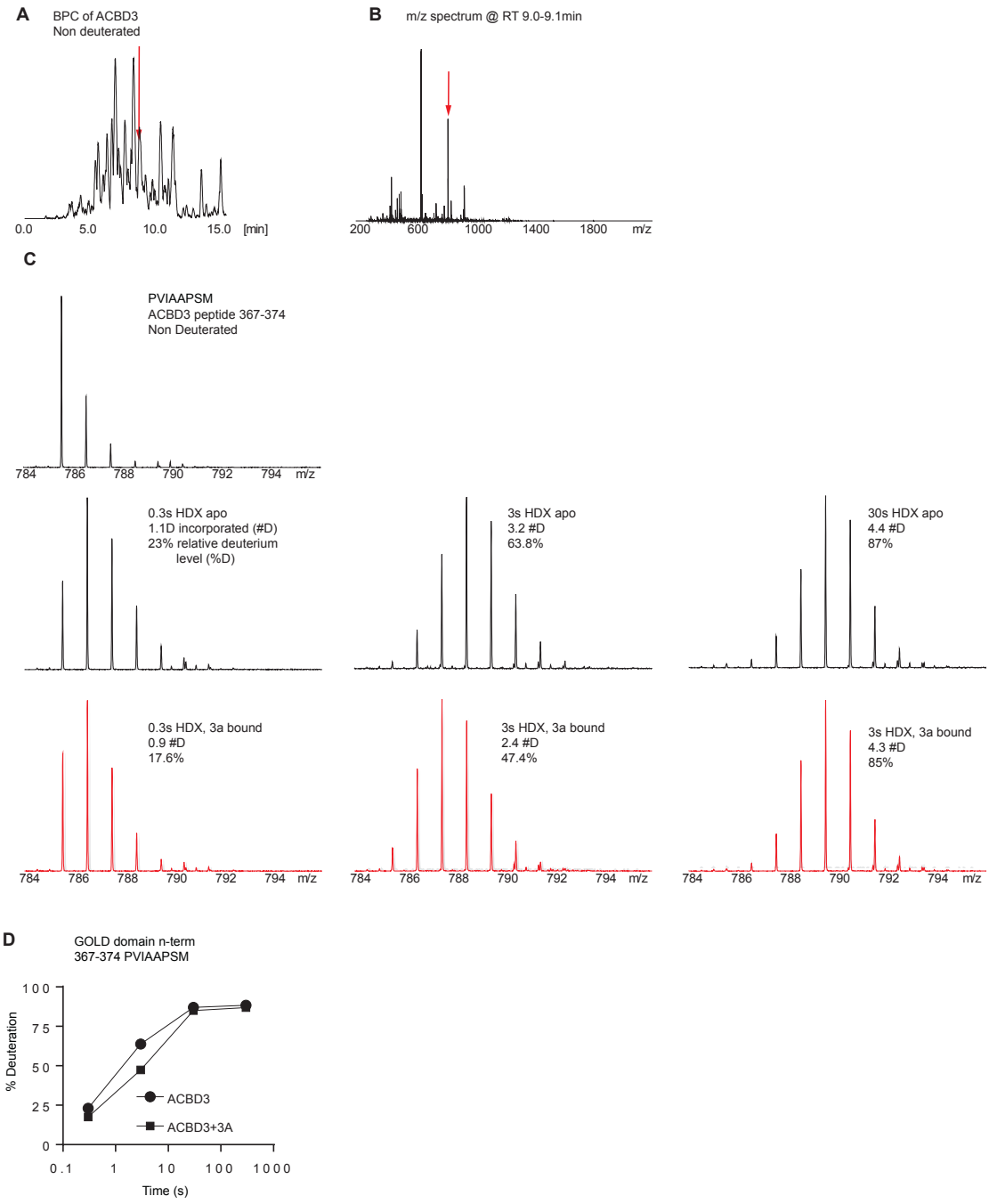

Appendix B. HDX-MS methodology (refers to Fig. 2.2 and 2.5).
(A) Representative UPLC base peak chromatogram (BPC) trace of an ACBD3 peptic digest. **(B)** MS spectra for the time window selected in the BPC in A. **(C)** Raw data for the peptide 367-374 in ACBD3 with and without 3A showing the shift in mass centroid upon deuterium incorporation after 0.3, 3, and 30 s exposure to D_2O buffer. **(D)** HDX incorporation plots for this peptide in the presence and absence of Aichi virus 3A protein.

Appendix C. Changes in HDX levels observed for constructs in apo and complex states tested for PI4K and ACBD3 (refers to Fig. 2.2).

The residue start number (**S**), residue end number (**E**), charge state (**Z**), retention time (**RT**), and sequence are displayed for each peptide. The four time points are labeled (0.3-300 seconds) for both states. The relative level of HDX is colored according to the figure in the legend. The data listed are the average of 2-3 independent experiments, with error represented as SD. Peptides with difference in exchange (>7%, 0.7 Da difference before FD correction) have the sequence colored with decreases shown in cyan (7-15%) and blue (>15%) and increases shown in orange (<-7 to -15%).

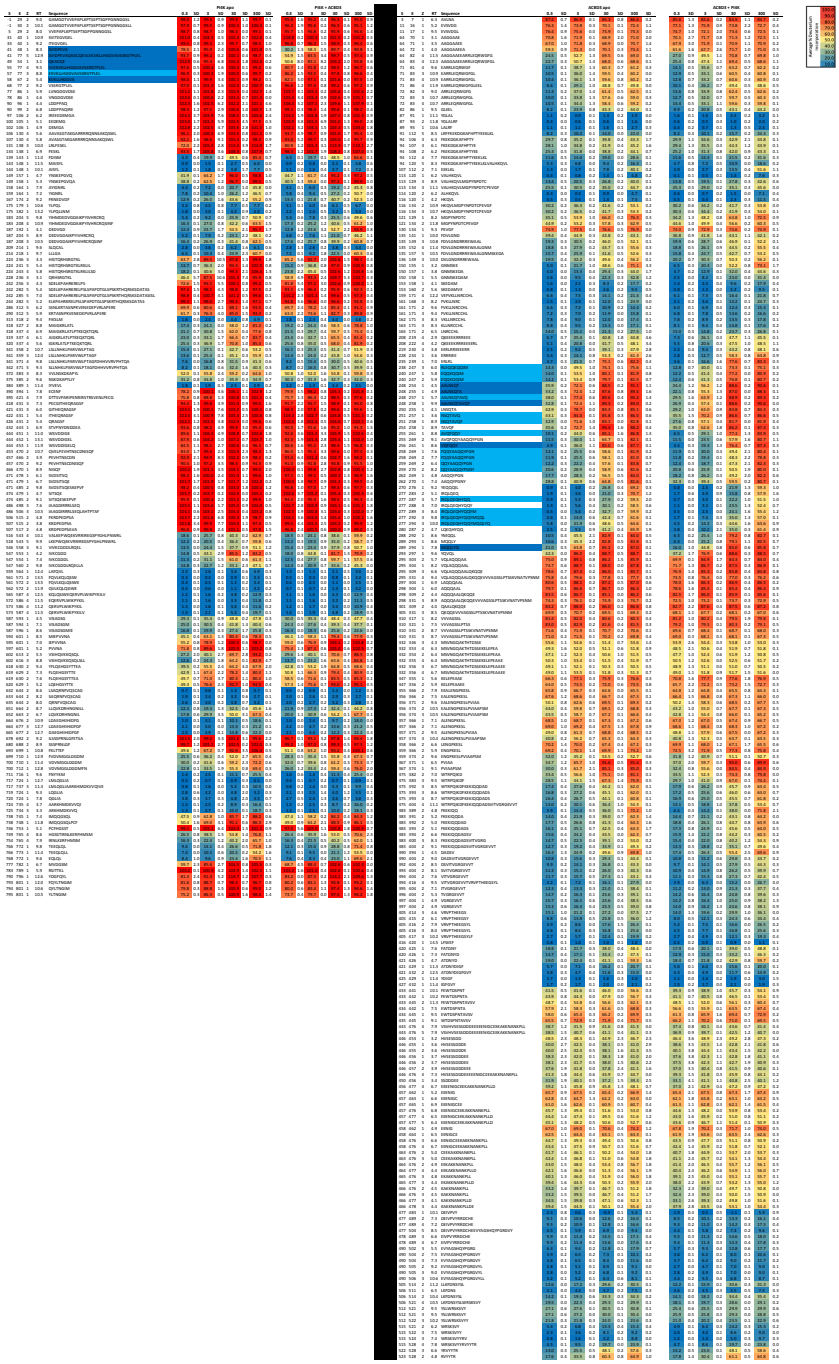

Appendix D. Changes in HDX levels observed for constructs in apo and complex states tested for ACBD3 and Aichi virus 3A (refers to Fig. 2.5).

The residue start number (**S**), residue end number (**E**), charge state (**Z**), retention time (**RT**), and sequence are displayed for each peptide. The four time points are labeled (0.3-300 seconds) for both states. The relative level of HDX is colored according to the figure in the legend. The data listed are the average of 2-3 independent experiments, with error represented as SD. Peptides with difference in exchange (>7%, 0.7 Da difference before FD correction) have the sequence colored with decreases shown in cyan (7-15%) and blue (>15%) and increases shown in orange (<-7 to -15%).

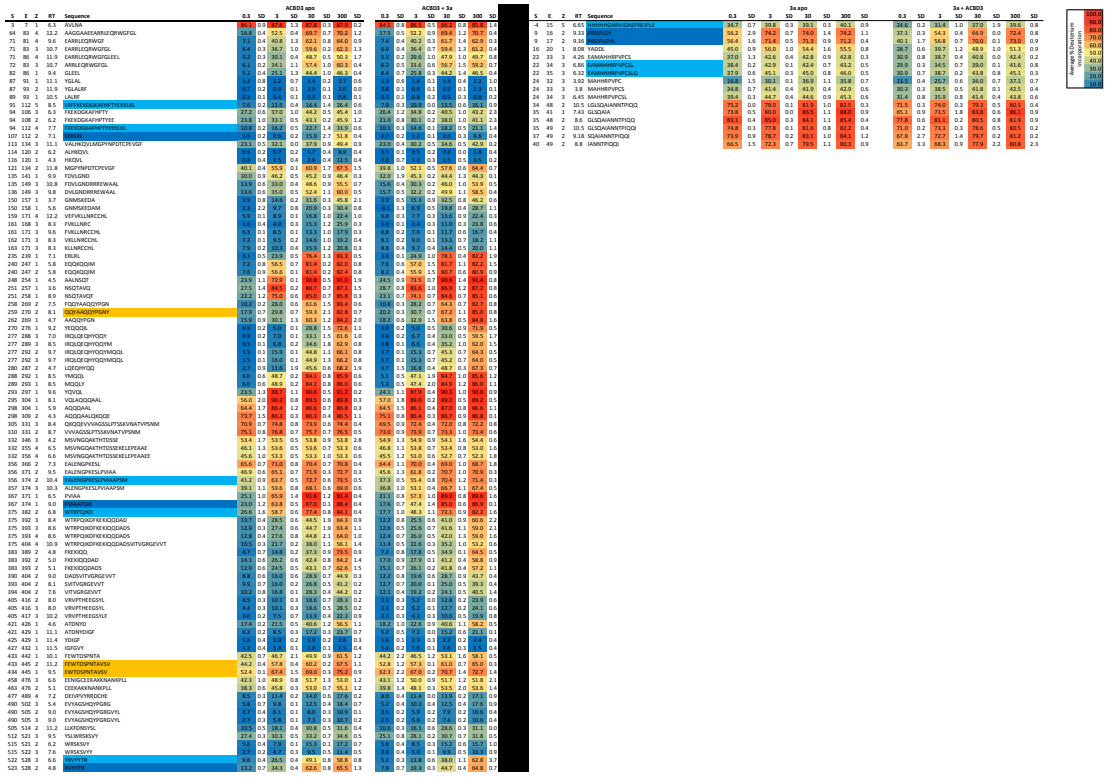

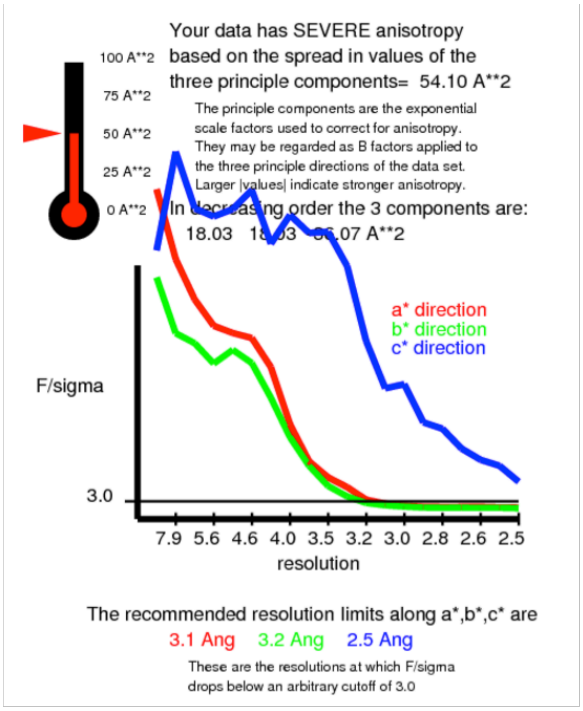

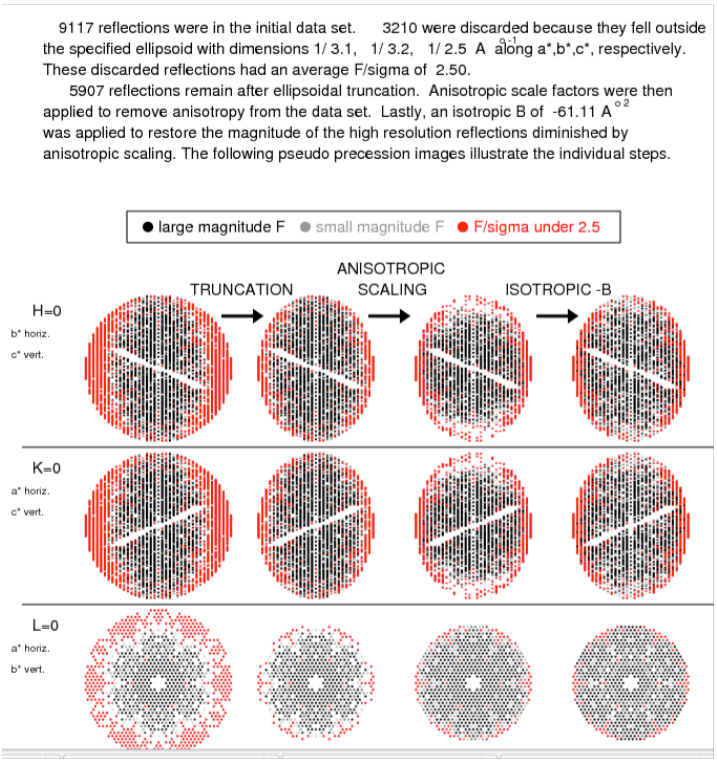

Appendix E. Details of anisotropic data processing (refers to Table 2.1, 2.2 and Fig. 2.4).
The output from the anisotropic data processing server is shown. The revised data completeness after anisotropic truncation and scaling is shown in Table 2.2. (http://services.mbi.ucla.edu/anisoscale/).

Appendix F. Full statistics on all hydrogen deuterium exchange experiments according to the guidelines from the International Conference on HDX-MS (196) (refers to Fig. 3.2).

Data Set	PI4KB	c10orf76	FLH409AAA c10orf76 mutant
HDX reaction details	$\%D_2O$=87.4% $pH_{(read)}$= 7.5 Temp= 23°C	$\%D_2O$=87.4% $pH_{(read)}$= 7.5 Temp= 23°C	$\%D_2O$=90.5% $pH_{(read)}$= 7.5 Temp= 23°
HDX time course	3s at 1°C 3s, 30s, 300s at 23°C	3s at 1°C 3s, 30s, 300s at 23°C	3s, 300s at 23°C
HDX controls	N/A	N/A	N/A
Back-exchange	Corrected using a fully deuterated (FD) sample	Corrected based on $\%D_2O$	Corrected based on $\%D_2O$
Number of peptides	185	108	111
Sequence coverage	96.9%	73.9%	72.8%
Average peptide length/ redundancy	Length = 13.8 Redundancy = 3.2	Length = 12.1 Redundancy = 1.9	Length = 10.7 Redundancy = 1.7
Replicates	3	3	3
Repeatability	Average StDev = 1.2%	Average StDev = 0.6%	Average StDev = 1%
Significant differences in HDX	>7% and >0.5 Da and unpaired t-test <0.05	>7% and >0.5 Da and unpaired t-test <0.05	>7% and >0.5 Da and unpaired t-test <0.05

Appendix G. Changes in HDX levels observed for PI4KB in apo and c10orf76 complex states (refers to Fig. 3.2).

The residue start number (S), residue end number (E), charge state (Z), retention time (RT), and sequence are displayed for each peptide. The four time points are labeled (0.3-300 seconds) for both states. The relative level of HDX is colored according to the figure in the legend. The data listed are the average of 2-3 independent experiments, with error represented as SD.

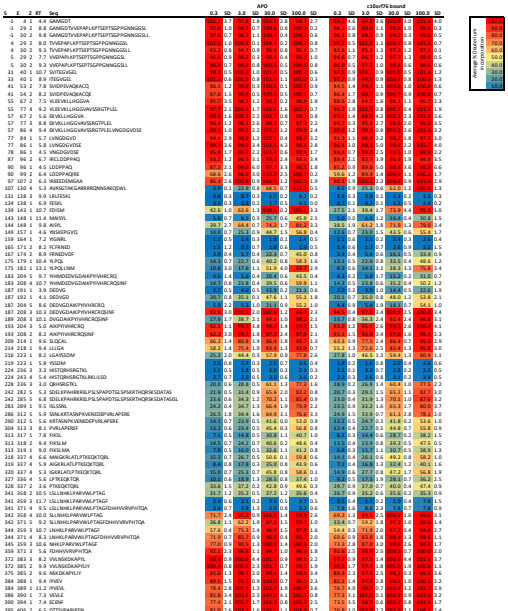

Appendix H. Changes in HDX levels observed for c10orf76 in apo and PI4KB complex states (refers to Fig. 3.2).

The residue start number (S), residue end number (E), charge state (Z), retention time (RT), and sequence are displayed for each peptide. The four time points are labeled (0.3-300 seconds) for both states. The relative level of HDX is colored according to the figure in the legend. The data listed are the average of 2-3 independent experiments, with error represented as SD.

					APO								PI4KIIB bound							
S	E	Z	RT	Seq	0.3	SD	3.0	SD	30.0	SD	300.0	SD	0.3	SD	3.0	SD	30.0	SD	300.0	SD
-3	4	1	7.7	YFQGAQVE	79.6	2.3	78.7	1.0	80.1	0.8	80.7	0.7	80.4	0.8	81.0	0.8	81.4	1.0	81.4	1.4
-3	9	2	7.5	YFQGAQVEKRGGL	69.9	0.4	70.4	1.5	70.4	0.8	69.6	0.9	69.1	0.8	70.0	1.1	69.4	0.4	69.7	0.8
-3	27	5	6.8	YFQGAQVEKRGGLLRKSSASKKPLKEKVVLM	35.3	0.9	37.8	1.0	44.8	0.7	46.5	1.2	34.6	0.7	37.5	2.2	45.2	0.1	46.3	1.4
3	26	5	4.9	VEKRGGLLRKSSASKKPLKEKVVL	30.5	1.0	32.5	1.6	38.0	1.1	41.3	0.9	30.4	1.6	32.5	0.8	41.0	0.1	41.4	1.4
10	22	3	3.0	LRKSSASKKPLKE	49.6	1.6	47.1	1.8	46.9	0.6	48.8	0.4	49.1	1.5	48.8	2.1	49.7	1.5	51.1	1.0
10	26	5	4.4	LRKSSASKKPLKEKVVL	29.2	0.8	32.5	1.6	41.2	0.3	45.7	0.6	30.2	1.5	34.1	0.5	45.5	0.1	46.4	1.2
10	27	5	5.1	LRKSSASKKPLKEKVVLM	25.9	1.0	30.4	1.1	41.6	0.7	46.6	0.7	26.8	0.9	31.8	1.1	46.5	0.1	47.4	1.4
11	27	4	5.0	RKSSASKKPLKEKVVLM	27.5	0.9	32.7	0.9	46.4	1.3	50.5	0.3	28.8	1.0	34.4	1.0	50.0	0.3	50.9	0.9
27	32	1	12.2	MYDEIF	2.1	0.7	2.3	0.1	6.4	0.2	21.8	0.4	1.7	0.1	3.0	0.2	14.5	0.5	33.2	0.2
28	32	1	11.4	YDEIF	1.3	0.5	1.8	0.1	4.7	0.3	16.6	0.8	1.2	0.2	2.4	0.1	11.0	0.5	29.3	0.7
28	33	1	12.3	YDEIFM	2.1	0.8	2.3	0.1	6.1	0.3	21.0	0.2	1.7	0.1	3.0	0.2	13.8	0.7	32.2	0.4
56	62	1	8.7	EYLEGKL	1.5	0.3	1.8	0.2	6.5	0.4	30.5	0.3	1.6	0.2	2.4	0.3	16.1	0.1	43.4	0.4
56	70	2	11.2	EYLEGKLESLDGEEL	9.0	0.2	14.0	0.2	23.7	1.1	36.8	1.4	9.5	0.3	14.9	0.7	31.3	0.3	46.6	0.4
63	70	1	9.1	ESLDGEEL	16.6	0.4	23.5	0.4	45.2	1.7	53.4	1.2	17.2	0.8	24.1	1.2	49.1	1.5	55.2	0.6
71	80	2	8.7	MKIKDNINCL	1.7	0.3	2.9	0.1	7.0	0.4	20.3	0.3	1.5	0.1	2.8	0.4	8.7	0.2	23.0	0.3
81	88	2	8.9	FQHCIQAL	2.1	0.5	1.3	0.4	1.6	0.1	3.4	0.4	1.7	0.3	1.3	0.4	2.6	0.3	4.7	0.4
81	99	4	8.6	FQHCIQALGEEHPIRVVNA	2.3	0.2	4.6	0.2	11.1	0.4	16.2	0.8	2.4	0.1	4.5	0.5	11.2	0.1	16.6	0.2
81	100	3	9.8	FQHCIQALGEEHPIRVVNAL	2.1	0.2	3.8	0.1	8.5	0.2	13.5	0.2	2.3	0.1	4.0	0.2	9.8	0.1	14.6	0.1
81	103	4	10.8	FQHCIQALGEEHPIRVVNALQTL	1.3	0.1	2.4	0.1	6.2	0.3	10.2	0.1	1.4	0.0	2.4	0.1	6.8	0.9	10.9	0.2
89	100	3	6.9	GEEHPIRVVNAL	3.4	0.2	6.5	0.3	13.4	0.6	18.8	0.2	3.3	0.1	6.3	1.0	14.5	0.3	19.7	1.4
106	120	3	4.7	LIRGVHQKNKSTSGF	20.1	0.8	21.2	1.7	19.9	0.9	24.1	1.1	21.9	1.3	22.4	0.8	23.5	0.4	25.4	1.4
107	120	3	4.1	IRGVHQKNKSTSGF	23.1	0.7	23.9	2.0	22.6	0.6	26.8	1.0	24.9	1.7	26.0	0.8	26.8	0.2	28.8	1.3
121	126	1	12.9	DIINIML	1.8	0.7	6.1	0.1	32.4	0.8	56.5	1.0	1.9	0.3	6.6	0.7	35.7	0.3	55.0	0.7
135	143	1	11.5	CMKNLMESL	3.9	3.5	2.0	0.4	2.7	1.1	10.5	0.7	2.5	0.7	2.0	1.5	4.3	0.4	11.7	1.0
137	143	2	10.5	KNLMESL	0.7	0.2	0.7	0.1	0.5	0.4	2.6	0.0	2.3	0.2	2.3	0.4	2.7	0.3	4.5	0.3
193	207	4	5.0	QILSHPPSRREHGYD	1.2	0.1	3.7	0.5	11.4	0.5	15.6	1.4	1.3	0.2	4.0	0.6	14.0	0.3	16.5	0.9
193	208	4	5.2	QILSHPPSRREHGYDA	1.4	0.0	4.0	0.5	11.6	0.6	15.7	1.4	1.6	0.1	4.2	0.5	14.1	0.3	16.2	0.6
213	231	3	10.9	ALLVNYRKYESVNPYIVKL	14.9	0.4	23.1	0.4	26.0	0.7	34.8	2.3	11.4	0.3	23.0	0.6	27.1	0.0	32.5	0.4
216	231	4	9.9	VNYRKYESVNPYIVKL	18.1	0.5	29.9	0.4	33.5	0.1	42.3	1.1	13.8	0.8	28.6	0.2	34.8	0.1	38.3	0.3
232	237	1	6.2	SIVDDE	14.7	1.2	30.0	1.4	35.1	1.3	38.8	0.5	16.3	1.2	30.0	2.0	38.3	0.2	38.4	2.1
232	240	1	9.3	SIVDDEATL	11.8	0.4	25.4	0.1	30.9	0.8	40.1	0.8	12.7	0.8	25.9	0.7	33.0	0.2	40.9	0.3
245	249	1	6.7	LVIAQ	0.8	0.3	1.0	0.3	0.8	0.2	1.0	0.2	0.6	0.1	0.7	0.2	0.9	0.3	0.8	0.3
245	250	1	7.3	LVIAQA	0.9	0.3	0.9	0.2	0.9	0.1	1.2	0.1	0.9	0.1	1.1	0.3	1.2	0.1	1.3	0.4
245	253	1	10.0	LVIAQALSE	1.0	0.2	1.6	0.2	6.1	0.1	11.4	0.2	0.9	0.1	1.5	0.1	6.7	0.1	11.6	0.1
245	269	4	10.3	LVIAQALSEYNRQYKDKEEEHQSGF	12.0	0.4	18.0	0.7	32.9	0.4	37.6	1.4	12.6	0.6	20.4	0.4	33.5	0.1	38.8	0.1
246	253	1	7.3	VIAQALSE	1.1	0.1	2.1	0.1	6.7	0.6	13.2	0.3	3.4	0.5	2.7	0.1	8.7	0.0	14.0	0.2
281	295	2	7.2	FIADAHEKISVQTNE	55.1	1.4	64.8	1.6	67.2	0.6	66.5	1.6	55.6	1.4	65.6	1.5	68.3	0.4	68.5	1.2
297	301	1	12.4	ILLAL	0.8	0.1	0.1	0.3	0.5	0.0	0.7	0.1	0.5	0.2	0.6	0.1	0.5	0.3	1.0	0.1
302	307	1	8.4	YEAVHL	1.6	0.3	1.3	0.2	1.4	0.1	1.5	0.3	1.1	0.1	1.1	0.3	1.6	0.0	1.5	0.3
302	315	2	11.5	YEAVHLNRNFITVL	3.1	0.2	3.1	0.2	7.5	0.7	15.7	0.9	1.6	0.1	1.9	0.1	6.3	0.2	12.2	0.3
308	314	2	9.2	NRNFITV	3.4	0.8	4.6	0.7	20.4	0.7	40.7	1.3	3.1	1.0	4.1	0.6	14.7	2.3	24.8	0.2
308	315	2	10.9	NRNFITVL	1.2	0.2	2.5	0.1	14.3	0.5	31.2	0.4	1.1	0.1	1.7	0.3	8.9	0.2	19.7	0.2
324	348	2	8.9	LVTTPVSPAPTTPVTPLGTTPPSSD	80.4	0.3	81.9	0.2	83.2	0.3	82.6	0.2	79.1	0.6	81.4	0.8	81.8	0.5	81.9	0.3
325	348	2	8.5	VTTPVSPAPTTPVTPLGTTPPSSD	80.6	0.3	83.2	0.6	83.7	0.2	83.4	0.5	80.0	0.5	82.6	0.6	82.8	0.2	83.1	0.2
325	352	2	9.4	VTTPVSPAPTTPVTPLGTTPPSSDVISS	78.7	0.5	82.7	0.8	83.1	0.2	83.1	1.0	76.5	0.6	80.6	0.5	81.8	0.7	81.1	0.3
348	352	1	5.1	DVISS	67.7	2.1	73.1	1.3	69.9	1.6	74.6	0.9	69.9	1.3	76.0	1.3	77.4	0.9	77.1	1.4
352	359	1	10.2	SVELPLDA	48.6	1.6	66.0	0.7	67.2	0.2	70.3	0.3	50.6	2.0	69.6	0.7	72.3	1.2	73.8	0.3
353	359	1	9.9	VELPLDA	47.6	1.9	66.3	0.7	66.1	1.3	69.2	0.9	49.4	1.9	69.7	0.2	72.4	0.2	73.1	0.2
360	366	1	6.6	DVQTSNL	58.8	1.8	77.1	0.9	82.5	1.6	82.3	1.6	60.3	1.9	77.4	1.6	82.4	0.4	82.1	0.9
367	371	1	13.2	LITFL	1.0	0.4	0.9	0.0	1.2	0.2	4.7	0.2	0.9	0.2	0.9	0.2	1.4	0.3	5.1	0.2
371	375	1	4.4	LKYSS	2.2	0.6	2.5	0.3	2.3	0.3	2.7	0.1	2.7	0.3	2.6	0.9	3.7	0.3	3.7	1.1
376	394	4	7.5	IVMQDTKDEHRLHSGKLCL	5.7	0.2	8.8	0.5	9.6	0.6	12.1	0.2	5.5	0.3	8.4	0.7	9.4	0.1	12.0	0.7
379	392	4	4.1	QDTKDEHRLHSGKL	10.3	0.6	14.4	1.5	16.4	0.5	20.8	0.7	10.7	1.3	14.7	0.7	19.5	0.5	21.8	1.3
379	394	2	6.6	QDTKDEHRLHSGKLCL	5.4	0.6	8.2	0.2	8.9	1.3	11.3	0.5	5.2	0.3	7.7	0.9	9.4	0.0	11.1	1.1
380	394	5	6.7	DTKDEHRLHSGKLCL	3.8	0.2	6.7	0.6	7.5	0.5	9.6	0.5	3.0	0.4	5.4	0.8	6.8	0.7	7.6	0.8
395	399	1	9.3	IILTC	0.7	0.3	1.2	0.2	1.1	0.1	1.1	0.0	0.9	0.2	0.9	0.2	0.9	0.1	1.2	0.2
396	400	1	9.2	ILTCI	0.7	0.1	0.8	0.1	1.0	0.0	0.9	0.2	0.5	0.2	0.6	0.2	0.6	0.1	1.0	0.2
398	402	1	5.3	TCIAE	1.4	0.7	0.8	0.2	1.0	0.4	1.4	0.3	0.4	0.4	0.6	0.5	0.7	0.2	1.1	0.4
398	404	1	5.2	TCIAEDQ	15.1	1.1	14.0	0.4	15.6	0.2	22.9	0.3	14.3	0.3	14.5	0.7	15.5	0.0	18.3	0.9
400	404	1	3.5	IAEDQ	24.8	0.1	23.7	0.9	26.0	0.2	38.3	0.5	24.6	0.6	25.3	0.9	26.1	0.6	31.3	1.2
400	408	1	6.4	IAEDQYANA	12.0	0.3	14.5	0.4	25.6	1.0	42.9	0.3	12.0	0.5	13.0	0.6	20.0	0.6	29.6	0.5
402	408	1	5.0	EDQYANA	14.0	2.2	15.9	0.5	30.0	0.6	50.0	0.8	12.0	0.9	13.1	0.9	22.6	0.6	32.3	0.9
403	408	1	4.7	DQYANA	2.8	0.7	5.9	0.2	24.8	0.9	48.4	0.1	2.0	0.3	3.6	0.6	15.4	0.4	28.2	1.0
409	417	1	10.1	FLHDDNMNF	9.6	1.4	21.7	0.2	33.0	0.1	34.8	0.6	8.0	0.5	20.1	0.5	34.3	0.1	35.4	0.4
422	444	5	5.0	HRMPMRHRKKAADKNLPCRPLVC	17.4	1.7	19.3	1.5	19.0	1.3	22.6	1.0	18.5	1.2	20.1	1.2	23.2	0.2	23.5	1.3
445	449	1	10.5	AVLDL	1.7	1.2	0.5	0.2	1.3	0.0	1.7	0.4	0.8	0.1	0.6	0.1	1.5	0.2	1.3	0.3
453	466	2	12.5	FIVTHMMKEFPMDL	14.8	1.1	19.2	0.4	24.9	0.9	36.4	1.0	16.0	0.3	20.5	0.7	28.1	0.6	40.3	0.9
454	466	2	11.3	IVTHMMKEFPMDL	14.0	0.5	18.3	0.5	26.4	0.5	37.2	1.5	13.9	0.3	19.0	0.2	24.8	0.2	35.5	0.5
459	466	2	12.3	MKEFPMDL	17.8	0.5	25.2	1.1	36.1	0.2	54.7	0.8	18.5	0.3	27.1	0.5	40.3	0.1	55.5	1.2
471	479	1	8.2	IQVVHKLLC	0.9	0.1	0.9	0.1	1.4	0.1	1.4	0.6	0.8	0.1	0.8	0.3	1.1	0.2	1.2	0.4
500	510	2	13.9	INLLKFLMSNE	4.8	0.3	9.4	0.7	11.3	0.5	14.5	1.2	6.0	1.0	11.3	0.4	13.4	0.9	18.3	0.7
525	529	1	10.7	MIVNL	-0.5	0.7	0.0	0.4	-0.3	0.4	0.6	0.5	1.1	0.4	0.6	0.3	1.3	0.1	0.7	0.1
533	547	2	12.8	FITYGDTFLPTPSSY	5.5	0.1	7.3	0.2	15.8	0.6	28.3	0.9	4.7	0.3	5.7	0.2	8.5	0.1	12.0	0.2
534	547	1	11.9	ITYGDTFLPTPSSY	7.3	0.7	9.6	0.5	21.8	0.2	37.5	0.6	6.0	0.3	7.0	0.3	10.8	0.3	15.9	0.3
551	557	2	10.8	YYEIIRM	0.6	0.2	0.4	0.1	0.4	0.0	1.3	0.1	0.7	0.2	0.6	0.1	0.8	0.0	1.5	0.1
551	564	2	11.0	YYEIIRMHQSFDNL	4.8	0.6	3.9	0.9	7.0	0.6	13.2	1.1	4.5	0.3	5.0	0.4	9.5	0.8	16.1	0.9
558	564	1	8.2	HQSFDNL	2.9	0.4	4.9	0.5	15.1	0.6	33.2	0.5	2.9	0.4	5.6	0.8	19.5	0.1	39.2	1.1
569	591	4	10.3	LRLSTNAGQWKEAASKVTHALVN	22.6	0.5	33.1	0.5	51.3	1.4	64.9	0.8	22.2	0.6	33.1	0.7	48.7	0.3	62.4	0.4
569	594	5	11.0	LRLSTNAGQWKEAASKVTHALVNIRA	17.5	0.4	25.1	1.0	41.5	1.7	54.3	0.9	16.9	0.5	25.9	0.7	40.4	0.1	53.2	0.5
570	591	3	9.8	RLSTNAGQWKEAASKVTHALVN	20.9	0.4	30.5	0.4	49.4	1.1	63.3	1.1	19.6	0.3	30.0	0.3	46.6	0.4	61.7	0.7
570	594	5	10.7	RLSTNAGQWKEAASKVTHALVNIRA	15.8	0.5	22.0	1.2	37.8	1.0	50.4	1.0	14.5	0.6	22.7	0.5	35.4	0.1	48.5	1.3
570	605	5	13.1	RLSTNAGQWKEAASKVTHALVNIRAIINHFNPKIES	7.1	0.2	9.4	0.6	18.8	0.2	33.3	0.7	7.0	0.4	10.0	0.5	19.7	0.4	33.7	0.1
572	592	3	11.4	STNAGQWKEAASKVTHALVNI	18.4	0.2	27.7	0.7	47.0	2.0	63.5	0.5	17.7	0.5	27.3	0.7	46.2	0.5	63.0	0.1
578	594	4	8.5	WKEAASKVTHALVNIRA	5.3	0.2	11.0	0.7	26.2	1.1	44.0	1.2	5.0	0.2	10.3	0.8	23.9	0.1	42.7	0.6
593	605	3	7.2	RAIINHFNPKIES	1.6	0.1	3.0	0.1	11.0	0.5	25.1	0.1	1.2	0.2	2.4	0.6	10.1	0.5	25.0	0.4
595	605	3	7.2	IINHFNPKIES	1.6	0.1	3.3	0.1	13.3	0.7	30.9	0.4	1.5	0.0	2.9	0.6	13.5	0.3	30.5	0.5
595	606	3	8.4	IINHFNPKIESY	1.5	0.1	3.5	0.1	16.5	0.8	34.4	0.5	1.3	0.0	2.9	0.5	16.8	0.1	34.2	0.4
606	615	2	8.5	YAAVNHISQL	31.9	0.6	41.0	0.8	65.0	0.7	67.7	0.9	32.3	0.1	41.3	1.1	64.4	0.3	68.2	0.6
607	615	1	7.6	AAVNHISQL	35.4	0.5	43.4	0.8	62.4	1.0	67.8	0.9	34.8	1.1	43.7	0.9	61.9	0.3	66.4	1.3
608	615	1	7.3	AVNHISQL	36.1	1.6	43.7	0.3	52.4	1.4	53.7	0.2	36.4	0.9	45.0	1.2	53.6	0.5	53.8	1.1
622	628	1	5.9	EVVRANY	6.0	0.3	12.4	0.4	22.6	1.0	35.7	0.7	5.0	0.3	11.5	0.9	22.7	0.6	33.7	0.9
623	628	1	5.0	VVRANY	8.1	0.6	15.8	0.4	29.1	0.9	45.0	0.5	7.6	0.5	15.8	1.1	29.6	0.3	42.8	1.1
632	640	2	8.5	TLKLQDGLD	49.7	0.3	57.2	1.5	71.1	1.2	68.7	1.1	39.2	0.9	45.2	0.6	57.9	1.3	64.2	1.1
632	641	2	8.4	TLKLQDGLDQ	48.7	0.7	55.9	1.4	71.8	0.9	71.9	1.0	38.6	0.7	44.4	0.7	59.5	0.3	68.5	0.8
633	640	1	8.1	LKLQDGLD	54.3	1.3	60.3	1.3	65.8	0.7	65.3	1.2	43.3	1.5	49.8	0.8	62.3	1.1	64.6	1.0
634	641	2	6.2	KLQDGLDQ	45.6	0.8	51.0	1.2	62.7	2.0	66.4	1.7	43.8	0.8	49.4	1.9	61.8	0.2	66.1	2.1
634	654	4	9.2	KLQDGLDQYERYSEQHKEAAF	37.2	0.3	45.2	0.4	57.5	0.3	58.1	1.5	34.8	1.6	45.4	0.8	55.9	1.3	58.4	0.4
641	654	3	6.4	QYERYSEQHKEAAF	25.5	0.6	32.5	1.2	42.6	2.2	46.1	0.6	25.0	0.6	31.1	1.9	43.8	0.2	46.3	2.1
642	653	3	3.9	YERYSEQHKEAA	29.6	0.8	33.3	2.0	43.8	0.4	49.4	1.1	29.6	1.4	33.9	0.7	47.0	0.2	51.1	1.9
642	654	3	6.3	YERYSEQHKEAAF	21.1	0.4	28.5	0.8	38.7	1.8	42.8	0.9	20.7	0.5	27.0	1.7	39.8	0.3	42.8	2.2
655	661	2	5.9	FKELVRS	4.5	0.3	4.0	0.4	6.4	0.6	16.4	0.4	4.8	0.3	4.7	1.0	8.6	1.4	16.8	1.5
655	664	2	7.6	FKELVRSIST	1.6	0.2	1.9	0.2	3.0	0.3	9.9	0.2	2.1	0.3	2.1	0.3	4.1	0.3	9.7	0.6
655	665	2	7.3	FKELVRSISTN	1.9	0.1	2.2	0.2	3.6	0.5	13.0	0.4	1.6	0.1	1.9	0.5	4.0	0.2	11.3	0.6
658	664	2	5.3	LVRSIST	3.3	0.2	3.8	0.3	5.2	0.4	17.7	0.9	3.5	0.0	3.8	0.6	7.3	0.7	17.9	0.8
665	672	1	7.5	NVRRNLAF	29.2	0.5	42.3	0.5	58.0	1.1	67.0	0.9	29.3	0.8	42.4	1.0	58.2	0.5	65.9	1.1
673	680	1	8.4	HTLSQEVL	55.8	1.0	67.9	2.0	71.9	0.9	70.0	1.0	54.5	2.4	69.6	1.7	71.1	0.2	70.8	1.0
681	688	1	7.9	LKEFSTIS	57.7	1.2	64.3	0.5	68.8	3.3	67.1	0.9	57.7	1.4	67.5	1.3	70.1	0.1	70.2	0.9
684	688	1	6.8	FSTIS	63.3	0.2	75.8	0.9	82.7	0.9	82.8	0.6	63.8	1.2	77.4	1.7	85.0	0.8	84.1	1.7

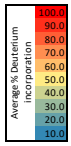

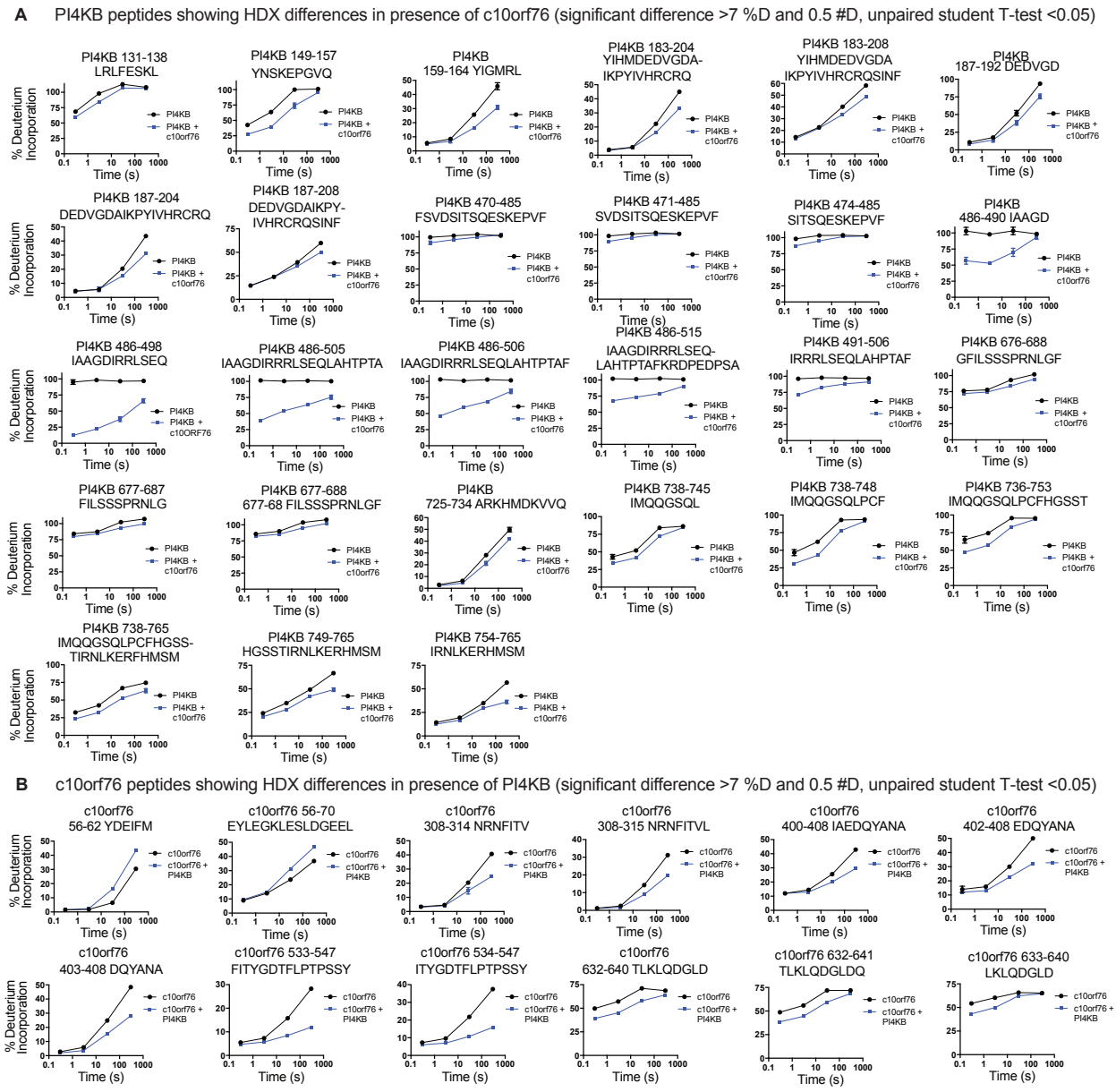

Appendix I. PI4KB and c10orf76 form an extended interface with spanning multiple regions (refers to Fig. 3.2).

(A, B) All peptides of both PI4KB **(A)** and c10orf76 **(B)** with a significant difference in H/D exchange of >7% decrease in exchange, >0.5 Da difference, and unpaired two-tailed student t-test $p<0.05$ at any time point (3s at 1 ºC; 3s, 30s, and 300s at 23 ºC). Error bars represent standard deviation of independent technical replicates (n=3), and are typically smaller than the size of the point on the graph.

Appendix J. Changes in HDX levels observed for wild-type c10orf76 and FLH409AAA c10orf76 (refers to Fig. 3.4).

The residue start number (S), residue end number (E), charge state (Z), retention time (RT), and sequence are displayed for each peptide. The two time points are labeled (3 or 300 seconds) for both proteins. The relative level of HDX is colored according to the figure in the legend. Error bars represent standard deviation of 2-3 independent technical replicates independent technical replicates.

						WT c10orf76				FLH410AAA c10orf76			
S	E	Z	RT	Seq	3.0	SD	300.0	SD	3.0	SD	300.0	SD
10	27	4	5.92	LRKSSASKKPLKEKVVLM	42.5	1.9	59.1	1.1	40.5	0.5	57.0	0.1
10	27	5	5.92	LRKSSASKKPLKEKVVLM	41.1	1.4	56.8	0.8	38.9	0.4	55.0	1.1
27	32	1	12.65	MYDEIF	5.1	0.3	46.6	0.2	3.7	0.4	40.2	0.8
28	32	1	11.65	YDEIF	3.6	0.6	46.8	0.3	2.5	0.1	36.6	0.8
28	33	1	12.26	YDEIFM	4.7	1.0	45.0	1.5	3.4	0.2	39.2	0.9
33	44	3	8.05	MTEDPSKCSPRF	55.4	0.7	71.4	3.3	58.7	0.5	73.9	0.4
48	54	2	11.45	LFLMKVN	30.2	1.5	89.4	1.0	27.6	0.5	83.5	0.3
56	62	2	9.07	EYLEGKL	2.5	0.0	50.3	2.3	1.9	0.3	44.7	0.0
56	70	2	11.57	EYLEGKLESLDGEEL	17.0	0.9	53.1	6.2	19.1	0.2	53.0	1.0
63	70	1	9.43	ESLDGEEL	28.3	0.6	65.0	2.3	30.3	0.8	65.0	0.6
66	70	1	7.08	DGEEL	20.7	3.7	68.7	2.2	21.4	1.2	66.2	0.8
70	80	2	9.74	LMKIKDNINCL	3.0	0.4	28.9	1.0	4.0	0.2	32.0	0.4
71	80	2	9.08	MKIKDNINCL	2.2	0.1	25.3	0.9	3.6	0.1	25.9	0.6
81	87	2	7.08	FQHCIQA	-0.6	0.1	4.4	0.2	0.5	0.5	5.4	0.9
81	99	4	8.93	FQHCIQALGEEHPIRVVNA	5.5	0.2	18.9	0.7	6.6	0.1	20.9	0.0
81	100	4	10.3	FQHCIQALGEEHPIRVVNAL	4.5	0.6	18.0	1.2	5.1	0.1	18.0	0.4
87	99	3	7.5	ALGEEHPIRVVNA	8.2	0.3	27.2	0.7	10.5	0.5	29.3	0.2
88	99	2	6.8	LGEEHPIRVVNA	9.1	0.7	23.9	2.9	9.5	0.3	24.6	0.9
88	100	3	8.74	LGEEHPIRVVNAL	4.8	0.2	15.0	1.7	5.6	0.2	19.1	0.3
89	100	3	7.13	GEEHPIRVVNAL	8.4	0.4	22.6	0.3	9.4	0.9	24.7	0.7
106	120	3	5.4	LIRGVHQKNKSTSGF	28.0	0.5	32.0	0.8	30.5	1.0	33.5	0.3
121	125	1	10.45	DIINM	9.5	1.8	70.5	2.6	8.2	0.5	67.8	0.3
121	126	1	13.16	DIINML	9.3	0.9	66.7	1.5	8.9	0.6	66.3	1.0
135	143	2	11.9	CMKNLMESL	1.2	0.8	11.6	0.2	1.9	0.2	13.2	3.8
169	174	1	6.05	VTDNIS	2.1	1.6	1.1	1.1	3.1	0.4	1.1	1.0
193	208	4	5.05	QILSHPPSRREHGYDA	7.2	1.1	21.7	2.2	7.3	0.7	20.9	0.3
215	231	4	10.41	LVNYRKYESVNPYIVKL	36.1	1.2	49.9	1.2	35.8	0.1	48.9	0.0
218	231	4	9.99	YRKYESVNPYIVKL	30.6	0.4	39.4	1.1	31.7	0.5	39.8	0.5
232	236	1	6	SIVDD	29.9	1.7	42.7	2.0	29.4	0.4	41.3	0.5
232	237	1	6.63	SIVDDE	37.5	0.4	45.4	0.6	37.0	1.1	44.4	0.1
232	240	1	9.59	SIVDDEATL	30.8	0.1	46.3	1.2	31.9	0.4	48.2	0.3
232	244	1	10.05	SIVDDEATLNGMG	22.1	0.8	34.1	1.4	22.1	0.2	35.0	0.5
237	244	1	7.66	EATLNGMG	5.1	1.2	24.6	1.4	4.9	0.2	22.3	0.8
238	244	1	7.18	ATLNGMG	4.5	0.1	15.3	0.5	4.0	0.9	12.4	0.9
245	250	1	7.89	LVIAQA	1.1	0.2	1.6	0.4	1.5	0.4	1.7	0.7
245	253	1	10.35	LVIAQALSE	2.4	0.1	13.9	0.3	1.7	0.0	12.7	0.1
245	269	4	10.66	LVIAQALSEYNRQYKDKEEEHQSGF	25.4	0.4	48.4	0.2	24.0	0.5	45.0	0.4
246	251	1	7.65	VIAQAL	1.1	0.1	1.5	0.2	1.5	0.5	1.8	0.2
246	253	1	7.35	VIAQALSE	3.1	0.7	13.6	0.7	0.7	0.4	14.3	0.1
254	269	4	5.51	YNRQYKDKEEEHQSGF	42.9	1.9	51.3	1.4	38.9	1.2	49.7	0.6
270	276	1	10.35	FSALTNM	91.6	0.5	91.3	3.7	93.8	0.4	93.8	0.6
277	281	1	10.19	VGSMF	77.8	1.3	79.1	0.8	81.5	3.0	79.4	1.5
281	295	3	7.52	FIADAHEKISVQTNE	74.2	1.5	77.9	1.0	76.7	0.9	78.1	1.1
282	295	2	6.16	IADAHEKISVQTNE	71.2	1.5	79.0	1.9	72.1	0.4	75.0	0.5
288	295	2	5.45	KISVQTNE	79.3	2.3	90.7	6.0	88.6	0.6	95.0	1.0
302	307	1	8.82	YEAVHL	2.3	0.3	3.4	0.2	2.8	0.5	2.8	0.4
302	315	3	11.94	YEAVHLNRNFITVL	4.8	0.5	26.2	0.8	5.2	0.2	23.5	0.4
304	315	3	11.32	AVHLNRNFITVL	4.9	0.7	29.2	1.2	6.5	0.5	28.1	1.0
308	315	2	11.45	NRNFITVL	3.0	0.3	44.7	0.6	3.6	0.2	37.4	0.1
311	315	1	12.19	FITVL	2.0	0.8	45.1	0.5	5.1	0.1	34.7	0.2
316	323	2	4.86	AQSHPEMG	69.5	3.2	69.0	2.5	67.5	1.3	67.0	0.9
316	324	1	8.25	AQSHPEMGL	60.8	1.3	60.5	0.4	61.7	1.4	60.7	1.2
316	347	3	9.81	AQSHPEMGLVTTPVSPAPTTPVTPLGTTPPSS	87.8	0.6	89.3	0.4	88.2	1.1	88.2	0.6
324	347	2	9.29	LVTTPVSPAPTTPVTPLGTTPPSS	96.1	1.2	98.1	1.3	98.5	1.4	99.2	0.3
325	348	3	8.88	VTTPVSPAPTTPVTPLGTTPPSSD	91.6	0.5	91.4	1.1	92.3	1.4	91.8	1.5
348	352	1	5.7	DVISS	81.4	0.7	81.6	2.6	84.0	0.3	83.0	1.1
352	359	1	10.55	SVELPLDA	70.2	0.8	76.2	0.3	76.6	2.1	77.2	0.9
353	358	1	9.55	VELPLD	0.3	0.2	0.1	0.1	0.5	0.6	0.8	0.7
353	359	1	10.3	VELPLDA	77.4	0.9	78.4	0.4	79.7	0.1	80.9	0.5
360	366	1	6.92	DVQTSNL	85.1	2.4	85.1	1.5	89.5	0.9	93.8	0.5
360	367	1	9.95	DVQTSNLL	67.6	2.1	79.0	7.7	69.1	1.7	78.5	1.3
367	371	1	13.85	LITFL	0.7	0.5	22.7	0.8	1.7	0.4	6.0	0.3
371	378	2	9.98	LKYSSIVM	1.7	2.0	4.7	4.2	3.9	1.4	3.9	1.1
376	394	4	7.9	IVMQDTKDEHRLHSGKLCL	9.0	0.7	14.0	1.1	10.4	0.3	13.9	0.4
379	394	2	6.99	QDTKDEHRLHSGKLCL	8.4	1.4	14.3	1.5	9.4	0.1	13.2	0.9
395	399	1	9.71	IILTC	3.5	1.1	4.9	1.1	2.3	0.2	2.3	0.4
398	404	1	5.59	TCIAEDQ	29.2	4.7	46.9	1.7	24.5	3.1	31.9	3.2
400	404	1	3.49	IAEDQ	33.6	2.6	62.3	3.7	31.4	0.8	44.5	4.4
400	408	1	6.75	IAEDQYANA	58.8	1.6	70.7	1.2	17.7	0.3	51.4	0.4
403	408	1	5.1	DQYANA	73.6	2.2	80.9	1.3	10.9	4.8	51.8	1.3
409	417	1	9.48	AAADDNMNF	69.8	1.8	69.2	0.6	30.0	1.2	44.5	2.0
445	449	1	10.95	AVLDL	0.4	0.6	2.0	0.3	1.0	0.6	4.9	0.6
453	466	3	13.52	FIVTHMMKEFPMDL	27.1	0.2	49.7	2.2	26.5	0.5	47.3	0.9
454	466	3	12.52	IVTHMMKEFPMDL	23.7	0.7	45.3	1.0	25.2	0.5	44.7	0.8
471	479	1	8.12	IQVVHKLLC	2.7	1.2	4.8	2.0	3.9	0.0	5.1	1.4
525	529	1	10.62	MIVNL	9.5	11.4	0.9	0.9	1.9	1.2	0.1	0.2
551	557	2	11.21	YYEIIRM	0.6	0.1	1.4	0.5	1.0	0.1	1.5	0.2
552	564	3	10.21	YEIIRMHQSFDNL	4.3	0.4	16.3	1.1	4.5	0.5	16.0	0.3
554	564	2	8.95	IIRMHQSFDNL	4.3	1.9	20.3	3.4	7.5	0.1	21.6	1.1
558	564	2	8.61	HQSFDNL	4.8	0.5	40.6	1.8	6.0	0.0	35.1	0.0
565	569	1	11.32	YSMVL	-0.1	1.6	7.1	0.5	0.3	0.4	6.3	0.5
569	577	2	6.41	LRLSTNAGQ	72.9	7.6	71.9	1.0	85.0	1.0	90.2	1.5
569	592	5	11.95	LRLSTNAGQWKEAASKVTHALVNI	34.8	0.6	69.1	1.4	32.8	0.6	66.5	0.3
570	594	5	11.03	RLSTNAGQWKEAASKVTHALVNIRA	28.0	0.2	56.4	1.3	27.6	0.4	56.7	0.2
572	594	4	11.2	STNAGQWKEAASKVTHALVNIRA	28.1	0.4	64.5	0.9	27.3	0.2	60.0	0.5
572	605	5	13.62	STNAGQWKEAASKVTHALVNIRAIINHFNPKIES	14.2	0.2	41.5	1.9	13.7	0.3	41.4	0.9
589	605	4	12.07	LVNIRAIINHFNPKIES	2.9	1.1	22.0	1.1	2.7	0.1	21.2	0.9
593	605	3	7.49	RAIINHFNPKIES	4.5	0.4	27.7	0.8	3.5	0.2	27.2	0.1
593	606	4	8.46	RAIINHFNPKIESY	2.3	0.1	29.4	0.5	3.2	0.0	29.2	0.2
595	605	3	7.69	IINHFNPKIES	4.1	0.2	34.3	0.5	4.0	0.1	34.2	0.4
595	606	3	8.88	IINHFNPKIESY	3.9	0.2	39.4	0.7	4.5	0.2	39.5	0.3
606	614	2	6.02	YAAVNHISQ	41.8	1.0	87.5	1.7	43.3	0.6	84.3	1.2
606	615	1	8.97	YAAVNHISQL	49.3	0.6	75.8	1.4	48.3	0.5	77.0	1.4
606	615	2	8.97	YAAVNHISQL	47.2	0.4	79.7	1.3	48.5	0.6	79.6	0.3
607	615	1	7.57	AAVNHISQL	48.8	1.8	75.3	1.2	50.3	1.0	77.2	2.8
622	628	1	6.35	EVVRANY	14.7	0.0	40.4	1.4	14.2	0.3	40.0	0.5
622	632	2	8.11	EVVRANYDTLT	39.5	2.9	57.7	1.4	36.1	0.0	59.8	1.0
623	628	2	5.57	VVRANY	18.7	0.2	47.2	2.6	17.4	0.6	49.6	1.1
632	641	2	8.71	TLKLQDGLDQ	67.8	1.9	82.8	1.2	63.6	0.3	83.2	0.6
633	641	2	8.45	LKLQDGLDQ	68.4	0.8	78.9	3.6	65.2	0.4	79.6	0.4
634	641	2	6.54	KLQDGLDQ	65.1	0.6	75.0	1.7	59.0	0.6	75.3	0.6
641	654	3	6.82	QYERYSEQHKEAAF	42.3	1.2	53.2	2.9	38.6	0.2	53.4	0.7
642	648	2	5.26	YERYSEQ	74.9	1.4	80.3	0.6	72.7	1.3	83.9	0.7
642	654	3	6.65	YERYSEQHKEAAF	38.6	0.9	50.8	2.2	34.7	0.5	50.7	0.4
655	664	2	7.99	FKELVRSIST	2.0	0.1	11.0	0.4	2.1	0.1	11.0	0.1
655	665	2	7.64	FKELVRSISTN	3.1	0.4	15.2	0.8	3.0	0.2	14.5	0.6
656	664	2	5.82	KELVRSIST	3.6	1.7	13.4	2.1	3.1	0.6	13.8	1.4
658	664	2	5.92	LVRSIST	5.3	0.3	20.8	0.8	4.3	0.6	21.5	0.5
665	672	2	8.14	NVRRNLAF	46.5	0.7	70.4	0.6	48.9	0.8	80.0	1.1
673	677	1	3.83	HTLSQ	79.8	1.1	81.6	3.0	84.3	2.5	84.3	1.7
673	680	1	8.87	HTLSQEVL	74.0	0.3	73.8	3.4	83.3	0.5	83.7	0.7
681	688	1	8.3	LKEFSTIS	76.3	3.2	76.9	1.7	80.4	0.8	83.7	0.1
684	688	1	7.18	FSTIS	86.7	1.0	94.4	1.5	90.8	0.8	97.2	1.2

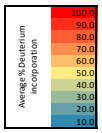

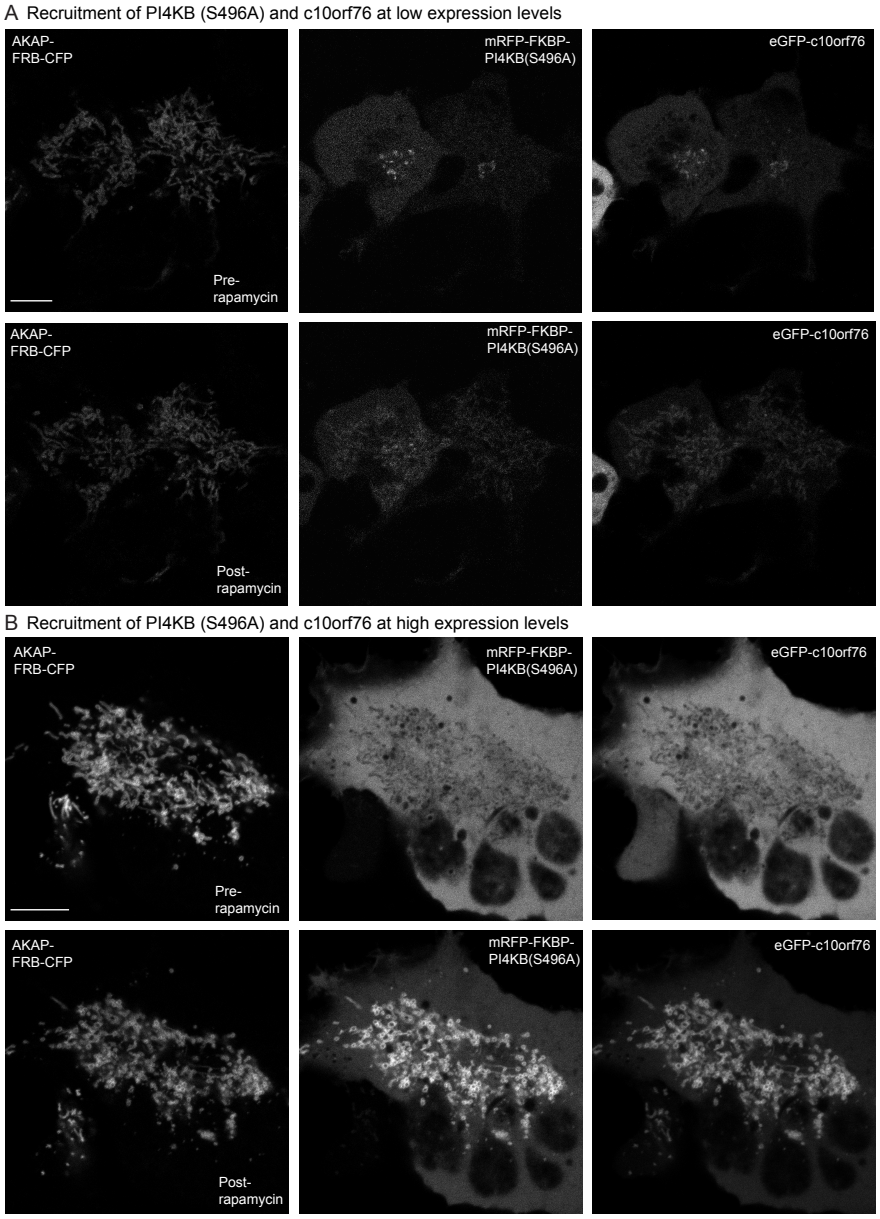

Appendix K. PI4KB (S496A) does not affect PI4KB or c10orf76 recruitment to the Golgi *in vivo* (refers to Fig. 3.5)

(**A**) Mitochondria recruitment experiment with PI4KB(S496A) and c10orf76 at low expression levels. Left: AKAP1-FRB-CFP is localized to the mitochondria before (top) and 5 minutes after rapamycin (100 nM) treatment (bottom). Middle: mRFP-FKBP12-PI4KB(S496A) at a low expression level is located at the Golgi before rapamycin (top) and translocates to the mitochondria after rapamycin induction (bottom). Right: eGFP-c10orf76 at a low expression level is located at the Golgi before rapamycin (top) and translocates to the mitochondria after rapamycin induction (bottom). (**B**) Mitochondria recruitment experiment with PI4KB(S496A) and c10orf76 at high expression levels (single cell zoom-in). Left: AKAP1-FRB-CFP is localized to the mitochondria before (top) and 5 minutes after rapamycin (100 nM) treatment (bottom). Middle: mRFP-FKBP12-PI4KB(S496A) at a high expression level saturates the Golgi and cytosol before rapamycin (top) and robustly translocates to the mitochondria after rapamycin induction (bottom). Right: eGFP-c10orf76 at a high expression level saturates the Golgi and cytosol before rapamycin (top) and robustly translocates to the mitochondria after rapamycin induction (bottom). Data information: Scale bars represent 10 μm.

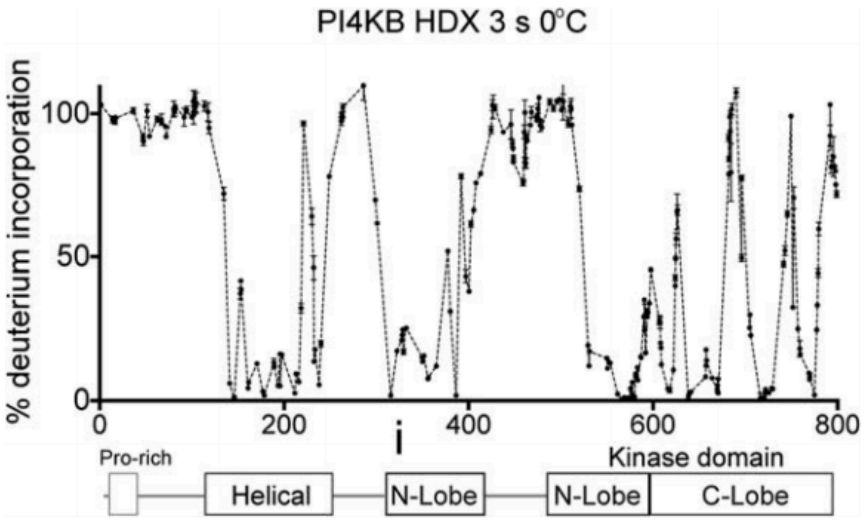

Appendix L. Identification of dynamic regions in PI4KIIIβ (refers to Fig. 4.2).
Hydrogen deuterium exchange levels for the full length PI4KIIIβ enzyme after 3 seconds of deuterium exposure at zero degrees. Every point in the graph represents an individual peptide, with the central residue (i) graphed on the x-axis versus HDX on the y-axis. The domain organization is shown below, with areas showing high levels of deuterium incorporation shaded gray. Experiments were carried out in triplicate, and error bars are shown on the graphs (most are smaller than the size of the point, average standard deviation across entire dataset was 1.01%).